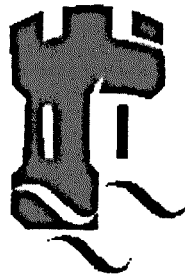


# **Microstructural evolution in AlSn–based gas atomised powder and thermally sprayed coatings**



**Chang Jing Kong, MSc**

**Thesis submitted to University of Nottingham  
for the degree of Doctor of Philosophy**

**July 2004**

# Contents

## Acknowledgments

## Abstract

## Chapter 1 Introduction ----- 1

## Chapter 2 Literature review ----- 5

2.1	Introduction -----	5
2.2	Bearing alloys -----	5
2.2.1	<i>The history of bearing development</i> -----	5
2.2.2	<i>The structure of bearings</i> -----	6
2.2.3	<i>Relative factors for selecting bearing materials</i> -----	7
2.2.4	<i>The metallurgy of bearing materials</i> -----	9
2.2.5	<i>The manufacturing process of bearings</i> -----	11
2.3	High velocity oxy-fuel thermal spraying -----	11
2.3.1	<i>Introduction</i> -----	11
2.3.2	<i>The development of HVOF spraying</i> -----	12
2.3.3	<i>The HVOF technique</i> -----	13
2.3.4	<i>HVOF thermally sprayed coatings</i> -----	14
2.3.5	<i>HVOF thermally sprayed Al-Sn based materials</i> -----	17
2.4	Al-Sn(Cu) and Al-Sn (Si) phase equilibrium diagrams -----	18
2.5	Microstructure formation mechanisms of different immiscible alloys -----	23
2.6	Mechanisms of separated liquid droplet coarsening in a liquid matrix -----	34
2.7	Factors affecting particle distribution and shape, and matrix phase growth velocity -----	35
2.8	The orientation relationship between Sn particles and Al matrix -	37
2.9	Cooling rate and undercooling during rapid solidification -----	38
2.9.1	<i>Principle of heat transfer</i> -----	39
2.9.2	<i>Gas atomised powder</i> -----	41
	2.9.2.1 Cooling rate -----	41
	2.9.2.2 Undercooling -----	44
2.9.3	<i>Thermal spray coating</i> -----	48
2.10	Effect of annealing Al-Sn (Cu, Si) alloys -----	49
2.10.1	<i>The mechanisms of liquid droplet coarsening within a solid matrix</i> ---	49
2.10.2	<i>Precipitation in supersaturated Al-Cu alloys during heat treatment</i> -	52
2.11	The basic concept of corrosion -----	54
2.11.1	<i>Metallurgical factors</i> -----	54
2.11.2	<i>The corrosion of pure Al, Sn and two phase Al-Sn alloy</i> -----	55



2.12	Summary -----	57
	References -----	58
<b>Chapter 3 Experimental method -----</b>		<b>65</b>
3.1	Introduction -----	65
3.2	Materials - gas atomised powder -----	65
3.3	High velocity oxy-liquid fuel (HVOLF) spray deposition and heat treatment of the coatings -----	66
3.3.1	<i>HVOLF thermal spraying</i> -----	66
3.3.2	<i>Heat treatment of the coatings</i> -----	70
3.4	Characterisation -----	70
3.4.1	<i>XRD</i> -----	70
3.4.2	<i>Interaction of the electron beam with matter</i> -----	71
3.4.3	<i>SEM</i> -----	72
3.4.4	<i>TEM</i> -----	73
	3.4.4.1 TEM sample preparation technique -----	73
	3.4.4.2 TEM (BF, DF and WB techniques) -----	75
	3.4.4.3 EDX -----	77
	3.4.4.4 Moiré pattern -----	78
	3.4.4.5 HRTEM -----	79
	3.4.4.6 EELS and EFTEM -----	79
3.4.5	<i>Image analysis of particle distribution</i> -----	80
3.5	Evolution of properties -----	81
3.5.1	<i>Corrosion testing</i> -----	81
3.5.2	<i>Microhardness</i> -----	81
3.6	Summary -----	82
	References -----	83
<b>Chapter 4 Al<sub>12</sub>Sn<sub>1</sub>Cu gas atomised powder and as sprayed coating-Result and Discussion -----</b>		<b>84</b>
4.1	Introduction -----	84
4.2	Characterisation of gas atomised powder -----	85
4.2.1	<i>XRD analysis</i> -----	85
4.2.2	<i>Microstructure investigation</i> -----	85
	<u>SEM observation</u> -----	85
	<u>TEM observation</u> -----	88
4.3	Characterisation of as-sprayed coatings -----	103
4.3.1	<i>XRD analysis</i> -----	103
4.3.2	<i>Microstructure investigation</i> -----	103
	<u>SEM observation</u> -----	103
	<u>TEM observation</u> -----	105
4.4	Discussion -----	117
4.4.1	<i>Introduction</i> -----	117

4.4.2	<i>Qualitative analysis of microstructure formation from the thermodynamic and kinetic point of view</i> -----	118
4.4.3	<i>Quantitative understanding of the effect of cooling rate on the phase selection</i> -----	123
	4.4.3.1 Introduction-----	123
	4.4.3.2 The relationship between cooling rate, heat transfer coefficient and gas atomised particle size-----	124
	4.4.3.3 The relationship between cooling rate and extent of undercooling-----	129
4.4.4	<i>The effect of different Sn and Cu contents on liquid phase separation</i>	133
4.4.5	<i>The microstructure formation mechanisms of gas atomised AlSnCu powders</i> -----	134
4.4.6	<i>The microstructure formation mechanisms in HVOLF thermally sprayed coatings</i> -----	139
4.5	<b>Summary</b> -----	143
	<b>References</b> -----	145
<b>Chapter 5 Al<sub>12</sub>Sn<sub>1</sub>Cu heat treated coatings</b> -----		147
5.1	<b>Introduction</b> -----	147
5.2	<b>X-ray spectra of annealed coatings</b> -----	147
5.3	<b>The effect of heat treatment on the microstructure of the coatings</b>	148
5.3.1	<i>The Sn particle size change with heat treatment</i> -----	148
	<u>SEM micrographs</u> -----	148
	<u>Quantitative statistics of large Sn particles</u> -----	149
	<u>Associated TEM micrographs</u> -----	150
5.3.2	<i>Cu in the annealed coatings</i> -----	151
	<u>EDX-TEM results</u> -----	151
	<u>EELS and EFTEM results</u> -----	152
5.3.3	<i>Orientation relationship between the Sn particles and the Al matrix for the coating annealed at 300°C for 1 hour</i> -----	152
5.4	<b>The effect heat treatment time and temperature on the coating / substrate interface</b> -----	153
5.5	<b>Discussion</b> -----	173
5.6	<b>Summary</b> -----	177
	<b>References</b> -----	179
<b>Chapter 6 The relationship of corrosion resistance to the microstructure</b> -----		180
6.1	<b>Introduction</b> -----	180
6.2	<b>Polarization curve of Al<sub>12</sub>Sn<sub>1</sub>Cu thermally sprayed coatings</b> ----	180
6.3	<b>SEM analysis of corroded as-sprayed and annealed coatings</b> ----	181
6.3.1	<i>The corroded as-sprayed coatings</i> -----	182
	<u>Surface observation</u> -----	182
	<u>Cross-section observation</u> -----	183

6.3.2	<i>The corroded coatings annealed at 300°C for 1 hour</i> -----	184
	<u>Surface observation</u> -----	184
	<u>Cross-section observation</u> -----	184
6.3.3	<i>The corroded coatings annealed at 450°C for 1 hour</i> -----	185
	<u>Surface observation</u> -----	185
	<u>Cross-section observation</u> -----	187
6.4	<b>Discussion</b> -----	199
6.5	<b>Summary</b> -----	203
	<b>References</b> -----	204

## **Chapter 7 Al<sub>20</sub>Sn<sub>3</sub>Si powder, as sprayed and annealed coatings-Results and Discussion**----- 205

7.1	<b>Introduction</b> -----	205
7.2	<b>Characterisation of gas atomised Al<sub>20</sub>Sn<sub>3</sub>Si powder</b> -----	206
7.2.1	<i>XRD spectrum of the Al<sub>20</sub>Sn<sub>3</sub>Si</i> -----	206
7.2.2	<i>SEM microstructure of the Al<sub>20</sub>Sn<sub>3</sub>Si gas atomised powder</i> -----	206
7.3	<b>Characterisation of as-sprayed Al<sub>20</sub>Sn<sub>3</sub>Si coatings</b> -----	207
7.3.1	<i>XRD spectrum of the as-sprayed Al<sub>20</sub>Sn<sub>3</sub>Si coatings</i> -----	207
7.3.2	<i>SEM microstructure of the as-sprayed Al<sub>20</sub>Sn<sub>3</sub>Si coatings</i> -----	207
7.3.3	<i>TEM microstructure of the as-sprayed Al<sub>20</sub>Sn<sub>3</sub>Si coatings</i> -----	208
7.3.4	<i>HRTEM microstructure of the as-sprayed Al<sub>20</sub>Sn<sub>3</sub>Si coatings</i> -----	210
7.4	<b>Characterisation of the Al<sub>20</sub>Sn<sub>3</sub>Si annealed at 300°C for 1 hour</b> 211	
7.4.1	<i>XRD spectrum of the Al<sub>20</sub>Sn<sub>3</sub>Si coatings annealed at 300°C for 1 hour</i> 211	
7.4.2	<i>SEM microstructure of the Al<sub>20</sub>Sn<sub>3</sub>Si coatings annealed at 300°C for 1 hour</i> -----	211
7.4.3	<i>TEM microstructure of the Al<sub>20</sub>Sn<sub>3</sub>Si coatings annealed at 300°C for 1 hour</i> -----	212
7.5	<b>The microhardness of the Al<sub>20</sub>Sn<sub>3</sub>Si gas atomised powder, as-sprayed coatings and coatings annealed at 300°C annealed at 1 hour</b> -----	213
7.6	<b>Discussion</b> -----	236
7.6.1	<i>Gas atomised powder</i> -----	236
7.6.2	<i>As-sprayed Al<sub>20</sub>Sn<sub>3</sub>Si coatings</i> -----	237
7.6.3	<i>Al<sub>20</sub>Sn<sub>3</sub>Si coatings annealed at 300°C for 1 hour</i> -----	239
7.7	<b>Summary</b> -----	240
	<b>References</b> -----	242

## **Chapter 8 Conclusions** ----- 243

### **Further work** ----- 247

### **Publications** ----- 249

## Acknowledgments

I wish to express my appreciation to my supervisors Prof. D. Graham McCartney and Dr. Paul D. Brown. Over the past 3 years they have given me a lot of help in my work and my life. Whenever I have a discussion with Professor McCartney, he always promotes a deeper understanding of the science. I also especially appreciate the help of Dr. Paul D. Brown for supervising the operation of the TEM and for discussing scientific phenomena. He also shows his patience by revising my clumsy thesis English many times.

I would also like to thank the support staff within the School of Mechanical, Materials, and Manufacturing Engineering. Keith Dinsdale, Aubrey Martin, Nikki Weston and Julie Thornton etc. They are the best in the worlds and have always given me strong support whenever needed.

Thanks also to my colleagues Dr. Andrew Horlock, Dr. Mike Fay, Dr. Deen Zhang and Dr. Grigore Moldovan and Miss Pearl Agyakwa for helping with my experiments and for discussions. Especial thanks to Mike Fay who patiently helped me to do EELS.

I am also grateful to Professor Sam Harris for constructive discussions on the understanding of experimental results. Thanks also to Dr. Donald Kingerley and Dr. Peter Borden for helpful discussions of the corrosion results.

I specially thank my mother for her support looking, after my son. Family support has helped me overcome many difficulties in this period.

## Abstract

This thesis reports on the microstructure of Al-Sn based powders and the development of Al-Sn based coatings for automotive shell bearing applications deposited using the high velocity oxy-liquid fuel (HVOLF) thermal spray technique. The microstructure of the coating and its associated physical and chemical properties, such as microhardness and corrosion resistance, are investigated as a function of the HVOLF thermal spraying parameters. In particular, a detailed microstructural understanding of the thermal sprayed coatings is developed to explain the coating properties.

Two alloy systems, Al-12wt.%Sn-1wt.%Cu and Al-20wt.%Sn-3wt.%Si have been investigated in detail using X-ray diffraction (XRD), scanning electron microscopy (SEM), transmission electron microscopy (TEM) and energy dispersive X-ray (EDX) analysis. The high resolution transmission electron microscope (HRTEM), electron energy loss spectroscopy (EELS) and energy filtered TEM have also been used to examine nanoscale precipitates as supplementary methods. The statistical image analysis of fine scale particulate dispersions has also been used to study the second phase evolution with annealing.

The microstructure of the large gas atomised powder particles used in the HVOLF thermal spray process comprise dendritic Al and interdendritic Sn, whilst the small powder particles exhibit fine scale Sn particles distributed within an Al matrix. The as-sprayed coatings comprise a mixture of melted and partially melted splats due to the full and partial melting of the deposited powder. Nanoscale Sn particles distributed in the Al matrix are present in fully melted regions, whilst micron / sub-micron Sn particle distributions and Sn-particle free Al regions delineate partially melted regions. Cu

remains in solid solution within the Al matrix of the Al-12wt.%Sn-1wt.%Cu as-sprayed coatings, whilst Si formed nanoscale particles in the Al-20wt.%Sn-3wt.%Si as-sprayed coatings.

The critical cooling rate to form the metastable liquid phase separation within Al-12wt.%Sn alloys is put forward according to calculation. If the cooling rate is lower than the critical cooling rate, dendritic Al and interdendritic Sn are formed, thereby explaining the structure of large gas atomised powder particles. If the cooling rate is higher than the critical cooling rate, a liquid phase separation reaction occurs to form fine scale Sn dispersion. The calculated critical Al-12wt.%Sn powder diameter for liquid phase separation is close to the experimentally observed Al-12wt.%Sn-1wt.%Cu powder diameter. The discrepancy between experiment result and theoretical calculation is attributed to the additional element Cu promoting the liquid phase separation. The nano and sub-micron scale Sn distribution in small gas atomised powder particles and the as-sprayed coatings is attributed to the cooling rate being higher than the critical cooling rate. The dendritic structure of the large Al-Sn-Cu gas atomised powder is due to the cooling rate being lower than the critical value.

Heat treatments are applied to the as-sprayed coatings to alter the mechanical and chemical properties, such as, microhardness and corrosion resistance, of the bearing material coatings. Annealing causes the nanoscale and sub-micron Sn particles to coarsen within both Al-12wt.%Sn-1wt.%Cu and Al-20wt.%Sn-3wt.%Si coatings according to the analysis of SEM and TEM images. The Sn particles coarsen greatly within the Al-12wt.%Sn-1wt.%Cu coatings annealed at 300°C for 5 hours, as compared with coatings annealed for 1 hour. The  $\theta'$ -phase ( $\text{CuAl}_2$ ) also precipitates in the Al-12wt.%Sn-

1wt.%Cu coatings after annealing at 300°C. Annealing also causes fine scale Si particles to coarsen greatly in the Si containing alloy. The microhardness decreases in the annealed coatings for both alloys and is attributed to a coarsening of Sn particles and the release of residual strain within the as-sprayed coatings.

As compared with the as-sprayed coatings and the coatings annealed at 300°C for 1 hour, the corrosion rate in 0.1M NaCl solution of Al-12wt.%Sn-1wt.%Cu coatings annealed at 450°C for 1 hour is very greatly reduced. However, an annealing temperature of ~ 450°C is not appropriate for these coatings because of the introduction of interlayer cracks and a coating / substrate reaction which might degrade the mechanical properties of the bearing.

# Chapter 1

## Introduction

---

The design characteristics of modern, highly loaded engines place increasing demands on bearing systems <sup>[1, 2]</sup>. These characteristics usually result in an increased specific load on the bearings; due either to a reduction in the size of components or an increase in the applied loading, or both. Under these circumstances, bearings are required to balance conflicting properties, with regard to a simultaneous need for strength and compliance under all the operational conditions encountered.

Bearings for automotive engine applications traditionally comprise a two or three layered structure formed in a half-shell <sup>[3]</sup>. Applications which require the highest fatigue strength typically use a tri-metal bearing design comprising a strong bearing alloy bonded to a steel backing, plus a thin layer of softer material on the working surface <sup>[1]</sup>. The high wear rate and high cost are the main drawbacks preventing tri-metal bearings being universally adopted. For applications with a lower fatigue strength requirement, bi-metal bearings based on aluminium alloys have been developed where the layer bonded to the steel substrate does not require an overlay for operation. These alloys have suitable bearing properties and, because of their low inherent wear characteristics compared with tri-metals, allow tolerances in the bearing system to be maintained close to their assembled values over relatively long time periods. The challenge for bearing manufacturers is to develop such materials for use in applications which are more demanding.



Conventional fabrication methods for bimetal bearings include casting, powder metallurgy and roll bonding processes. An alternative approach based on high velocity oxy-gas fuel (HVOGF) thermal spraying has been developed to produce shell bearings directly onto steel substrates by McCartney and Harris in 1998, thereby simplifying the conventional manufacturing process <sup>[4]</sup>. Rapid solidification combined with the high velocity of particle impingement associated with HVOGF thermal spraying lead to the development of a complex, intermixed microstructure. Due to the consideration of bearings properties, such as, compatibility, conformability, embeddability, fatigue strength, corrosion resistance etc, the spraying materials were selected as an Al-Sn based alloy. This adapts the metallurgical design of a bearing, involving discrete soft phase pockets distributed within a strong matrix. In the conventional bearing manufacturing process, the Sn phase has provide a self-lubricant function which offers excellent tribological properties <sup>[5]</sup>. Tin could also improve the inherently poor compatibility of a bearing. Additions of silicon, copper, nickel, magnesium or manganese act to strengthen the aluminium <sup>[6-8]</sup> through solid-solution and precipitation mechanisms. In the HVOGF thermally sprayed coatings <sup>[9]</sup>, the nanoscale Sn particles dispersed in an Al matrix are found in Al-Sn, Al-Sn-Cu and Al-Sn-Cu-Si systems formed by high velocity oxy-gas fuel (HVOGF) thermal spraying. As-sprayed Al-Sn coatings are found to be highly reactive with water, but the addition of Cu acts to increase the corrosion resistance of the as-sprayed coatings as compared with the binary Al-Sn alloy.

Although all the evidence is promising for bearing manufacture, a limitation still exists in that the design of the HVOGF thermal spraying system presently employed is not well suited to spraying metals with a melting point below 750°C. The feedstock powder can readily block the nozzle of the spraying gun. The

relatively low spraying temperature and high particle impingement velocity of the high velocity oxy-liquid fuel (HVOLF) thermal spraying technology may resolve these problems. The whole project aims to investigate the manufacture of AlSn-based bearing coatings by the HVOLF thermal spraying technique. The effect of the HVOLF thermal spraying parameters on the microstructural development and the resultant properties of the coatings, such as wear resistance, fatigue resistance and corrosion resistance, are also considered. As part of the whole project, the main theme of this thesis is focused on the microstructural evolution of gas atomised powder and thermally sprayed Al-Sn based alloy coatings and how these microstructures relate to some of the coating properties. Chapter 2 introduces background information necessary to understand the microstructural evolution of thermally sprayed bearing materials and the gas atomised powders. Chapter 3 introduces the experimental methods used for the coating characterisation. Chapter 4 explains the microstructural formation mechanisms of gas atomised powder particles and the as-sprayed coatings of Al<sub>12</sub>Sn<sub>1</sub>Cu alloys. The concept of critical cooling rate which affects the liquid phase separation of Al-Sn based alloys is advanced in accordance with theoretical calculations. Chapter 5 considers the effect of annealing on the microstructure, the microhardness and the coating /substrate interface, and the effect of microstructural change in the mechanical properties of Al<sub>12</sub>Sn<sub>1</sub>Cu coatings. In Chapter 6, Al<sub>12</sub>Sn<sub>1</sub>Cu coatings, following corrosion testing, are characterised and the relationship between the microstructure and the corrosion resistance of the as-sprayed and subsequently annealed Al<sub>12</sub>Sn<sub>1</sub>Cu coatings analysed. Chapter 7 introduces the microstructure and microhardness evolution of the Al<sub>20</sub>Sn<sub>3</sub>Si gas atomised powder, and the as-sprayed and annealed coatings. Finally, in Chapter 8, the conclusions of these investigations are emphasized.

## References

1. W. P. Brown, H. Galand, G. R. Kingsbury and M. Scott, *Aluminium bi-metal bearing developments for automotive and medium speed diesel applications*. Industrial Lubrication and Tribology, 1996. **48**(3): p. 4-11.
2. G. C. Pritt. *Aluminium alloys for automotive crankshaft bearing*. in *Proceeding of Japan International Tribology Conference*. 1990, p.125-130. Nagoya, Japan. Publisher: Japanese Society of Tribologists, Kikai Shinko Kaikan No. 407-2, 2-8 Shiba Koen 3-Chome Minatoku, Tokyo 105, Japan.
3. The ASM Committee, *Materials for sliding bearings*. Metals Handbook, 1980. **3**: p. 802-822.
4. S. J. Harris, D. G. McCartney, A. J. Horlock and C. Perrin, *Production of ultrafine microstructure in Al-Sn, Al-Sn-Cu and Al-Sn-Cu-Si alloys for use in tribological application*. Materials Science Forum, 2000. **331-337**: p. 519-526.
5. W. J. Whitney. *An advanced aluminium-tin-silicon engine bearing alloy and its performance characteristics*. in *SAE International conference and exposium*. 1995: p.1-5, Detroit, USA.
6. M. Fujita, A. Ohgawara, T. Salai, T. Ohgaki and T. Ohsaki, *Aluminium bearing alloy and two-layer bearing materials having layer of aluminium bearing alloy therein*. 1988: USA Patent US4789609.
7. T. Tanaka, M. Sakamoto and Y. Sato, *Multi-layer slide bearing having Al-Sn alloy layer with high fatigue strength and conformability*. 1995: USA Patent US5284205.
8. M. Nakano, T. Tanaka, M. Sakamoto and Y. Satoh, *Bearings*. 1992: UK Patent GB2252565.
9. A. J. Horlock, *HVOF Spraying of Novel Bearing Materials*, in *School of Mechanical, Materials, Manufacturing Engineering and Management*. 1999, University of Nottingham (PhD thesis): Nottingham.

## **Chapter 2**

### **Literature review**

---

#### **2.1 Introduction**

In this chapter, the basic background about bearings, the HVOF thermal spraying technique and the HVOF thermal spraying of bearings is introduced to help understand this project. The emphasis is on knowledge introduction of the relationship between processing and the microstructure of limited solid solution alloys during rapid solidification. The mechanisms of microstructure formation for Al-Sn alloys are investigated, according to a comprehensive understanding of similar immiscible alloys during rapid solidification. The resultant microstructure, such as the second phase morphology and size, has been connected to the heat extraction rate during rapid solidification. The effective parameters such as heat transfer coefficient, cooling rate and extent of undercooling of powder particles and the thermally sprayed coatings are also introduced. The mechanisms of liquid droplet coarsening in the solid matrix and the precipitation that occurs during the annealing process are also introduced. Finally, some basic principles of the corrosion of Al alloys are described.

#### **2.2 Bearing alloys**

##### **2.2.1 The history of bearing development**

Plain bearing principles have been employed in rotating mechanical devices since about 3000 BC <sup>[1]</sup>. However, the first use of a metal alloy for its special properties in a bearing application was probably Isaac Babbitt's adaptation of a

pewter composition in 1839. The so-called Babbitt alloys are still recognised as important bearing materials at the present time, and may be tin based (Sn-8wt.%Cu-8wt.%Sb) or lead based (Pb-10wt.%Sn-15wt.%Sb). The early bearings were made by the machining of massive or cast alloys. Since the 1930s, bearing developments have proliferated with respect to materials systems, mechanical design and manufacturing technology. Bearings range from simple duplex alloys to multilayer-laminated metals and alloys where a sophisticated combination of metallurgical, chemical and mechanical processes is employed.

### **2.2.2 The structure of bearings**

Bearings are frequently classified according to the material construction, i.e. as solid (single-metal), bimetal (two-layer), or tri-metal (three-layer) bearings <sup>[1]</sup>. These terms indicate the number of principal mechanically functional layers, not including cosmetic surface finishes, bonding layer diffusion zones or other microscopically thin interfacial layers. All three of these constructions are in widespread commercial use, in a wide variety of applications. The use of two or three separate layers provides a means of exploiting combinations of properties that cannot be obtained with single metals and has proved to be one of the most important factors in the successful development of cost-effective bearing materials.

Nowadays, most automotive bearings are made of a bimetal or tri-metal design, because they are required to withstand severe loading and cyclic loading conditions, shaft deflection effects, corrosion and high temperatures <sup>[2]</sup>.

By way of example, a tri-metal bearing may consist of a steel backing, a copper or aluminium intermediate layer and a lead alloy surface layer. In such cases, the tri-metal bearing design is appropriate for use in severe applications, such as combined high loading and cyclic loading. However, some drawbacks of the tri-

metal bearing system prevent its universal adoption. Firstly, the lead-based layer invariably wears at a higher rate than the lining material. Secondly, corrosion is a consideration for the overlay and the lining below if a copper-lead alloy is used. Thirdly, tri-metal bearings generally have higher costs and require more complicated production processes.

Currently, bimetal bearing designs which have better properties than single-metal systems and cost less as compared with tri-metal systems are used in most situations.

Bimetal systems employ a strong bearing backing (e.g. steel) to which a softer, weaker, relatively thin layer of bearing alloy is metallurgically bonded. Low-carbon steel is by far the most widely used backing material although alloy steel, bronzes, brasses and aluminium alloys are also used. When steel backing are employed, the load-capacity ratings for both copper and aluminium alloys are sharply increased above those of the corresponding single metals, without degradation of any other properties. Similarly, the strong backing material permits the use of lead or tin containing alloys that have extremely good surface properties but otherwise are so low in strength that they can only be used themselves as single-metal bodies under very light loads.

### **2.2.3 Relative factors for selecting bearing materials <sup>[1,3]</sup>**

The choice of materials to be specified for bearings will be dependent on a number of factors. This includes the load, speed and lubrication that the bearings endure. Related material properties, such as compatibility, conformability, embeddibility, fatigue strength and corrosion resistance etc, need to be considered.

Bearings are machine elements designed to transmit loads or reaction forces. When a bearing is working, the unit load on the bearing is affected by its rotation

speed. The real load on the bearing will increase when the rotation speed increases. In this context, the steel backed bimetal bearing design seems a positive factor to endure high loads.

Oil and grease are generally used to minimise friction associated with the sliding movement. However, under the actual conditions of bearing operation, some contact between the shaft and bearing surface is unavoidable. Wear of the bearing surface becomes excessive under this condition. More severe failure will cause seizure or partial melting of the bearing liner. This requires the bearing materials to exhibit good anti-friction properties.

Although automotive bearings usually are not required to operate in extreme chemical environments, it is possible, for corrosion problems to develop in lubricating oils as a result of oxidation or by reaction with the engine coolant or combustion products.

Compatibility is an antiseizure / antiscoring characteristic that relates the ease with which the bearing and journal surface may adhere or weld together under the influence of pressure and heat, in the absence of lubricant or some other interfering surface film. Factors of influence include the relative difference between the atomic diameters of bearing materials and the nature of the bonds (metallic or covalent) that may form. For example, if the journal is steel then the compatibility should be good if the atomic diameter of the bearing material is greater, by at least 15%, than that of iron (i.e., not less than 0.285nm). Only seven commercially significant metals meet these criteria, namely, silver, cadmium, indium, tin, gold, lead and bismuth. Of these, tin and lead offer the most attractive combination of cost, availability and engineering properties. These elements may be used as the base alloy, for example

within Babbitt alloys, or as the major microconstituents, such as in aluminium-tin alloys.

Both conformability and embeddability depend on the yield and plastic flow of the bearing material under load. Thus, it is not surprising that the low modulus metals of lead and tin exhibit good properties. Conversely, stronger, higher modulus materials such as copper and aluminium exhibit high load and high fatigue strength. Useful compromises between these sets of conflicting requirements are provided by the use of multiphase structural alloys and by employing a layered construction in which softer and weaker surface layers are reinforced by one or much harder, stronger backing layers.

#### 2.2.4 The metallurgy of bearing materials

When examining the structure of bearing materials, three general microstructural features <sup>[1]</sup> can be distinguished: (1) **Soft matrix with discrete hard particles** (lead and tin Babbitt alloys are of this type). (2) **Interlocked soft and hard continuous phases** (many copper-lead alloys are of this type). (3) **Strong matrix with discrete soft phase pockets** (e.g., leaded bronzes and aluminium alloys). The structures of the third system typically consist of a continuous copper-base or aluminium-base metallic matrix of intermediate to high strength that contains discrete pools or pockets of lead or tin. Conformability, embeddability, strength and hardness are dictated by the strength of the matrix phase. Compatibility is enhanced if the soft-phase material is exposed at the bearing surface.

Aluminium alloys used as a bearing material originate from about 1940, when low-tin aluminium alloy castings were introduced to replace solid bearings for heavy machinery. Nowadays, both bimetal and tri-metal aluminium alloy systems are commercially used in automotive bearings.<sup>[2, 4]</sup> Additions of silicon, copper, nickel or



manganese act to strengthen the aluminium <sup>[5-7]</sup> through solid-solution and precipitation mechanisms, while fatigue strength and the opposing properties of conformability and embeddability are also largely controlled by these elements. Tin, cadmium and lead are instrumental in improving the inherently poor compatibility of aluminium.

As one of the bearing alloys, Al-Sn offers excellent tribological properties<sup>[8]</sup> that have led to its extensive use in engineering applications, particularly automotive shell bearings. The anti-friction characteristics of Al-Sn alloys come from the soft Sn, whilst additional elements, e.g. Cu, Si and Mn, can strengthen the alloy. In addition, Cu is found to improve the corrosion resistance of the alloy and to introduce slight age hardening effects during the lifetime of the bearings <sup>[9, 10]</sup>.

An alloy composition commonly used for bearing applications is Al-(12~20)wt.%Sn-(1~3)wt.%X (X = Cu, Si, Mn or Ni). This alloy was originally developed in Germany during World War II as a substitute for the more traditional Cu-Pb alloys and has been used extensively since the 1960s <sup>[10]</sup>. As a consequence of the limited solid solubility of Sn in Al, the as-cast structure of this alloy is entirely dendritic, with tin in elemental form as interdendritic phase. Plastic deformation causes the break up of the tin network and following annealing (typically at 500°C) the tin agglomerates and spheroidises, thereby increasing the ductility of the alloy and making it suitable for bearings.

For commercial bearing alloys containing 1-2wt%Cu, the majority of the copper is expected to remain within solid solution in the condition in which the bearing is supplied (i.e. as a non-equilibrium cooled material). However, in service (i.e. at operating at temperatures up to 250°C) the copper may precipitate as a hardening phase. Advantage may be taken of this feature, i.e. during the early stages

of use the bearing has good conformability properties, but over time the bearing alloy hardens, thereby improving wear and fatigue properties.

In commercial bearing alloys, compositions containing 3 ~ 4wt% silicon are typical, with the silicon precipitated as a hard phase to confer improved wear properties. Si normally adopts the form of a needle-like morphology within a cast structure. A morphology of near-spherical Si rich particles is found in alloys used in industry modified by appropriate heat treatments.

More recent developments of Al-Sn based alloys include the variation of the distribution of the Sn dispersion that progressively increases toward the wear resistance, fatigue resistance, super seizure resistance and good comfortability<sup>[5-7]</sup>.

### **2.2.5 The manufacturing process for bearings**

Conventional fabrication methods for bimetal bearings include casting, powder metallurgy and roll bonding processes<sup>[1]</sup>. However, nearly all commercial manufacture of bimetal aluminium alloy bearing strip materials is currently done by roll bonding the alloy to a steel backing strip. In the roll bonding process of Al-Sn bimetal bearings, an ingot of Al-Sn alloy is rolled down to a thin strip and annealed. Then, the Al-Sn strip is rolled bonded to a thin interlayer of pure Al following annealing. Further, they are then rolled to bond to a steel substrate. A typical structure consists of a 1.5 mm thick steel substrate, a 50 µm pure Al interlayer and a 300 µm thick Al-Sn bearing material.

## **2.3 High velocity oxy-fuel (HVOF) thermal spraying**

### **2.3.1 Introduction**

Thermal spraying covers a number of techniques which modify a surface by the deposition of a coating layer. The thermal spray processes are differentiated by the energy source (combustion or electrical), feed materials (particulate or solid) and

surrounding environment (air, low pressure, inert gas) <sup>[11]</sup>. Therefore, they have different names <sup>[12]</sup>, such as flame spraying, plasma spraying or high velocity oxy-fuel (HVOF) spraying. The schematic diagram of Figure 2.1 categories the different thermal spraying methods. HVOF thermal spraying is based on a high-pressure internal combustion process, similar to a miniature rocket engine.

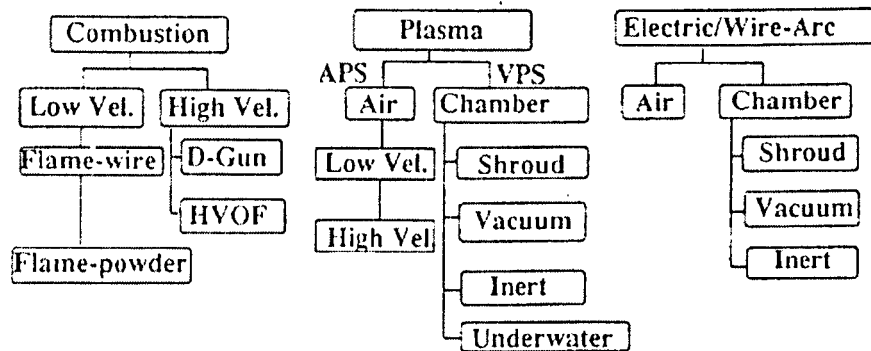


**Figure 2.1** An illustration of thermal-spray methods

### 2.3.2 The development of HVOF spraying

A number of variants of HVOF spray torches have been introduced into the marketplace during the last decade <sup>[12, 13]</sup>. The original HVOF torch, called the Jet Kote, was invented by Jim Browning and licensed to Cabot Corporation and, subsequently Deloro Stellite. Since this original device, Sulzer Metco has introduced two versions of the HVOF torch, under the name Diamond Jet. These operate in either air cooled or water-cooled modes using a variety of combustion gases. Praxair Surface Technology in the United States and UTP based in Europe have introduced a higher-enthalpy version of the HVOF spray torch that allows deposition of refractory ceramics, the Top Gun system. More recently, the TAFA Corporation (now Praxair TAFA) introduced a liquid-fuel version of the HVOF torch, referred to as the JP-5000. In addition, another liquid fuel gun, almost identical to the JP-5000, is

manufactured in the UK and called the Met Jet. Here, oxygen is combined with kerosene to provide a high velocity, low-thermal input spray torch, enabling the formation of high-density deposits.

### 2.3.3 The HVOF technique

The difference between HVOF and conventional flame spraying is that the combustion is internal to the nozzle, and the gases are at a much higher pressure than those undergoing atmospheric combustion in a flame spray. HVOF thermal spraying has a high velocity for the combustion gas, up to  $2400 \text{ ms}^{-1}$  [14]. The high gas velocity causes particle velocities around  $400$  to  $800 \text{ ms}^{-1}$  [15]. Some analysis concludes that the particles with size of  $10\mu\text{m}$  achieve a velocity as high as  $1050 \text{ ms}^{-1}$ , whilst the particles with size of  $50\mu\text{m}$  gain a velocity of  $\sim 500 \text{ ms}^{-1}$ . [16] However, the flame temperature is similar to that of low-velocity combustion processes, about  $3000^\circ\text{C}$  [14]. Therefore HVOF thermal spraying can be used to spray metal, ceramic and polymer coatings for different applications [17-21], such as aerospace, industrial gas turbine and automotive industries. It has been reported [12, 15] that the HVOF high-pressure combustion jet leads to improved particle heating and acceleration as compared with the flame spray processes, resulting in more effective acceleration of the particles to higher velocities, leading to denser, lower oxide content, and more uniformly dispersed relatively thick coatings.

Figure 2.2 shows a schematic diagram of the HVOF thermal spray process. The internally combusted gases are subsequently directed into a nozzle or a barrel where the injected powders are mixed with the high-pressure, high-velocity and high temperature combustion gases for heating and acceleration. The gases and entrained particles are confined by the nozzle and barrel and the expanding gas jet exits supersonically into the ambient atmosphere. The molten and semi-molten high

velocity particles impinge on the substrate and form splats that rapidly solidify. The deposit is built up by scanning the gun to give successive impingement and inter-bonding among the splats. According to the type of combustion fuel used, the HVOF thermal spray process may be divided into HVOGF (gas fuel) and HVOLF (liquid fuel) thermal spraying.

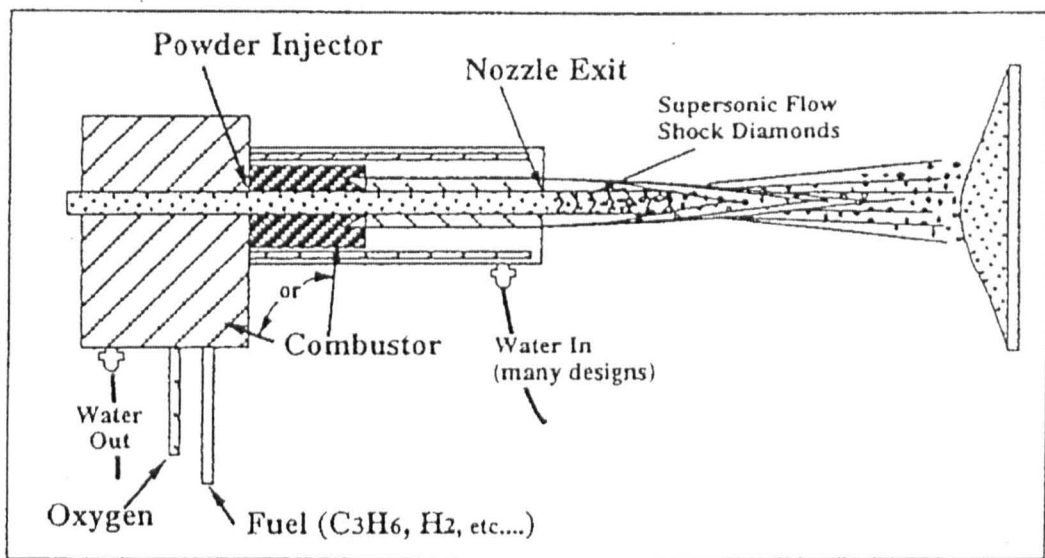
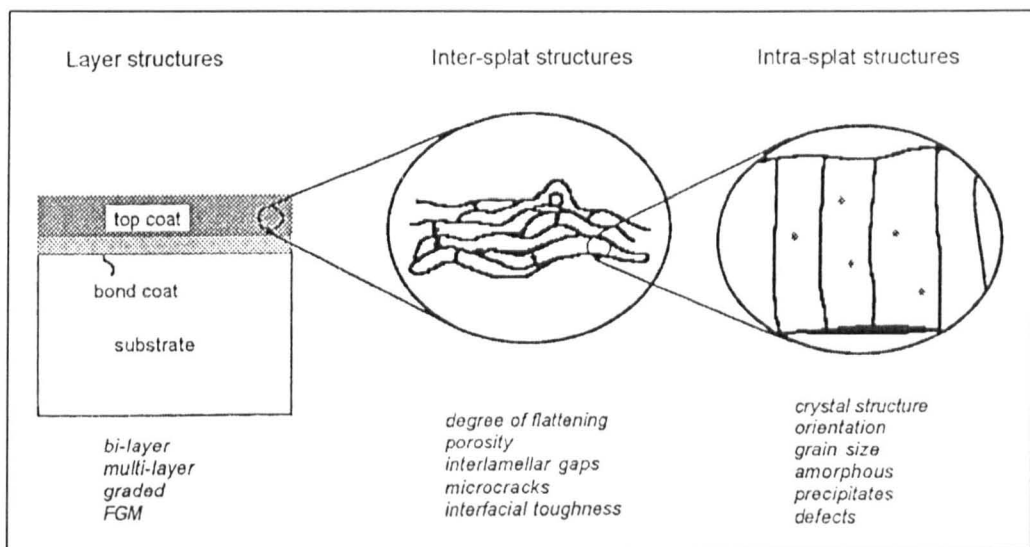


Figure 2.2 Schematic of the HVOF thermal spray process <sup>[11]</sup>

#### 2.3.4 HVOF thermally sprayed coatings

Like other thermal spray coatings, HVOF thermally sprayed coatings exhibit an inter-splat structure due to the splat bonding process and an intra-splat structure as shown in the cross-section of Figure 2.3. According to the scale of observation, from macroscopic (left) to microscopic (right), the coating may be described with reference to 1) the layer structure, 2) the inter-splat structure or 3) the intra-splat structure. The layer structures may be most readily controlled in the thermal spray process by switching the feed material from one to another to obtain the desired thickness. The inter-splat structure is defined by the degree of flattening of each splat, the ratio of contact between lamellae, the density of micro-cracking, oxidation

and porosity. These features are particular to thermal sprayed deposits and affect most significantly the mechanical properties of the resultant coating. Intra-splat features may be described with reference to grain size, grain orientation, crystal structure and defect density etc, which are determined by the solidification process within each splat. The different sizes of the thermal sprayed particles can lead to inhomogeneity within the coating. It is generally accepted that the interlayer bonding is metallurgical bonding, possibly with intersplat oxides in metallic coatings, but the bonding between coating and substrate is mechanical <sup>[15]</sup>.



**Figure 2.3 Hierarchy of the structure of a thermal sprayed coating <sup>[22]</sup>**

The characteristics of high velocity and moderate temperature associated with the HVOF thermal spraying process result in spray coatings comprising molten, semi-molten and totally un-melted particles <sup>[23]</sup>. This increases the non-uniformity of the coatings. However, oxide inclusions will be decreased within the coatings compared with plasma sprayed. The cooling rate of thermal spray coatings is regarded as being greater than  $10^6 \text{Ks}^{-1}$ , <sup>[11]</sup> even reaching to  $10^7 \text{Ks}^{-1}$ . <sup>[24]</sup> The rapid solidification of coating materials will impart a microstructure with non- equilibrium

characteristics a refinement of the grain size, a modification of the segregation pattern, the formation of metastable phases and a high concentration of point defects [22]. These sprayed structures may possess modified magnetic, mechanical or chemical properties as compared with conventionally processed materials. Rapidly quenched structures generally cannot be obtained in bulk materials because the requirement of high cooling rate necessitates the melt layer to be thin.

Residual stresses are another important phenomenon within HVOF thermally sprayed coatings. There are two sources of residual stress [22]. The first is the intrinsic stress arising due to the solidification of the sprayed particles. The second is the thermal stress that arises due to the mismatch in thermal expansion coefficient between the coating and the substrate leading to a temperature gradient within the work piece. The latter arises because different materials are joined at high temperature with microscopic defects developing as the object is cooled down. The former arises due to the solidification contraction of the individual sprayed particles. During the HVOF thermal spraying process, the thermal temperature (about 2000°C or lower) and high velocity (400-800ms<sup>-1</sup>) of impacting particles can lead to a very non-uniform distribution of stress within the coatings. In a process where the majority of the sprayed particles are not fully melted but attain a high velocity, plastic deformation on the surface layer of the target material will occur. This can affect the microstructure, e.g. by the formation of a large number of dislocations in the coatings. It is regarded that plastic deformation of partially melted powders in HVOF thermal spraying coatings tends to generate compressive stresses [12]. An important consequence of this is that much thicker coatings can be fabricated than by flame or plasma spraying without spontaneous delamination or cracking.

Delimitation tends to occur if the coating is stressed in tension with respect to the substrate during spraying.

### **2.3.5 HVOF thermally sprayed Al-Sn based bearing materials**

In 1998, a novel method for bearing manufacture was developed by McCartney and Harris <sup>[25]</sup>. This involved using the HVOF thermal spraying technique to coat Al-Sn bearing alloys directly onto steel substrates. This technology can spray alloys directly onto the bearing half-shell, thereby simplifying the manufacturing process for bimetal bearings. It was found that the rapid solidification associated with the HVOF process leads to a microstructural change within the bearing alloys <sup>[10]</sup>. Nanoscale Sn particles dispersed in the Al matrix have been found in the Al-Sn and Al-Sn-Cu, Al-Sn-Cu-Si systems formed by high velocity oxy-gas fuel (HVOGF) thermal spraying. The as-sprayed Al-Sn coatings were found to be highly reactive with water. The addition of Cu was found to increase the corrosion resistance of the as-sprayed coating as compared with Al-Sn alloys.

Although all the evidence is promising for bearing manufacture, a limitation still exists in that the design of the HVOGF spraying system employed is not well suited to spraying metals with a melting point below 750°C, because the melted materials can easily block the inner barrel of the spraying gun. The development of the high velocity oxy-liquid fuel (HVOLF) thermal spraying technology may resolve these problems by decreasing the thermal spraying temperature and increasing the velocity of particle impingement at the substrate. Therefore, this project focuses on the manufacture of bearing alloy coatings by the HVOLF thermal spray technique. The main theme of this thesis is focused on a microstructural understanding of the high velocity liquid fuel (HVOLF) thermal sprayed coatings and their relationship with the coating properties. In order to understand the development of the coating



microstructure, the associated phase diagrams will be reviewed in the following section.

## 2.4 Al-Sn (Cu) and Al-Sn (Si) phase equilibrium diagrams

Although thermally sprayed coatings undergo rapid solidification, it is necessary to understand the associated equilibrium phase reactions to help interpret what happens during rapid solidification.

The compositions of the alloys used for thermal spraying during this project were Al-(12-20)wt.% Sn-X (X = Cu and Si). The proportion of the variable element (X) was in general less than 5wt.%. Therefore, the Al-Sn binary phase diagram will have a controlling effect on the formation of the microstructure. By way of example, the binary phase diagrams of Al-Cu, Sn-Cu, Al-Si, Sn-Si and the ternary phase diagram of Al-Sn-Cu are presented (Figure 2.4 to Figure 2.9) to help develop an understanding of the final microstructure of the ternary Al-Sn-Cu and Al-Sn-Si alloy systems. Of course, ternary alloys may differ from what the binary phase diagrams predict. However, binary phase diagrams can be used to make an approximation if a ternary phase diagram is not available.

Figure 2.4 shows the equilibrium phase diagram for an alloy of Al-Sn. The Al-Sn alloy has a eutectic reaction at 228°C with a composition of 99.5wt.% Sn. The solubility of Sn in the face centred cubic (fcc)  $\alpha$  - Al, and that of Al in the body centred tetragonal (bct)  $\beta$  - Sn is very limited.

Figure 2.5 shows the equilibrium aluminium-copper phase diagram. The area of interest in this study, and for bearing alloys in general, typically lies within compositions containing 1-2wt.%Cu. This indicates a significant solid solubility of copper within aluminium at high temperature which decreases rapidly at lower

temperature: 5.7wt% at 548°C; 2.5wt% at 450°C; 0.45wt% at 300°C and 0.1-0.2wt% at 250°C from the phase diagram.

Figure 2.6 shows the tin-copper phase diagram. The composition of the Al-12wt.%Sn-1wt.%Cu alloy may be considered with respect to 7.7wt.%Cu in 92.3wt.%Sn. At this composition, copper has a very limited solubility in Sn although it is possible for  $\eta$  precipitation during an annealing process.

Figure 2.7 shows the Al-Sn-Cu ternary phase diagram with the liquidus surface of the Al-Sn-CuAl<sub>2</sub> partial system. In this diagram,  $e_1$  is the eutectic point for the CuAl<sub>2</sub>/Al binary system which occurs at 82.7at.%Al and 548°C, and  $e_3$  is the eutectic point for the Al-Sn binary system which occurs at 0.06at.%Sn and 228°C. The diagram predicts, when starting at  $e_1$ , that small additions of Sn result in a decrease in the liquidus temperature to the point  $E_1$  (at 530°C) where an invariant equilibrium exists, of the form Liquid ( $L'$ )  $\leftrightarrow$  CuAl<sub>2</sub> + Al +  $L''$  (being a monotectic four-phase equilibrium). The 530°C tie-line connects to a second point  $E_1$  where the same invariant reaction occurs, albeit with  $L''$  at a different composition. From this second point  $E_1$ , the liquidus temperature decreases to a point  $D_1$  corresponding to the point of a eutectic four phase equilibrium at 228°C.

Figure 2.8 shows the equilibrium Al-Si phase diagram. This indicates a eutectic at 12.6wt%Si in aluminium at a temperature of 577°C, the limited solubility of silicon in the aluminium, and zero solubility of aluminium in silicon.

Figure 2.9 shows the Sn-Si phase diagram. In this instance, the composition of the Al-20wt.%Sn-3wt.%Si alloy may be considered with respect to an alloy of 13wt.%Si in 87wt.%Sn. The phase diagram again predicts that Si in Sn and Sn in Si both have a very limited solubility and as such they are expected to separate out within the Al-Sn-Si HVOF sprayed alloys.

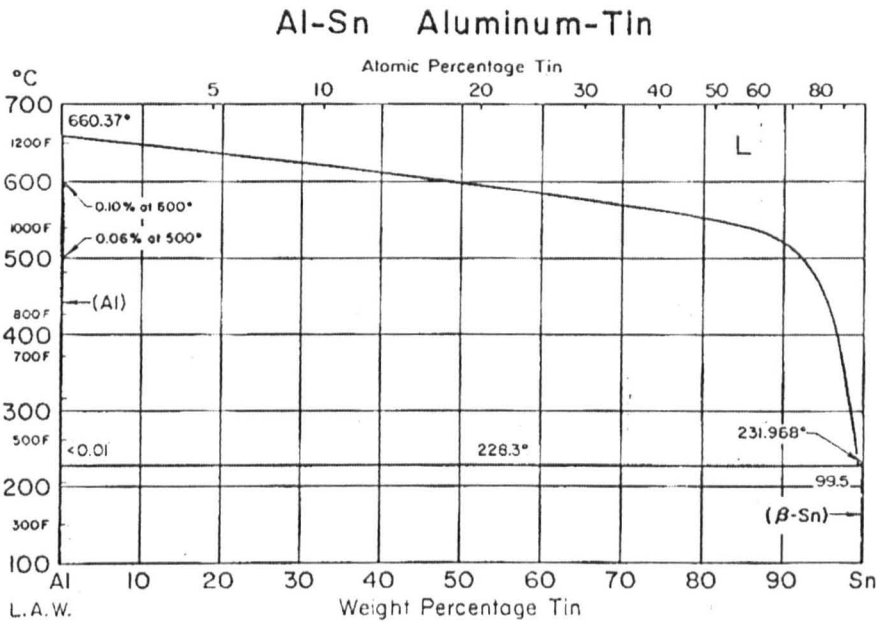


Figure 2.4 The equilibrium phase diagram of Al-Sn <sup>[26]</sup>

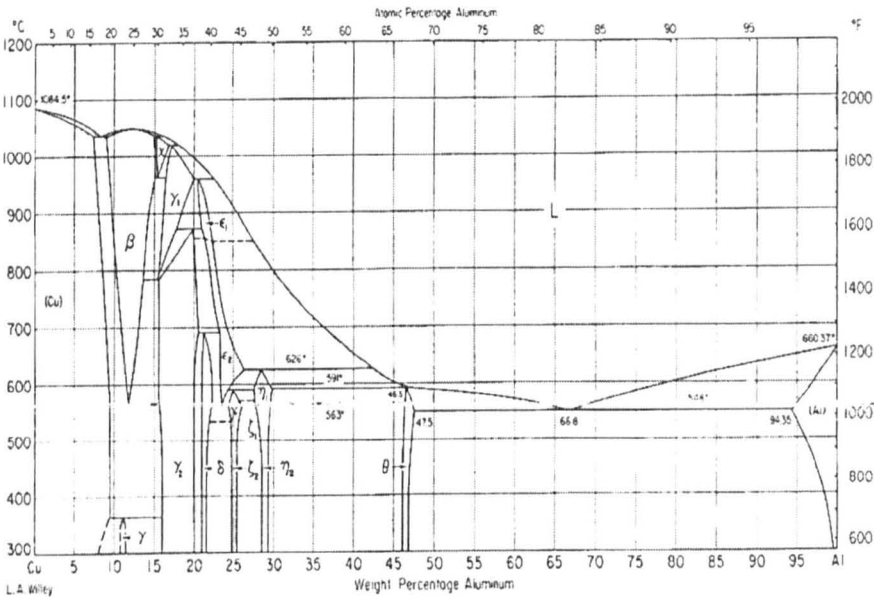


Figure 2.5 The equilibrium phase diagram of Al-Cu <sup>[27]</sup>

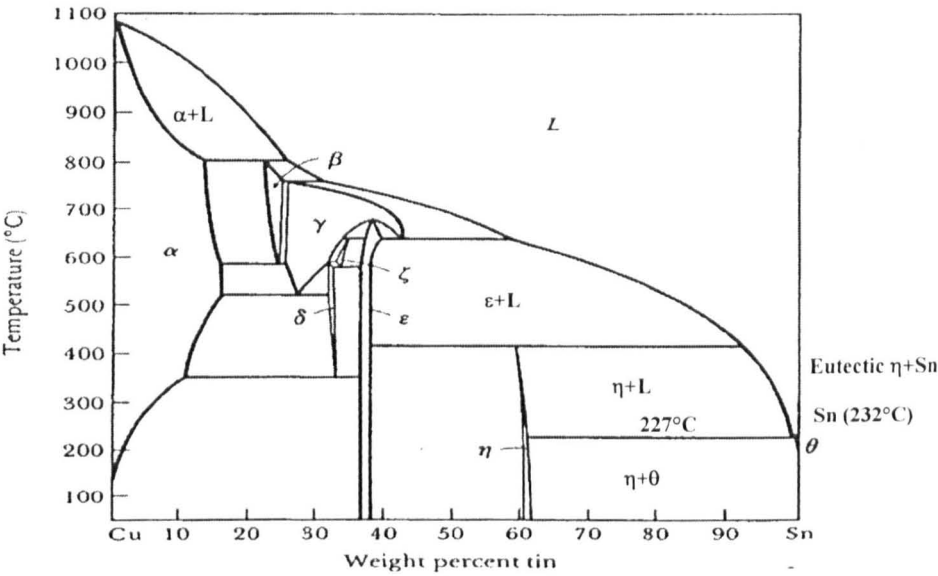


Figure 2.6 The equilibrium phase diagram of Sn-Cu <sup>[28]</sup>

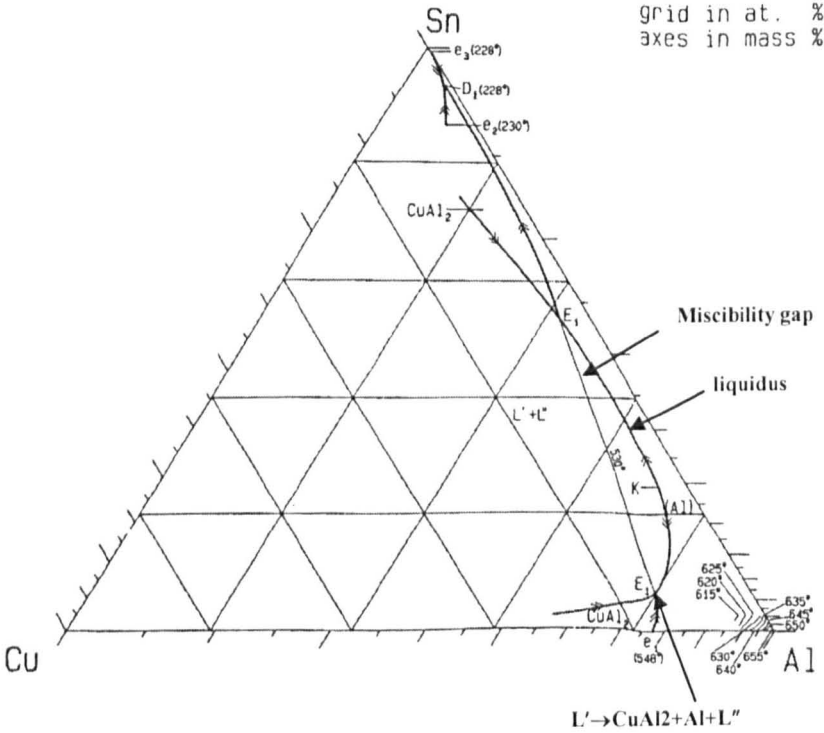


Figure 2.7 The liquidus surface projection of the Al rich end of the Al-Sn-Cu phase diagram <sup>[29]</sup>

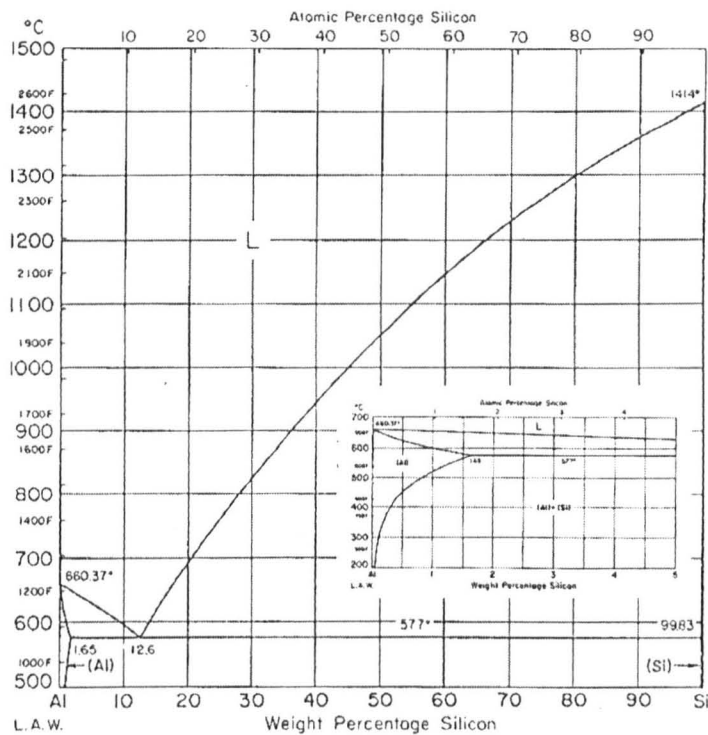


Figure 2.8 The equilibrium phase diagram of Al-Si <sup>[27]</sup>

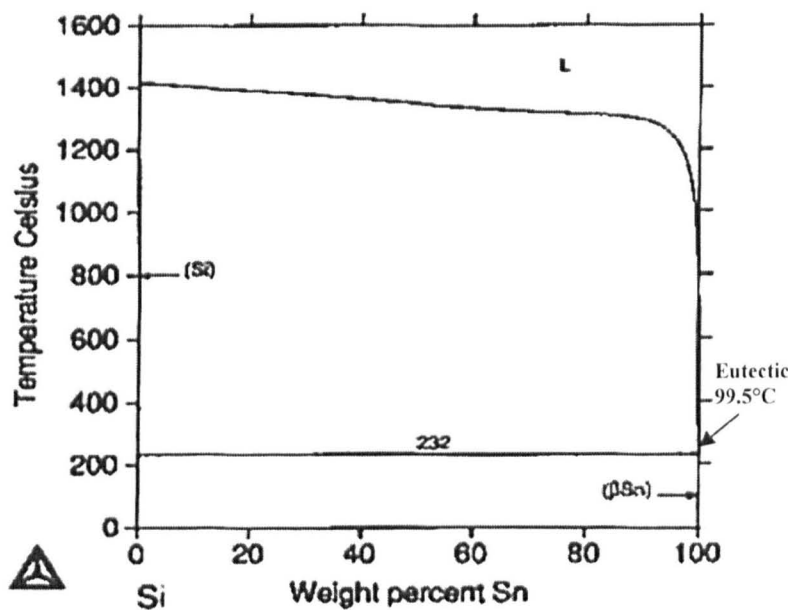


Figure 2.9 The equilibrium of Sn-Si <sup>[30]</sup>

## 2.5 Microstructure formation mechanisms of different immiscible alloys

It is well known that thermal spraying is a rapid solidification process. Powder produced by gas atomisation can also be regarded as rapidly solidified. Therefore, the explanation of the microstructure of Al-Sn based thermal sprayed coatings and gas atomised powders can be interpreted with reference to other techniques or other alloys undergoing rapid solidification. In recent years, interest has focused on studying the solidification behaviour of alloys which exhibit limited solubility. These alloys include Al-Cd <sup>[31, 32]</sup>, Al-Pb <sup>[33]</sup>, Al-In <sup>[32]</sup>, Al-Sn <sup>[32, 34, 35]</sup>, Al-Be <sup>[36-39]</sup>, Pb-In <sup>[40]</sup>, Zn-Bi <sup>[41]</sup>, Zn-Pb <sup>[42]</sup>, Cu-Co <sup>[43-48]</sup>, Co-Fe <sup>[49, 50]</sup> and Cu-Co-Fe <sup>[51]</sup>. The techniques comprise of melt spinning <sup>[31-33, 41, 42, 52]</sup>, electron beam melting <sup>[49, 51]</sup>, laser beam melting <sup>[36]</sup>, electromagnetic levitation <sup>[46]</sup>, drop tube techniques <sup>[46, 48]</sup>, glass fluxing techniques <sup>[50]</sup> and HVOF thermal spraying <sup>[25]</sup>.

The microstructure of these alloys during rapid solidification reveals particles of one phase distributed within the matrix. Three kinds of mechanisms have been used to explain the microstructure formation of these alloys, namely equilibrium monotectic reaction, undercooling causing metastable liquid phase separation and massive transformation plus decomposition.

Table 2.1 summarises the microstructures of these alloy processed by different solidification techniques and their proposed formation mechanisms.

As compared with their phase diagrams, these alloys can be divided into equilibrium liquid phase separation and metastable liquid phase separation (i.e., liquid phase separation depressed below the equilibrium liquidus.)

The behaviour of equilibrium liquid phase separation is readily observed in systems in which the phase diagram exhibits an equilibrium miscibility gap and a monotectic reaction, with examples being the Al-Pb, Al-In, Al-Cd and Zn-Bi alloy

systems. Liquid phase separation can occur under conditions of equilibrium cooling. However, a similar type of behaviour has also been noted, under rapid solidification conditions, in alloys in which a metastable miscibility gap exists beneath the equilibrium liquidus line of the phase diagram. Alloys of Al-Sn, Al-Be, Co-Cu and Cu-Fe alloy are examples of such systems. The summary schematic diagrams for equilibrium liquid phase separation and metastable liquid phase separation are shown in Figure 2.10.

For alloys undergoing equilibrium liquid phase separation, investigations reported to date have generally concentrated on those alloy compositions near the monotectic / eutectic point. The microstructure of these hypomonotectic / hypoeutectic alloys, or hypermonotectic / hypereutectic alloys with composition close to the monotectic / eutectic reaction point always show a uniform, fine scale second phase distribution of particles. Schematic compositions are denoted by the lines  $X_1$ ,  $X_2$ , in Figure 2.10 (a). The solidification mechanism of Al-4.5wt%Cd<sup>[32]</sup>, Al-7wt%In<sup>[32]</sup>, Al-10wt%Cd<sup>[42]</sup>, Zn-2wt%Bi<sup>[42]</sup>, Zn-10wt%Bi<sup>[42]</sup>, Al-8wt%In<sup>[42]</sup>, Zn-0.6at%Bi<sup>[41]</sup> and Zn-3.3at.%Bi<sup>[41]</sup>, may be described with reference to the monotectic reaction mechanism,  $L \rightarrow \alpha + L_2$ . However, if the composition of a hypermonotectic alloy is far from the monotectic reaction point (Figure 2.10a, line  $X_3$ ), then such alloys initially undergo an equilibrium liquid phase separation process,  $L \rightarrow L_1 + L_2$ , followed by a monotectic reaction,  $L_1 \rightarrow \alpha + L_2$ . The microstructure of such alloys generally exhibit a bimodal distribution of second phase material, with larger scale, second phase particles coming from the liquid separation, whilst small scale, second phase particles arise from the monotectic reaction. By way of example, the Al-5wt%Pb and Al-5wt%Pb-0.5wt%X (where X =

Mn, Cu, Zn, Fe, Si) <sup>[40]</sup>, Zn-10wt%Pb and Al-10wt%Pb alloys <sup>[42]</sup> all adopt this mechanism.

For alloys which undergo metastable liquid phase separation, a uniform distribution of second phase particles has similarly been identified. For the composition close to the eutectic / peritectic point (Figure 2.10b, Y<sub>1</sub> and Y<sub>2</sub>) the same monotectic reaction ( $L \rightarrow \alpha + L_2$ ) has been used to explain the formation of the microstructure of Al-4.4at%Be to Al-11at%Be<sup>[36, 52]</sup>. However, for conditions which are far removed from the eutectic reaction, the process of liquid phase separation occurs ( $L \rightarrow L_1 + L_2$ ) following alloy undercooling below the liquid miscibility gap (Figure 2.10b, line Y<sub>3</sub>). Indeed, the Al-20at%Be <sup>[52]</sup>, Al-5wt%Sn and Al-10wt%Sn <sup>[32]</sup> alloys and all the Cu-Fe and Cu-Co alloys investigated <sup>[43-48, 50, 51]</sup>, adopt this solidification mechanism. For such alloy systems, the second phase particle size is strongly dependent on the cooling rate. A high cooling rate will reduce the particle size of the second phase.

However, previous investigations have not given a clear description for the formation mechanism of Al-Sn alloys. The rapid solidification of the Al-Sn alloy was first investigated by Kim and Cantor <sup>[32]</sup> using the melt spinning technique. Investigation of the microstructure of Al-5wt%Sn and Al-10wt%Sn alloys revealed a distribution of that Sn particle sizes in the range 20-100 nm embedded in the Al matrix. The particles were found to have the tetragonal  $\beta$ -Sn structure. Even though the Al-Sn equilibrium phase diagram with a metastable liquid miscibility gap had been calculated, the microstructure formation mechanism was explained in term of a monotectic reaction. The solidification process of Al-(5 and 10)wt%Sn together with Al-7wt%Cd and Al-7wt%In was explained by a four stage process: Primary aluminium grain nucleation (heterogeneous) on the chilled wheel surface with lateral



growth to form a stable set of columnar aluminium grains, and rapid solute build up ahead of the aluminium growth front, until the liquid  $L_1$  composition reaches the miscibility gap. The solute-rich liquid  $L_2$  is then nucleated either homogeneously ahead of the aluminium growth front or heterogeneously in contact with the aluminium growth front. The  $L_2$  phase grows cooperatively with the aluminium. This is generally understood to mean that a liquid forms a solid and another liquid,  $L_1 \rightarrow S + L_2$ . In their related paper <sup>[35]</sup>, two possible mechanisms were advanced to explain the formation of the Sn droplets. 'During primary aluminium solidification, tin droplets can form and be entrained in the aluminium matrix, by two postulated mechanisms. Firstly tin atoms can partition at the primary aluminium solid/liquid interface, segregate into intercellular and dendritic regions and then be incorporated as droplets by the advancing aluminium interface. Secondly, tin droplets can form by liquid phase separation in the undercooled liquid ahead of the primary aluminium solid/liquid interface, and then be incorporated by the advancing interface'. The former explanation essentially describes a monotectic reaction mechanism, while the latter mechanism assumes that nucleation of Sn rich liquid droplets is kinetically favoured with respect to heterogeneous nucleation of solid aluminium.

Moore and Cantor <sup>[33, 40]</sup> suggested that both liquid phase separation and a monotectic reaction are responsible for the formation of large and small scale Pb particles, respectively, within chill cast and melt spun Al-Pb alloys. This explanation is appropriate because Al-Pb equilibrium liquid phase separation is possible at their investigated composition.

In Goswami and Chattopadhyay's explanation <sup>[41, 42]</sup> for the microstructure formation of the Al-In, Al-Cd and Zn-Pb alloys produced by melt spinning, liquid phase separation or massive solidification plus precipitation mechanisms were used

to explain the formation of the microstructure. It was suggested that a suppression of the equilibrium phases during rapid solidification occurred, leading to a competition between the kinetics of liquid phase separation and that of massive solidification, leading to the resultant fine scale particle dispersion. If these alloys are allowed to cool below the homogeneous nucleation temperature, then liquid separation followed by second liquid trapping is inevitable. Above this temperature, massive transformation of the solid, presumably influenced by heterogeneous nucleation, followed by subsequent decomposition remains a highly probable pathway. When describing the Bi particle distribution in melt spun Zn-10wt%Bi, Goswami and Chattopadhyay state that large size particles come from liquid separation, whilst smaller particles arise from massive solidification and subsequent solid state decomposition<sup>[42]</sup>.

A monotectic reaction has also been suggested for hypereutectic Al-Be alloys prepared by laser melting and melt spinning <sup>[52]</sup>, for compositions close to the eutectic point, with a resultant fine scale dispersion of second phase Be particles within the Al matrix. Further, the Al-rich side of Al-Be phase diagram with the suggested metastable monotectic reaction and submerged metastable liquid miscibility gap clearly shows that the alloy undergoes monotectic reaction or liquid separation plus monotectic reaction depending on the composition of Al-Be (Figure 2.11). The Al-20at%Be alloy undergoes liquid phase separation to form large scale Be particles and then monotectic reaction with the production of fine scale Be particles. Another investigation <sup>[37]</sup> explained that ultrafine Be particles formed during rapid solidification of the Al-Be system were caused by the undercooling accessible with the high cooling rate. A numerical model predicted that the

homogeneous Be-rich droplets could nucleate within the Al liquid via liquid phase separation with undercooling being the key point to forming ultrafine particles.

In the investigation of the rapid solidification of the Cu-Co and Cu-Fe systems, the concept of undercooling and cooling rate was also frequently used to describe the microstructure formation process. Nakagawa<sup>[43]</sup> first found a metastable miscibility gap in the Cu-Co and Cu-Fe alloys in the undercooled state. These alloy systems have been further investigated<sup>[44, 45, 50]</sup> especially by Munitz,<sup>[48, 49, 51]</sup> using electron beam melting, arc melting, copper chill, electromagnetic levitation, drop tube and casting techniques. The alloy system has also been expanded to the ternary Cu-Co-Fe alloys with various compositions. The microstructure of second phase particles distributed within the matrix was attributed to liquid phase separation because the temperature of the undercooled liquid was below the miscibility gap. A high cooling rate and its associated undercooling in the electron beam, arc melting or copper chill techniques are the key factors to form the fine scale second phase particles. In the electromagnetic levitation and drop tube techniques, the coarsening effect of the separated liquid droplets is due to the comparatively slow cooling rate of these methods. A schematic phase diagram<sup>[47]</sup> of Cu-Co (Figure 2.12) explains the microstructure formation process for Cu-10wt%Co. When the liquid had been undercooled to 190K, the liquid will separate to form  $L_1$  (Co-rich) and  $L_2$  (Cu-rich) phases. A higher undercooling ( $\Delta T_{L1}$ ) of the  $L_1$  phase than that of  $L_2$  ( $\Delta T_{L2}$ ) had been obtained. Therefore, the  $L_1$  will nucleate and first solidify and then entrap  $L_2$  droplets. The composition effects on the final structure by the promotion of liquid phase separation under low undercooling conditions has been reported, such as for the Cu-Co<sup>[44]</sup> and Cu-Fe<sup>[43]</sup>. These suggest that addition of boron (B) and carbon (C) to promote liquid phase separation. Further, Co-rich particles were found in the Cu

matrix for the Cu rich side of the alloy composition, whilst Cu-rich particles were found in the Co matrix for the Co-rich side of the alloy composition <sup>[46]</sup>.

From the above analysis, it is clear that the formation mechanism of nanoscale Sn particles embedded in an Al matrix for the Al-(5 and 10)wt%Sn alloys produced by melt spinning <sup>[34]</sup> could more likely, be due to the metastable liquid phase separation rather than metastable monotectic reaction. The schematic phase diagrams of Figure 2.10 are useful tools to predict the solidification mechanisms of different composition immiscible alloys.

Table 2.1

Alloy system	Phase diagram prediction	Authors	Manufacture method	Second phase particle size	Proposed solidification mechanism
Al-5wt%Pb Al-5wt%Pb-0.5%X (X=Mn,Cu, Zn Fe Si)	Equilibrium liquid separation + Monotectic reaction	Moore & Cantor [33, 40]	Chill cast  Melt spun	Large 1-2 $\mu$ m Small 5-50 $\mu$ m ----- Large 50-100nm Small 5-10nm	Large particle-liquid separation Small particle-monotectic solidification
Al-4.5wt%Cd	Hypomonotectic alloy monotectic	Kim, Zhang & Cantor [32, 35, 53]	Melt spun		1. Al grains nucleate heterogeneously. 2. Solution builds up ahead of Al growth front. Liquid L1 composition reaches the miscibility gap. 3. L2 homogeneously nucleates or heterogeneously nucleates 4 $V_{Al}$ and $V_{L2}$ decide the final structure. ( monotectic reaction)
Al-7wt% In	Hypomonotectic Monotectic reaction				
Al-5wt%Sn Al-10wt%Sn	Hypoeutectic alloy				
Al-10wt%Cd	Hypermonotectic alloy	Goswami & Chattopadhyay[42]	Melt spun	Uniform particle size	Below homogeneous nucleation T ( $T_{NH}$ ), get liquid separation + trapping of second phase
Al-8wt%Zn	Phase diagram not available				
Zn-10wt%Pb	Hyper-E-L1+L2			8-200nm [two size particle distribution]	Above $T_{NH}$ , massive transformation + decomposition ( $T_{NH}$ is the heterogeneous nucleation temperature)
Zn-2wt%Bi	Hypomonotectic			15-75nm, (25) average	
Zn-10wt%Bi	Hypermonotectic			8-160nm, (10) average	
Al-10wt%Pb	Hyper -E-L1+L2			20-200nm (30) average	
Al-8wt%In	Hypomonotectic alloy			20-160nm(80) average	
Cu-10wt%Pb	Hypo-monotectic			100-400nm (100) average	
Zn-0.6at.%Bi	Hypo-monotectic	Same as above[41]		Uniform particle	Same as above
Zn-3.3at.%Bi	Hyper- E-L1+L2			Two size particle distribution	
Al-4.4 at.%Be	Hypo-eutectic	D. C. Van Aken[52]	Melt spun		Monotectic reaction
Al-5.8at.%Be	hyper			5nm	
Al-20at.%Be	Hyper-metastable L1+L2			Bimodal particle distribution	Liquid separation plus monotectic reaction
Al-4.4at.%Be	Hypo	Same above[36]	Laser surface melt /melt spin	5-20nm	Monotectic co-operative growth between Al and L2
Al-5.8at.%Be	Hyper			uniform particle distribution	
Al-11at.%Be	hyper				

Alloy system	Reasons	Authors	Manufacture method	Second phase particle size	Solidification mechanism
Al-5at.%Be	Hypereutectic Monotectic reaction	Elmer [37]	Not known	10-15nm Be particle Mentioned Al particles in Be rich matrix on Be rich side of the diagram	Monotectic reaction
Cu-10,15, 20wt%Co	Metastable miscibility gap L1+L2	A. Munitz (1998)[51]	Electron beam surface melting	In arc melt, all compositions show dendrites	Liquid separation
Cu-30wt%Co					Liquid separation dendrites
Cu-50wt%Co	Doubt- cannot be seen			Reason-cannot see or slow cooling rate	
Cu-80wt%Co	Do not reach MM gap				Dendrite structure
Cu-15wt% Fe-5, 10,15 wt%Co	Third element promotes L1+L2 separation				Liquid separation Fe +Co Composition < 45wt%
Cu-25Fe-20wt%Co					
Cu40wt%Fe-15wt%Co					
Fe-Cu (50,65,57,80,85)wt%		A. Munitz (1987)[49]	Electron beam melting		Liquid separation
Cu-(15,30, 50)wt %Co	Undercooled liquid	A. Munitz (1991)[48]	Drop tube		Liquid separation
Cu-(10,13,20)wt.% Co	Undercooled liquid	A. Munitz (1992) [47]	Electron beam surface melting		Liquid separation
Co-(18.8, 38.2, 55.1 and 58.2)at %Cu	Underccoled below miscibility gap	M Koble (2002)[46]	Drop tube Electromagnetic levitation	Co rich particle in Cu matrix and Cu rich particle in Co matrix	Liquid separation

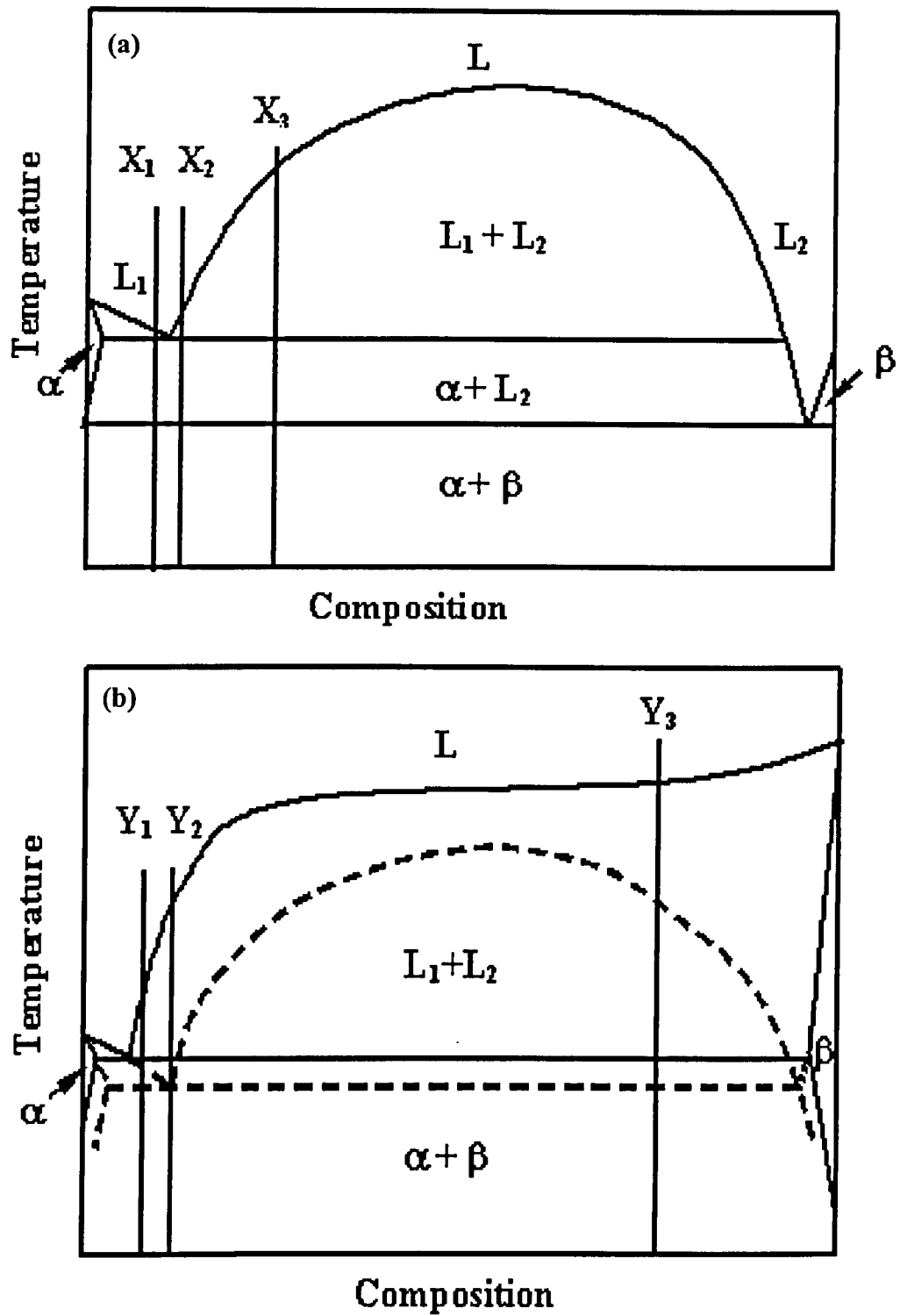


Figure 2.10 Schematic phase diagram of (a) equilibrium liquid phase separation and (b) metastable liquid separation

2.6 Mechanisms of supercooled liquid crystal formation

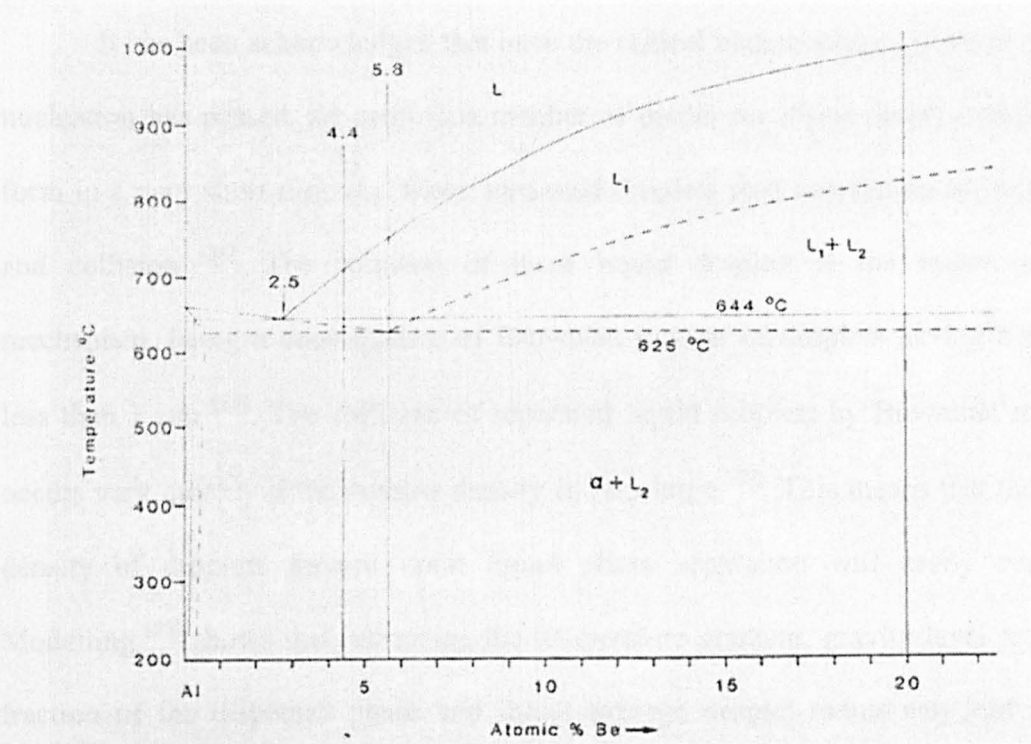


Figure 2.11 The Al rich side of the Al-Bi diagram with the suggested metastable monotectic reaction represented by the dashed lines [52]

2.6.1.1 Metastable miscibility gap in the Cu-Co system

The Cu-Co system is a binary system with a large temperature range and a complex phase diagram. The phase diagram shows a large miscibility gap between the two components, which is a characteristic feature of this system. The diagram is shown in Figure 2.12.

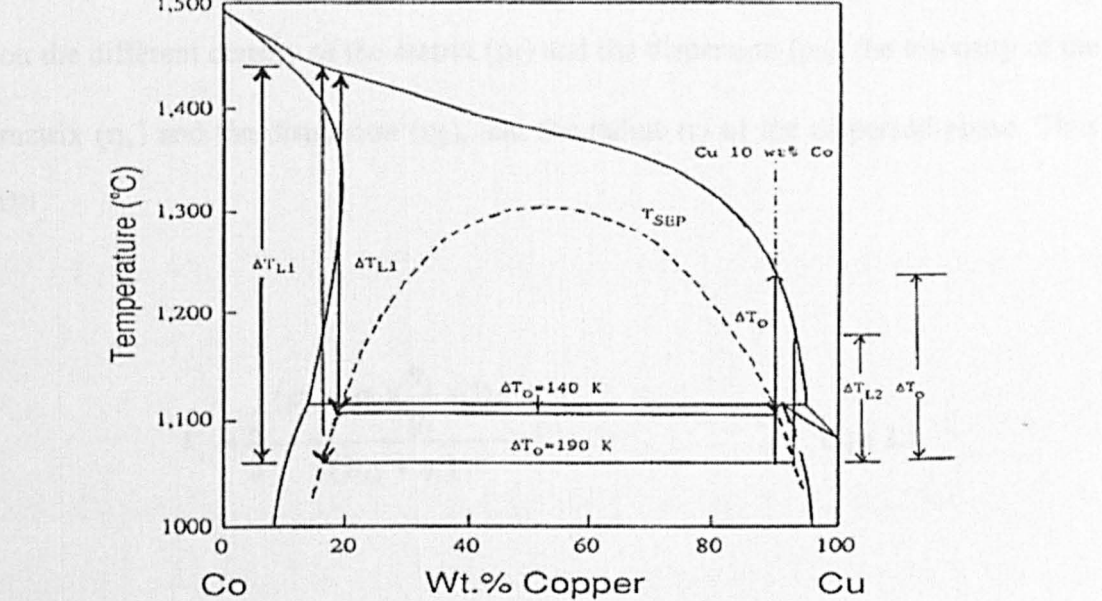


Figure 2.12 The Cu-Co phase diagram with metastable miscibility gap [47]



## 2.6 Mechanisms of separated liquid droplet coarsening in a liquid matrix

It has been acknowledged that once the critical undercooling for homogenous nucleation has passed, an enormous number of nuclei for liquid droplet separation form in a very short time and those separated droplets start coarsening by diffusion and collision <sup>[54]</sup>. The collision of these liquid droplets is the major growth mechanism, being a consequence of Brownian motion of droplets having a radius less than 1  $\mu\text{m}$  <sup>[55]</sup>. The collision of separated liquid droplets by Brownian motion occurs very quickly if the number density is very large <sup>[50]</sup>. This means that the high density of droplets formed upon liquid phase separation will easily coarsen. Modelling <sup>[55]</sup> shows that increasing the temperature gradient, gravity level, volume fraction of the dispersed phase and initial average droplet radius can lead to an increased rate of droplet growth due to collision and coalescence. The velocity of a separated droplet movement has been described by two ways, Stokes motion and Marangoni motion.

The Stokes motion velocity ( $V_s$ ) of a single droplet in a liquid matrix depends on the different density of the matrix ( $\rho_1$ ) and the dispersion ( $\rho_2$ ), the viscosity of the matrix ( $\eta_1$ ) and the dispersion ( $\eta_2$ ), and the radius ( $r$ ) of the dispersed phase. Thus <sup>[55]</sup>,

$$V_s = \frac{2}{3} \frac{(\rho_2 - \rho_1) \left( \frac{\eta_2}{\eta_1} + 1 \right) g}{(3\eta_2 + \eta_1)} r^2 \quad \text{Eqn 2.1}$$

where  $g$  is termed the residual acceleration vector. Therefore, for a definitive liquid matrix and dispersion, the separated liquid droplets are predicted to coarsen faster with increasing droplet radius.

Marangoni migration is caused by the surface tension gradient of a dispersed droplet in the matrix phase, which is related to the gradients of local concentration and temperature. The migration velocity ( $V_m$ ) depends on the thermal conductivity of the matrix and the dispersion, the surface tension gradient and the radius ( $r$ ) of the dispersed phase. Thus<sup>[50]</sup>,

$$V_M = -\frac{2k_1 \nabla \sigma}{(2k_1 + k_2)(2\eta_1 + 3\eta_2)} r \quad \text{Eqn 2.2}$$

Where  $k_1$  and  $k_2$  are the thermal conductivities of the matrix and the dispersion phase, respectively, and  $\nabla \sigma$  is the surface tension gradient.

The above description indicates that the viscosity of the matrix and dispersion phase, the radius of the dispersoids and the thermal conductivity of the matrix could affect the coarsening of the separated second phase, in addition to the density of the particles. The important factor here is that a small cooling rate provides a sufficient time for separated droplet coarsening.

## **2.7 Factors affecting the particle distribution and shape, and the matrix phase growth velocity**

Several papers describe the relationship between the growth velocity of matrix interface and the second phase particle distribution. In a model explaining the dispersion of nanoscale Sn in a melt spun Al-Sn alloy, Kim et al. suggest<sup>[32]</sup> that the final microstructure depended on the growth velocity of the Al and the Sn. This

model is based on the mechanism of monotectic reaction of the Al-Sn alloy during rapid solidification. The model is described as following.

A variety of microstructures are considered to form, depending on the difference in growth speed of solid Al and liquid droplets,  $L_2$  (Figure 2.13), denoted  $V_{Al}$  and  $V_{L2}$ . The  $V_{Al}$  is the Al growth velocity and  $V_{L2}$  is the particle formation velocity. With  $V_{Al} \gg V_{L2}$ , a fine scale, random distribution of  $L_2$  (Sn) droplets developed within the Al grains. For the condition  $V_{Al} > V_{L2}$ , or when the  $L_2$  droplets are pushed ahead of the Al growth front, the droplet size increases, leading to a more cellular structure. When  $V_{Al} = V_{L2}$ , co-operative growth is continuous, leading to the formation of an aligned rod microstructure followed by capillary breakdown of the aligned droplets. These models are constructed by presuming a monotectic reaction mechanism ( $L_1 \rightarrow Al + L_2$ ) leads to the nanoscale Sn particle formation. The comparison of the growth speeds of the solid Al and liquid Sn droplets is the key aspect.

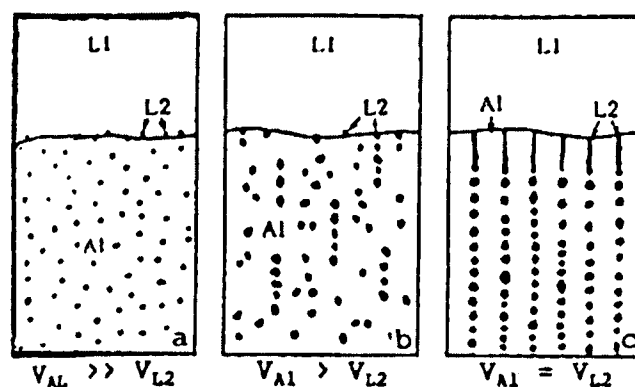


**Figure 2.13** Schematic diagram of a monotectic microstructure as a function of the relative Al and  $L_2$  growth velocities ( $V_{Al}$  and  $V_{L2}$ ) <sup>[32]</sup>

A similar discussion of the interface velocity effect is presented for an Al-Be alloy <sup>[37]</sup>. A critical interface velocity, i.e. solid phase growth velocity, is believed to

exist, above which the Be particles are trapped by growing Al, and below which the particles are pushed ahead of the growing interface.

The interface velocity ( $dx/dt$ ) has a relationship with the cooling rate ( $-dT/dt$ ) as follows <sup>[56]</sup>.

$$\frac{dx}{dt} \times \frac{dT}{dx} = \frac{dT}{dt} \quad \text{Eqn 2.3}$$

Thus, the thermal gradient ( $dT/dx$ ) at the solid-liquid interface is related to the cooling rate. A high cooling rate could cause a high interface growth velocity of the matrix phase. The cooling rate seems to be the critical factor controlling the final structure of the second phase particles.

In this context, cooling rate may be a critical factor for microstructure formation in Al-Sn alloys.

## 2.8 The orientation relationship between Sn particles and the Al matrix

Fine scale particles within a matrix may show some orientation relationships with the matrix. This is due to the minimization of the surface energy of the particles. The phenomenon has been observed in some alloy systems produced by melt spinning <sup>[35, 40]</sup> and ion implantation <sup>[57]</sup>, such as Pb particles in Al alloys <sup>[40, 57, 58]</sup>, Pb particles in Si single crystals <sup>[59, 60]</sup>, Pb-Cd combined particles in Al alloys <sup>[61, 62]</sup> and Sn particles in Al alloys <sup>[35, 63]</sup>.

The orientation relationships of nanoscale Sn particles within an Al matrix have been investigated for melt spun <sup>[35]</sup>, ion implantation <sup>[63]</sup> and rapidly quenched <sup>[64]</sup> Al-Sn alloys. In the melt spun material <sup>[35]</sup>, the fine scale Sn particles are found to exhibit two distinct relationships with the Al matrix and a variety of different facets.

About half of the Sn particles were within  $\pm 10^\circ$  of  $\{111\}_{\text{Al}} // \{100\}_{\text{Sn}}$  and  $\langle 211 \rangle_{\text{Al}} // \langle 011 \rangle_{\text{Sn}}$ , with the main facets parallel to  $\{111\}_{\text{Al}}$  and  $\{100\}_{\text{Sn}}$ ; while the remaining half were within  $\pm 10^\circ$  of  $\{100\}_{\text{Al}} // \{100\}_{\text{Sn}}$  and  $\langle 011 \rangle_{\text{Al}} // \langle 011 \rangle_{\text{Sn}}$ , with the main facets parallel to  $\{100\}_{\text{Al}}$  and  $\{100\}_{\text{Sn}}$ . Re-melting and solidification investigations found that small Sn particles within the Al grains solidified by catalytic nucleation on  $\{100\}_{\text{Al}}$  and  $\{111\}_{\text{Al}}$ . The ion implantation<sup>[63]</sup> of Sn within an Al matrix also leads to the formation of nanoscale Sn with the orientation relationship  $(111)_{\text{Al}} // (100)_{\text{Sn}}$  and  $[211]_{\text{Al}} // [010]_{\text{Sn}}$ . However, in contrast in the rapid quenched<sup>[64]</sup> Al-Sn materials, the spherical Sn particles have orientation relationships of  $(200)_{\text{Al}} // (200)_{\text{Sn}}$  and  $(220)_{\text{Al}} // (200)_{\text{Sn}}$ .

## 2.9 Cooling rate and undercooling during rapid solidification

Non-equilibrium phases and fine scale microstructures are achieved by imposing on system a large undercooling prior to the onset of solidification. Large undercoolings are achieved, practically, in one of two ways. Firstly, by suppression of the nucleation onset temperature. This includes decreasing the impurity content in the liquid to avoid heterogeneous nucleation by the dispersion of liquid into fine droplets<sup>[39, 65-70]</sup>; the interruption of nucleation by using the magnetic levitation method<sup>[46]</sup>; or by reducing the gravity effect for heterogeneous nucleation using a drop tube technique<sup>[46, 48]</sup>. Secondly, by increasing the rates of heat extraction in a system. The latter is the more common and practical means of achieving undercooling and is used in the process of gas atomisation, melt spinning, laser melting, electron beam melting and thermal spray deposition<sup>[71-74]</sup>. The extent of undercooling in most case is related to the cooling rate. The attainment of high cooling rates in the range of  $10^4$  to  $10^8 \text{ Ks}^{-1}$  is possible, with the highest estimation of

$10^{10} \text{ Ks}^{-1}$  [72]. In order to model the cooling rate, the principles of heat transfer will be considered.

### 2.9.1 Principles of heat transfer

Heat transfer is energy in transit due to a temperature difference. Whenever a temperature difference exists in a medium or between media, heat transfer must occur. Basically, there are three different types of heat transfer process, i.e. conduction, convection and radiation [75]. Conduction refers to heat transfer caused by a temperature gradient in a stationary media, which may be solid or a fluid. In contrast, the term convection refers to heat transfer that will occur between a surface and a moving fluid when they are at different temperatures. The third mode of heat transfer is termed thermal radiation or black body radiation. All surfaces of finite temperature emit energy in the form of electro-magnetic waves. Hence, in the absence of an intervening media, there is net heat transfer by radiation between two surfaces at different temperatures. Simply, the heat transfer is a kind of energy transfer, which may be quantified by a rate equation. First, the heat transfer rate ( $q$ ) is related to the heat transfer coefficient ( $h$ ), the surface area where heat transfer happens ( $A$ ) and the temperature difference ( $T_2 - T_1$ ) between the two points to be considered at heat transfer, i.e. [75]

$$q = hA(T_2 - T_1) \quad \text{Eqn 2.4}$$

On the other hand, the heat flow is also a function of transient temperature change ( $dT$ ) and is related to the material itself. In this case,

$$hA(T_2 - T_1)dt = mC_p dT \quad \text{Eqn 2.5}$$

where,  $m$  is the mass of the material,  $C_p$  is the heat capacity of the material and  $dT$  is the transient temperature change of the material. Since  $m = \rho V$ , the equation may be expressed as,

$$hA(T_2 - T_1)dt = \rho V C_p dT \quad \text{Eqn 2.6}$$

where,  $\rho$  is the material density and  $V$  is the volume of the material.

Equation 2.6 may be expressed by the format,

$$\varepsilon = -\frac{dT}{dt} = \frac{hA(T_2 - T_1)}{\rho V C_p} \quad \text{Eqn 2.7}$$

where  $\varepsilon$  or  $-dT/dt$  is the cooling rate.

Two kinds of geometry are considered for the process of heat transfer (Figure 2.14). The first is a sphere and the second is a flat plane.

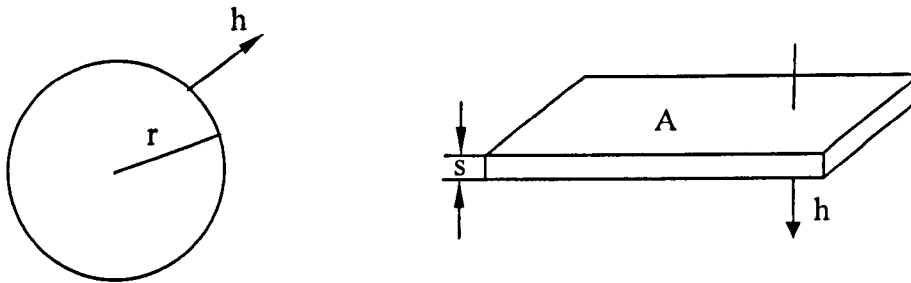


**Figure 2.14 Schematics of a sphere and a plate under heat transfer**

If the object is a sphere, the cooling rate ( $-dT/dt$ ) may be expressed in terms of the radius ( $r$ ), instead of area or volume, according to equation 2.7,

$$\varepsilon = -\frac{dT}{dt} = \frac{hA(T_2 - T_1)}{\rho V C_p} = \frac{h4\pi r^2(T_2 - T_1)}{\rho \frac{4}{3}\pi r^3 C_p} = \frac{3h(T_2 - T_1)}{\rho C_p r} \quad \text{Eqn 2.8}$$

If the object is a flat plate, the cooling rate may be expressed in terms of the thickness of the plate(s), according to equation 2.7,

$$\varepsilon = -\frac{dT}{dt} = \frac{hA(T_2 - T_1)}{\rho V C_p} = \frac{hA(T_2 - T_1)}{\rho A s C_p} = \frac{h(T_2 - T_1)}{\rho C_p s} \quad \text{Eqn 2.9}$$

Here, the specific heat transfer circumstances and the material condition (solid or liquid) have been ignored.

## 2.9.2 Gas atomised powder

### 2.9.2.1 Cooling rate

The heat transfer model of a gas atomised powder particle is very similar to the model for a sphere as described in the previous section. The three kinds of heat transfer are operational in here, i.e., conductive heat transfer within the droplet, and convective and radiative heat transfer from the surface of the droplet to the carrier gas. For methods of most gas atomisation, particularly those involving an inert gas, the temperature gradient within a droplet may be ignored because the conductive heat transfer component is high as compared with the convective and radiative heat transfer from the surface to the carrier gas. The radiative heat transfer could also be ignored due to its low heat transfer coefficient as compared with that of convection. Therefore, the convective process dominates the transfer of surface heat. This convective model is called the Newtonian model. Several works <sup>[76-81]</sup> have considered the heat transfer and cooling rate of gas atomised droplets. A quantitative expression for the heat transfer coefficient (h) for a spherical gas atomised powder is:

[82]

$$h = \frac{2K_G}{d} + 0.6(K_G^2 C_p)^{\frac{1}{3}} \left(\frac{\rho u}{d}\right)^{\frac{1}{2}} \left(\frac{1}{\mu}\right)^{\frac{1}{6}} \quad \text{Eqn 2.10}$$

where  $K_G$  is the gas thermal conductivity,  $C_p$  is the isobaric heat capacity of the gas,  $\rho$  is the density of gas,  $\mu$  is the viscosity of the gas,  $u$  is the relative gas / droplet velocity and  $d$  is the gas atomised particle size.



In this case, the cooling rate of the gas-atomised powder, as expressed in equation 2.8, uses the heat transfer coefficient of equation 2.10. The term,  $(T_2 - T_1)$  represents the temperature difference between gas-atomised powder particle and the cooling inert gas;  $\rho$  is the density of liquid droplet;  $C_p$  is the droplet specific heat capacity and  $r$  is the radius of the gas-atomised droplet.

A physical calculation of particle cooling rate associated with heat transfer has been considered by Levi<sup>[83]</sup>. He considers the enthalpy balance of a spherical droplet. Consideration of the thermal history of a supercooled droplet allows the rate of change of enthalpy ( $dH/dt$ ) balance for a spherical droplet of radius  $r_0$  cooling in a gas environment at a temperature  $T_G$  to be determined:

$$\frac{dH}{dt} = -(3h\Omega/r_0)(T - T_G) \quad \text{Eqn 2.11}$$

Where  $\Omega$  is the molar volume and  $h$  is the heat transfer coefficient at the droplet / gas environment interface and  $T$  is the melt temperature of the liquid used for atomising.

For a system containing both liquid and solid phases, the molar enthalpy ( $H$ ) may be related to the temperature,  $T$ , and the solid fraction,  $f$ , by <sup>[83]</sup>,

$$H = [\Delta H_M + C_L(T - T_M)](1 - f) + C_S(T - T_M)f \quad \text{Eqn 2.12}$$

Where  $\Delta H_M$  is the latent heat,  $T_M$  is the melting temperature, and  $C_L$  and  $C_S$  are the molar heat capacities of the liquid and solid, respectively. Prior to solidification the droplet is single phase ( $f = 0$ ). The equation 2.12 may be expressed as,

$$H = \Delta H_M + C_L(T - T_M) \quad \text{Eqn 2.13}$$

hence, in the form of a differential equation 2.13 is expressed as in follows:

$$\frac{dH}{dt} = C_L \frac{dT}{dt} \quad \text{Eqn 2.14}$$

Combining equations 2.11 and 2.14, the cooling rate of a spherical powder particle under gas atomisation conditions is:

$$\varepsilon = -\frac{dT}{dt} = 3 \frac{\Omega(T - T_G)}{C_L} \cdot \frac{h}{r} \quad \text{Eqn 2.15}$$

where  $\varepsilon$  or  $-dT/dt$  is the cooling rate,  $T$  is the liquid droplet temperature,  $T_G$  is the carrier gas temperature,  $C_L$  is the heat capacity of the liquid droplets,  $\Omega$  is the molar volume of metal droplets,  $h$  is the heat transfer coefficient of the carrier gas and  $r$  is the radius of the droplets. If the volume change from liquid droplet to powder particle is ignored,  $r$  may also be regarded as being the gas atomised powder particle radius. If the diameter ( $d$ ) of the particle is used instead of the radius ( $r$ ), this equation may be expressed as,

$$\varepsilon = -\frac{dT}{dt} = 6 \frac{\Omega(T - T_G)}{C_L} \cdot \frac{h}{d} \quad \text{Eqn 2.16}$$

Which in the same expression as proposed by Clyne<sup>[76]</sup> and Stone<sup>[78]</sup>.

According to Levi<sup>[83]</sup>, the second part of equation 2.10 may be ignored for a powder particle radius of less than 200  $\mu\text{m}$ . Therefore, if the convective heat transfer coefficient is taken to an approximation as  $K_G/r_0$ , the cooling rate becomes,

$$\varepsilon = -\frac{dT}{dt} = 3 \frac{\Omega(T - T_G)}{C_L} \cdot \frac{K_G}{r_0^2} \quad \text{Eqn 2.17}$$

Where,  $r_0$  is the radius of the powder particle and  $K_G$  is the thermal conductivity of gas.

The relationship between gas atomised particle size and the heat transfer coefficient, and between the particle size and the cooling rate has also been established by Clyne<sup>[76]</sup> and Stone<sup>[78]</sup>. The heat transfer coefficient decreases as the gas atomised powder particle size increases. An increase of the relative gas to droplet

velocity could act to increase the heat transfer coefficient. Helium gas, for example, has stronger heat transfer ability as compared with nitrogen gas. Therefore, helium gas induces a higher cooling rate to the same sized powder particle as compared with nitrogen gas.

Comparing equations of 2.8 and 2.15, there are several common points. The heat transfer coefficient and liquid droplet radius are the same. The term  $(T_2-T_1)$  in equation 2.8 has the same meaning as the expression  $(T-T_G)$  in equation 2.15. If the material is liquid, the term  $C_p$  in equation 2.8 has the same meaning as  $C_L$  in equation 2.15. Here the only difference is  $\Omega$  and  $\rho$ . The former is the molar volume of metal droplet and latter is the density of a liquid droplet. The relationship between them is,

$$\rho = \frac{M}{\Omega} \quad \text{Eqn 2.18}$$

where the  $M$  is the mass of 1 mole of material. So, the equations 2.8 and 2.15 are essentially different expressions of the same thing.

### 2.9.2.2 Undercooling

It is now acknowledged that ability to undercool is a major constraint to achieving high interface velocities and the corresponding microstructural benefits of rapid solidification of metal powders. The maximum attainable extent of undercooling ( $\Delta T$ ) will be that for homogeneous nucleation. In this context, the number of nuclei,  $n$ , formed per unit volume, is given by the following equation <sup>[84]</sup>,

$$n = - \int_{T_N}^{T_L} \frac{J(T)dT}{\varepsilon} \quad \text{Eqn 2.19}$$

where  $J(T)$  is the nucleation rate of the solid in the liquid per unit volume, which depends on the temperature,  $T$ ;  $\epsilon$  is the cooling rate,  $T_N$  is the nucleation temperature and  $T_L$  is the liquidus temperature of the alloy.

The probability of forming one nucleus in a volume,  $V$ , taken to be the critical condition, is given by  $J(T_N)Vdt$  where  $dt$  is the time increment  $\sim 0.01\Delta T/(dT/dt)$  to enter the regime of  $T \sim T_N$  corresponding to the onset of rapid nucleation. The above equation may be expressed by a Taylor series expansion of  $J$  about  $J(T_N)$ . Thus, the critical condition is <sup>[84]</sup>,

$$\frac{0.01JV\Delta T}{dT/dt} \cong 1 \quad \text{Eqn 2.20}$$

The expression for the homogenous nucleation rate is rewritten in term of common metal properties for the typical case <sup>[84]</sup>,

$$J = 10^{-2} 4\pi(\nu/\alpha)^2 (\alpha/\Omega) D \exp\left(-\frac{16\pi\gamma^3\Omega T_L^2}{3kT_N\Delta H^2\Delta T^2}\right) \quad \text{Eqn 2.21}$$

where

- $10^{-2}$  is the so-called non-equilibrium factor,
- $\nu$  is the critical nucleus radius,
- $\alpha$  is the atomic diameter,
- $D$  is the liquid diffusivity,
- $\gamma$  is the solid-liquid interface energy,
- $\Omega$  is the atomic volume,
- $k$  is Boltzmann's constant,
- $T_L$  is the liquidus temperature,
- $T_N$  is the temperature of nucleation,
- $\Delta H$  is the heat of fusion,

- $\Delta T$  is the undercooling pertinent to nucleation,

Combining equations 2.20 and 2.21 and rearranging, the undercooling versus particle size and cooling rate for a spherical particle becomes,

$$\Delta T^2 = \frac{16\pi\gamma^3\Omega^2T_L^2}{3kT_N\Delta H^2 \ln(10^{-3}d^3(\nu/\alpha)^2(\alpha/\Omega)D\Delta T/\varepsilon)} \quad \text{Eqn 2.22}$$

where  $d$  is the particle diameter and  $\varepsilon$  is the cooling rate. The variables, which can be controlled to maximize  $\Delta T$  are to increase  $\varepsilon$  and decrease  $d$ .

According to the equation 2.22, Levi developed an expression <sup>[83]</sup>:

$$\Delta T_N^2 = F_1(T_N) / \log[F_2(T_N)r_0^3 / \varepsilon] \quad \text{Eqn 2.23}$$

where  $r_0$  is the radius of the particle. And  $F_1(T_N)$  and  $F_2(T_N)$  expressed as following:

$$F_1(T_N) = \frac{16\pi\gamma^3\Omega^2T_L^2}{3kT_N\Delta H^2} \log e \quad \text{Eqn 2.24}$$

$$F_2(T_N) = \frac{1}{8} 10^{-3} (\nu/\alpha)^2 (\alpha/\Omega) D \Delta T \quad \text{Eqn 2.25}$$

Combining equations of 2.17 and 2.23, the following equation may be expressed,

$$(\Delta T_r)_N^{-2} = F_3 + F_4 \log r_0^5 \quad \text{Eqn 2.26}$$

where  $\Delta T_r$  is given by,

$$\Delta T_r = \frac{\Delta T}{T_m} = \frac{T - T_N}{T_M} \quad \text{Eqn 2.27}$$

where  $T_m$  is the melting temperature of the solid.

By way of illustration, the achievable undercooling calculated using this numerical model for Al and Ni droplets is plotted in Figure 2.15. The cooling gas is He and the relatively velocity between the gas and particle is taken as 100 m/s. The model couples a Newtonian heat transfer formulation with classical homogenous nucleation.

In summary, equation 2.10 illustrates the relationship between gas atomised powder particle size ( $d$ ) and the heat transfer coefficient ( $h$ ). Equation 2.16 illustrates the relationship between particle size ( $d$ ) and the cooling rate ( $\epsilon$ ). Equation 2.15 and 2.16 describe the same thing as equation 2.8. Figure 2.15 and equation 2.23 illustrate the relationship between the radius ( $r_0$ ) of He gas atomised Al powder particles and undercooling ( $\Delta T$ ). This basic knowledge of cooling rate and undercooling in the context of the rapid solidification process will help us to understand their effects on the microstructural development of the Al-Sn alloy system, as developed further in Chapter 4.

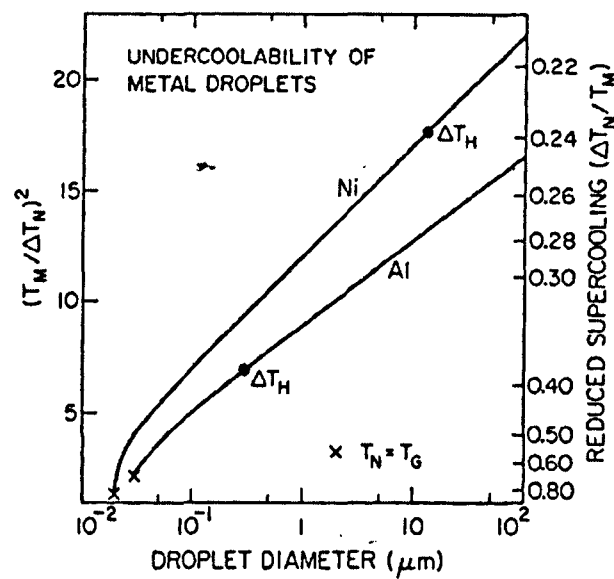


**Figure 2.15 Achievable undercooling prior to homogeneous nucleation in Ni and Al droplets <sup>[83]</sup>**

### 2.9.3 Thermally sprayed coating

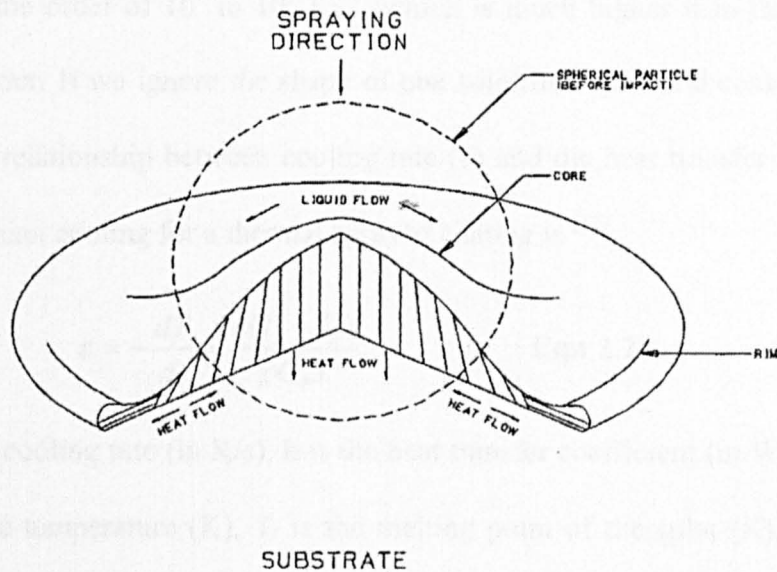


**Figure 2.16 Heat flow and related grain structure in a solidifying splat <sup>[12]</sup>**

A number of variables affect the cooling rate of a thermally sprayed coating<sup>[12, 22]</sup>. These include the roughness and oxides of the substrate surface, the substrate temperature and variation in size of each splat. The roughness and oxides of the substrate surface may affect heat transfer by changing the flatting and cooling time of the coatings. The schematic image of Figure 2.16 shows a splat from a single powder particle during the spraying process; such a thermal splat is considered to be flat for ease of calculation of the heat transfer. However, the local cooling rate depends on the splat thickness and can vary greatly within a given splat depending on position. The heat transfer within a splat and in the substrate is approximately regarded as being conductive. However, the roughness of the substrate and the condition of the coating substrate interface dominates the heat transfer between them. Thus, the limiting heat transfer coefficient for the system is difficult to ascertain. Some experiments have been done to measure the cooling rate directly and then

calculated the heat transfer coefficient in the plasma thermally spraying technique [12]. According to some experimental results, the cooling rate of a thermally sprayed coating is of the order of  $10^7$  to  $10^8$  Ks<sup>-1</sup>, which is much higher than that of a gas atomised powder. If we ignore the shape of one solidified splat and consider it as a flat plate, the relationship between cooling rate ( $\epsilon$ ) and the heat transfer coefficient ( $h$ ) for Newtonian cooling for a thermal sprayed coating is [12],

$$\epsilon = -\frac{dT}{dt} = \frac{h(T_i - T_s)}{\rho C_p s} \quad \text{Eqn 2.28}$$

where  $\epsilon$  is the cooling rate (in K/s),  $h$  is the heat transfer coefficient (in W/m<sup>2</sup> K),  $T_s$  is the substrate temperature (K),  $T_i$  is the melting point of the splat (K),  $C_p$  is the specific heat capacity of the splat (J kg K), and  $s$  is the splat thickness (m).

The final microstructure of a thermally sprayed coating is related to these solidification parameters, i.e. the solidification rate, the heat transfer coefficient and the mode of cooling. Thus, an understanding of the cooling rate and undercooling of each splat will help to explain the resultant microstructure formed.

## 2.10 Effect of annealing on Al-Sn (Cu, Si) alloys

The as-sprayed Al-Sn based coatings need to be annealed to adjust their microhardness and improve the chemical properties by reducing the reactivity with water. For a bearing, the microhardness should be around 45-65 kg/mm<sup>2</sup>. The microstructure will change in the annealing process. In the next section, the possible mechanisms of the microstructural changes are introduced.

### 2.10.1 The mechanisms for liquid droplet coarsening within a solid matrix

This section introduces mechanisms for dispersed particle coarsening within the matrix during annealing.



The microstructure of a two or more phase alloy is always unstable if the total interfacial free energy is not a minimum. Therefore, small particles tends to coarsen into a low number of large particles to reduce the total interfacial energy <sup>[85]</sup>. It is generally accepted that the coarsening of the second phase is via elemental diffusion within the matrix. However, if the annealing temperature is higher than the melting temperature of the particle, the process of coarsening will differ from that of simple element diffusion. One mechanism is that the liquid droplets may move within the solid matrix if the annealing temperature is above the melting temperature of the dispersed phase. Several authors have explained the mechanism by which a liquid droplet can migrate in a solid <sup>[86-88]</sup>.

Figure 2.17 shows schematically a liquid droplet within a solid matrix. The presence of a temperature gradient generates a concentration gradient within any material containing two or more components. This results from the variation of equilibrium solubility with temperature. For the case of a liquid inclusion within a solid matrix, the upper side of the droplet has a higher temperature as compared with at lower side of the droplet ( $T_L > T_0$ ), the corresponding concentration of the matrix is lower at the upper side of the droplet as compared with the bottom side of the droplet. Accordingly, the matrix material diffuses down the concentration gradient in the liquid droplet and forms at the high temperature upper side, i.e. the solid phase dissolves at the hot upper end of the droplet and condenses at the cool end with a result that the liquid droplet migrates up the temperature gradient.

It is noted that the inclusions remain spherical during migration rather than elongating in the direction normal to the thermal gradient which indicates that in the competition between the thermal gradient and surface energy, the latter dominates in establishing the shape of the inclusion <sup>[86]</sup>.

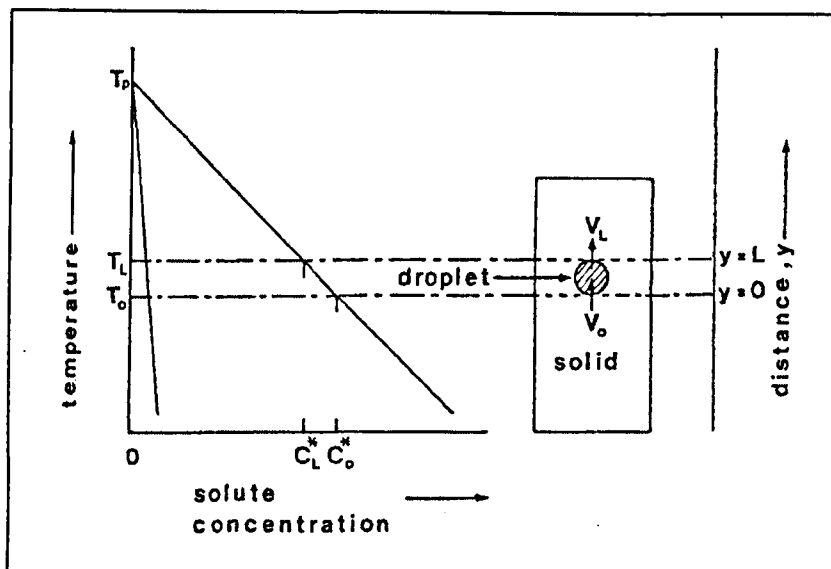


**Figure 2.17** Schematic diagram of a liquid droplet moving in a temperature gradient zone.

When two migrating liquid droplets move together, liquid droplet coalescence can occur. The driving force for coalescence of two spheres is the minimisation of the surface energy<sup>[89]</sup>.

Another mechanism<sup>[90]</sup> of solid and liquid particle coarsening is through the dragging effect of the migration of matrix grain boundaries. The speed of the boundaries is limited by the speed at which a particle can be dragged. Particles accumulate on the boundary, which leaves a particle-denuded zone behind it. At high temperature, the particles within the Cu matrix are fairly fluid, and all the particles investigated ( $\text{SiO}_2$ ,  $\text{GeO}_2$  and  $\text{B}_2\text{O}_3$ ) are equally mobile. Their mobility appears to be limited by the diffusion of matrix atoms (Cu) around the particles. At low temperature, the particle mobility depends on the composition. The mobility of a given composition particle depends on its viscosity, and thus on the rate of transport or self-diffusion within the particle. Particle motion involves both the removal of matrix atoms from in front of the particle, and the flow of particle atoms or

molecules into the space thus formed. This second process controls the mobility of solid or very viscous particles.

### 2.10.2 Precipitation in supersaturated Al-Cu alloys during heat treatment

Under rapid solidification conditions, Cu may become supersaturated within the Al matrix. This supersaturated Cu could subsequently precipitate within the alloy following an annealing process. The precipitation in supersaturated Al-Cu alloys has previously been discussed <sup>[85, 91]</sup>. Figure 2.18 indicates the precipitates predicted to form at the Al-rich end of the Al-Cu alloy phase diagram for different annealing temperatures. If the temperature rises above the curve marked  $\theta$ , all the copper will be in solid solution as the stable fcc  $\alpha$  phase. By quenching the sample rapidly in water, there is no time for any transformation to occur so the solid solution is retained largely unchanged at room temperature. However, the solid solution is supersaturated with copper and hence there is a driving force for the precipitation of the equilibrium  $\theta$  phase,  $\text{CuAl}_2$ . If the alloy is aged by holding it for a period of time above or at room temperature, Cu-rich GP zones will initially form. Copper rich zones in Al-Cu alloys were first detected in 1938 by Guinier and Preston <sup>[85, 91]</sup> from streaks in X-ray diffraction patterns. The zones are fully coherent with the matrix and adopt a disk shape perpendicular to the elastically soft  $\langle 100 \rangle$  direction, to minimise their strain energy. If the supersaturated alloy was heat treated at a relatively high temperature, then the  $\theta''$ ,  $\theta'$  and  $\theta$  phases would precipitate. The  $\theta''$  phase adopts a tetragonal unit cell and is essentially a distorted fcc structure in which the Cu and Al atoms are ordered on the (001) plane. The atomic structure of the (001) plane is identical to that of the matrix. The (010) and (100) planes are also very similar, apart from a small distortion in the [001] direction. The  $\theta''$  phase forms as a fully coherent

plate-like precipitate with an  $\{001\}_\alpha$  habit plane and the following orientational relationship with the matrix:

$$(001)_{\theta''} // (001)_\alpha$$

$$[100]_{\theta''} // [001]_\alpha$$

The  $\theta'$  phase is also tetragonal with an approximate composition of  $\text{CuAl}_2$  and again has an (001) plane that is identical with  $\{001\}_\alpha$ . The (100) and (010) planes, however, have a different crystal structure to the matrix and a large misfit in the [001] direction.  $\theta'$  therefore forms as plates on  $\{001\}_\alpha$  but still adopts the same orientation relationship as the  $\theta''$  phase. The  $(001)_{\theta'}$  zones are initially coherent with the matrix, but lose coherency as the plates grow.

The  $\theta$  phase has the approximate composition of  $\text{CuAl}_2$  and adopts a complex body centred tetragonal structure. There are no planes of good matching with the matrix and hence it is incoherent with the matrix.

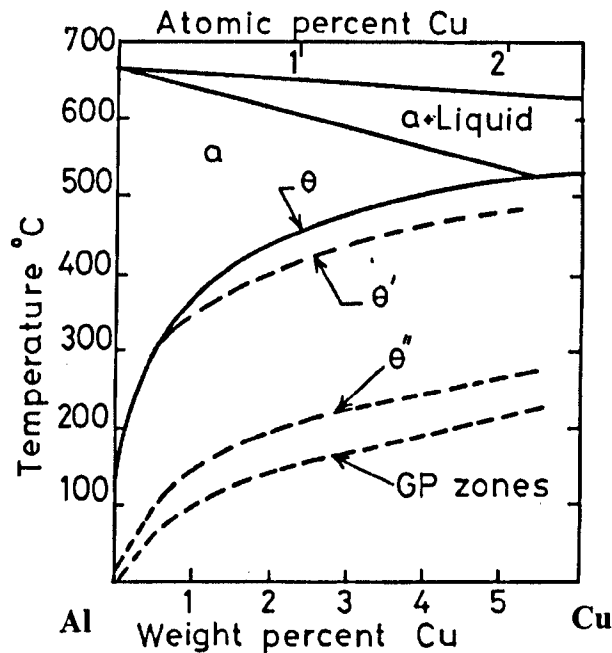


Figure 2.18 Phase diagram of Al-Cu showing metastable solution lines <sup>[85]</sup>

## 2.11 The basic concepts of corrosion

Any fundamental approach to the phenomenon of corrosion must involve consideration of the structural features of the metal, the nature of the environment and the reactions that occur at the metal / environment interface. There are three important factors involved <sup>[92]</sup>. Firstly, the metal composition, which includes details of the atomic structure, microscopic and macroscopic heterogeneities and stress (tensile, compressive and crystal). Secondly, the environment, such as the chemical nature and concentration of deleterious reactive species, pressure, temperature and velocity of impingement. Thirdly, the metal / environment interface, such as the kinetics of metal oxidation and dissolution, the kinetics of reduction of a species in solution, the nature and location of corrosion products, film growth and film dissolution. From these considerations, it is evident that the detailed mechanisms specific to metallic corrosion are likely to be highly complex and that an understanding of such phenomena will involve many branches of pure and applied science, e.g. metal physics, physical metallurgy, various branches of chemistry etc. whilst the emphasis may also vary with the particular system under consideration.

### 2.11.1 Metallurgical Factors

Corrosion is an electrochemical phenomenon. Thus, it might be expected that alloys composed of one homogenous phase or of two or more phases, all of which have very similar solution (galvanic) potentials, would be more resistant to attack than an alloy composed of two or more phases with widely different electrochemical potentials <sup>[93]</sup>. This expectation is generally fulfilled. For example, pure aluminium or single-phase alloys of Al-Mg or Al-Si are found to be relatively resistant to corrosion attack. Al-Cu alloys heat treated and quenched to retain the copper solution are much

more resistant to attack than are similar alloys treated so that the copper has precipitated out of solution as a constituent,  $\text{CuAl}_2$ , which differs from the solution potential of the solid solution matrix and may cause intergranular corrosion. For two or more phase materials, the different solution potential of the second phase and the matrix determined whether the materials are easily attacked. For example, Al-Mn alloys are highly resistant to corrosion although the manganese constituent is present as a separate phase. The reason for this is that the manganese constituent has a solution potential very similar to that of the matrix.

### 2.11.2 The corrosion of pure Al, Sn and two phase Al-Sn alloys

Pure aluminium, as indicated by its associated standard electrode potential, is a thermodynamically reactive metal. Aluminium owes its excellent corrosion resistance and its usage as one of the primary metals of commerce to the barrier oxide film that bonds strongly to its surface<sup>[93, 94]</sup>. If damaged, this thin film reforms immediately in most environments and continues to protect the aluminium from corrosion. If the film is removed or damaged under conditions such that self-repair cannot occur, corrosion takes place. Neutral or nearly neutral (pH levels from about 5 to 8.5) solutions of most inorganic salts have negligible or mild action on aluminium-base alloys at room temperature. This is true for both oxidising and non-oxidising solutions. Any attack that does occur in such solutions is likely to be highly localised (leading to pitting) with little or no general corrosion. Solutions containing chlorides are likely to react more actively with Al than other solutions.

Pure tin will react with both strong acids and strong alkalis, but is relatively resistant to nearly neutral solutions<sup>[93]</sup>. Oxygen greatly accelerates corrosion in aqueous solution. The metal is mainly covered with a thin invisible film of stannic oxide, which may be completely removed by acids or alkaline, or penetrated at

isolated points to produce pits. Salts with acidic reaction in solution attack Sn in the presence of oxidising agents or air. The oxide film on tin is not entirely removed by neutral solutions of the chloride or sulphate type, and when corrosion occurs, if at all, it is by thickening the oxide film to give a visible tarnish, or by localised attack to give pitting and black spots.

In most environments, the corrosion of an aluminium alloy is associated with the flow of an electric current between anodic and cathodic regions. The extent of electrochemical corrosion produced depends on the potentials of these regions. Corrosion generally happens in the form of localised corrosion which includes pitting corrosion, crevice corrosion, galvanic corrosion, intergranular corrosion and biological corrosion etc. Each electrochemical mechanism is caused by a difference in the corrosion potential of local cells with regard to the metal surface. The effect is usually emphasised at the surface layer because of the presence of cathodic microconstituents that can be insoluble intermetallic compounds or single elements. For the standard hydrogen electrode, the electromotive force for  $\text{Al}^{3+}$  to form Al is -1.66V and  $\text{Sn}^{2+}$  to form Sn is -0.136V <sup>[93]</sup>. Thus, it may be predicted that Al is more active than Sn. In almost all cases of localised corrosion, the process of interaction with an Al-Sn alloy is dominated by the reaction with water:



The corrosion product is almost always aluminium oxide trihydroxide (bayerite). Localised corrosion does not usually occur in extremely pure water at ambient temperature or in the absence of oxygen, but it can occur in more conductive solutions because of the presence of ions such as chlorides or sulphates. Some works confirm that pure Al is more noble than the Al-Sn alloy in NaCl solution <sup>[95, 96]</sup>.

However, others prove that Al-Sn alloys are completely resistant to corrosion by high temperature engine oils <sup>[97]</sup>.

## 2.12 Summary

The manufacture of automotive shell bearings using the high velocity oxy-fuel HVOF thermal spray process is a new concept. Therefore, the associated background relating to bearing alloys and the HVOF technique have been introduced briefly, along with an introduction to the development of HVOF spraying of bearing materials. The microstructural evolution of the pre-deposited gas atomised powder and the thermally sprayed coatings are all related to the processing. In immiscible AlSn-based alloys, thermally sprayed coatings may develop a different microstructure when processed by HVOF as compared with the traditional manufacturing methods. Thus, emphasis is given to the microstructure formation mechanisms for different immiscible alloys. An analysis of heat transfer rate, cooling rate and undercooling have also been introduced to help explain the mechanisms of solidification. The effect of annealing Al-Sn and Al-Cu alloys is introduced in order to help understand the microstructure development within the annealed thermally sprayed coatings. Finally, some basic principles of corrosion are also introduced.



## References

1. The ASM Committee, *Materials for sliding bearings*. Metals Handbook, 1980. 3: p. 802-822.
2. W. P. Brown, H. Galand, G. R. Kingsbury and M. Scott., *Aluminium bi-metal bearing developments for automotive and medium speed diesel applications*. Industrial Lubrication and Tribology, 1996. 48(3): p. 4-11.
3. G. C. Pratt, *Materials for plain bearings*. International Metallurgical Reviews, 1973. 18: p. 62-88.
4. G. C. Pratt. *Aluminium alloys for automotive crankshaft bearing*. in *Proceeding of Japan International Tribology Conference*. 1990: p.125-130. Nagoya, Japan. Publisher: Japanese Society of Tribologists, Kikai Shinko Kaikan No. 407-2, 2-8 Shiba Koen 3-chome Minatoku, Tokyo 105 Japan.
5. M. Nakano, T. Tanaka, M. Sakamoto and Y. Satoh., *Bearings*. 1992: UK Patent GB2252565.
6. T. Tanaka, M. Sakamoto, and Y. Sato, *Multi-layer slide bearing having Al-Sn alloy layer with high fatigue strength and conformability*. 1995: USA Patent US5284205.
7. M. Fujita, A. Ohgawara, T. Salai, T. Ohgaki and T. Ohsaki. *Aluminium bearing alloy and two-layer bearing materials having layer of aluminium bearing alloy therein*. 1988: USA Patent US4789609.
8. W. J. Whitney. *An advanced aluminium-tin-silicon engine bearing alloy and its performance characteristics*. in *SAE International conference and exposium*. 1995: p1-5. Detroit, USA.
9. A. J. Horlock, A. H. Dent, D. G. McCartney and S. J. Harris. *Controlling sacrificial corrosion properties of sprayed aluminium alloy coatings*. in *Proceedings of the 15th International Thermal Spray Conference, 25-29, May, 1998: p38-41, Nice, France*.
10. A. J. Horlock, *HVOF Spraying of Novel Bearing Materials*, in *School of Mechanical, Materials, Manufacturing Engineering and Management*. 1999, University of Nottingham (PhD thesis): Nottingham.
11. R. W. Smith and R. Knight, *Thermal spraying I: Powder consolidation - from coating to forming*. JOM, 1995 (August): p. 32-39.
12. H. Herman, S. Sampath and R. McCune, *Thermal spray: Current status and future tends*. MRS Bulletin, 2000 (July): p. 17-25.
13. P. Fauchais, A. Vardelle, and B. Dussoubs. *Quo vadis thermal spraying? in Thermal Spray 2001, New Surface for a New Millennium*. 2001: p.1-32 Singapore: ASM International, Materials Park, Ohio, UAS.
14. R. Thorpe, H. Kopech and N. Gagne, *HVOF thermal spray technology*. Advanced Materials & Processes, 2000 (April): p. 27-29.

15. M. R. Dorfman, *Thermal spray basics*. Advance Materials & Processes, 2002 (July): p. 47-50.
16. M. L. Thorpe and H. J. Richter, *A pragmatic analysis and comparison of HVOF processes*. Journal of Thermal Spray Technology, 1992. 1(2): p. 161-170.
17. R. W. Smith and R. D. Fast, *The future of thermal spray technology*. Weld Journal, 1994. 73: p. 7-14.
18. F. N. Longo, *Industrial guide - Markets, materials, and applications for thermal-sprayed coatings*. Journal of Thermal Spray Technology, 1992. 1(2): p. 143-146.
19. D. S. Parker, *Practical application of HVOF thermal spray technology for navy jet engine overhaul & repair*. Plating & Surface Finishing, 1995 (July): p. 20-23.
20. T. Miyamoto and S. Sugimoto. *Current condition and future trends of thermal spray technology in the Japanese automobile industry*. in *Proceeding of the 14th International Thermal Spray Conference, 22-26, May, 1995, Thermal Spraying Current Status and Future Trent*. 1995; p.3-8. Kobe, Japan.
21. J. H. Clare and D.E. Crawmer, *Thermal spray coatings*. Metals Handbook. 1980. 5: p.361-374.
22. S. Kurodas. *Properties and characterization of thermal spray coatings - A review of recent research progress*. in *Proceeding of the 15th International Thermal Spray Conference 25-29 May, . 1998: p.539-550*. Nice, France.
23. J. He, M. Ice, and E. Lavernia, *Particle melting behaviour during high-velocity oxygen fuel thermal spraying*. Journal of Thermal Spray Technology, 2001. 10(1): p. 83-93.
24. C. Moreau, P. Cielo, M. Lamontagne, S. Dallaire and J. C. C. Moreau. *Temperature evolution of plasma-sprayed niobium particles impacting on a substrate*. Surface and Casting Technology, 1991. 46: p. 173-187.
25. S. J. Harris, D. G. McCartney, A. J. Horlock and C. Perrin. *Production of ultrafine microstructure in Al-Sn, Al-Sn-Cu and Al-Sn-Cu-Si alloys for use in tribological application*. Materials Science Forum, 2000. 331-337: p. 519-526.
26. L. F. Mondolfo, *Aluminium alloys: Structure and Properties*. 1976; p. 377-379.
27. The ASM committee, *Metallography, structures and phase diagram, 8th edition*. Metal Handbook. 1973, 8. American Society for Metal.
28. D. R. Askeland, *The Science and Engineering of Materials*. 2 edition, p. 438. Publisher: Chapman & Hall.
29. G. Petzow and G. Effenberg, *A comprehensive compendium of evaluated constitutional data and phase diagrams*. Ternary Alloys, 1990. 3: p. 23-37. Publisher: VCH, Germany.
30. *SGTE Phase diagram collection*. Web.met.kth.se/dct/pd/element/Si-Sn.html, 1986.

31. D. L. Zhang, K. Chattopadhyay and B. Cantor, *Heterogeneous nucleation of solidification of cadmium particles embedded in an aluminium matrix*. Journal of Materials Science, 1991. **26**: p. 1531-1544.
32. W. T. Kim, D. L. Zhang and B. cantor, *Microstructure of rapidly solidified aluminium-based immiscible alloys*. Materials Science and Engineering A, 1991. **A134**: p. 1133-1138.
33. K. I. Moore and B. Cantor. *Microstructure of rapidly solidified hypermonotectic Al-Pb alloys*. in *Solidification Proceeding*. 1987: p.515-517. Sheffield, UK.
34. D. L. Zhang, W.T. Kim and B. Cantor. *Melt spun Al bearing alloys*. in *Advanced Aluminium and Magnesium alloy*. 1990: p409-413. Amsterdam, the Netherlands.
35. W. T. Kim and B. Cantor, *Solidification of tin droplets embedded in an aluminium matrix*. Journal of Materials Science, 1991. **26**: p. 2868-2878.
36. D. C. Van Aken and H. L. Fraser. *Nucleation in the presence of a metastable liquid miscibility gap in the Al-Be system*. in *Undercooled Alloy Phase*. 1987. New Orleans, Louisiana.
37. J. W. Elmer, M. J. Aziz, L. E. Tanner, P. M. Smith and M. A. Wal., *Formation of bands of ultrafine berllium particles during rapid solidification of Al-Be alloys: Modelling and direct observation*. Acta Metall. Mater., 1994. **42**(4): p. 1065-1080.
38. D. C. Van Aken and H. L. Fraser. D. C. Van Aken and H. L. Fraser. *The microstructures of rapidly solidified Hyper-eutectic Al-Be alloys*. Acta Metall., 1985. **33** (6): p 963-974.
39. B. A. Mueller, L. E. Tanner, and J. H. Perepezko, *Microstructure development in undercooled Al-Be powder*. Materials Sciences and Engineering, 1992. **A150**: p. 123-132.
40. K. L. Moore, D. L. Zhang and B. Cantor, *Solidification of Pb particles embedded in Al*. Acta Metall. Mater., 1990. **38**(7): p. 1327-1342.
41. R. Goswami and K. Chattopadhyay, *Microstructural evolution and transformation pathways in the near monotectic Zn rich Zn-Bi alloys during rapid solidification*. Acta Metall. Mater., 1994. **42**(2): p. 282-293.
42. R. Goswami and K. Chattopadhyay, *Microstructure development in rapidly solidified monotectic alloys*. Materials Science and Engineering A, 1994. **A179/A180**: p. 163-167.
43. Y. Nakagawa, *Liquid immiscibility in copper-iron and copper-cobalt system in the supercooled state*. Acta Matallurgica, 1958. **6**(11): p. 704-711.
44. I. Yamauchi, N. Ueno, M. Shimaoka and I. Ohnaka, *Undercooled Co-Cu alloys and its effect on solidification structure*. Journal of Materials Science, 1998. **33**: p. 371-378.
45. Z. Sun, X. Song, Z. Hu, S. Yang, G. Liang and J. Sun, *Supercooling, isothermal socking and liquid phase separation of Cu-Co alloys*. Journal of Alloy and Compounds, 2001. **319**: p. 226-270.

46. M. Kolbe, C. D. Cao, P. K. Galenko, J. Fransaer and D. M. Herlach, *Dynamics solidification and microstructure evolution in undercooled Co-Cu alloy with metastable miscibility gap*. in *EPD congress 2002 and Fundamental of Advanced Materials for Energy Conversion*. 2002. Seattle, Washington, USA: The Minerals, Metals & Materials Society, p. 539-553.
47. A. Munitz, S. P. Elder-Randall, and R. Abbaschian, *Supercooling effect in Cu-10wt% pct Co alloy solidified at different cooling rates*. Metallurgical Transactions A, 1992. **23A** (June): p. 1992-1817.
48. A. Munizt and R. Abbaschian, *Two-melt separation in supercooled Cu-Co alloys solidifying in a drop-tube*. Journal of Materials Science, 1991. **26**: p. 6458-6466.
49. A. Munitz, *Liquid separation effect in Fe-Cu alloys solidified under different cooling rates*. Metallurgica Transaction, 1987. **18B**: p. 565-575.
50. X. Y. Lu, C. D. Cao, and B. Wei, *Microstructure evolution of undercooled iron-copper hypoperitectic alloy*. Materials Science and Engineering A, 2001. **313**(1-2): p. 198-206.
51. A. Munitz and R. Abbaschian, *Liquid separation in Cu-Co and Cu-Co-Fe alloys solidified at high cooling rate*. Journal of Materials Science, 1998. **33**: p. 3639-3649.
52. D. C. Van Aken and H. L. Fraser. *The microstructure of rapid solidification hyper-eutectic Al-Be alloys*. in *Acta Metall. Mater.* 1985, **33** (6): p. 963-974
53. W. T. Kim, Z. L. Zhang and B. Cantor, *Nucleation of solidification in liquid droplets*. Metallurgical Transactions, 1991. **22A** (October): p. 2487-2501.
54. Y. C. Suh and Z. H. Lee, *Nucleation of liquid Pb phase in hypermonotectic Al-Pb melt and the segregation of Pb-droplets in melt-spun ribbon*. Scripta Metallurgica et Materialia, 1995. **33**(8): p. 1231-1237.
55. J. R. Rogers and R. H. Davis, *Modelling of collision and coalescence of droplets during microgravity processing of Zn-Bi immiscible alloys*. Metallurgical Transactions A, 1990. **21** (January): p. 59-68.
56. A. K. Srivastava, *On cooling rate, interface velocities and particle sizes in spray atomization*. Journal of Materials Science Letters, 2000. **19**: p. 1217-1219.
57. E. Johnson, A. Johansen, U. Dahmen, S. Chen and T. Fujii., *Shape and sizes of nanoscale Pb inclusion in Al*. Materials Science and Engineering A, 2001. **304-306**: p. 187-193.
58. U. Dahmen, E. Jonson, S. Q. Xiao and A. Johansen., *High-resolution electron-microscopy investigation of nanosize inclusions*. MRS Bulletin, 1997 (August): p. 49-52.
59. E. Johnson, A. Johansen, L. Sarholt and U. Dahmen., *Nanosized lead inclusions in Si produced by iron implantation*. Nuclear Instruments and Methods in Physics Research B, 1999. **148**: p. 1034-1038.
60. V. S. Toubltsev, E. Johnson, U. Jonansen, L. Sarholt and S. Q. Xiao. *Formation of Pb inclusions in Si by ion implantation*. in *Materials Research Society Symposium Proceeding*. 1998. p 411-416

61. L. Sarholt, E. Johnson, A. Johansen, T. B. Stibius Jensen, A. B. Stibius Jensen and U. Dahmen, *Nanosized lead-cadmium inclusion in aluminium*. Materials Science Forum, 1999. **312-314**: p. 299-304.
62. S. Hagege and U. Dahmen, *Morphology, structure and thermal behaviour of small eutectic Pb-Cd inclusions in aluminium*. Philosophical Magazine Letters, 1996. **1996(74)**: p. 256-266.
63. E. Johnson, C. R. H. Bahl and V. S. Touboltsev and A. Johansen. *Nanoscale Sn inclusion in Al-structure and melting-solidification properties*. in *Materials Research Symposium Proceedings*. 2000: p. 177-182, Materials Research Society.
64. H. Ichinose and Y. Ishida, *High resolution electron microscopy of rapid quenched Al-Sn alloy*. Scripta Metallurgica, 1985. **19**: p. 5-9.
65. J. H. Perepezko, J. L. Sebright, P. G. Hockel and G. Wilde, *Undercooling and solidification of atomized liquid droplets*. Materials Science and Engineering, 2002. **A326**: p. 144-153.
66. C. G. Levi and R. Mehrabian, *Microstructures of rapid solidified aluminium alloy submicron powders*. Metallurgica Transactions, 1982. **13A**: p. 13-23.
67. J. H. Perepezko. *Role of nucleation in rapid solidification*. in *Science and Technology of the Undercooled Melt*. 1985. p. 29-51, Theuern, FRG.
68. J. H. Perepezko, *Nucleation in undercooled liquids*. Materials Science and Engineering, 1984. **65**: p. 125-135.
69. J. H. Perepezko, S. E. LeBeau, B. A. Mueller and G. J. Hildeman, *Rapid solidification of highly undercooled Aluminium powder*. in *Rapid Solidified Powder Aluminium Alloys*. 1984. p. 118-136, Philadelphia, Penney.
70. J. H. Perepezko and D.R. Allen. *Kinetic competition in undercooled liquid alloys*. in *Thermodynamics and kinetics of phase transformations, Materials Research Society Proceeding*. 1996, **398**: p.3-14 Boston, Massachusetts, UAS: Materials Research Society.
71. H. Jones, *Microstructure of rapid solidified materials*. Materials Science and Engineering, 1984. **65**: p. 145-156.
72. H. Jones, *Review - The status of rapid solidification of alloys in research and application*. Journal of Materials Science, 1984. **19**: p. 1043-1076.
73. F. Duflos and J-F. Stohr, *Comparison of the quench rates attained in gas-atomized powders and melt-spun ribbons of Co- and Ni- base superalloys: influence on resulting microstructures*. Journal of Materials Science, 1982. **17**: p. 3641-3652.
74. L. A. Jacobson and J. McKittrick, *Rapid solidification processing*. Materials Science and Engineering, 1994. **R11**: p. 255-408.
75. F. P. Incropera and D. P. Dewitt, *Introduction of heat transfer*. 2nd ed. 1990: p.8, John Wiley & Sons, Inc.
76. T. W. Clyne, R. A. Ricks and P. J. Goodhew, *The production of rapid-solidified aluminium powder by ultrasonic gas atomization Part I: Heat and fluid flow*. International Journal of Rapid Solidification, 1984-85. **1**: p. 59-80.

77. W. J. Boettinger, L. Bendersky and J. G. Early, *an analysis of the microstructure of Rapid Solidified Al-8 Wt Pct Fe powder*. Metallurgical Transactions, 1986. 17A (May): p. 781-790.
78. I. C. Stone and P. Tsakirooulos, *Cooling rates in gas atomised Al-4wt%Cu alloy powders*. International journal of rapid solidification, 1992. 17: p. 177-190.
79. G. Shao and P. Tsakirooulos, *Prediction of phase selection in rapid solidification using time dependent nucleation theory*. Acta Metall. Mater., 1994. 9: p. 2937-2942.
80. C. G. Levi and R. Mehrabian, *Heat flow during rapid solidification of undercooled metal droplets*. Metallurgica Transaction, 1982. 13A: p. 221-234.
81. P. Shukla, R. K. Mandal, and S. N. Ojha, *Non-equilibrium solidification of undercooled droplets during atomization process*. Bull. Materials Science, 2001. 24(5): p. 547-554.
82. S. Kou. Transport Phenomena and Materials Processing. 1996: p.169. New York. John Wiley & Sons.
83. C. G. Levi, *The evolution of microcrystalline structures in supercooled metal powders*. Metallurgica Transactions, 1988. 19A: p. 699-708.
84. J. P. Hirth, *Nucleation, undercooling and homogeneous structures in rapidly solidified powders*. Metallurgica Transactions, 1978. 9A: p. 401-404.
85. D. A. Porter and K. E. Easterling, *Phase Transformation in Materials and Alloys*. 1983: Van Nostrand Reinhold (UK) Co. Ltd.
86. M. McLean and M. S. Loveday, *In-situ observations of the annealing of liquid lead inclusions entrained in an aluminium matrix*. Journal of Materials Sciences, 1974. 9: p. 1104-1114.
87. W. A. Tiller, *Migration of a liquid zone through a solid: Part I*. Journal of Applied Physics, 1963. 34(9): p. 2757-2762.
88. D. R. H. Jones and G. A. Chadwick, *The experimental determination of the Kinetics of solid-liquid interface in transparent materials using temperature-gradient zone migration*. Philosophical Magazine, 1917. 24: p. 1327-1345.
89. M. McLean, *The kinetics of spheroidization of lead inclusions in aluminium*. Philosophical Magazine, 1973. 1973: p. 1253-1266.
90. M. F. Ashby and R. M. A. Centamore, *The dragging of small oxide particles by migrating grain boundaries in copper*. Acta Metallurgica, 1968. 16, p. 1081-1092.
91. R. E. Samallman and R. J. Bishop, *Modern physical metallurgy and materials engineering*, ed. H. Butterworth. 1999: Reed Educational and Professional Ltd..
92. H. H. Uhlig, ed. *Corrosion Handbook*. 1984: New York Hohn Wiley & Son, Inc. London Chapman & Hall, Limited.

93. J. R. Davis, *Corrosion of aluminium and aluminium alloys*. 1999: ASM International. The Materials Information Society, Materials Park, OH 44073-0002.
94. E. J. Lee and S. I. Pyun, *The effect of oxide chemistry on the passivity of aluminium surfaces*. Corrosion Science, 1995. **37**(1): p. 157-168.
95. H. A. El Shayeb, F. M. Abd El Wahab and S. Z. E. Abedin, *Electrochemical behaviour of Al, Al-Sn, Al-Zn and Al-Zn-Sn alloys*. Journal of Applied Electrochemistry, 1999. **29**: p. 473-480.
96. C. W. Park and S. R. Y., *Effect of tin content and heat treatment on the anodic of aluminium - tin alloy*. Han'guk Pusik Hakhoechi, 1985. **14**(3): p. 31-39.
97. G. C. Pratt. *Metallic and nonmetallic bearing*. in *Innovation Management in Metallurgy*. 1975. p. 73-80, Institute of Metallurgist, London, England.

## Chapter 3

### Experimental methods

#### 3.1 Introduction

In order to understand the microstructure evolution and its relationship with the mechanical and chemical properties of the thermally sprayed coatings, basic information including the gas atomised powder, the thermal spray parameters and post annealing conditions; the characterisation methods including the mechanical and chemical property testing methods are introduced in this chapter.

#### 3.2 Materials – gas-atomised powder

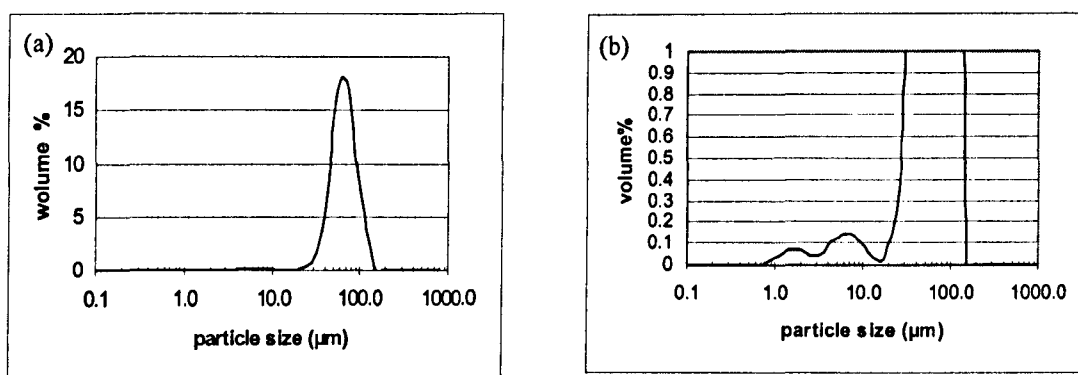


**Figure 3.1 Particle size distribution of Al12Sn1Cu gas atomised powder particles as obtained by laser diffractometry**

Two different powders were employed in this study. The Al-12wt%Sn-1wt.%Cu gas atomised powder supplied by Phoenix Scientific Industries Ltd. UK had a nominal particle size range of 38-106 μm. The size distribution was analysed by laser diffractometry using a Malvern Instruments, Laser Mastersizer and is



shown in Figure 3.1<sup>[1]</sup>. The mean particle size was determined to be  $\sim 65 \mu\text{m}$  (Figure 3.1a). It is also noted that a small amount of the powder had a size range less than  $10 \mu\text{m}$  (Figure 3.1b).

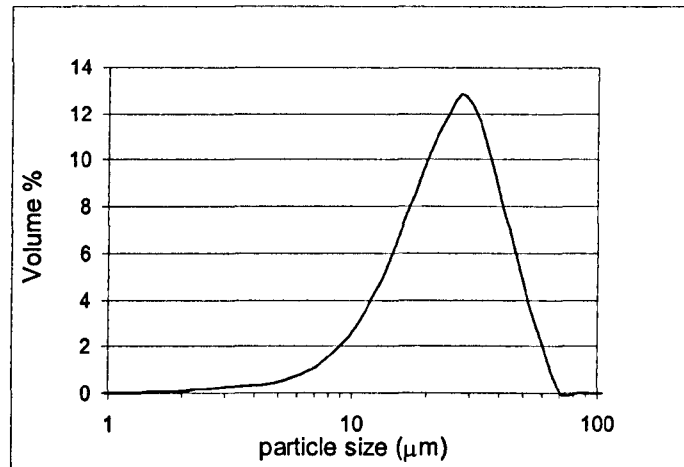


**Figure 3.2 Particle size distribution of Al<sub>20</sub>Sn<sub>3</sub>Si gas atomised powder particles as obtained by laser diffractometry**

The powder of nominal composition Al-20wt%Sn-3wt%Si was produced by Praxair Surface Technologies Inc., USA, with a nominal size range of 15-45 $\mu\text{m}$ . The size distribution of this powder is shown in Figure 3.2<sup>[1]</sup>. The mean particle size was determined to be  $\sim 28 \mu\text{m}$ .

### 3.3 High velocity oxy-liquid fuel (HVOLF) spray deposition and heat treatment of the coatings

#### 3.3.1 HVOLF thermal spraying

A schematic of the HVOLF thermal spray system is shown in Figure 3.3. Kerosene ( $\text{C}_{12}\text{H}_{26}$ ) and oxygen were fed from the back of the combustion chamber where they reacted. The combusted gas passed through a converging-diverging nozzle where it was accelerated before powder was injected radially into the hot gas

stream. Entrained powder was accelerated down a parallel-sided barrel, 100 mm long, before it became part of a free jet, which impinged on to the steel substrate. These were mounted onto the circumference of a horizontal turntable and rotated with a tangential velocity of  $1 \text{ ms}^{-1}$ . The spraying gun traversed vertically at  $5 \text{ mm s}^{-1}$  at a stand-off distance of 365 mm for the Al12Sn1Cu alloy and 229 mm for the Al20Sn3Si alloy from the end of the barrel. Coatings up to  $300 \mu\text{m}$  thick were formed after  $\sim 20$  passes of the gun across the substrate for the Al12Sn1Cu coatings. For the Al20Sn3Si alloys, the thickness of coatings attained was  $320 \mu\text{m}$  after 40 passes.

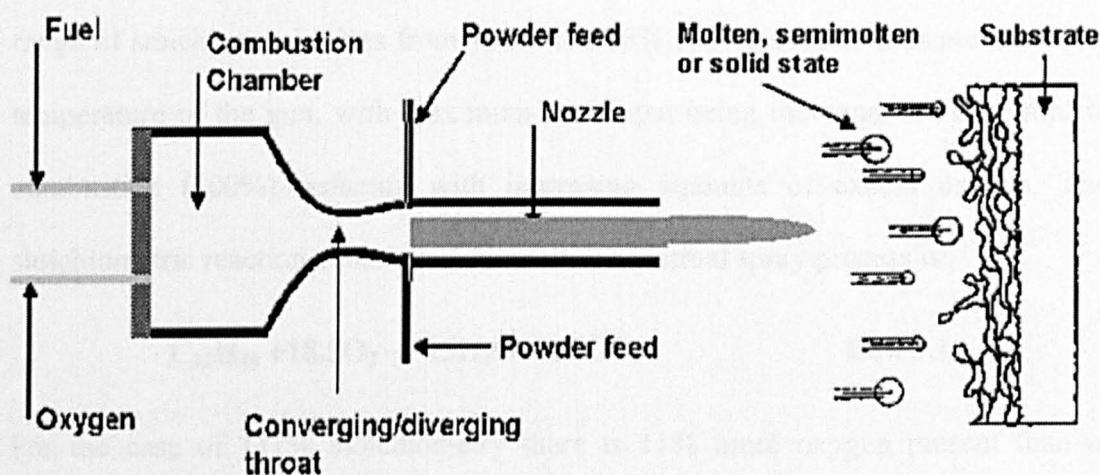


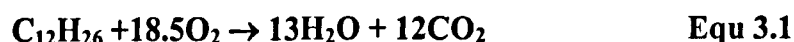
Figure 3.3 HVOLF thermal spray process

The thermal spraying parameters of the alloys are shown in the Table 3.1. The liquid fuel ( $\text{C}_{12}\text{H}_{26}$ ) is used to combust with the oxygen to form a high temperature gas to melt the deposit powder. Carrier gas ( $\text{N}_2$ ) is used to transport the gas-atomised powder. These parameters are decided empirically for the thermal spraying process.

Table 3.1

Materials	Fuel flow rate (lmin <sup>-1</sup> )	O <sub>2</sub> flow rate (lmin <sup>-1</sup> )	Carrier N <sub>2</sub> gas flow(lmin <sup>-1</sup> )	Powder feed rate (gmin <sup>-1</sup> )
Al12Sn1Cu	0.40	828	16.8	25
Al20Sn3Si	0.22	854	7.6	11

The combustion of fuel and oxygen enable thermally sprayed coatings to be produced. A 'spray map' can be produced by plotting the fuel flow against oxygen flow, in litres per minute, for a range of conditions incorporating lines relating to stoichiometry (i.e. fuel and oxygen) and total powder mass input. Figure 3.4 expresses a 'spray map' of kerosene fuel and oxygen conditions used for aluminium alloys designed for bearing applications. Each diamond point represents a specific condition used during the wider research programme into HVOLF coatings. The range of stoichiometric lines from 100% to 308% can be used to indicate the flame temperature of the gun, with maximum heat input being the condition of complete combustion (100%) reducing with increasing amounts of excess oxygen. The stoichiometric reaction equation of the HVOLF thermal spray process is:



For the case of 111% stoichiometry there is 11% more oxygen present than is necessary for complete combustion. This excess oxygen causes a reduction in the temperature by removing energy during combustion in the chamber. Also plotted are mass flow rate lines ranging from 17.25 to 28 g/s kerosene plus oxygen. As the mass flow rate increases there is a corresponding increase in the amount of combustion gases being produced with a resulting increase in gas velocity. Therefore moving along a stoichiometric line (green) will not principally increase the temperature but will mainly affect the amount of combustion gases, which determines the velocity of both the gas and the particles. An additional consideration is the 'dwell time' of the

particles in the combustion chamber, reduction of which affects the amount of heat that can be absorbed into the powder particles. Moving down a total mass input line (red) will keep the total constituents constant but will change the stoichiometry and thus decrease the combustion temperature.

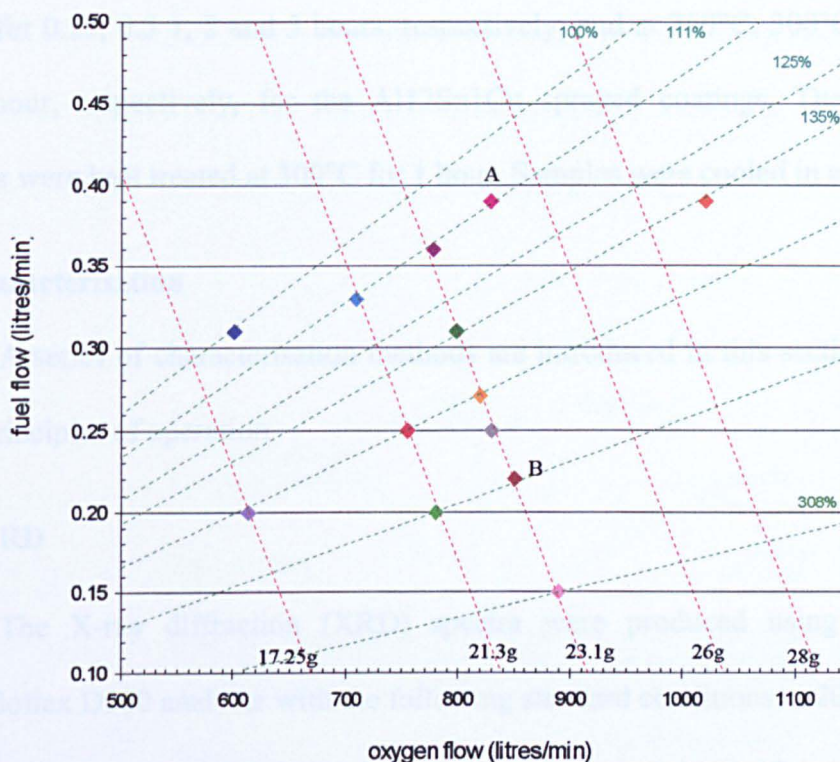


**Figure 3.4 The relationship between fuel flow and oxygen flow during the thermal spraying, Lines of constant oxygen stoichiometry (%) and constant mass flow rate are shown <sup>[1]</sup>**

The diamond points marked as A and B shown in Figure 3.4 indicate the specific thermal spray conditions which were investigated in this thesis. The point A is a relatively high temperature condition as compared with point B, with a slightly greater energy input. This condition (A) was used to spray Al12Sn1Cu particles in the range 40-106  $\mu\text{m}$ , whereas the lower energy condition (B) was used for the Al20Sn3Si powder in the range 15-45  $\mu\text{m}$ . A reduced temperature was required in the latter case to prevent the smaller particles from overheating.

### 3.3.2 Heat treatment of the coatings

A series of experiments was undertaken to determine the effect of heat treatment on the Al-Sn-X (X= Cu, Si,) HVOLF sprayed coatings. A Carbolite air recirculating furnace was used for the heat treatments which were carried out at 300°C for 0.25, 0.5, 1, 2 and 5 hours, respectively; and at 250°C, 300°C and 400°C for 1 hour, respectively, for the Al<sub>12</sub>Sn<sub>1</sub>Cu sprayed coatings. The Al<sub>20</sub>Sn<sub>3</sub>Si coatings were heat treated at 300°C for 1 hour. Samples were cooled in air.

### 3.4 Characterisation

A series of characterisation methods are introduced in this section including some principles of operation.

#### 3.4.1 XRD

The X-ray diffraction (XRD) spectra were produced using a Siemens Krystalloflex D500 analyser with the following standard conditions: a  $2\theta$  range of 20 to 140 degrees, a step size of 0.05 degrees and a counting time of 2 seconds at each step for the Al-12wt.%Sn-1wt.%Cu powder and the sprayed coatings. Sections of the sprayed mild steel coupons, upon which the coatings had been applied, were supported in a suitable holder. For the early analyses, a small quantity of pure silicon powder spread onto the surface of the coating was used to check the calibration of the diffractometer.

The Al-20wt.%Sn-3wt.%Si gas atomised powder and sprayed coatings were analysed using the conditions of: a  $2\theta$  range of 25 to 85 degrees, a step size of 0.02 degrees and a counting time of 3 seconds at each step.



### 3.4.2 Interaction of the electron beam with matter

The basic principles of electron beam interaction with matter are introduced here to help understand the SEM, TEM and EDX etc characterisation methods used. When a high energy beam of electron interacts with matter, many kinds of signal such as X-rays, back scattered electrons and elastic or inelastic scattered electrons are produced depending on the thickness of the sample. When a high-energy beam of electrons interacts with a thin specimen, the signals generated are shown on Figure 3.5.

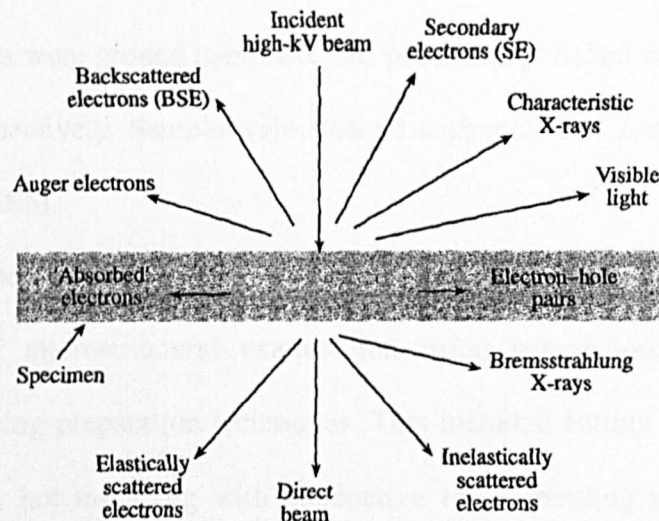


**Figure 3.5 Signals generated when a high-energy beam of electrons interacts with a specimen** <sup>[2]</sup>

In scanning electron microscopy (SEM), the samples are generally very thick. Thus, secondary electrons or backscattered electrons are used to form an image. In conventional TEM, where the samples are very thin, elastically scattered electrons are used to form bright field and dark field images, and diffraction patterns.

The signals created by high-energy electron interaction with a material (Figure 3.5) provide the basis for analytical electron microscopy (AEM). This gives

chemical information from techniques such as X-ray energy dispersive spectrometry (XEDS or EDX), making use of characteristic X-rays, and electron energy-loss spectrometry (EELS) that makes use of inelastically scattered electrons.

### 3.4.3 SEM

The morphology of the gas atomised powder sample was observed in the SEM by sticking conductive two-sided paper onto a sample holder and then spreading the powder onto the glue.

Sections through the gas atomised powder were prepared by spreading the powder uniformly onto a sample mounting machine and embedding in conductive resin. Then, samples were ground using wet SiC paper and polished with 6 and 1  $\mu\text{m}$  diamond paste, respectively. Sample were cleaned with methanol and dried prior to observation in the SEM.

Sections from the as-deposited and annealed coatings were similarly prepared for SEM microstructural examination using conventional mechanical grinding and polishing preparation techniques. This included cutting cross-sections through a coupons, hot mounting with conductive resin, grinding using wet SiC paper and polishing with 6 and 1  $\mu\text{m}$  diamond paste, respectively, and then cleaning the sample with methanol and drying. The sample was stored in a desiccator for the interval between polishing and analysis.

Samples were observed in a JEOL 6400SEM in the backscattered electron (BSE) image mode at an operational voltage of 10 ~ 15 kV and a working distance of about 15mm. These samples were also observed in an FEI XL30 FEG-ESEM in the BSE mode (in hi-vac mode) to gain very high resolution images.

The corroded tested samples were also observed in the FEI XL30 FEG-ESEM. The corroded samples were cleaned by immersing in methanol using a

Soniprobe, manufactured by DAWE Instrument Ltd (type 7530A). The surfaces of the corroded samples were observed by wet mode in the FEG-ESEM, using a gas filled detector, because the samples were mounted in non-conductive resin for corrosion testing. After surface observation, the non-conducting mounting resin was removed and samples were cut to obtain a cross section of the corroded coatings. These samples were then mounted in conducting resin and mechanically ground and polished for SEM cross section observation.

EDX was used to investigate the compositions of the gas atomised powder, the thermally sprayed coatings and the corrosion reaction products.

### 3.4.4 TEM

#### 3.4.4.1 TEM sample preparation technique

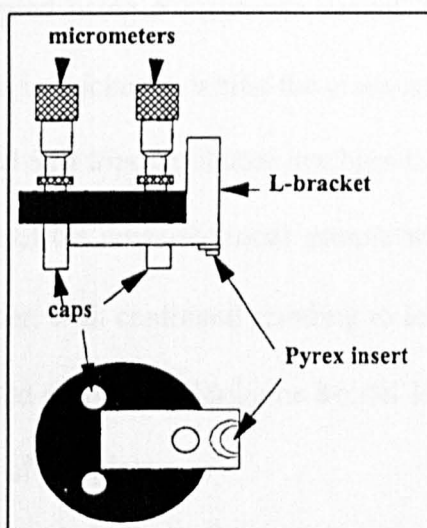


**Figure 3.6 Schematic of the tri-pod polisher <sup>[3]</sup>**

Electron transparent sample foils were prepared from the starting powder, the as-sprayed coatings and the annealed coatings. Epoxy resin was used to disperse the powder at close separation to ensure the sample foil held together during thinning. The resin-dispersed samples were mounted on copper washers and mechanically ground using a tripod polisher. Particular care was needed when polishing soft



samples because of the ease of embedding polishing grit into the material. Samples were polished on both sides using diamond impregnated film from 30  $\mu\text{m}$  sequentially down to 0.5  $\mu\text{m}$  until they were less than 10  $\mu\text{m}$  in thickness. Low angle ion beam milling was then used for the final perforation of the samples.

The as-sprayed and annealed samples were mechanically cut into 3 mm diameter discs using a Fischione model 170 ultrasonic disk cutter, parallel to the substrate, (i.e. planar view). The cross-section samples were prepared by cutting 2×1 mm pieces of the sprayed coating using a Struers Accutom-5 cut off machine and then glued using epoxy resin face to face to provide a depth profile of the microstructure. Both samples were ground and polished in the same way as for preparing SEM samples until the sample thickness was less than 100  $\mu\text{m}$ . The plan-view samples were dimpled using a Fischione model 2000 specimen preparation system to less than 20  $\mu\text{m}$  in thickness, whilst the cross-section samples were ground on both sides using model 910 tripod polisher machine from South Bay Technology Inc.. When the thickness of the cross-sectional sample was less than 50  $\mu\text{m}$ , it was stuck onto a copper washer, with continued grinding to less than 10 $\mu\text{m}$ . Finally, low angle ion beam milling and polishing (Fischione Model 1010) was used for the final perforation of both kinds of samples.

A schematic of a tripod polisher is shown in Figure 3.6. Two back micrometers and one pyrex insert holding the sample were used to define the polishing plane. By adjusting the back micrometer, the sample on the pyrex insert could be ground and polished in a controlled fashion.

### 3.4.4.2 TEM (BF, DF and WB techniques)

The specimens were observed using a double tilting stage in a Jeol 2000fx transmission electron microscope (TEM) operating at an accelerating voltage of 200kV and a Jeol 4000fx TEM operated at 400kV. Bright field (BF), dark field (DF) and weak beam (WB) techniques were initially used to characterise the microstructure of the coatings.

For conventional TEM, a sample should be typically less than 1  $\mu\text{m}$  in thickness and usually  $< 100\text{ nm}$  for reliable diffraction contrast analysis and  $< 10\text{ nm}$  for HRTEM (phase contrast) imaging. Thus, if a specimen is thin enough a significant number of electrons are transmitted, with some electron beams being elastically scattered, i.e. diffracted.

When a plane wave of electrons interacts with a material, diffraction of electrons within the crystal occurs. Because many inorganic materials adopt a symmetrical relationship of atoms, electron diffraction can be used to explore the symmetry of a crystal lattice. At a strong zone axis, the diffraction patterns exhibit high symmetry, otherwise termed a low index orientation. Such diffraction patterns are formed by many beams arising from the many different diffracting planes and many electron scattering events.

In order to produce good strong diffraction contrast, it is necessary to tilt the crystal away from the low index zone orientation to set up a “two beam” case, which includes the central beam plus one other strong scattering beam. In a very thin crystal ( $< 100\text{ nm}$ ), electrons could be scattered just once by a set of diffracting planes (otherwise termed kinematical diffraction). For example, the area that appears bright in a DF image is the area where the planes are at the Bragg condition. So it becomes relatively easy to interpret contrast and it is possible to obtain the Burgers

vector of a dislocation, for example, by looking at the crystal from different orientations (i.e., diffracting conditions), building up a 3D picture from the 2D projected images. If the sample is thick,  $> 100$  nm, but not too thick, and a two-beam diffraction orientation is adopted, some electrons that undergo Bragg diffraction may also undergo inelastic scattering and a pair of Kikuchi lines bounding the central beam and the diffracted spot may be observed.

A diffraction pattern contains electrons from the whole area of the specimen imaged. However, TEM foils may be distorted to some extent or there may be a range of angles of illumination, so that the diffraction conditions change as we cross the specimen. Thus, a selected area aperture is used in practise to define a limited area from which electrons are taken to form the diffraction pattern.

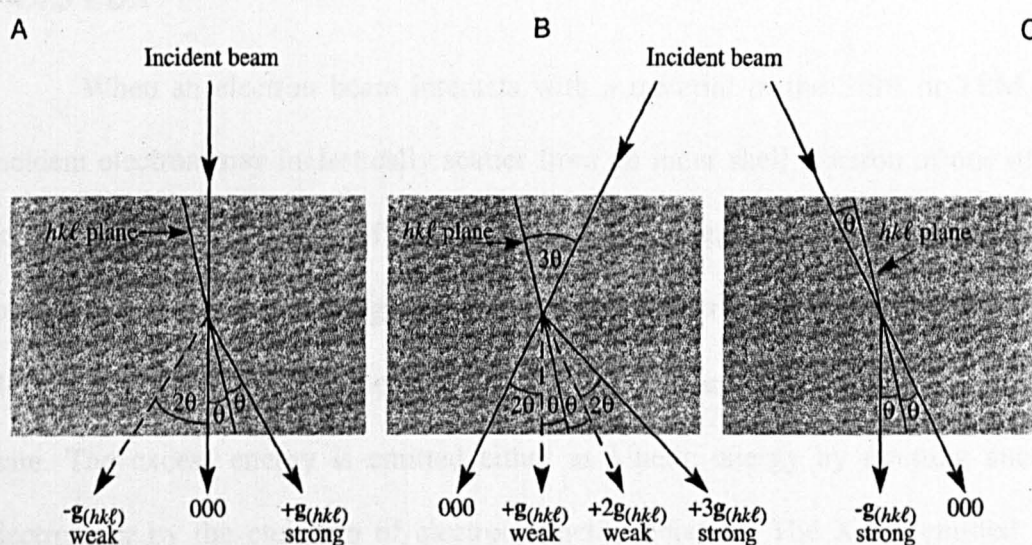


**Figure 3.7 (A) Standard two beam condition; (B) Weak beam dark field condition and (C) Dark field condition** <sup>[4]</sup>

When a selected-area diffraction (SAD) pattern is projected onto the viewing screen, we can orientate the pattern to best form the image in the TEM. A two beam SAD pattern will contain a bright centre spot, i.e. the direct electron (000) beam and one other diffracted beam. If one diffracted beam is strong ( $+g_{(hkl)}$ ), the

corresponding ( $-g_{(hkl)}$ ) diffraction spot is weak, as shown in Figure 3.7(a), and the direct beam (000) is selected by the objective aperture, the resultant image is termed a bright-field (BF) image. If the diffracted beam ( $-g_{(hkl)}$ ) is selected down the optic axis, a centred dark-field (CDF) image is formed, as shown in Figure 3.7(c). In practice, we move the weak diffracted beam to the optic axis to form a centred DF image in order to minimise the effect of aberrations and astigmatism (and to avoid re-tilting the sample). If we use the strong diffracted beam to form the image by moving it to the optic axis without tilting the sample, we can form a “weak beam” (WB) dark field image, as shown in Figure 3.7(b). The weak beam imaging technique may be used e.g. for detailed stacking fault analysis or dislocation characterisation.

#### 3.4.4.3 EDX

When an electron beam interacts with a material in the SEM or TEM, the incident electron may inelastically scatter from an inner shell electron of one of the component atoms. As result of this inner shell scattering, the target atom is left in an excited state. The excess energy will quickly be lost in a de-excitation process, as an electron of a lower binding energy will make a downward transition into the vacated state. The excess energy is emitted either as kinetic energy by emitting another electron, or by the emission of electromagnetic radiation. The X-ray emitted will have an energy that is characteristic of the transition between the two shells and can therefore be used to identify the atomic number of the target. These characteristic X-rays provide compositional information on the sample, being used to form the X-ray energy-dispersive (EDX) spectra.

### 3.4.4.4 Moiré patterns

Moiré patterns are a kind of phase-contrast image which can be formed by interfering two sets of fringes which have nearly common periodicities. There are three kinds of moiré effects (Figure 3.8): A) translational moiré fringes (formed by two parallel planes with slightly different lattice spacing; B) rotational moiré fringes (formed by two planes with the same lattice spacing rotated by some angle and C) mixed moiré fringes (formed by two different lattice spacing planes rotated by some angle).

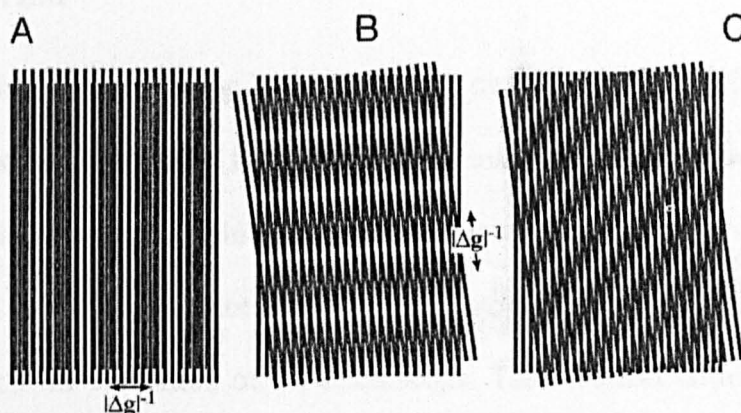


**Figure 3.8** The relationship between fringes and their constituent lattices. (A) Translational moiré fringes; (B) rotational moiré fringes; (C) mixed moiré fringes

The translational moiré fringes have the following relationship,

$$g_{im} = g_2 - g_1 \quad \text{Equ 3.2}$$

where  $g_1$  and  $g_2$  are the g-vectors of the two sets of parallel planes, respectively. If the lattice spacing of two set of planes are  $d_1$  and  $d_2$ , the moiré fringe spacing  $d_{im}$  is given by  $1/d_{im}$  (otherwise written  $(|\Delta g|^{-1})$ ),

$$d_{im} = \frac{1}{g_{im}} = \frac{1}{g_2 - g_1} = \frac{\frac{1}{g_2} \cdot \frac{1}{g_1}}{\frac{1}{g_1} - \frac{1}{g_2}} = \frac{d_2 d_1}{d_1 - d_2} \quad \text{Equ 3.3}$$

For the case of rotational moiré fringes and a rotation angle,  $\beta$ , the fringe spacing  $d_{rm}$  is:

$$d_{rm} = \frac{1}{g_{rm}} = \frac{1}{2g \sin \frac{\beta}{2}} = \frac{d}{2 \sin \frac{\beta}{2}} \quad \text{Equ 3.4}$$

For the case of mixed moiré fringes:

$$d_{gm} = \frac{d_1 d_2}{((d_1 - d_2)^2 + d_1 d_2 \beta^2)^{\frac{1}{2}}} \quad \text{Equ 3.5}$$

#### 3.4.4.5 HRTEM

During high resolution TEM (HRTEM) observation, otherwise termed phase contrast imaging, images are formed due to the interference of electrons scattered by different planes within a thin specimen in a low index orientation. This type of observation can be sufficient to image the atomic structure of thin specimen, depending on the resolution of the microscope. The resultant lattice fringe images provides information about the crystal orientation on the very fine scale, but it is difficult to precisely determine where atoms are located <sup>[4]</sup>. In the present work, HRETEM has been used to analyse the fine scale structure of precipitates of Sn and Si. HRTEM images are sensitive to many factors, including precise alignment of the beam with respect to both the specimen and the optical axis, the thickness and tilt of the sample, the defocus of the objective lens, the chromatic aberration of the lenses, and the coherence of the beam <sup>[5]</sup>.

#### 3.4.4.6 EELS and EFTEM

Electron energy loss spectroscopy (EELS) is the analysis of the energy distribution of electrons that have scattered inelastically (as shown in Figure 3.5).

These inelastic collisions provide a tremendous amount of information about the composition and electronic structure of the specimen, with details of the nature of these atoms, their binding and nearest-neighbour distributions, and their dielectric response [6].

The zero-loss peak, which consists primarily of elastic forward-scattered electrons, also contains electrons that have suffered minor energy losses. The low-loss region, up to an energy loss of ~50 eV, contains electrons which have interacted with the weakly bound outer-shell electrons of the atoms in the specimen, providing information on the electronic properties of the specimen. Electrons in the high-loss region have interacted with the more tightly bound inner-shell or “core” electrons and contain information characteristic of the element in the specimen.

Energy filtered TEM (EFTEM) uses inelastically scattered electrons to form an elemental map of the investigated region, with acquisition of data at a specific energy window.

### **3.4.5 Image analysis of particle distributions**

The micron / sub-micron Sn particle distributions were investigated using the ImageJ software for BSE images taken from a JEOL 6400 SEM. Three SEM images representing each processing condition were selected for analysis. A grey-level based threshold was applied to each of the BSE images and the resulting binary maps were used to measure the projected area of the Sn particles. A criterion of a minimum of 9 pixels was used to determine the smallest Sn particles. Histograms of particle number against particle area, averaged across each set of images, were constructed using Origin 6.0.

### 3.5 Evolution of properties

#### 3.5.1 Corrosion testing <sup>[1]</sup>

The corrosion behaviour of the materials was evaluated by electrochemical measurements in the form of cyclic potentiodynamic polarization and constant potential tests. A three electrode cell was employed for the potentiodynamic tests using a method similar to the ASTM G5-94 test procedure. Samples were ground to a 1200 grit finishing on SiC paper for a smooth surface. Then, samples were mounted in non-conductive resin and masked off with Fortilac lacquer to give a square corrosion area on the surface and sealed on an electrical connection rod, leaving approximately 10×10 mm<sup>2</sup> of exposed surface area. The test solution comprised 0.1M sodium chloride solution de-aerated with nitrogen for 1 hour prior to measurement. The solution was held at 25°C with a platinum counter electrode and calomel electrode (SCE) as a reference electrode. Following introduction into solution, each sample was allowed to stabilise at its rest potential,  $E_{\text{corr}}$ , for a period of 3600s prior to the initial potential scan. The corrosion tests were potentiodynamically controlled using an ACM Grill 8AC potentiostat. Tests were run over a potential range of -1500 to -1400 mV (vs SCE) at a sweep rate of 20mV/minute.

#### 3.5.2 Microhardness

The thickness of the sprayed coatings was typically 180-350 µm, as a consequence of which, a Leco M400 microhardness tester was used to determine the hardness of the coatings. Samples were prepared by the same method as for SEM examination. Microhardness measurements were obtained from a series of indents along a line parallel to the coating/substrate interface, approximately half way



between the interface and the free surface. A 200g load was generally used. Fifteen separate hardness measurements were taken for each sample and the average value and standard deviation determined. The gradient of microhardness through the layer was examined by indenting from the coating / substrate interface up to the layer surface, again using a 200g load.

### 3.6 Summary

Characteristics of the pre-deposited gas atomised powder particles have been introduced. Then, the parameters for the thermal spraying of the coatings, the stoichiometry diagram of fuel and oxygen for this project on the manufacture of bearing materials, and the annealing conditions of the coatings have been introduced. The principles of the characterisation methods of XRD, SEM, TEM, EDX, HRTEM, EELS and EFTEM have also been introduced. The technique used for TEM sample preparation of large area thin foils of gas atomised powder and cross sections of the sprayed coatings using a tri-pod polisher have been described, with emphasis on the innovations developed by the author. An image analysis method to characterise particle distributions using ImageJ has also been introduced. Finally, methods for the assessment of coating properties, namely corrosion testing and microhardness measurement have been described.

## References

1. A. J. Horlock, *Unpublished Internal Report*. 2003.
2. D. B. Williams and C. B. Carter, *Transmission Electron Microscopy, Basics*. Vol. I. 1996: p.7. Plenum press, New York, A division of Plenum Publishing Corporation 233 Spring Street, New York, N. Y. 10013.
3. J. P. Benedict, R. M. Anderson and S.J. Klepeis. *Preparation of TEM plan view sections on specific devices using the tripod polisher*, in *Materials Research Symposium Proceeding, Electron Microscopy of Semiconducting Materials and ULSI Devices*. 1998. p. 19-30, France Ross.
4. D. B. Williams and C. B. Carter, *Transmission Electron Microscopy, Images*. Vol. III. 1996: p. 364, Plenum press, New York, A division of Plenum Publishing Corporation 233 Spring Street, New York, N. Y. 10013.
5. M. W. Fay, *Advanced electron microscopy of wide band-gap semiconductor materials*, in *Electronic & Electrical Engineers*. 2000, University of Sheffield (PhD thesis): Sheffield, UK.
6. David B. Williams and C.B. Carter, *Transmission Electron Microscopy, Spectrometry*. Vol. IV. 1996: Plenum press, New York, A division of Plenum Publishing Corporation 233 Spring Street, New York, N. Y. 10013.

## Chapter 4

### The Al-12wt.%Sn-1wt.%Cu alloy gas atomised powder and as-sprayed coatings

---

#### 4.1 Introduction

HVOF (gas fuel) thermally sprayed Al-12wt.%Sn-1wt.%Cu (Al<sub>12</sub>Sn<sub>1</sub>Cu) coatings have significant potential in the manufacture of automotive bearings <sup>[1]</sup>. This is because the HVOF thermal spraying technique can produce high quality coatings with low porosity, good mechanical adherence to the substrate and novel, non-equilibrium microstructures <sup>[2]</sup>. A new HVOLF (liquid fuel) thermal spray technique is introduced to thermally spray low melting temperature Al-Sn based bearing alloys to reduce the nozzle blocking problem in the gas fuel spraying process. Since different microstructures lead to different physical, chemical and mechanical properties of the coatings, it is necessary to understand how the coating microstructures develop. In this chapter, the microstructure of gas-atomised powder particles used as feedstock for HVOLF spraying and as-sprayed Al<sub>12</sub>Sn<sub>1</sub>Cu coatings are reported. The combined techniques of XRD, SEM, TEM and EDX are used to study the phases presented and the microstructures formed. The microstructures are initially described, and then the microstructural formation mechanisms and associated affect factors are discussed. The critical cooling rate for the liquid phase separation of Al-Sn alloys has been quantitatively analyzed. The microstructure of the gas atomized powder and the as-sprayed coatings are discussed using this mechanism. The basic processing conditions for the gas-atomised powders and the

HVOLF spraying parameters of the coatings have been described previously in Chapter 3.

## 4.2 Characterisation of the gas-atomised powder

### 4.2.1 XRD analysis

Figure 4.1 shows the XRD spectrum obtained from the gas-atomised powder. The principal peaks are found to be fcc Al and bct Sn. No other phases could be identified from the spectrum.

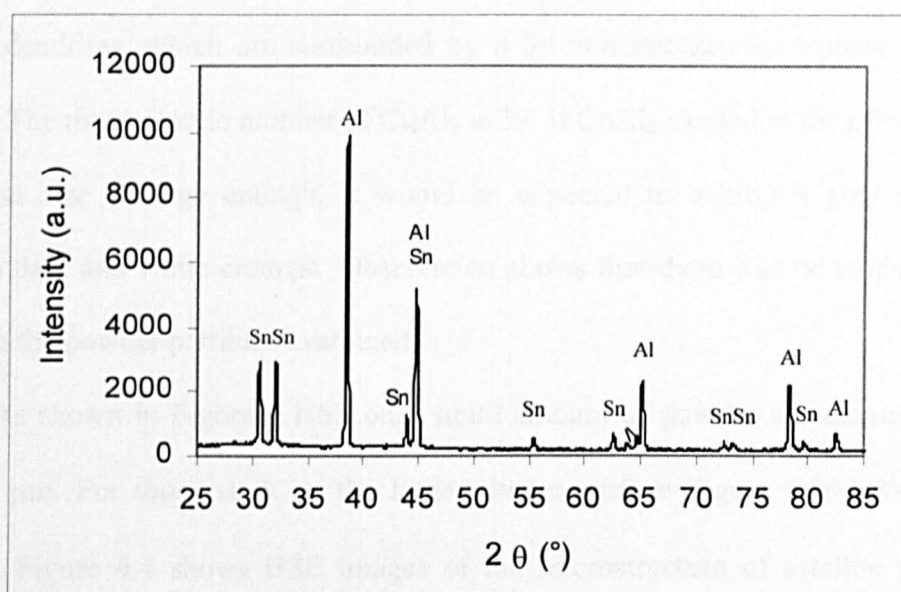


Figure 4.1 XRD pattern from gas-atomised Al<sub>12</sub>Sn<sub>1</sub>Cu powder

### 4.2.2 Microstructural investigation

#### SEM observation

The morphology of gas-atomised Al<sub>12</sub>Sn<sub>1</sub>Cu is shown in Figure 4.2. The low magnification secondary electron (SE) image of Figure 4.2(a) shows that most of the powder particles have adopted a spherical shape although a few exhibits an irregular morphology with most particles in the size range of 40-106  $\mu\text{m}$ . The higher

magnification SE image of Figure 4.2(b) shows the presence of small satellite powder particles, with globular metal attached to some of the large particles.

Cross-sectional BSE images of large scale powder particles ( $>10\text{ }\mu\text{m}$ ) show the presence of a cellular-dendritic structure (Figure 4.3a and b). Figure 4.3(b) is a higher magnification image of a region in Figure 4.3(a). The BSE images arise from atomic number contrast. The atomic number of Al and Sn are 27 and 118, respectively. Therefore, the dark regions represent the Al-rich phase and the light regions correspond to the Sn-rich phase. Figure 4.3 shows that the dark regions are Al-rich dendrites, which are surrounded by a Sn-rich interdendritic phase (lighter region). The mean atomic number of CuAl<sub>2</sub> is 39. If CuAl<sub>2</sub> existed in the powder and the phase size is large enough, it would be expected to exhibit a grey contrast between dark and white contrast. Observation shows that there was no evidence for CuAl<sub>2</sub> in the powder particles examined.

As shown in Figure 3.1(b), only small amount of powder has diameter less than  $10\text{ }\mu\text{m}$ . For those stick on the large powder surface Figure 4.2(b) look like satellite. Figure 4.4 shows BSE images of the microstructure of satellite powder particles  $< 10\text{ }\mu\text{m}$  in size. Satellite particles in the approximate size range  $6 \sim 10\text{ }\mu\text{m}$  exhibit a non-dendritic structure. Instead, they appear to comprise a dispersion of sub-micron Sn particles within the Al matrix, adopting either spherical or elongated shapes (Figure 4.4a-c). As the satellite powder particle size decreases (Figure 4.4a to f), the size of the Sn particles also appears to decrease. The small satellite particles show a bimodal Sn distribution within one powder particle (Figure 4.4d,e). In Figure 4.4(f), the shell of the material surrounding a satellite powder particle (arrowed) adopts a grey contrast. This is because the resolution of the BSE signal in the SEM is

not sufficient to distinguish individual Sn particles from the Al matrix background in this instance.

Some large powder shown in Figure 4.5 also show the fine scale features of the shell structure surrounding powder particles with dendritic cores. Figure 4.5(a) illustrates a powder particle surrounded by a grey contrast shell. The higher magnification BSE image of Figure 4.5(b) is an enlargement of the boxed region in Figure 4.5(a) and shows the very fine scale dispersion present at the centre of the grey contrast shell. These bright particles are presumably Sn as they exhibit the same contrast features as the interdendritic Sn in the larger powder particles. An EDX spectrum (Figure 4.5c) of the box region (Figure 4.5b) shows the presence of Al, Sn and a trace of Cu. A carbon peak also present in the spectrum is attributed to the conducting mounting resin at the edge of the powder particle. The semi-quantitative EDX analysis data of this region suggest a similar composition to the alloy provided which indicates these shell structures are formed as part of the atomisation process. Therefore, the light contrast features are indeed Sn particles. Figure 4.5(d) is an example of a powder with a cellular-dendritic core and relatively thick dendritic shell. In the shell, the dendrites are aligned to give a columnar structure.

Occasionally, a complex compound microstructure of irregular shaped powder is shown in Figure 4.6. A small powder particle with a mixture of fine scale dispersed Sn and fine scale cellular-dendritic Al is shown in Figure 4.6. An image of the cellular Al grain, located near the point of contact is shown in Figure 4.6(b, boxed C) and it is enlarged in Figure 4.6(c). Obviously, the dendrite arm spacing (Figure 4.6c) is smaller than the larger powder particle Figure 4.6(a). At a position further from the point of contact, the dendritic structure of Al adopts an elongated shape radiating from an apparent growth centre of the cellular-dendritic structure

(Figure 4.6b, arrowed). The tail of this small powder particle (Figure 4.6b) exhibits the uniform grey contrast indicative of the very fine dispersion of Sn particles similar to the shell structure (Figure 4.5a and b). The transition zone between dendritic Al and Sn and the fine dispersed Sn is shown in Figure 4.6(b), boxed D. The detail at the transition zone (Figure 4.6d) shows that the Sn particle size changes from small to intermediate to large across the interface if observed from the top of the image.

Also, in a very low frequency, highly complex mixed microstructures of other irregular shaped particles are formed. Figure 4.7(a and b) shows an irregular powder particle with a partially dendritic structure and a partially fine scale Sn dispersion within the Al matrix. Figure 4.7 (c) exhibits a microstructure of fine scale dendritic regime to the left of the particle adjacent to an irregular region on the right comprising coarse dendrite arms and a much finer scale Sn dispersion.

The different microstructures formed can presumably be attributed to the different cooling rates which will be discussed in detail in a later section.

### **TEM observation**

The TEM was used to investigate in detail the powder structure and was used to characterise both the large Sn particles (which comprised over 95% of the powder according to Figure 3.1) and the smaller particles. A TEM montage (Figure 4.8) illustrates the typical microstructure of the large gas atomised powders (> 10 µm in diameter). This reveals similar microstructural features to the BSE image of Figure 4.3. The light regions correspond to the Al-rich dendrites and the dark regions are due to an interdendritic Sn phase in such TEM images. The broad striations from top left to bottom right in the image Figure 4.8 arise from the mechanical preparation process of the sample. TEM images are able to provide more details as compared with BSE images.

Figure 4.9(a,b) shows the detail of the dendritic structure observed in Figure 4.8. In addition to the interdendritic Sn (dark), there is also precipitation of Sn within the Al-rich dendrites. Higher magnification images (Figure 4.10 and Figure 4.11), present similar features to these shown in Figure 4.9 and indicate the dendrite arms are composed of sub-grains. Precipitation of Sn is seen along the sub-grain boundaries in both discrete (Figure 4.10a) and also continuous forms (Figure 4.10c,d). Moreover, precipitation also occurs within the Al sub-grains (Figure 4.10b). It is also interesting to note that when the TEM specimen was tilted along an axis to view the precipitation at the sub-grains along different projections (Figure 4.11), the discrete precipitation was often observed only at the upper and lower positions of the sub-grain boundary (corresponding to the two surfaces of the TEM sample foil). Hence, care must be taken in distinguishing different kinds of structure because sample preparation may cause the precipitation to migrate to the upper and lower side of a thin foil, showing twin precipitates at the grain boundaries. The TEM images in Figure 4.12(a,b) also reveal the same phenomena.

In order to clarify the nature of precipitation in the sub-grain boundaries, EDX analysis was used to identify the elements present in this continuous and discrete precipitation. Figure 4.12(a and b) are TEM images of Al sub-grains and the associated discrete precipitation along the boundaries, whilst Figure 4.12(c-e) shows EDX spectra from regions of Figure 4.12(b) arrowed c, d and e respectively. The EDX spectra in Figure 4.12(c and d) come from two sub-boundary precipitates (Figure 4.12b, arrowed c,d) which confirm they are composed of Sn. Since the precipitation is smaller than the electron beam probe size used for analysis, an Al peak is also shown in the EDX spectra. Figure 4.12(e) is the EDX spectrum of an Al grain region (marked e in Figure 4.12b) where only the Al and Cu peaks are present



in the spectrum. It is considered that the Cu peak comes from copper washer used to hold the sample in this instance arising from background scintillation since the EDX spectra exhibit a very similar strong Cu intensity in both the Sn precipitate region and the Al-rich matrix region. The 1wt.% Cu present in the alloy would not give an intensity as strong as that present in the spectra. The same reason can be used to explain the Cu peak in Figure 4.12 (c,d).

The continuous sub-grain precipitation was also analysed by EDX (Figure 4.13). EDX analysis of different sub-grains showed that they were predominantly Al (Figure 4.13b,c and e) although in the spectrum (c), oxygen was also detected. Figure 4.13(d) shows that the continuous phase at the grain boundaries was also Sn. Again, the Cu peaks are attributed to the copper washer used to support the sample foil.

TEM observation of one small powder particle (~ 2 µm) is shown in Figure 4.14. Nanoscale Sn particles were distributed within the Al matrix (Figure 4.14 a). The Sn particle size is a little larger on the right side of the powder particle. Diffraction patterns of this powder particle show discrete diffraction spots from Al grains, which indicate the presence of a small number of Al grains in this small particle. The diffraction spots of Sn are very faint. However, there is a strong diffraction spot Sn<sub>(200)</sub> in the same direction of Al<sub>(044)</sub> which indicates that there is possibly one Sn plane parallel to the Al matrix with  $d_{\text{Sn}(200)} // d_{\text{Al}(044)}$  (Figure 4.14 b).

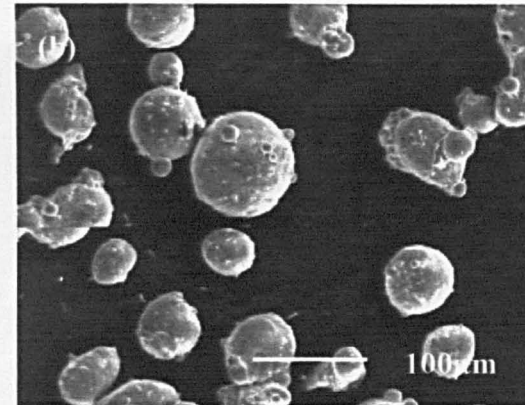
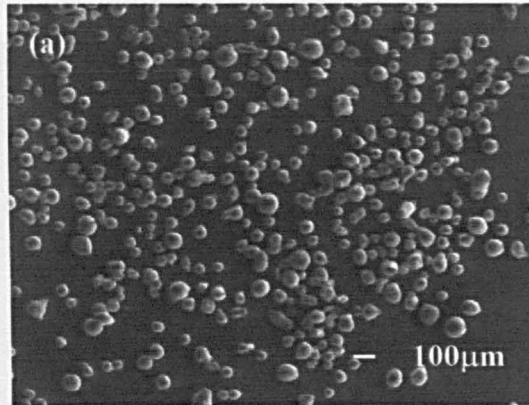


**Figure 4.2 SE images showing the morphology of Al-12wt.%Sn-1wt.%Cu powder particles at (a) low and (b) high magnification**

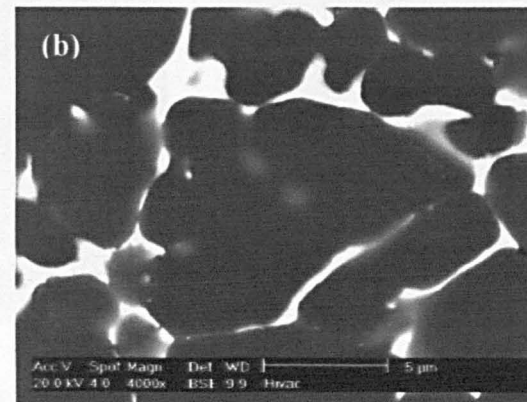
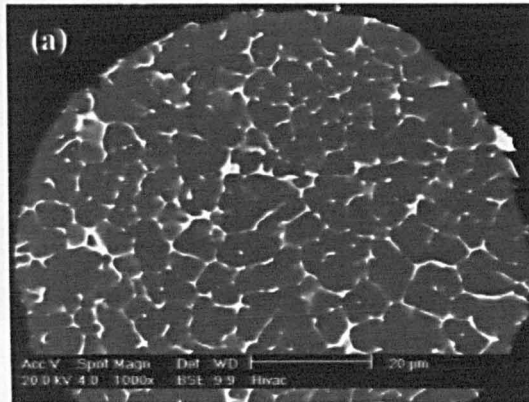


**Figure 4.3 BSE images showing the microstructure of powder particles larger than 10 μm. (a ) Cellular dendrites; (b) details of (a)**

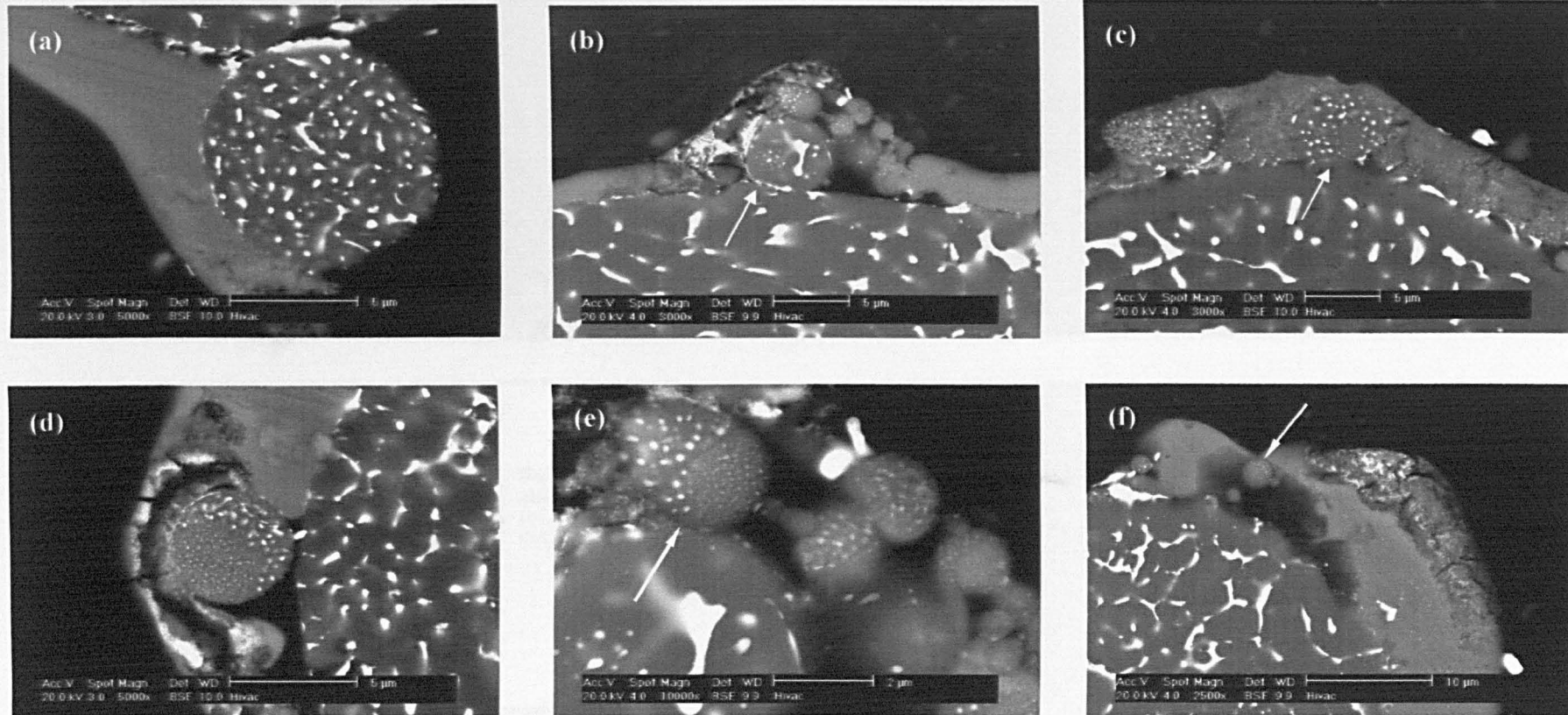


**Figure 4.4 BSE images showing the microstructure of satellite powder particles (<10  $\mu\text{m}$ ). (a-c) Large satellite powder particle (6 – 10  $\mu\text{m}$ ); (d-f) small satellite powder particles (< 5  $\mu\text{m}$ ).**



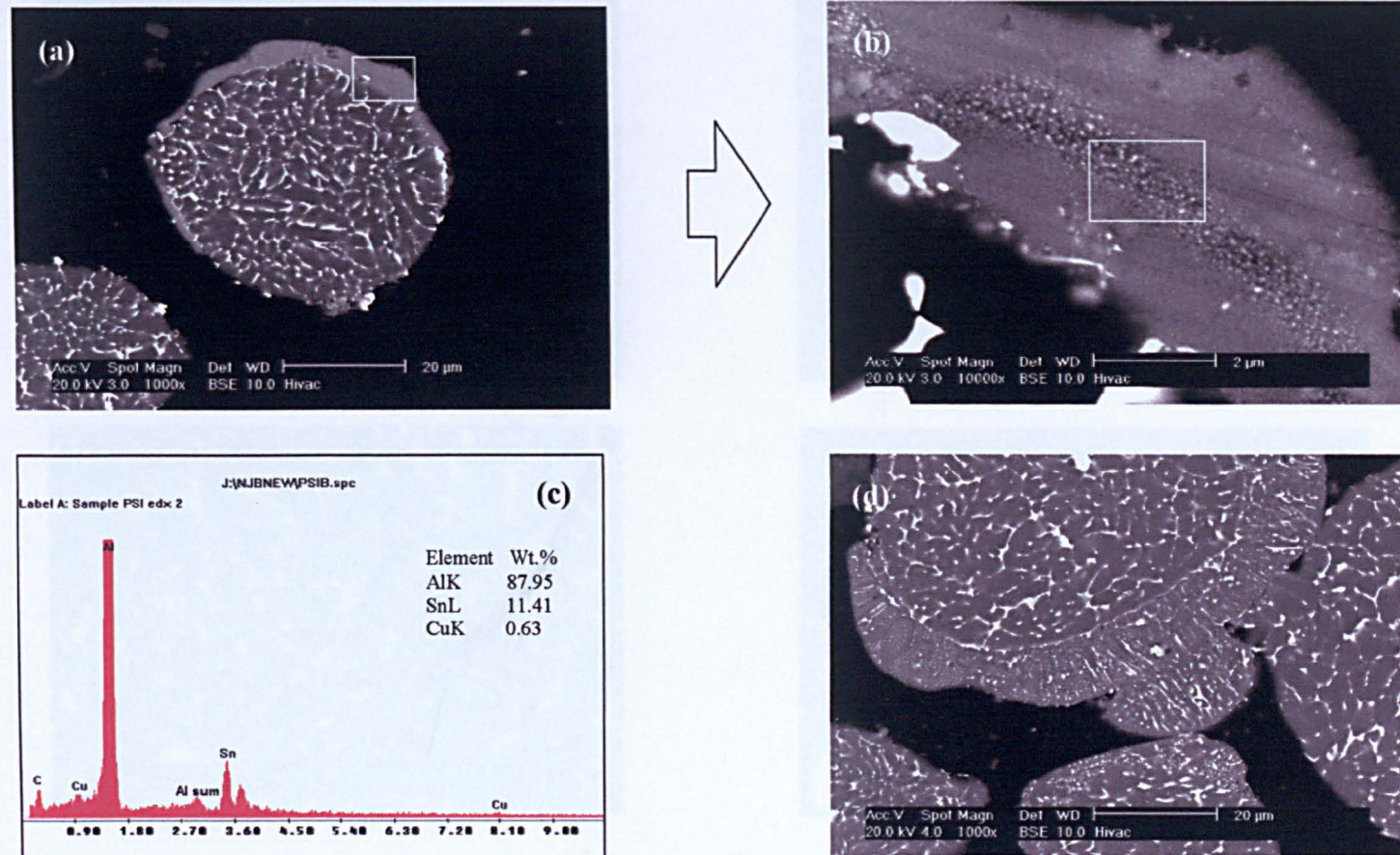


**Figure 4.5** The BSE images showing the microstructure of gas atomised powder particles with shell structure. (a) Particles with a grey contrast shell; (b) details of the boxed regions; (c) EDX spectrum of boxed region in (b); (f) particle with a thick shell structure.

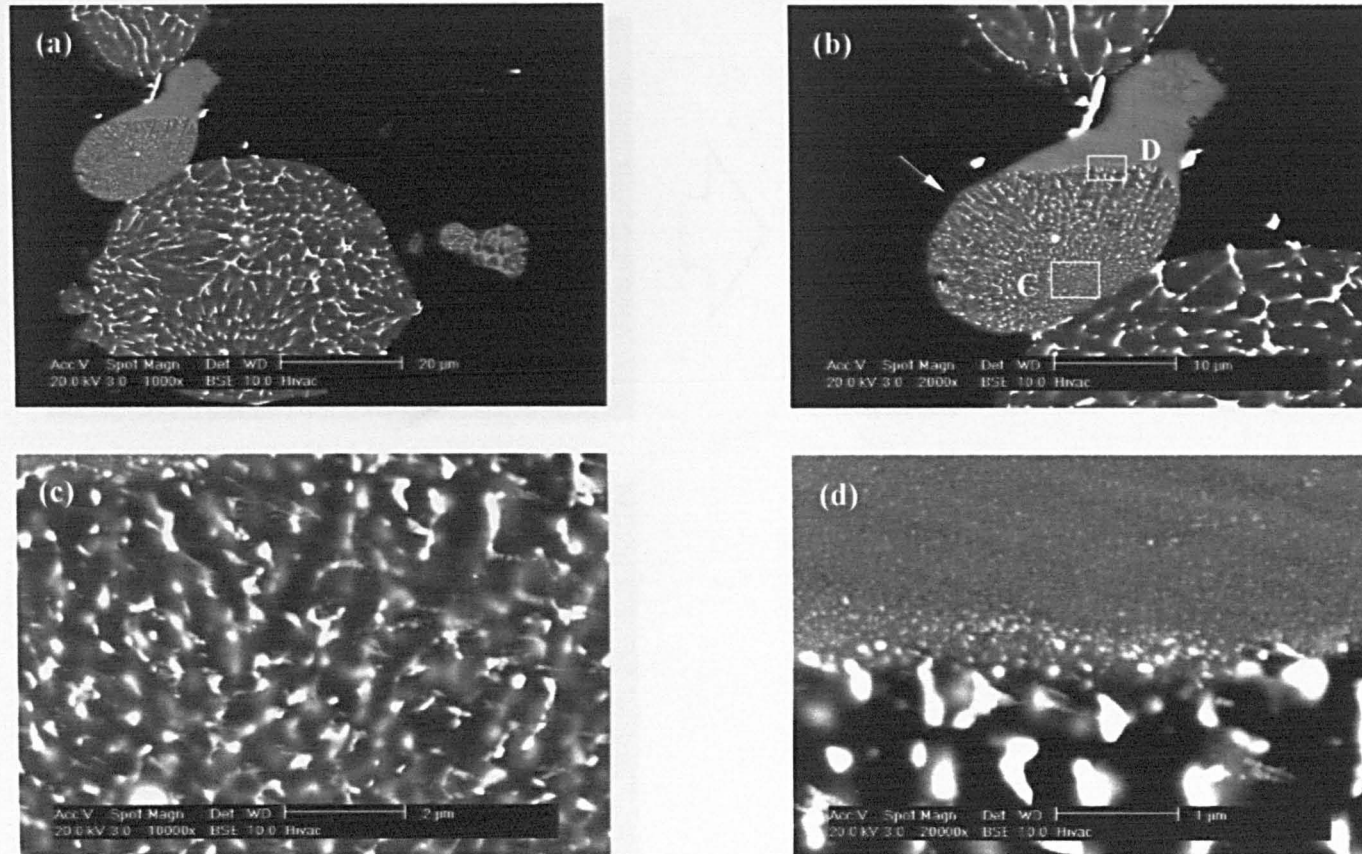


**Figure 4.6** BSE images showing the microstructure of a powder particle with irregular shape. (a, b) Irregular shaped particle; (c and d) details of (b).



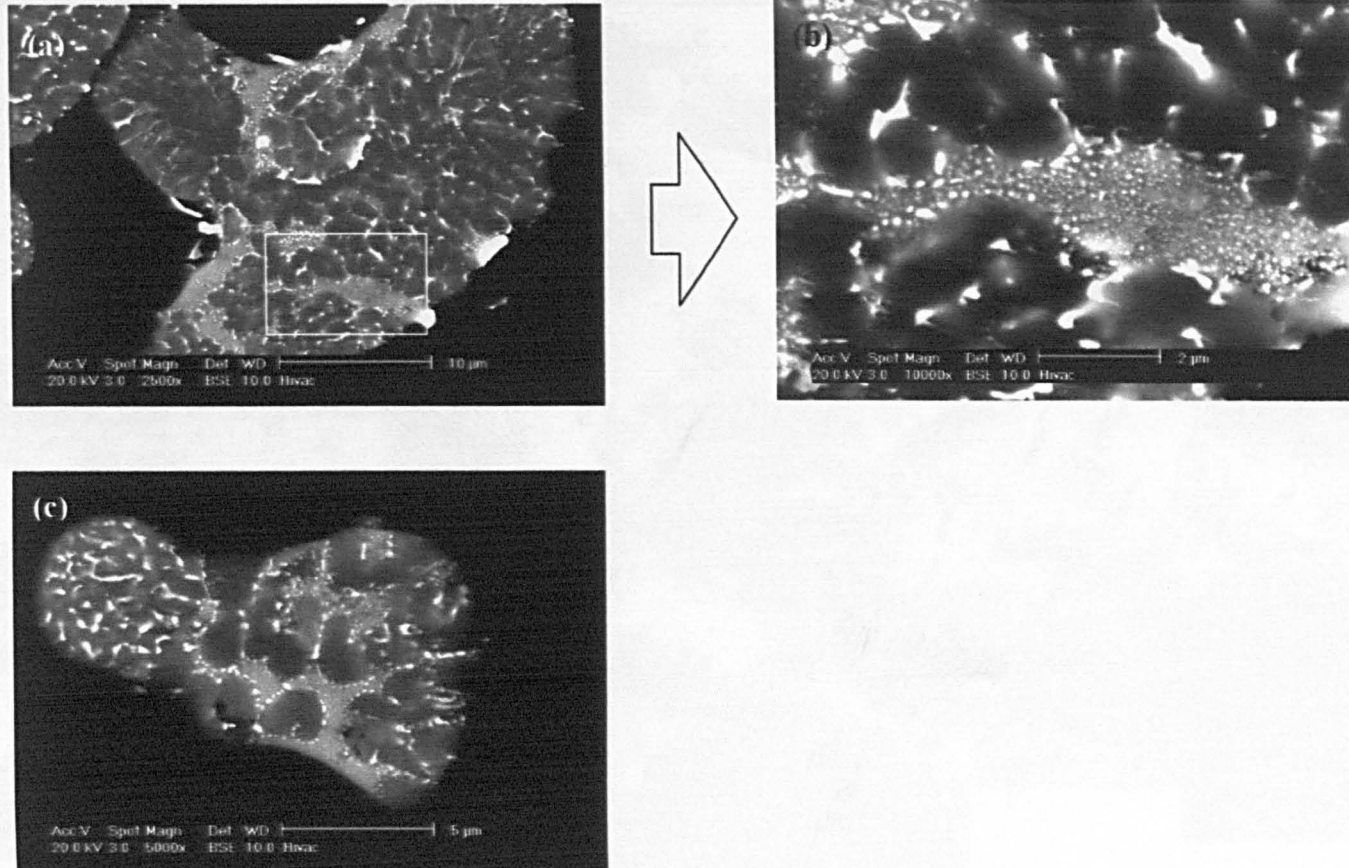


**Figure 4.7 BSE images showing the microstructure of powder particles with irregular shape. (a) Irregular particle and (b) details of boxed region in (a); (c) irregular powder particle.**

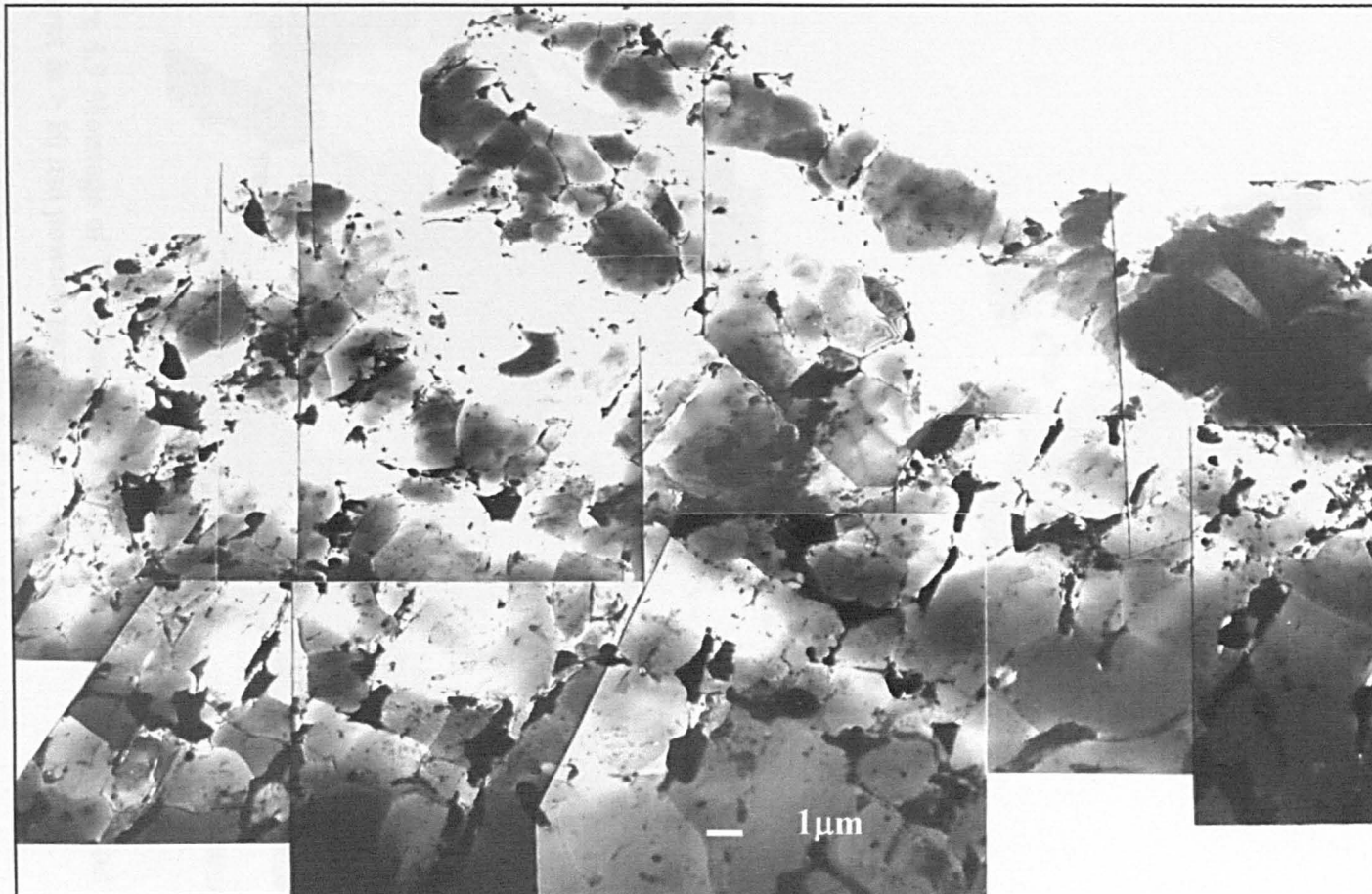


**Figure 4.8 TEM montage of a section through a typical powder (> 10 μm) in details**

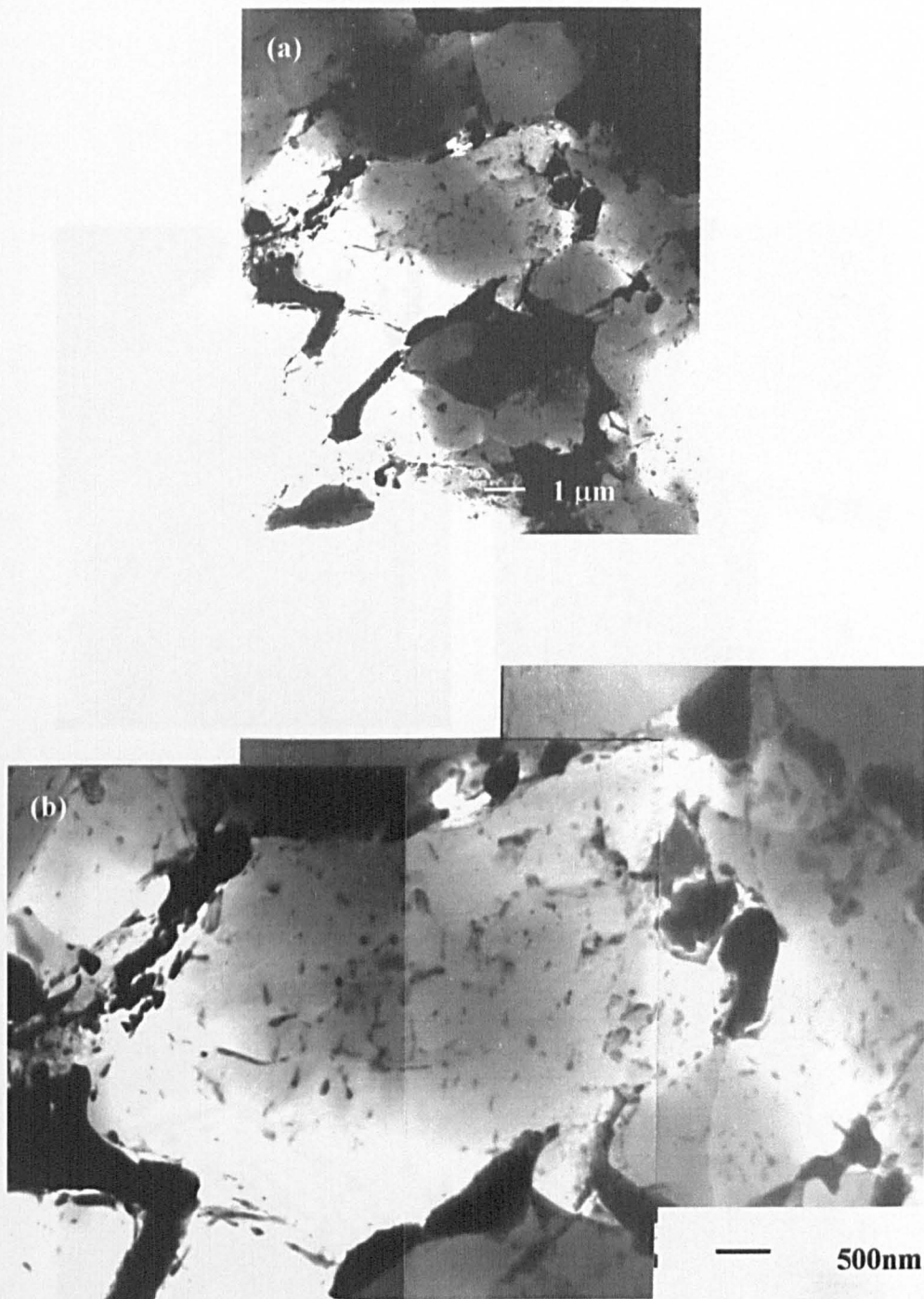


**Figure 4.9 Montage of TEM images showing details of Al matrix and Sn phase (present in  $> 10 \mu\text{m}$  powder particles)**



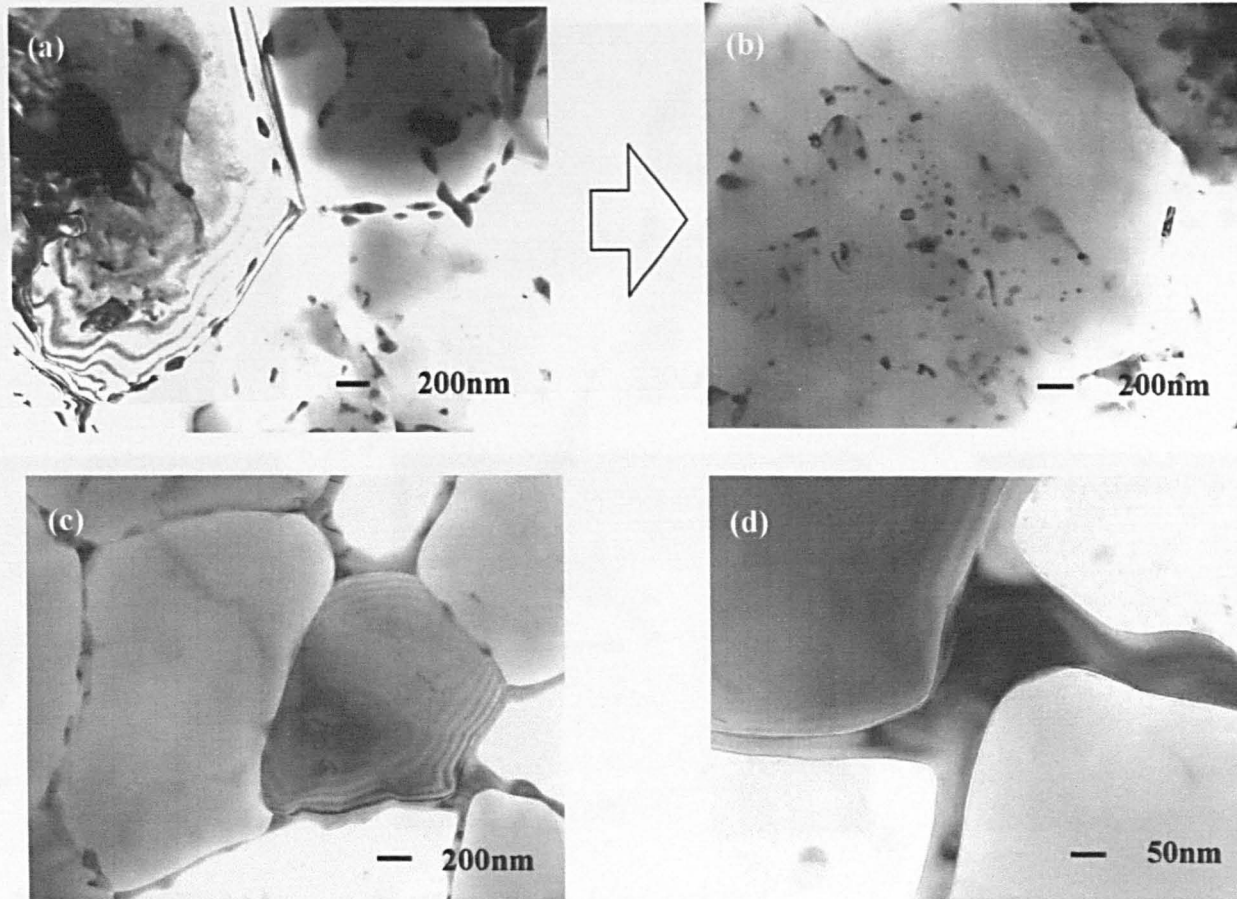


**Figure 4.10** TEM images of precipitates in the gas-atomised powder particles. (a) Discrete particles at sub-grain boundaries; (b) Intragranular precipitates; (c, d) continuous Sn precipitates

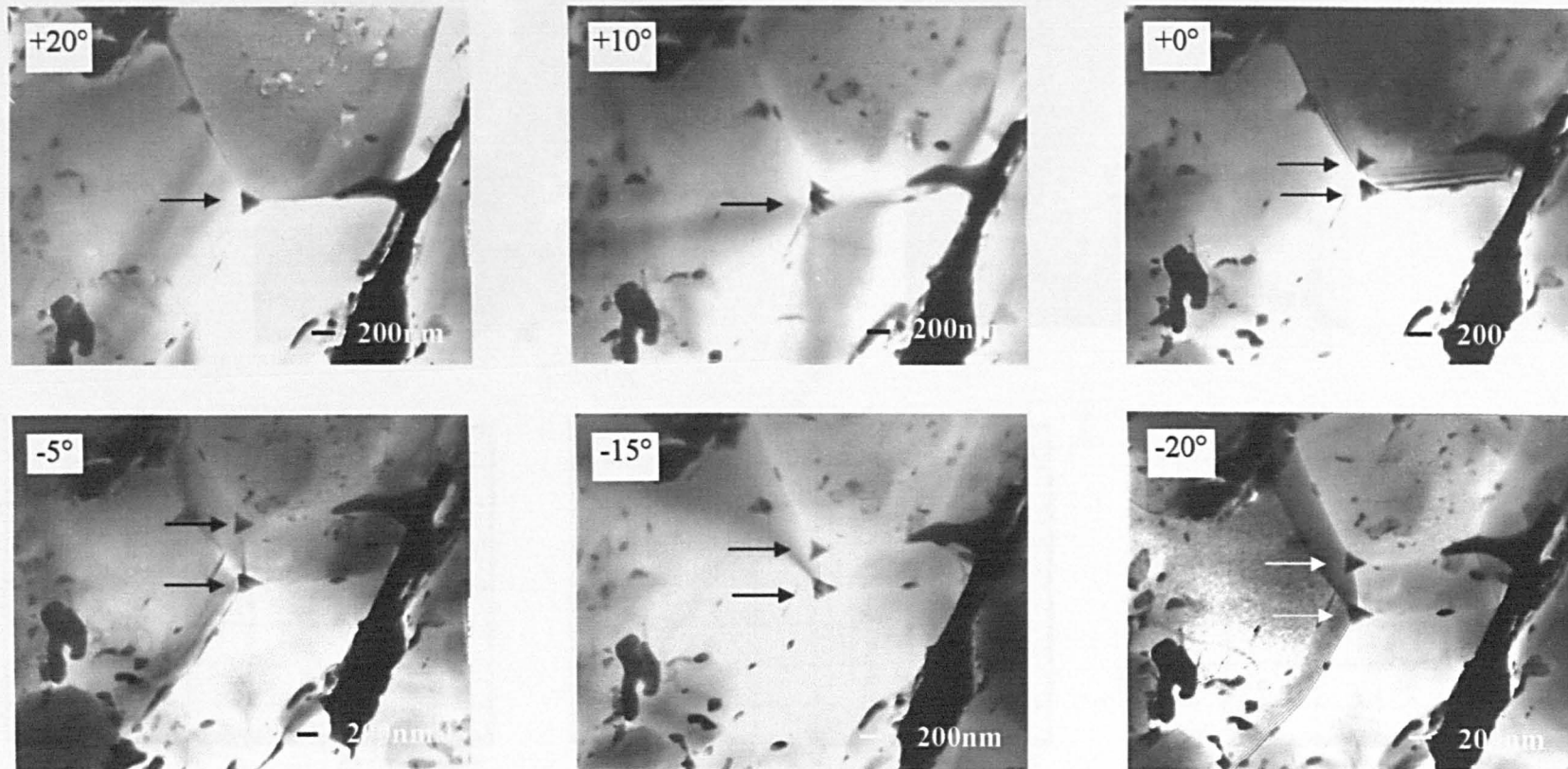
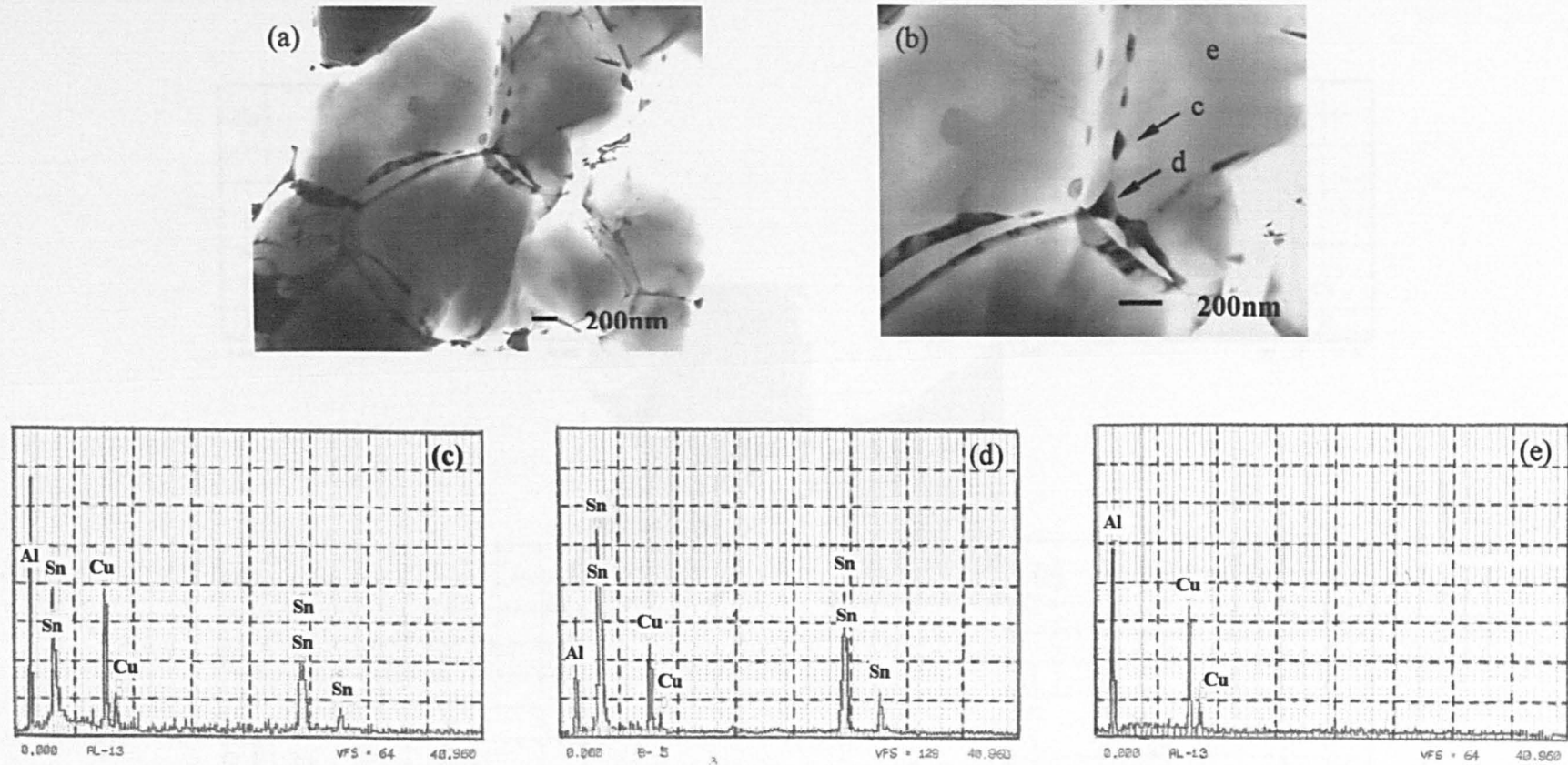
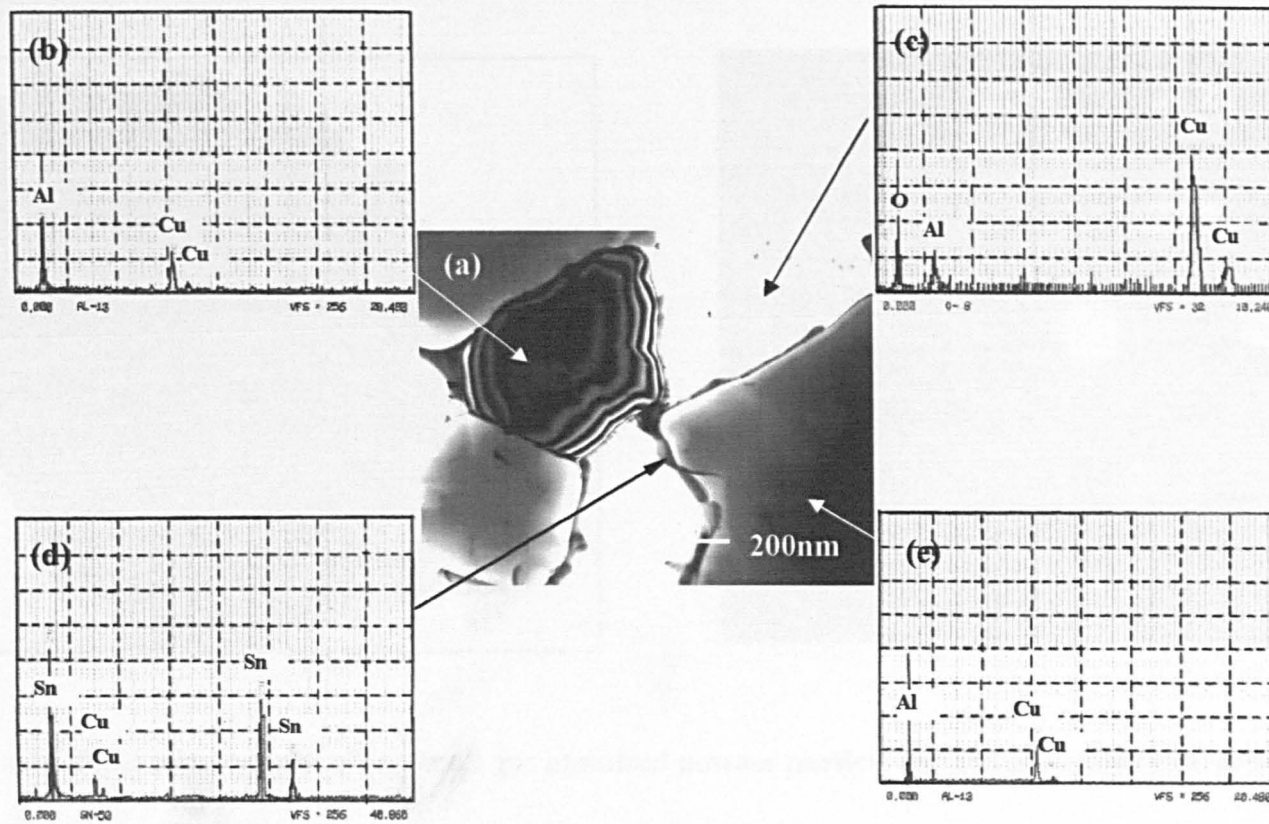


Figure 4.11 TEM images showing sub-grain boundaries precipitate (tilted at different degrees).



**Figure 4.12** TEM images and EDX spectra of discrete precipitates. (a, b) Precipitates in sub-grain boundaries, (c, d) EDX spectra confirming Sn precipitates, (e) EDX spectrum of a sub-grain showing the presence of matrix Al (and Cu due to background scintillation)



**Figure 4.13** TEM images and EDX spectra of continuous precipitation and sub-grains. (a) TEM image; (b, e) EDX spectra showing Al grains; (c) an Al grain possibly being an oxide and (d) continuous precipitation due to Sn precipitate



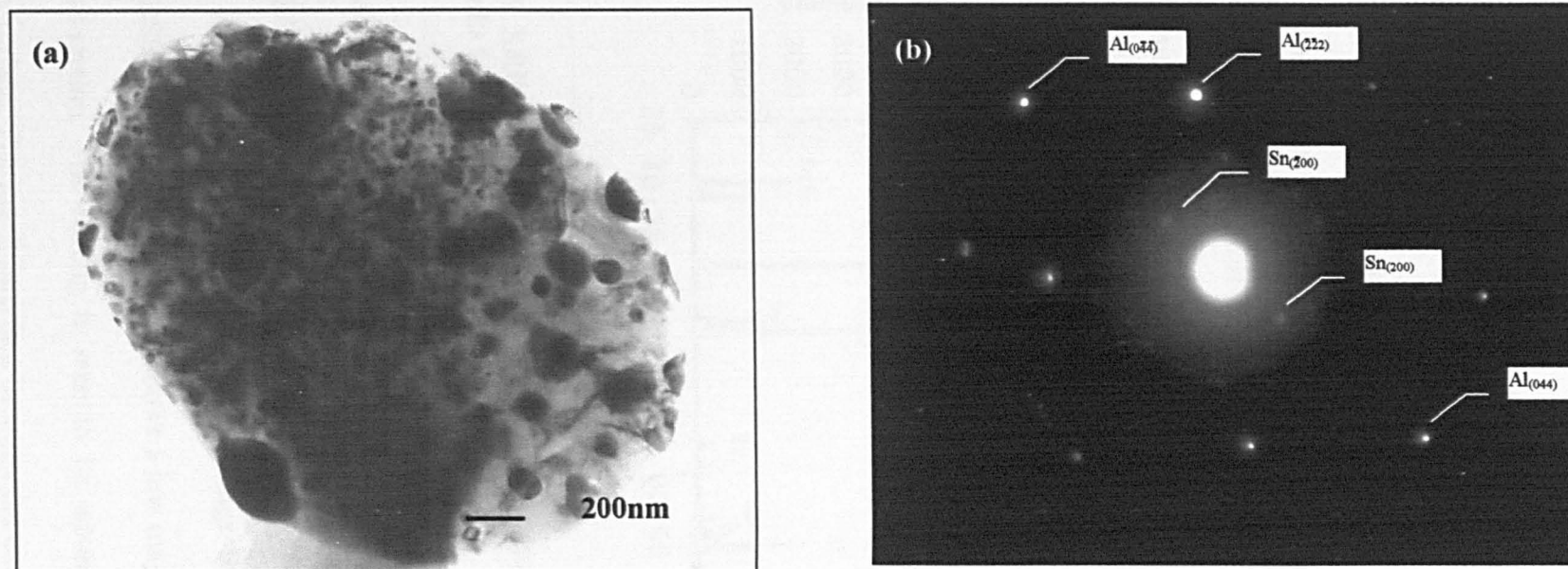


Figure 4.14 TEM micrographs of (a) small gas atomised powder particle and (b) associated diffraction pattern

### 4.3 Characterisation of the as-sprayed coatings

#### 4.3.1 XRD analysis

The Al<sub>12</sub>Sn<sub>1</sub>Cu gas atomised powder was deposited onto mild steel substrates using HVOLF thermal spraying. The XRD spectrum from the top surface of an as-sprayed coating is shown in Figure 4.15. Again, fcc Al and bct Sn are the principal peaks shown in the spectrum. The peak height ratios are similar to those found in the gas-atomised powder. There was no evidence for the presence of crystalline aluminium oxide or CuAl<sub>2</sub>.

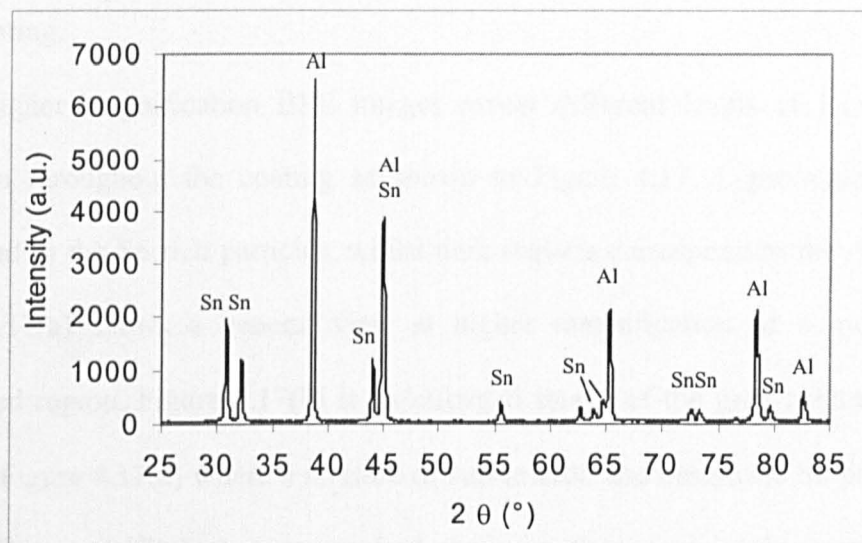


Figure 4.15 XRD pattern from an Al<sub>12</sub>Sn<sub>1</sub>Cu HVOLF as-sprayed coating showing peaks for Al and Sn

#### 4.3.2 Microstructural investigation

##### SEM observation

The HVOLF as-sprayed Al<sub>12</sub>Sn<sub>1</sub>Cu coatings were also characterised by SEM using BSE imaging. Figure 4.16(a) shows a low magnification BSE image of a coating cross-section. The coating is seen to be around 250 µm thick with an irregular top surface. The rough interface between the coating and steel substrate is

due to the grit blasting of the latter prior to coating deposition. A higher magnification BSE image of a typical region of an as-deposited coating is shown in Figure 4.16 (b). The regions of dark contrast (boxed A, B and C) show similar features to the large gas-atomised powder particles (Figure 4.3). These regions are probably partially melted powder. The regions of lighter contrast contain a dispersion of sub-micron particles, which are presumably Sn rich. These regions arise from powder which was molten at impact and then resolidified. The splat-like, layered features typical of thermally sprayed coatings are clearly visible in Figure 4.16. There was no evidence for either oxides or porosity observed in these cross-sections of the coating.

Higher magnification BSE images reveal different levels of localised Sn dispersion throughout the coating as shown in Figure 4.17. Light regions again correspond to the Sn rich particles, whilst dark regions correspond to the Al matrix. Figure 4.17(a) shows a general view at higher magnification of a melted and resolidified region. Figure 4.17(b) is an enlarged image of the grey contrast region boxed in Figure 4.17(a) where a mixture of sub-micron and nanoscale Sn particles is evident. Figure 4.17(c) shows a melted region with a coarser Sn particle size, apparently in between the splats. Figure 4.17(d) shows a very high magnification BSE image of a melted region. The high resolution images of Figure 4.17(e and f) present details of the melted region, which normally could be observed only in the TEM micrographs. Figure 4.17(e and f) shows a different melted region arrowed e and f in Figure 4.17(d). It is apparent that there are many localised variations in the Sn dispersion, with regions of nanoscale Sn particles (Figure 4.17e) and regions of sub-micron Sn particles surrounded by nanoscale Sn particle dispersions (Figure 4.17f).

Figure 4.18 shows high magnification BSE images of the partially melted powder regions in the coating. A distinguishing variant of this type of localised distribution is the association of fine and large scale Sn particles bounding regions of featureless Al matrix. A series of enlarged images reveal at high magnification, featureless Al (dark) surrounded by Sn particles. Figure 4.18(a and d) are from the region of Figure 4.16(b) labelled A. A broader zone of fine-scale Sn particles indicates more heat was transferred causing more localised melting of the  $\alpha$ -Al as well as the interdendritic Sn. Figure 4.18(b and e) illustrates another region of partially melted powder in the coating. The Sn particles are much coarser as compared with the images of Figure 4.18(a and d) suggesting less localised melting in this region. Figure 4.18(c) exhibits a cellular-dendritic structure similar to the large gas-atomised powder particles with interdendritic Sn and dendritic Al. The variation of Sn particle size in the microstructure of the partially melted zone in the coating implies an evolution of melting as a consequence of different local heat transfer effects.

The thin foils for TEM study (prepared from coating cross-sections) were first of all examined in the SEM using BSE imaging. Montages of BSE images observed in this way are shown in Figure 4.19 and Figure 4.20. It is apparent that the principal structural features have been retained through the sample preparation process and that very large, electron transparent areas have been produced, e.g. the box shown in Figure 4.20 which is  $\sim 20 \times 10 \mu\text{m}^2$ .

### **TEM observation**

A TEM montage of an HVOLF as-sprayed Al<sub>12</sub>Sn<sub>1</sub>Cu coating shows a general region of the coating (Figure 4.21). This image represents a quarter of the whole TEM montage obtained from the boxed region of the BSE montage in Figure



4.20. The microstructure of the coating exhibits several levels of complexity. Clustered nanoscale scale Sn particles (region A) are distinct from the large scale Sn particles forming loose chain like structures (region B). Region C illustrates an area with a lower concentration of Sn particles. The region of nanoscale Sn distribution (region A) exhibits the same features as in the BSE images of Figure 4.17(a,b, and e). The chain like sub-micron Sn particle distribution (region B) reveals similarity to the image of Figure 4.17(c) where melted Sn was located between the splats. Region C illustrates the unmelted Al matrix, which shows dark contrast in the BSE images (for example in Figure 4.18, dark regions)

A partially melted region is shown in detail in the TEM montage of Figure 4.22, which is similar to the BSE images of Figure 4.18 (a,d and b,e). The ellipse delineates a region of partially melted interdendritic Sn of the feedstock powder retained in the coating where the melted Sn and partially melted Al resolidified to form nanoscale and sub-micron Sn particles surrounding an unmelted Al region. Details of the transition (rectangular in Figure 4.22) from one unmelted Al dendrite to a region with a Sn particle distribution, then to another unmelted Al dendrite region, are shown in Figure 4.23. The nanoscale and sub-micron Sn particles are distributed in the melted region, whilst the unmelted region shows the Sn-free Al matrix.

A large number of high magnification TEM images show that there are several basic microstructures assembled in the as-sprayed coatings. Figure 4.24(a) illustrates the nanoscale Sn particles embedded inside the Al matrix and also along the grain boundaries. Figure 4.24 (d) shows sub-micron Sn particles exist at the triple point of the grain boundaries. Figure 4.24(b, e) are bright field and weak beam images showing dislocation tangles and dislocation loops exist within a Al grain,

respectively. Nanoscale Sn particles are also present in Figure 4.24(b,e). High magnification TEM observation of a region free from Sn particles (Figure 4.24c,f) shows that the Al grain size is much smaller as compared with that in the as-received powder (Figure 4.9).

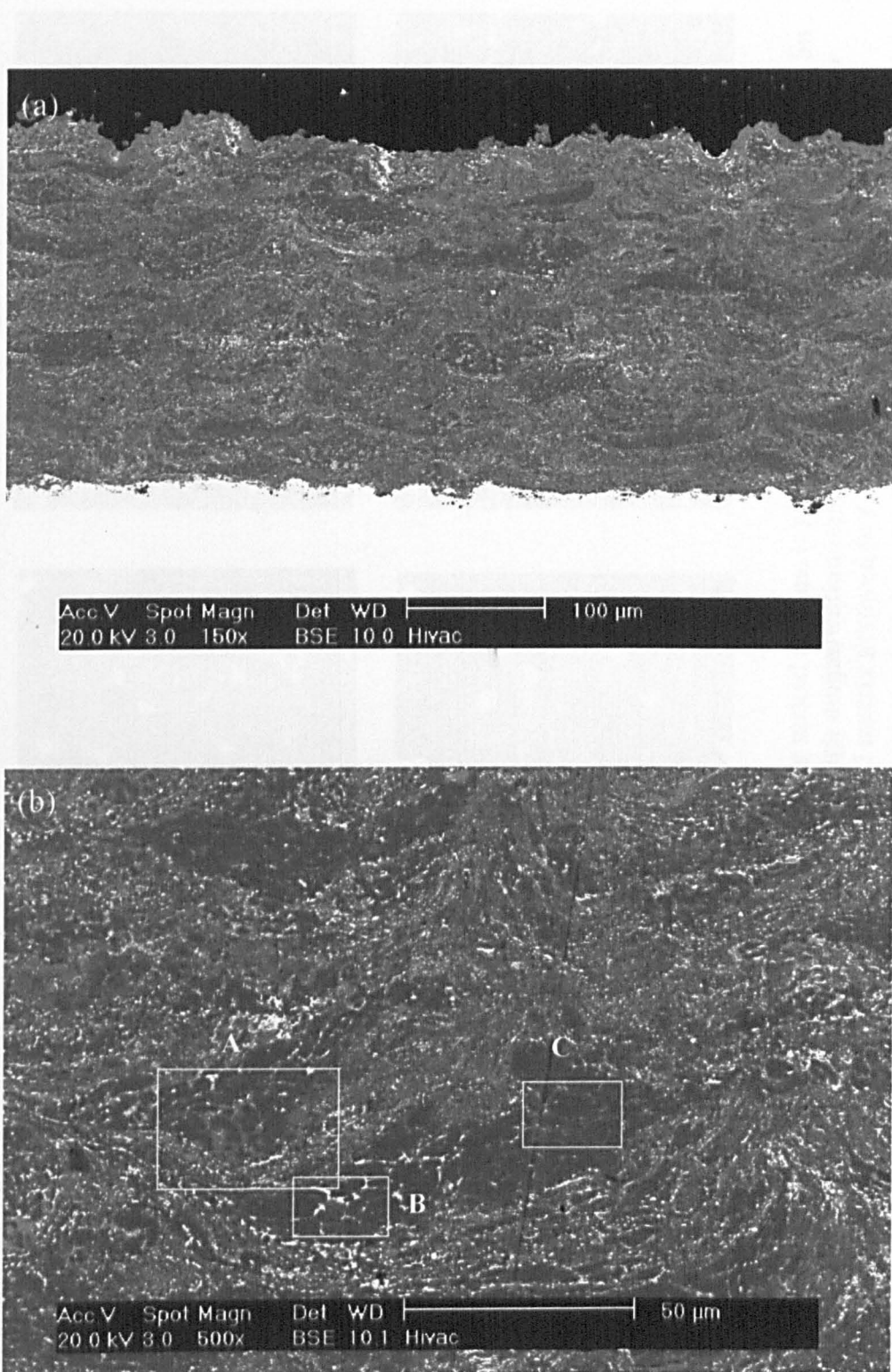


**Figure 4.16 BSE images of Al<sub>12</sub>Sn<sub>1</sub>Cu HVOLF as-sprayed coating**

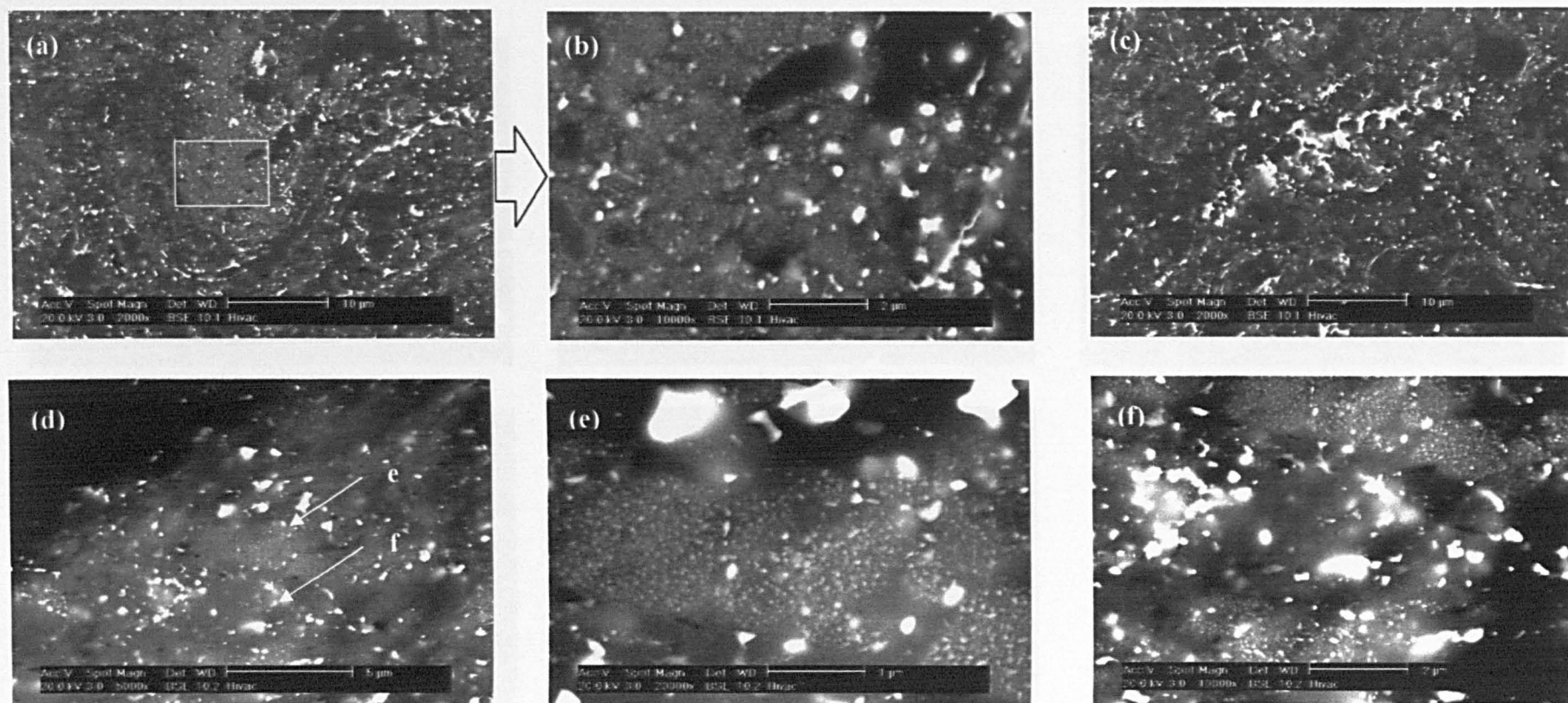


**Figure 4.17 High magnification BSE images showing the as-sprayed coating melted regions. (a) General melted region; (b) fine-scale Sn dispersion boxed in image (a); (c) large scale Sn phase cluster region; (d) high magnification image of melted region; (e) nanoscale Sn particle dispersion arrowed e in image (d); (f) sub-micron Sn particles in Al matrix arrowed in f in image (a).**

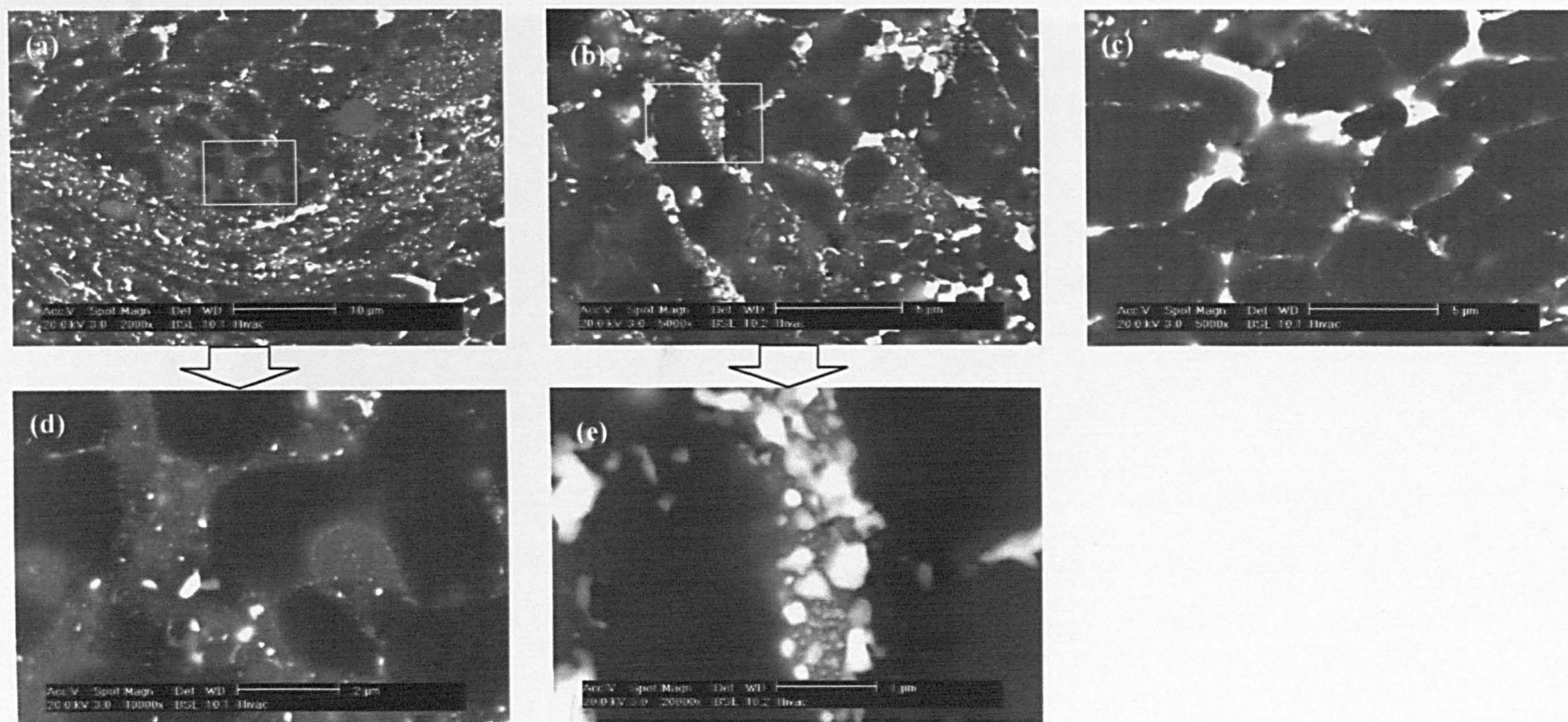


**Figure 4.18 BSE images showing the as-sprayed coating partially melted regions. (a, d) Melted Sn dissolve more surrounding Al; (b, e) melted Sn and intermediate melted Al; (c) melted Sn and less melted Al**



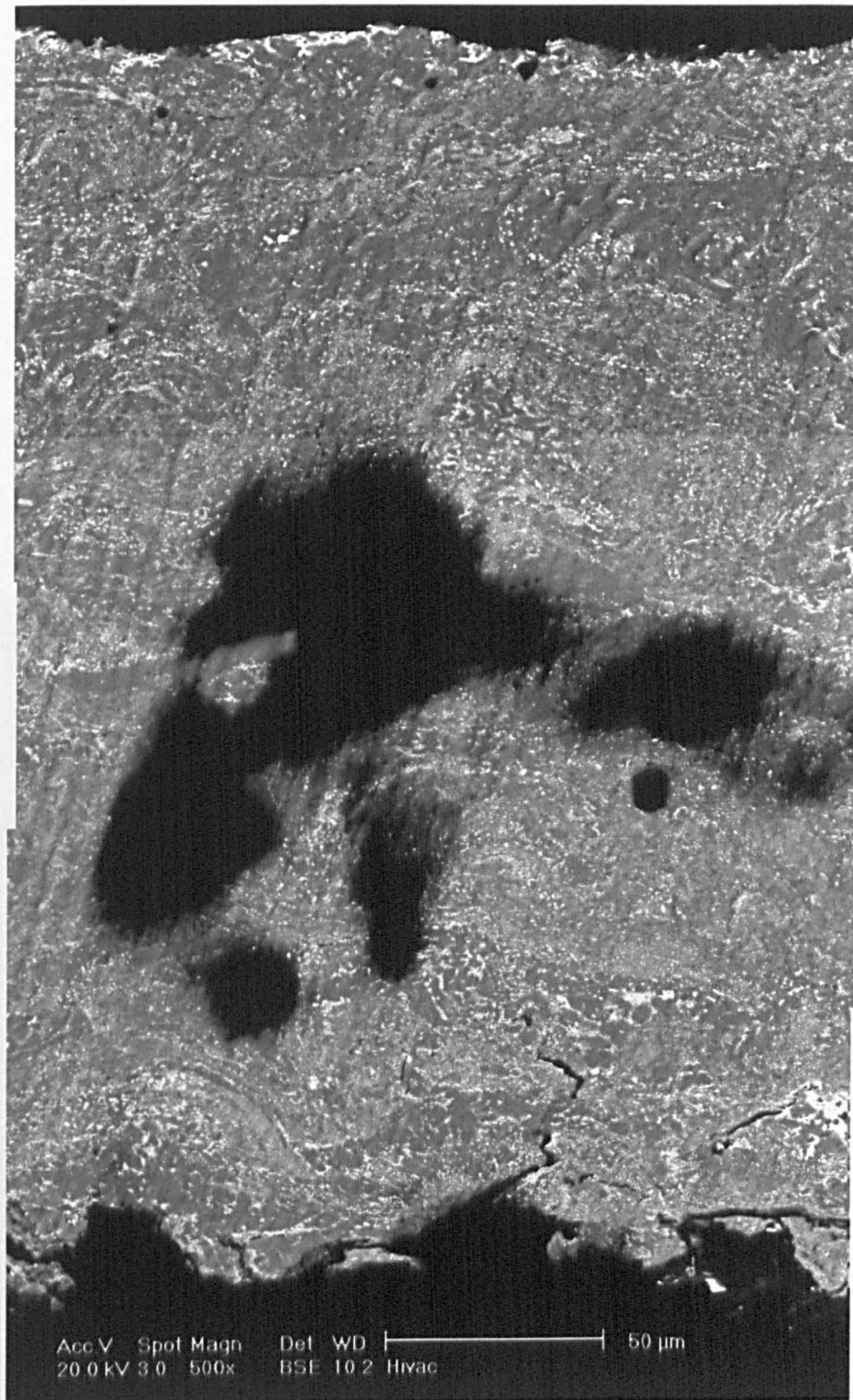


**Figure 4.19 BSE montage of a cross section of a coating prepared for TEM observation.**

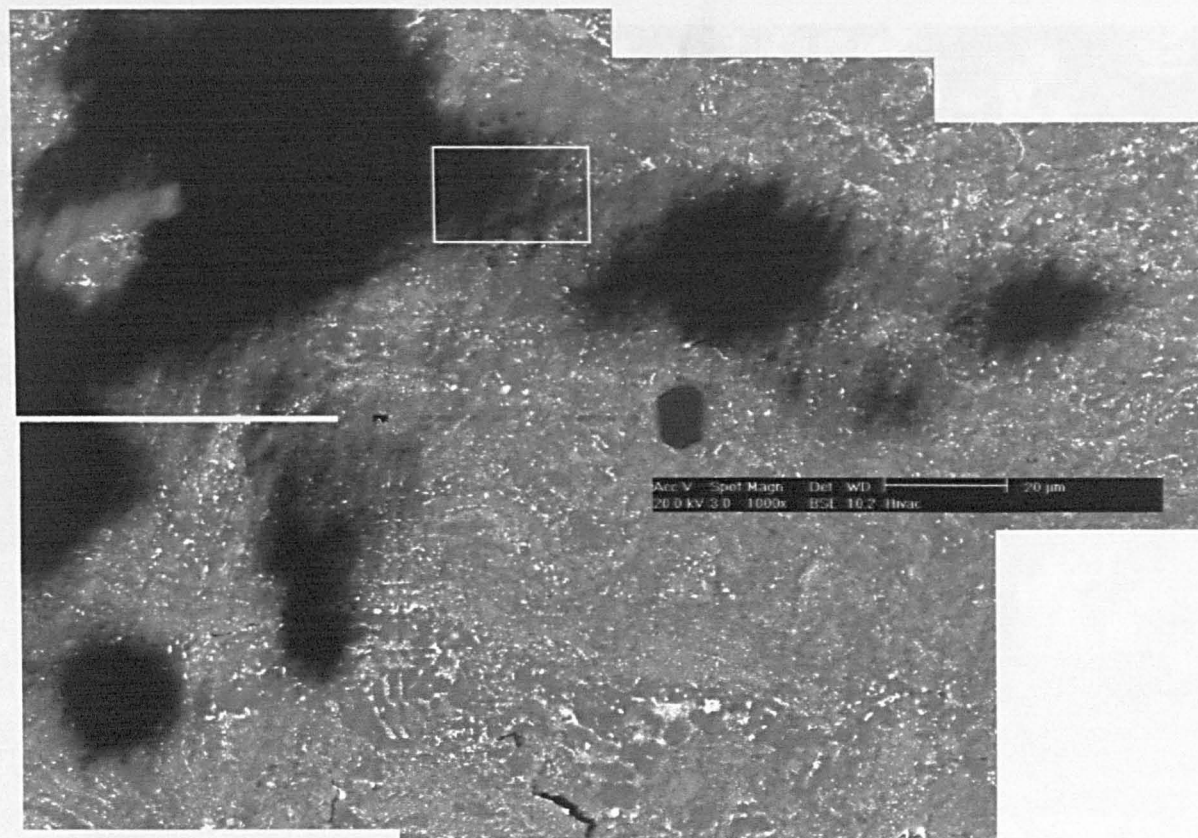
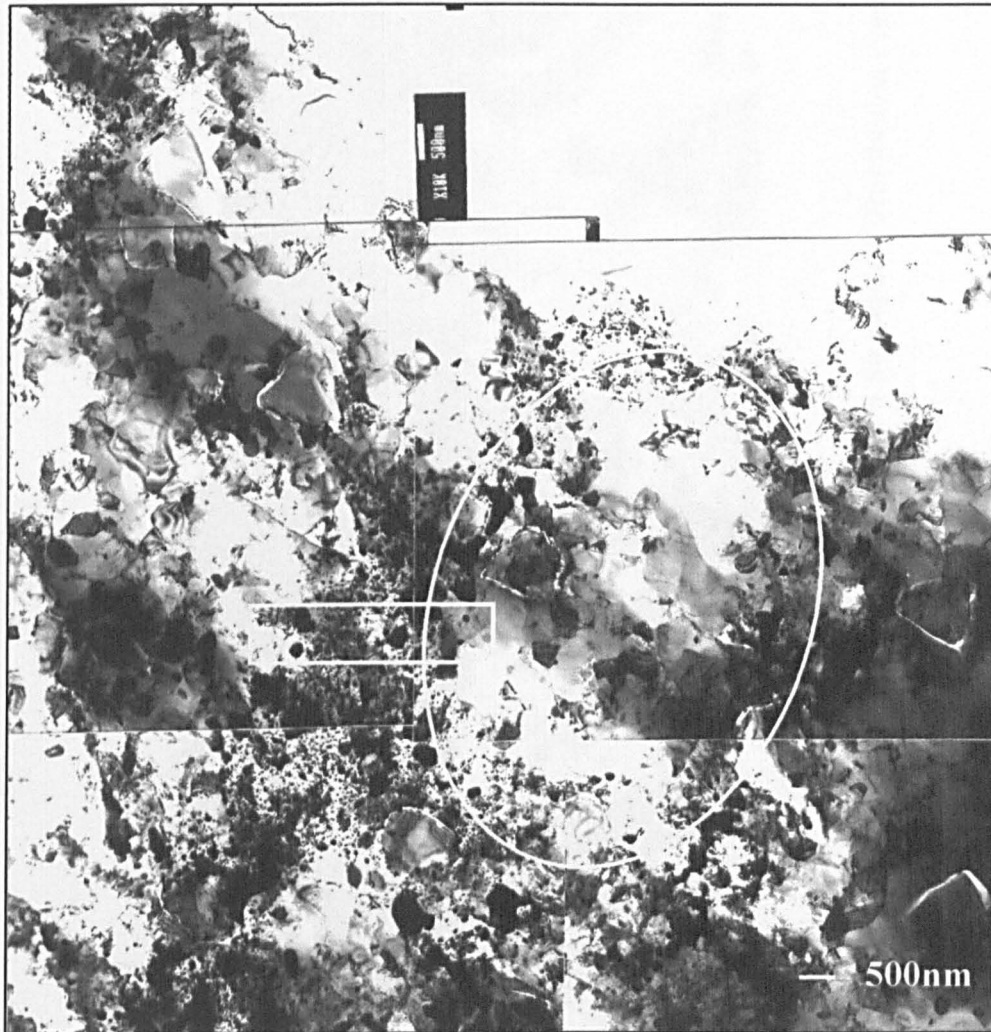


**Figure 4.20 BSE montage of part of the cross section of the coating in (Figure 4.20) prepared for TEM observation.**

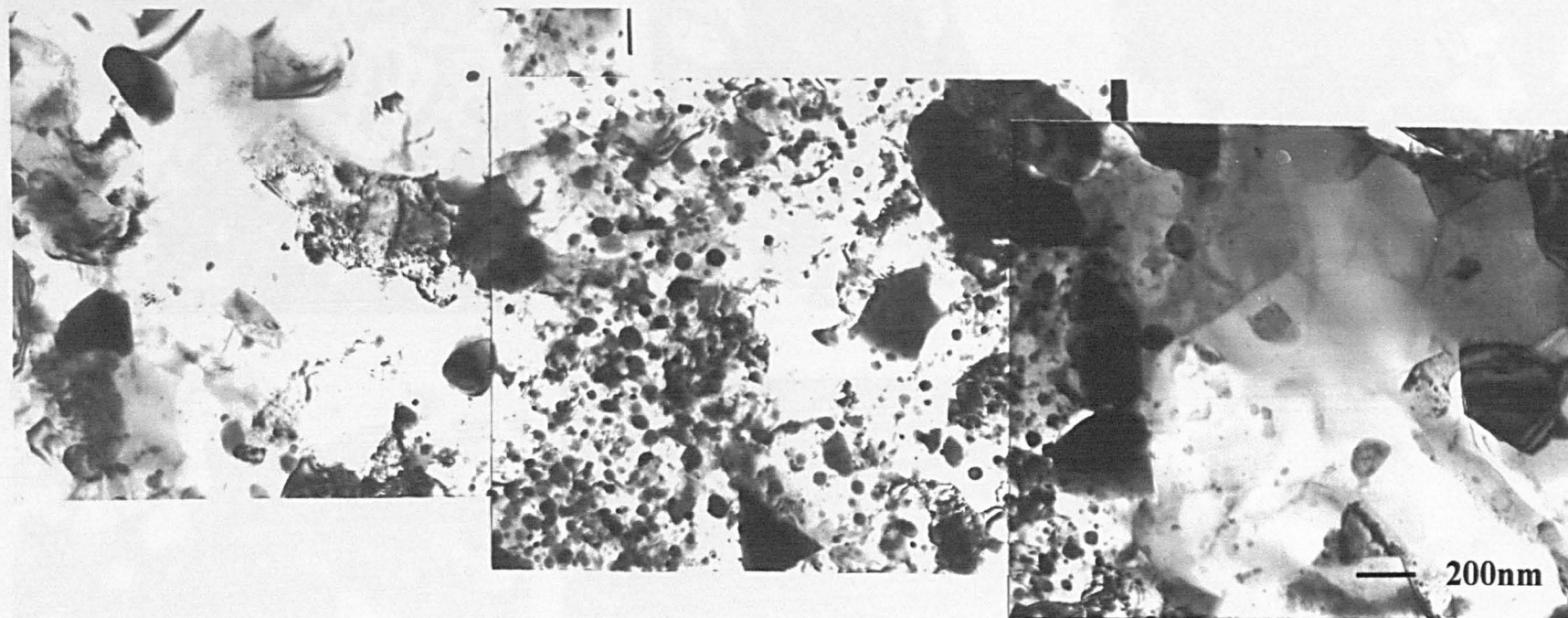


Figure 4.21 TEM montage of HVOLF as-sprayed coating





**Figure 4.22** TEM montage showing details of a partially melted region in the as-sprayed coating



**Figure 4.23 TEM montage showing the transition from a Sn-free Al grain region through a Sn particle distribution region, then back to Sn-free Al grained region from Figure 4.23 (rectangular boxed region)**

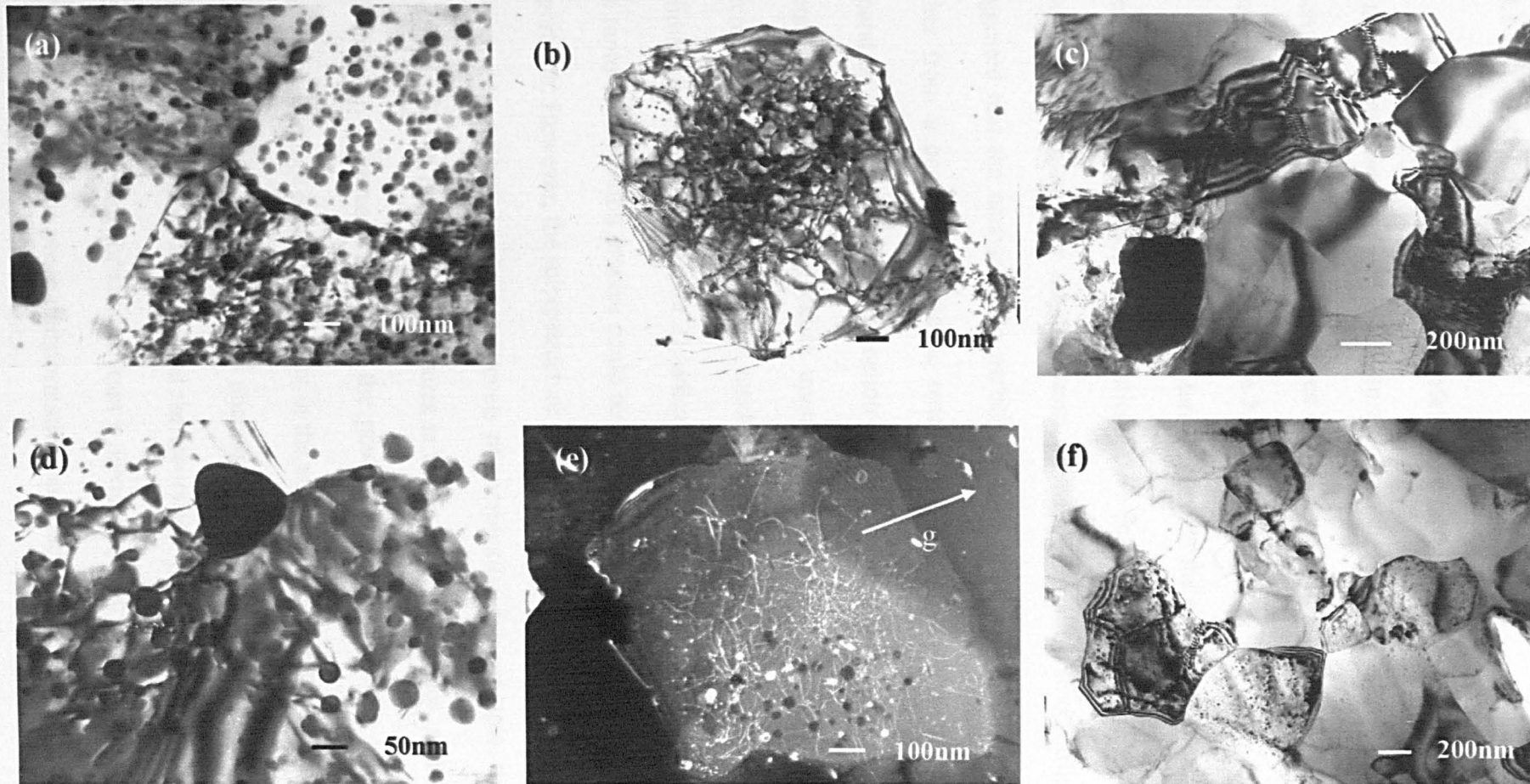


**Figure 4.24** High magnification TEM micrographs of Al<sub>12</sub>Sn<sub>1</sub>Cu as-sprayed coatings. (a,d) Fine scale Sn distributed within the grain and in the grains boundaries; (b,e) Bright field and weak beam images showing dislocation loops and tangles; (c,f) Al grain without Sn particles.

## 4.4 Discussion

### 4.4.1 Introduction

This discussion will mainly refer to the microstructure formation mechanism in the gas-atomised powder and as-sprayed coatings. The relationship between the microstructure of the thermally sprayed coatings and their application for automotive bearings will be discussed in Chapters 5 and 6.

Chapter 2 reviewed the literature relating to the rapid solidification of alloy systems showing similar characteristics to Al-Sn. Kim et al. [3, 4] described two possible mechanisms for the formation of the Al-Sn alloy microstructure. They suggested that the nanoscale Sn particles embedded in the Al matrix could arise either from a coupled monotectic reaction or from the process of liquid phase separation following by solidification of  $\alpha$ -Al and Sn separately, assuming a metastable miscibility gap exists upon rapid solidification. The analysis of the microstructure and the formation mechanism of different alloys under the rapid solidification process (Chapter 2) indicate that the nanoscale Sn particles formed in the rapid solidification process could be attributed to the mechanism of liquid phase separation. However, the microstructure of the Al<sub>12</sub>Sn<sub>1</sub>Cu gas atomised powder and as-sprayed coatings show several levels of complexity. For example, nanoscale Sn and micron / sub-micron Sn distributes in the as-sprayed coatings, and dendritic Al and fine Sn dispersoids exists in the powder. In this context, it is necessary to consider the effect of various factors in the microstructure formation of AlSn alloys in order to account for the principal phenomena observed. In this discussion section, schematic Al-Sn phase diagrams and the associated Gibbs energy curves are used to explain the phase transformations from a thermodynamic point of view. The kinetic effects involved in the phase transformations and factors such as the effect of cooling



rate and nucleation undercooling have been considered. The critical cooling rate and critical gas atomised particle size for liquid phase separation are calculated according to a heat transfer model. Further, the effect of composition on the size of nanoscale Sn particles within the Al matrix is also discussed. Finally, the microstructures of AlSnCu gas atomised powder and as-sprayed coatings are discussed using the mechanisms proposed.

#### 4.4.2 Qualitative analysis of microstructure formation from a thermodynamic and kinetic point of view

It is well known that the phase diagram of an alloy is derived from a thermodynamic analysis of the Gibbs free energy curves at various temperatures. The Gibbs free energy ( $G$ ) is a function of enthalpy ( $H$ ) and entropy ( $S$ ) which is associated with temperature according to the relationship <sup>[5]</sup>,

$$G = H - TS \quad \text{Eqn 4.1}$$

where  $T$  is the absolute temperature.

Phase diagrams are derived by considering the free energy, composition curves of the phases at different temperatures and measuring the free energy of the system with respect to the phases and their composition.

Figure 4.25 is a schematic phase diagram of the AlSn system and the associated free energy curve at temperature  $T_1$ . Figure 4.25(a) shows the free energy curve of solid Al, solid Sn and liquid. Figure 4.25(b) is the schematic AlSn equilibrium phase diagram. For an alloy at composition of  $X$ , it will form the  $\alpha$  phase and the liquid phase at temperature  $T_1$  in the equilibrium condition because the tangent of the solid Al free energy curve (Al-solid) and the liquid free energy curve

of Al and Sn (L) has the largest decrease of free energy, from point a to b. The remaining liquid will undergo a eutectic reaction when the temperature reaches  $E_1$ .

Figure 4.26 shows a schematic phase diagram of Al-Sn and the associated free energy curves at a temperature  $T_2$ . Figure 4.26(a) is the free energy curve at temperature  $T_2$  and Figure 4.26(b) shows the equilibrium and metastable equilibrium phase diagram. The temperature  $T_2$  is lower than temperature  $T_1$  in the previous figure. The liquid free energy curve increases and undergoes a shape change with two minima and the solid free energy curves of Sn and Al will decrease as compared with those at temperature  $T_1$ . For a composition X, the largest decrease of free energy is from points a to c, giving by the tangent of the Al-solid curve and  $L_2$ . In this case, the liquid will form the  $\alpha$  phase (point A) and another liquid composition (point B) at equilibrium. However, there is another possibility, the free energy of the liquid could also first decrease to an intermediate energy, from point a to b, giving by the tangent of  $L_1$  and  $L_2$ , instead of from a to c. A high undercooling could cause this non-equilibrium reaction to occur. Thus, liquid phase separation will happen to form an Al-rich liquid (point C) and a Sn-rich liquid (point D) prior to solidification.

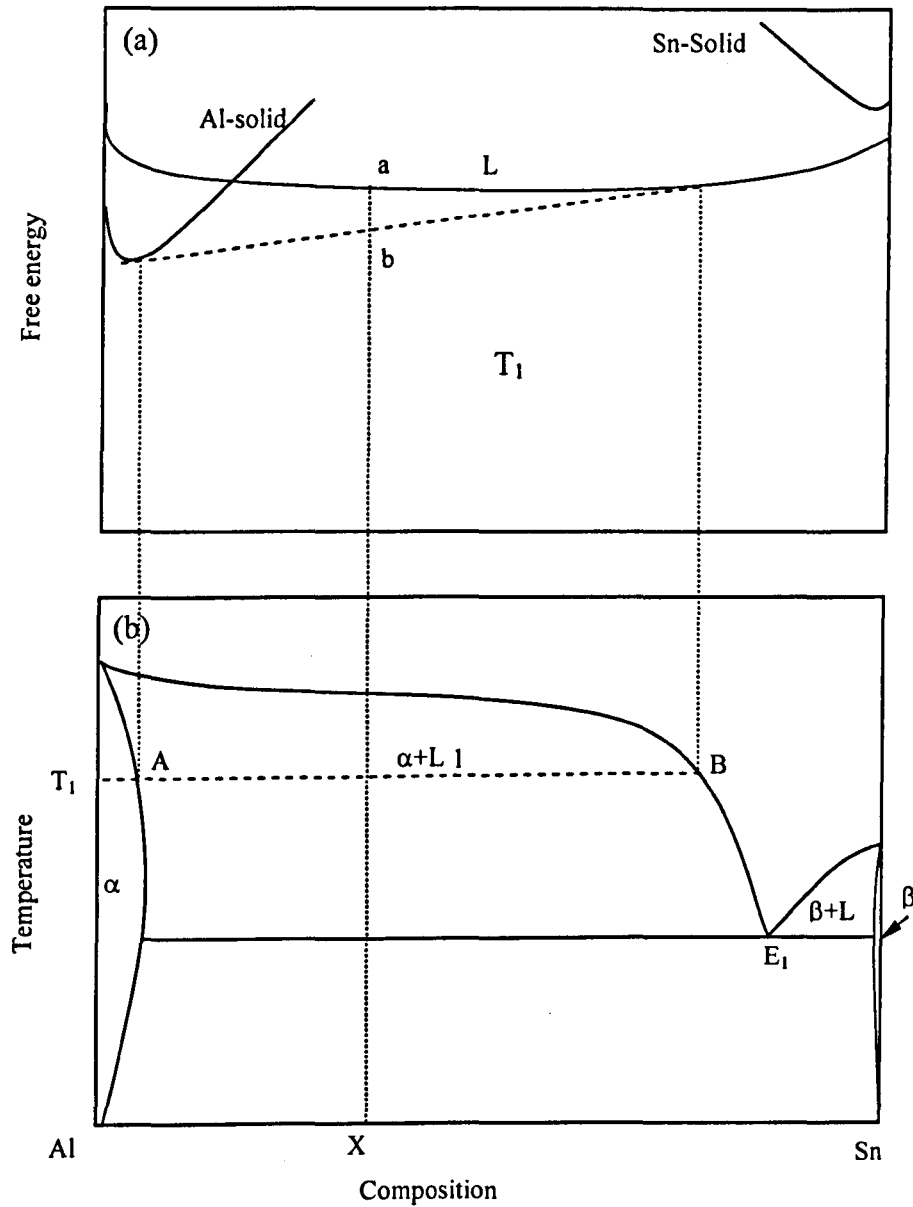


**Figure 4.25** Schematic of the equilibrium phase diagram of Al-Sn and the associated free energy curve at temperature  $T_1$

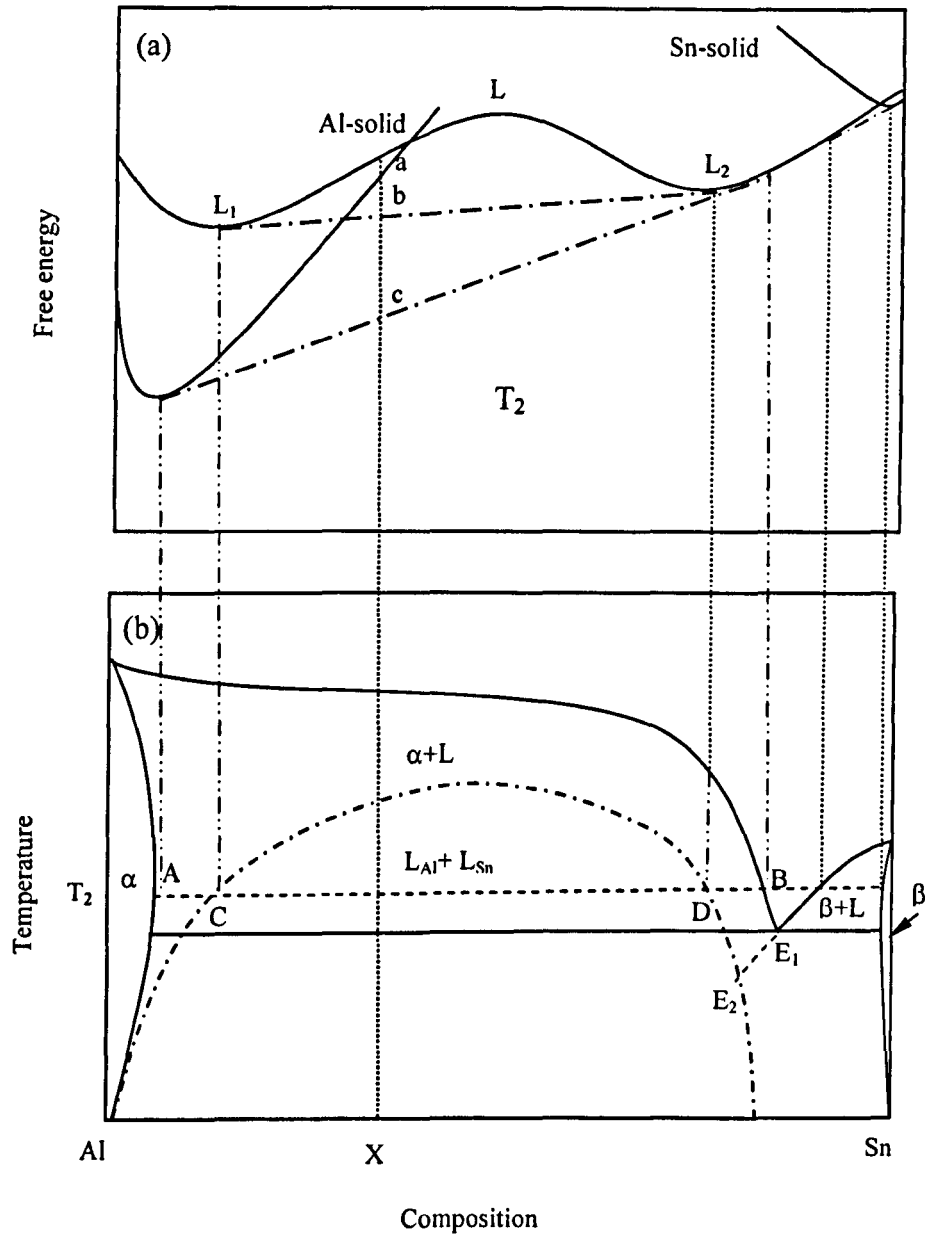


**Figure 4.26** Schematic of the equilibrium and metastable phase diagram of Al-Sn and the associated free energy curve at temperature  $T_2$



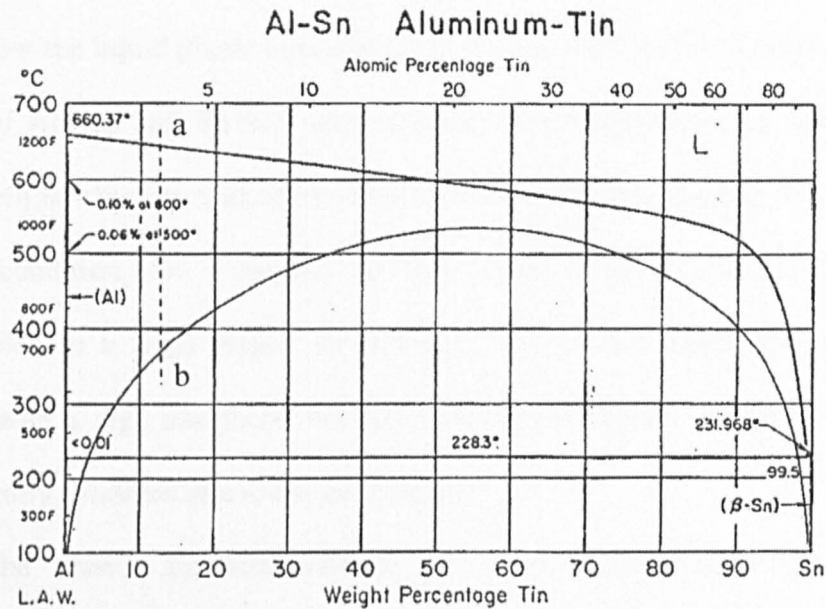


**Figure 4.27 Al-Sn equilibrium phase diagram with a metastable liquid miscibility gap**

Figure 4.27 shows the published Al-Sn binary equilibrium diagram <sup>[6]</sup> with the superimposed metastable liquid miscibility gap as calculated by Saunders <sup>[7]</sup>. It is evident that the calculated miscibility gap is similar to that illustrated in the schematic diagram of Figure 4.26. If the composition of Al-12wt%Sn is now considered it is possible to describe qualitatively the possible stable and metastable transformations which will occur on cooling. For the case of relatively slow cooling, undercooled liquid exists below the equilibrium liquidus but above the liquid separation line (Figure 4.27, between a and b). The Al phase will nucleate and grow to form Al dendrites, while on further cooling the composition of the liquid approaches the eutectic point close to pure Sn, whereupon Al growth from the primary solidified Al will continue and Sn will solidify between the Al dendrite arms. This equilibrium phase transformation sequence will form a dendritic Al structure and an interdendritic Sn phase.

However, at higher cooling rates, the liquid may undergo a greater level of undercooling prior to the onset of phase transformation. The undercooled liquid, once below the liquid phase separation line (Figure 4.27, below b) will separate into liquids of Al-rich and Sn-rich compositions. The compositions of these separated liquids will be closer to that of the pure elements for higher degrees of undercooling. In this condition, the separated Al rich liquid (with a low Sn content) has undercooled to a large extent. Accordingly, the Al-rich liquid will nucleate and solidify with a high interfacial velocity, thereby entrapping the Sn-rich liquid that subsequently solidifies at a lower temperature.

The above analyses indicate that the cooling rate will affect the microstructure formation. Therefore, the effect of cooling rate will be discussed in quantitative way.

#### **4.4.3 Quantitative understanding of the effect of cooling rate on phase selection**

##### **4.4.3.1 Introduction**

The purpose of this section is to find a critical cooling rate and hence estimate the critical size of gas atomised powder in which liquid phase separation will occur in preference to nucleation and growth of dendritic  $\alpha$ -Al. The relationship between He and N<sub>2</sub> gas atomised powder particle size and the heat transfer coefficient is first established according to the literature, then the relationship between particle size and cooling rate is considered.

The relationship between undercooling for nucleation of  $\alpha$ -Al and cooling rate may be approached from an analysis in the literature of pure Al<sup>[8]</sup>. Accordingly, the correlation of particle size, and the relationship between cooling rate and undercooling could be established. Using this relationship, the critical cooling rate of

an Al-Sn alloy for liquid phase separation can be estimated. Therefore, the critical gas atomised powder particle size for liquid phase separation in an Al-Sn alloy can be evaluated.

#### 4.4.3.2 The relationship between cooling rate, heat transfer coefficient and gas atomised particle size

The cooling rate of a gas atomised powder particle is a function of its heat transfer coefficient. In order to know the relationship between cooling rate and particle size, the first step is to calculate the heat transfer coefficient ( $h$ ) of the cooling gas.

Assuming Newtonian cooling, the cooling rate of a gas atomised powder particle is given by equation 2.16 in Chapter 2,

$$\varepsilon = -\frac{dT}{dt} = 6 \frac{\Omega(T - T_G)}{C_L} \cdot \frac{h}{d} \quad \text{Eqn 4.2}$$

The heat transfer coefficient of gas-atomised powder may be expressed by equation 2.10 in Chapter 2,

$$h = \frac{2K_G}{d} + 0.6(K_G^2 C_p)^{\frac{1}{3}} \left(\frac{\rho u}{d}\right)^{\frac{1}{2}} \left(\frac{1}{\mu}\right)^{\frac{1}{6}} \quad \text{Eqn 4.3}$$

By using the equation 4.3, the relationship between the heat transfer coefficient and the gas atomised powder particle size can be constructed.

Table 1 summarise the relevant parameters for He gas at a temperature of 300K <sup>[9]</sup>, plus the thermal conductivity of He gas from literature <sup>[10]</sup>.

**Table 4.1**

Symbol	Parameter	Units	Value
$K_G$	Thermal conductivity of He	$\text{Wm}^{-1}\text{K}^{-1}$	0.20
$C_p$	Specific heat capacity of He	$\text{J kg}^{-1}\text{K}^{-1}$	$5.2 \times 10^3$
$\rho$	Density of He	$\text{kg m}^{-3}$	0.18
$\mu$	Viscosity of He	$\text{Pa s}$	$1.993 \times 10^{-5}$
$u$	Relative velocity of powder and He gas	$\text{m/s}$	100

According to equation 4.3, the heat transfer coefficient for He gas is given by:

$$\begin{aligned}
 h &= \frac{2K_G}{d} + 0.6(K_G^2 C_P)^{\frac{1}{3}} \left(\frac{\rho u}{d}\right)^{\frac{1}{2}} \left(\frac{1}{\mu}\right)^{\frac{1}{6}} \\
 &= \frac{2 \times 0.20}{d} \left(\frac{Wm^{-1}K^{-1}}{m}\right) + 0.6(0.20^2 \times 5.2 \times 10^3)^{\frac{1}{3}} \left(\frac{0.18 \times 100}{d}\right)^{\frac{1}{2}} \left(\frac{1}{1.993 \times 10^{-5}}\right)^{\frac{1}{6}} \times \\
 &\quad (W^2 m^{-2} K^{-2} \cdot Jkg^{-1}K^{-1})^{\frac{1}{3}} \left(\frac{kgm^{-3} \cdot ms^{-1}}{m}\right)^{\frac{1}{2}} \left(\frac{1}{Pa \cdot s}\right)^{\frac{1}{6}} \\
 &= 0.4 \cdot Wm^{-2}K^{-1} + 0.6(0.20^2 \times 5.2 \times 10^3)^{\frac{1}{3}} (18)^{\frac{1}{2}} \left(\frac{1}{1.993 \times 10^{-5}}\right)^{\frac{1}{6}} \times \\
 &\quad (W^2 m^{-2} K^{-2} \times J \cdot kg^{-1} K^{-1})^{\frac{1}{3}} (kgm^{-3} s^{-1})^{\frac{1}{2}} (mkg^{-1} s)^{\frac{1}{6}} \\
 &= 0.4d^{-1} + 91.5d^{-\frac{1}{2}} (Wm^{-2}K^{-1})
 \end{aligned}$$

**Eqn 4.4**

Where h is given in  $W m^{-2}K^{-1}$  and d is in the unit of meters.

If the particle diameter (d) is in micrometers, the equation of heat transfer coefficient can be expressed as,

$$h = 4 \times 10^5 d^{-1} + 9.15 \times 10^4 d^{-\frac{1}{2}} = C1 + C2 \quad \text{Eqn 4.5}$$

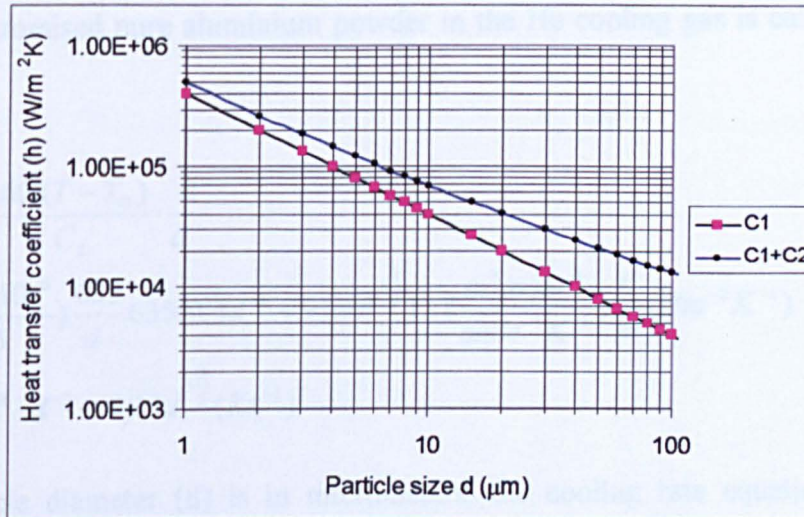


**Figure 4.28** Graph showing the relationship between the heat transfer coefficient and particle size with He gas cooling

The relationship between the heat transfer coefficient and the particle size using He as cooling gas may be expressed graphically,

Figure 4.28 shows that the term both C1 and C2 contribute to the heat coefficient, but the C2 effect will decrease with the particle size decreasing in the He gas atomisation powder.

Table 4.2 summarise the various parameters for pure aluminium. T is taken as the melting temperature of pure aluminium, i.e.  $660 + 273 = 933\text{K}$ . The He gas temperature is estimated as room temperature, e.g.  $25 + 273 = 298\text{K}$ . Hence,  $T - T_G = 933 - 298 = 635\text{ K}$ .

Table 4.2

Symbol	Parameters	Units	Value	Ref.
$\Omega$	Molar volume of Al	$\text{m}^3/\text{mole}$	$10.95 \times 10^{-6}$	[8]
$C_L$	Heat capacity of liquid of Al	$\text{J/mole K}$	29.31	[8]
$T - T_G$	T-melting temperature of liquid T <sub>G</sub> -gas temperature	K	635	Estimated
K	Thermal conductivity of He gas	$\text{Wm}^{-1}\text{K}^{-1}$	0.20	[10]

According to the parameter list in Table 4.2 and the equation 4.2, the cooling rate of gas-atomised pure aluminium powder in the He cooling gas is calculated as follows,

$$\begin{aligned}
 \varepsilon &= -\frac{dT}{dt} = \frac{6\Omega(T - T_G)}{C_L} \cdot \frac{h}{d} \\
 &= 6\left(\frac{10.95 \times 10^{-6}}{29.3}\right) \frac{635}{d} \cdot 635(0.4d^{-1} + 91.5d^{-\frac{1}{2}}) \times \left(\frac{\text{m}^3 \text{mole}^{-1}}{\text{mole}^{-1}\text{K}^{-1}}\right) \frac{\text{K}}{\text{m}} (\text{Wm}^{-2}\text{K}^{-1}) \quad \text{Eqn 4.6} \\
 &= 5.69 \times 10^{-4} \cdot d^{-2} + 0.13d^{-\frac{3}{2}} (\text{Ks}^{-1})
 \end{aligned}$$

If the particle diameter (d) is in micrometers, the cooling rate equation can be expressed as,

$$\varepsilon = -\frac{dT}{dt} = 5.69 \times 10^8 \cdot d^{-2} + 1.3 \times 10^8 d^{-\frac{3}{2}} \quad \text{Eqn 4.7}$$



The associated plot of cooling rate in He gas versus particle size is shown in Figure 4.29. The result shows that the second term of equation 4.7 could slightly increase the cooling rate.

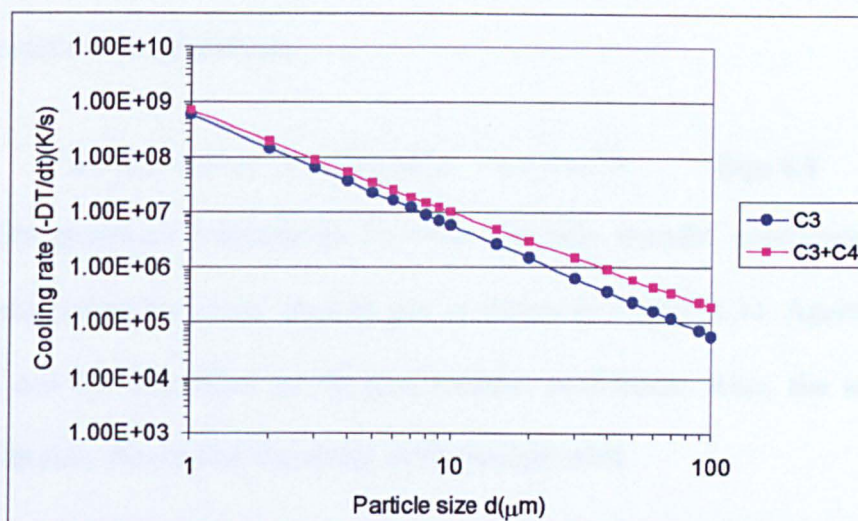


**Figure 4.29** The relationship between cooling rate and particle size for pure Al particle using He as cooling gas

The same equation 4.3 could be used to ascertain the relationship between the heat transfer coefficient and the particle size for  $\text{N}_2$  gas atomisation by substituting the  $\text{N}_2$  physical parameters.

Table 4.3 presents the physical parameters of  $\text{N}_2$  gas at a temperature at 300K

[9]

**Table 4.3**

Symbol	Parameters	Units	Value
K	Thermal conductivity of $\text{N}_2$	W/m K	0.026
$C_p$	Specific heat capacity of $\text{N}_2$	J/kg K	$1.04 \times 10^3$
$\rho$	Density of $\text{N}_2$	$\text{Kg/m}^3$	1.25
$\mu$	Viscosity of $\text{N}_2$	Pa s	$1.81 \times 10^{-5}$
u	Relative velocity of powder and $\text{N}_2$ gas	m/s	100

The heat transfer coefficient (h) of the  $\text{N}_2$  gas could thus be calculated as follows,



$$h = \frac{2K_G}{d} + 0.6(K_G C_P)^{\frac{1}{3}} \left(\frac{\rho u}{d}\right)^{\frac{1}{2}} \left(\frac{1}{\mu}\right)^{\frac{1}{6}} \quad \text{Eqn 4.8}$$

$$= 0.052d^{-1} + 29.19d^{-\frac{1}{2}} (Wm^{-2}K^{-1})$$

Again, if the particle diameter (d) is taken in micrometers, the heat coefficient equation could be expressed as,

$$h = 5.2 \times 10^4 d^{-1} + 2.92 \times 10^4 d^{-\frac{1}{2}} = C5 + C6 \quad \text{Eqn 4.9}$$

The graphical relationship between the heat transfer coefficient and the particle size using N<sub>2</sub> as the cooling gas is shown in Figure 4.30. Again, both the term C5 and C6 has effect to the heat transfer coefficient. Also, the smaller the particles in size, the smaller the effect of the second term.

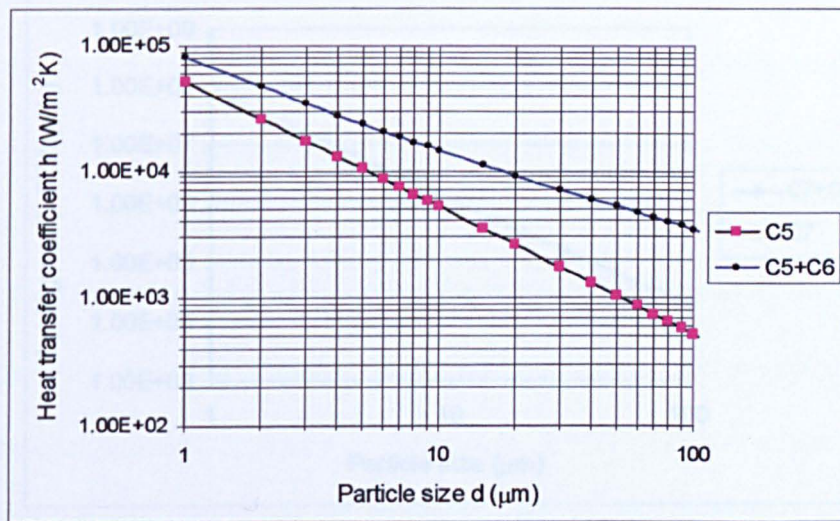


**Figure 4.30 Graph showing the relationship between the heat transfer coefficient and particle size with N<sub>2</sub> gas cooling**

By considering the two terms of heat transfer coefficient, the cooling rate for pure aluminium during N<sub>2</sub> gas-atomisation could be expressed as follows,

$$\varepsilon = -\frac{dT}{dt} = \frac{6\Omega(T - T_G)}{C_L} \cdot \frac{1}{d} \left[ \frac{2K_G}{d} + 0.6(K_G C_P)^{\frac{1}{3}} \left(\frac{\rho u}{d}\right)^{\frac{1}{2}} \left(\frac{1}{\mu}\right)^{\frac{1}{6}} \right] \quad \text{Eqn 4.10}$$

$$= 7.4 \times 10^{-5} d^{-2} + 4.16 \times 10^{-2} d^{-\frac{3}{2}} (Ks^{-1})$$



If the particle diameter ( $d$ ) is again in micrometers, the cooling rate equation becomes,

$$\varepsilon = -\frac{dT}{dt} = 7.4 \times 10^7 d^{-2} + 4.16 \times 10^7 d^{-\frac{3}{2}} = C7 + C8 \quad \text{Eqn 4.11}$$

The associated plot of cooling rate of  $N_2$  gas versus particle size is shown in Figure 4.31. C7 is the cooling rate from a consideration of the first part of the heat transfer coefficient. C7+C8 is the cooling rate considering the effect of both parts of the heat transfer coefficient. The result again demonstrates that the smaller the particle in size, the less the effect of the second term (C8) of the heat transfer coefficient on cooling rate.

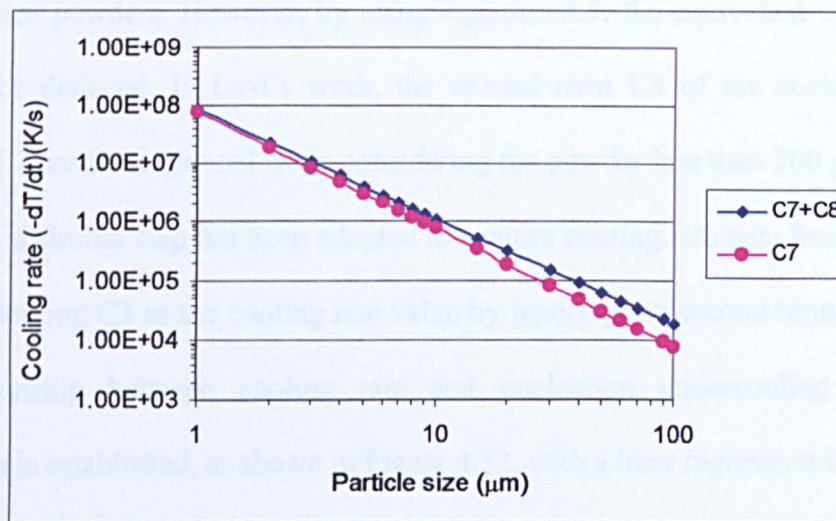


**Figure 4.31** Plot of the relationship between cooling rate and particle size for  $N_2$  gas cooling.

#### 4.4.3.3 The relationship between cooling rate and extent of undercooling

Levi <sup>[8]</sup> has considered the rapid solidification of pure Al, gas atomised with He and derived a relationship (by numerical calculation) between particle diameter and undercooling prior to nucleation of the solid  $\alpha$ -phase. This relationship has been introduced in Chapter 2 (Figure 2.15). Table 4.4 summaries the results obtained by



using the data from Figure 2.15. The value of particle diameter and  $(T_m/T-T_N)^2$  are taken from Figure 2.15 [8].  $\Delta T$  is calculated by assuming  $T_m$  (pure aluminium melting point) is 660°C.

Table 4.4

Taken from Levi [8]		Calculated	
Particle diameter for He gas-atomised ( $\mu\text{m}$ )	$(T_m/T-T_N)^2$	$\Delta T=(T-T_N)$ (K)	Equivalent cooling rate $dT/dt$ (Eqn 4.7) ( $\text{Ks}^{-1}$ )
1	9	311.0	$7.0 \times 10^8$
5	11.5	275.1	$3.4 \times 10^7$
10	12.5	263.9	$9.8 \times 10^6$
50	15.3	238.5	$6.0 \times 10^5$
100	16.6	229.0	$1.9 \times 10^4$

The data allow the calculation of undercooling for different diameters of He gas-atomised powders. However, by using equation 4.7, the equivalent cooling rate can also be deduced. In Levi's work, the second term C4 of the cooling rate in equation 4.7 has been ignored when considering the powder less than 200  $\mu\text{m}$  in size. Therefore, a similar step has been adopted to acquire cooling rate data from equation 4.7, i.e. adopting C3 as the cooling rate value by ignoring the second term C4. Thus, the relationship between cooling rate and nucleation undercooling for pure aluminium is established, as shown in Figure 4.32, with a liner regression line drawn.

In the present study the gas-atomised alloy is Al-12wt.%Sn-1wt.%Cu and, using the equilibrium and calculated metastable phase diagram, it becomes possible to estimate the critical undercooling needed (and hence the cooling rate required) to avoid the nucleation of  $\alpha$ -Al. If we approximate the liquidus temperature of the alloy to 640°C (that of Al-12wt.%Sn) and use the value of 364°C for the liquid phase separation temperature (taken from Figure 4.27), then the critical undercooling,  $\Delta T$ , is 276K. This value is shown as a dashed line in Figure 4.32 representing the

minimum undercooling for liquid phase separation of the Al-12wt.% Sn alloy. From Figure 4.32, it corresponds to a critical cooling rate of  $1.8 \times 10^7 \text{ Ks}^{-1}$ .

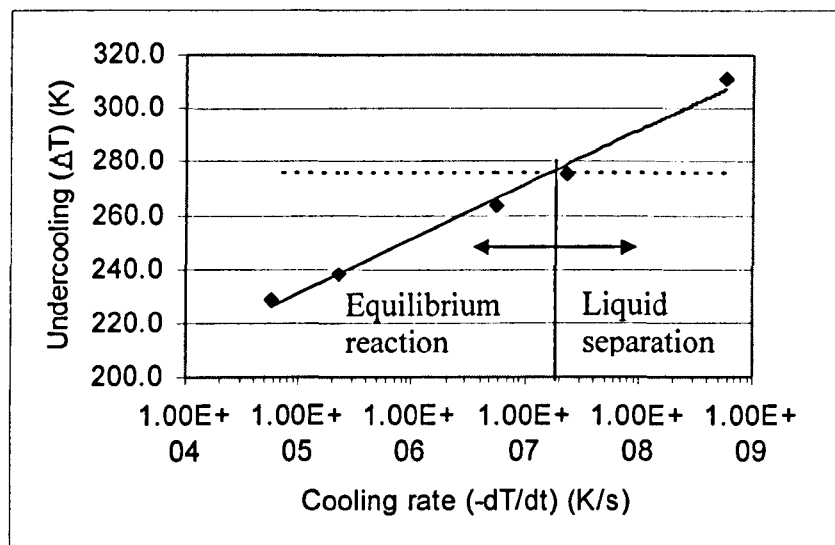


**Figure 4.32 The relationship between extent of undercooling prior to nucleation of  $\alpha$ -Al and the cooling rate**

This indicates that for this alloy, liquid phase separation will happen for a cooling rate higher than  $1.8 \times 10^7 \text{ Ks}^{-1}$  and nucleation of primary  $\alpha$ -Al will occur for a cooling rate lower than this value. This cooling rate value could be called a critical cooling rate. Using this value, we can estimate the critical maximum diameter for the gas-atomised powder which will exhibit liquid phase separation. Combining the critical cooling rate with Figure 4.29, the liquid phase separation would happen in He gas-atomised powder diameters less than  $\sim 6 \mu\text{m}$ . For the powder atomised by  $\text{N}_2$  gas, a combination of Figure 4.31 and the critical cooling rate value shows that liquid separation in gas atomised Al-Sn alloy will occur at a powder particle diameter less than  $\sim 3 \mu\text{m}$ . This seems to be in good agreement with the experimental observation (Figure 4.4 and Figure 4.14) which shows that Sn dispersoid is distributed within the

N<sub>2</sub> gas atomised powder of diameter less than 10 µm, and particular in those powders of diameter less than 6 µm. Two approximations have been made in this calculation. One is that the physical parameters used for the calculation is from pure Al instead of the Al-12wt.%Sn-1wt.%Cu alloy. The second approximation is the melting temperature and metastable liquid separation temperature is for the Al-12wt.%Sn alloy instead of the Al-12wt.%Sn-1wt.%Cu alloy.

Similarly, the cooling rate of the thermally sprayed coating could also be calculated using the equation 2.26.

$$\varepsilon = -\frac{dT}{dt} = \frac{h(T_1 - T_2)}{\rho C_p s} \quad \text{Eqn 4.12}$$

According to Figure 4.16, the thickness of the coating is 261µm for 20 passes of the thermal spray. Thus, the average thickness of one splat (s) is 13µm. The cooling rate can be calculated assuming the melting temperature of a splat (T<sub>1</sub>) is the Al-12wt%Sn melting temperature, 958K (Figure 4.27). The substrate temperature (T<sub>s</sub>) is 250°C from the experiment measurement. The density (ρ) of pure Al in the solid state is 2.39×10<sup>3</sup>kg/m<sup>3</sup> [9]. The specific heat capacity of pure Al is 0.897J/g·K [9]. The heat transfer coefficient number is from the plasma thermal spray pure Al coating, 3.5×10<sup>6</sup>kgW/m<sup>2</sup>K [11]. The cooling rate could be calculated,

$$\begin{aligned} \varepsilon &= -\frac{dT}{dt} = \frac{h(T_1 - T_2)}{\rho C_p s} \\ &= \frac{3.5 \times 10^6 \text{ Wm}^{-2} \text{ K}^{-1} (958 \text{ K} - 549 \text{ K})}{0.897 \text{ Jg}^{-1} \text{ K}^{-1} \times 2.39 \times 10^3 \text{ kgm}^{-3} \times 13 \mu\text{m}} \\ &= \frac{3.5 \times 10^6 \times 410}{0.897 \times 10^3 \cdot 2.39 \times 10^3 \cdot 13 \times 10^{-6}} \cdot \frac{\text{m}^2 \text{ kg} \cdot \text{s}^{-3} \text{ m}^{-2} \text{ K}^{-1} \times \text{K}}{\text{m}^2 \text{ kg} \cdot \text{s}^{-2} \cdot \text{kg}^{-1} \text{ K}^{-1} \times \text{kgm}^{-3} \times \text{m}} \\ &= 5.2 \times 10^7 \text{ Ks}^{-1} \end{aligned} \quad \text{Eqn 4.13}$$

The calculated value indicates that the cooling rate of thermal spray splats is higher than the critical cooling rate for Al-Sn alloy liquid phase separation.

Therefore, liquid phase separation definitely happens in the thermal sprayed coating.

#### **4.4.4 The effect of different Sn and Cu contents on liquid phase separation**

The precise composition of the Al-Sn-Cu alloy could also affect the microstructure during the process of rapid solidification.

The composition effect has not been given much attention in previous work. However, it is known <sup>[12]</sup> that the higher the Sn content in Al, the larger are the Sn particles dispersed within the Al matrix. In the study of the Al-Be system by laser surface remelting and melt spinning <sup>[13]</sup>, the same phenomenon is reported, i.e. that a higher weight percent of Be in the Al matrix causes larger second phase dispersoids as distinct from a higher density of small particles. Further, the other author claims <sup>[14]</sup> a distribution of Al particles within the Be matrix, on the Be rich side of the phase diagram. These observations all support the notion that composition has an effect on microstructure formation. As for the case of the Al-Sn alloy, inspection of the phase diagram (Figure 4.27) shows that with content of Sn increased from 12wt%, the separated Sn droplets increase in density which increases the coalescence probability of the Sn droplets. Therefore, coarser Sn particles would be anticipated within the high content Sn alloy. However, the Sn particle size would reach its coarsest size when the Sn content reaches 55wt%. After that, the Al particles would be expected to form in the Sn matrix. The lower the Al in content, the finer the Al particles observed if the liquid undergoes the same cooling rate. The suggestion that a large number density of droplets could coarsen quickly has been introduced in Chapter 2 (section 2.5). The coarsening mechanism may be through Brownian motion. The motion velocity can be expressed by stoke movement or Maragoni migration.

Similarly, it can be argued that a third element in the alloy will also affect the microstructure. A section of the Al-Sn-Cu ternary phase diagram <sup>[15]</sup> is shown in Figure 4.33. The precise composition of the Al-12wt%Sn-1wt%Cu alloy (shown as a black dot on the diagram) is very close to the apex representing pure Al. The point  $e_1$  corresponds to the Al-Cu eutectic point, whilst  $E_1$  denotes the Al-Sn-CuAl<sub>2</sub> ternary eutectic point. The effect of adding Cu will act to move the composition towards the  $L_1 + L_2$  liquid separation region. This will increase the tendency for liquid separation within these ternary alloys by acting to decrease the separation between the stable and metastable liquidus surface. For this reason, it is likely that Sn dispersoids will be slightly coarser in the AlSnCu ternary alloy than within the simple Al-Sn binary alloy.

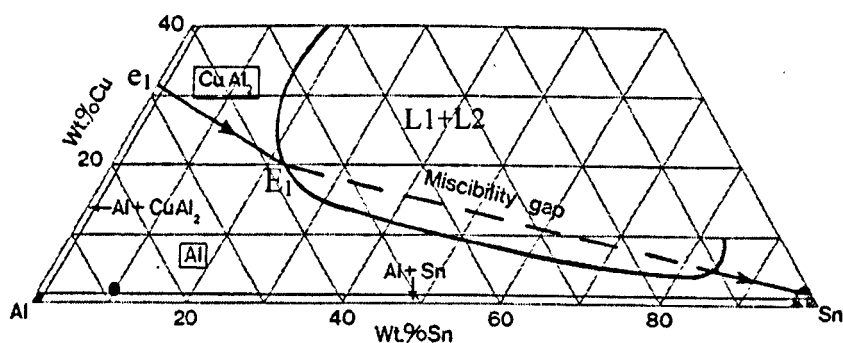


**Figure 4.33 Al-Sn-Cu ternary phase diagram**

#### 4.4.5 The microstructure formation mechanisms of gas atomised AlSnCu powders

The microstructure formation mechanism for the gas atomised Al-12wt%Sn-1wt%Cu powder is relatively easy to explain after understanding the basic mechanisms described in previous sections.

The X-ray diffraction spectrum of the gas atomised Al12Sn1Cu powder did not reveal any peaks from Cu compounds. One possibility is that the fraction of these Cu containing compounds is less than the detection limit of the XRD machine. Another possibility is that the Cu is in solution within the aluminium matrix. Indeed Cu remains in solid solution within Al at about 5.65wt.% at 550°C [6]. Although the solubility decreases greatly as the temperature decreases, the rapid cooling should ensure Cu is retained in solid solution.

The variety of morphologies of the Al12Sn1Cu gas atomised powder particles (Figure 4.2) is very important to explain the microstructure formed. As discussed below.

The large powder particles ( $> 10\ \mu\text{m}$ ) undergo relatively slow cooling, or the cooling rate is lower than the critical cooling rate for liquid separation. The undercooled liquid exists below the equilibrium liquids but above the liquid separation line. Nucleation of  $\alpha$ -Al occurs above the metastable two liquid region to form dendritic Al and interdendritic Sn. BSE images (Figure 4.3) and TEM images (Figure 4.8 to Figure 4.13) all support this mechanism. It is considered that some Sn solute within the solidified Al dendrites subsequently precipitates inside the grains and also at the sub-grain boundaries during the final stages of solidification (Figure 4.9 to Figure 4.13). The precipitate Sn at the sub-grain boundaries is either continuous or discrete. Figure 4.11 shows that the discrete Sn resides at the upper and lower sides of the sample foil. This means the discrete Sn might be slightly modified by the mechanical process used for TEM sample preparation. EDX analysis (Figure 4.12 and Figure 4.13) confirms that both the continuous and discrete precipitates are the Sn phase.

The satellite powder particles ( $< 10 \mu\text{m}$ ) experience higher cooling rates, i.e., the cooling rate is higher than critical cooling rate for critical liquid phase separation. The liquid is undercooled below the liquid phase separation line where liquid phase separation happens. Therefore, nanoscale Sn particles will form in the Al matrix (Figure 4.4 and Figure 4.14). The Sn dispersoids within the Al matrix are sub-micron in scale and decrease in size with particle size decreasing (Figure 4.4). The different cooling rate and hence extent of undercooling of differently sized particles is considered to be the dominant factor controlling the resultant dispersion. Decreasing the particle size increases the undercooling achievable prior to nucleation by effectively increasing the cooling rate of the liquid. It is also noted that the  $\alpha$ -Al interface velocity is also proportional to the cooling rate<sup>[16]</sup>. Therefore, small powder means a relatively higher Al interface velocity. In such circumstances, separated Sn-rich droplets within relatively small powder particles may quickly become entrapped by growing  $\alpha$ -Al without further coalescence. However, separated Sn droplets possible coarsen in the relatively larger powder due to the lower interface velocity of  $\alpha$ -Al. It is again noted that the process of liquid droplet coarsening is driven by Brownian motion or by stoke motion and Maragoni migration<sup>[17, 18]</sup>.

The microstructures of Figure 4.4 suggest there is a competition between the dendritic growth and the metastable liquid phase separation reaction during the cooling of particles of intermediate (Figure 4.4a-c) size. The distinction is dependent on the growth speed of the Al grains caused by undercooling / cooling rate that may lead to the dispersion of liquid Sn droplets or cause droplet further coarsening to form elongated shaped Sn particles (Figure 4.4a and b).

Two distinct fine scale Sn dispersions existing within the small powder particles ( $< 5 \mu\text{m}$  in size, Figure 4.4 d-e) may also be due to local variation of the Al

growth speed. It is probable that Al nucleates at one side of the powder and latent heat of nucleation causes the recalescence effect during solidification which reduces the cooling rate in the unsolidified part of the droplet. This causes a local decrease in the Al interface velocity resulting in local coarsening of the Sn droplets.

A maximum particle size of 3  $\mu\text{m}$  is predicted for  $\text{N}_2$  gas atomised Al-Sn powder corresponding to the critical cooling rate (Figure 4.31). However, the experimental observations show liquid separation occurs within particles somewhat larger than this. One reason for this discrepancy between experiment and theory prediction is that the parameters used for calculation were based on pure aluminium and Al-12%Sn alloy instead of the Al12Sn1Cu alloy. Further, according to Francis Duflos <sup>[19]</sup>, powder particles smaller than 100  $\mu\text{m}$  will experience a higher relative velocity of gas and particle, as compared with the particles larger than 100  $\mu\text{m}$ . In this context, the cooling rate of each powder particle up to  $\sim 10 \mu\text{m}$  cooled by  $\text{N}_2$  gas will adopt a higher value as compared with the calculated value (Figure 4.31). All of these cause the liquid phase separation to happen in somewhat larger powder particles. The other contributing factor is the Cu present in the alloy that also acts to promote liquid phase separation as explained previously.

The local rate of cooling may also be used to explain the differing particle shell microstructures, as shown in Figure 4.5. The liquid phase separation mechanism explains the observation of a fine Sn dispersion within the very thin shell structures (Figure 4.5 a,b) as a rapidly cooled liquid droplet surrounds a solidified powder particle. Since the shell is formed by a liquid metal striking a solidified powder, the cooling rate at the two surfaces of the shell will be higher as compared with the centre of the shell. The heat transfer from the shell is conductive into the solidified powder particle and convective through the cooling gas, whilst the heat



transfer from the centre of the shell is relatively lower. This relative decrease of the cooling rate at the shell centre causes the dispersion of slightly larger Sn particles within the centre of the shell (Figure 4.5b). Such competing cooling rate mechanisms may also be used to explain the microstructures exhibited by slightly thicker shell microstructures (Figure 4.5 d), where the formation of columnar Al grains delineated by striations of the Sn phase is controlled by the transformation to the  $\alpha$ -phase.

Greater insight into these solidification mechanisms is provided by the microstructures of irregularly shaped particles. The observation of an irregular shaped powder particle attached to a large dendritic powder particle (Figure 4.6) would suggest that a similar competition between the same solidification mechanisms has taken place. This particle has experienced an equilibrium eutectic reaction in the region next to the large dendritic powder particle, leading to a fine dendritic structure at the contact point with the large particle (Figure 4.6c), due to heat flow by conduction. Further away from this contact surface, a striated cast like microstructure (arrowed at Figure 4.6b) has formed again under equilibrium conditions but at a slower cooling rate. Conversely, it is considered that the tail structure of this particle has undergone liquid separation leading to the formation of a fine dispersion of Sn particles. Heat transfer via less efficient convection processes would have occurred in this instance. At the transition zone between these two regions (Figure 4.6d) there is evidence of local coalescence of some of these Sn particles corresponding the decreasing of the local cooling rate.

Thus, many of the microstructures observed can be explained with reference to the rate of cooling and the competition between the equilibrium reaction and the metastable liquid phase separation. However, a further level of complexity is introduced by Figure 4.7. In this instance, it is considered that the undercooling is

close to liquid phase separation, but has not quite reached there, which would promote primary  $\alpha$ -Al nucleation and growth. The remaining liquid achieves a liquid phase separation composition causing liquid separation to occur. Another explanation may be the irregular shape of the particles causes different regions to undergo different cooling rates. Therefore, the particle shows a combined structure of Al dendrites, Sn interdendrites and the fine scale Sn distributed within the Al matrix.

#### **4.4.6 The microstructure formation mechanisms in HVOLF thermal sprayed coatings**

The same mechanisms may be used to explain the resultant complex microstructures identified within the HVOLF as-sprayed coatings. Again, the critical cooling rate and extent of undercooling will dominate the microstructure of the AlSnCu thermal sprayed coatings. The composition effect becomes much more evident because of the non-uniformity of the coating, due to the mix of molten and semi-molten powders forming the coating.

The XRD pattern again does not show evidence of the presence of a Cu-rich compound within the as-sprayed coating. However, the limit of detection by XRD is ~2wt.%. TEM images also did not show any evidence for the existence of such a phase. In considering the formation of a coating, it is necessary to examine powder particle heating and degree of melting before looking at impact and solidification of particles for the coatings.

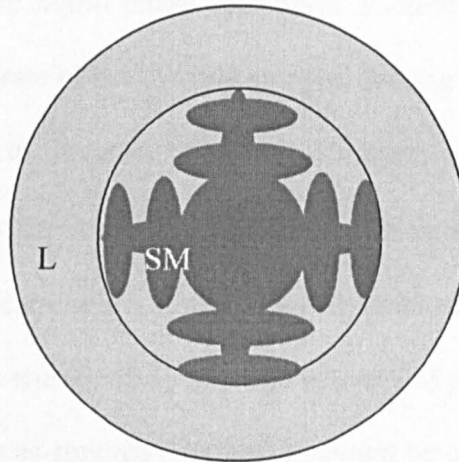


**Figure 4.34 Schematic of a thermal sprayed powder. L - liquid region, SM - semi-molten region**

The heat transfer and momentum transfer associated with the HVOLF thermal spraying process causes the individual particles to experience differing thermal effects. For example, small powder particles may become fully molten, whilst larger powder particles may take the form of a semi-molten core surrounded by a fully molten liquid surface before deposition (Figure 4.34). It is noted that only a small amount of powder of size  $< 10 \mu\text{m}$  exists in the nominal gas atomised powder of diameter range  $40\text{--}106 \mu\text{m}$ . Therefore, the main microstructure of the as-sprayed coating is from molten and semi-molten large powder ( $> 10 \mu\text{m}$ ). The detailed microstructure of the thermally sprayed coating may be explained from a consideration of the solidification mechanisms operative from this starting point. The extent of melting of the feedstock gas atomised powders will depend on the thermal spraying parameters and size of the powder particles. For completely molten particles, a homogeneous melt which will solidify to form (shown in Figure 4.16) the grey contrast region, Figure 4.17 and Figure 4.21 circle (a) and Figure 4.24 (a,b and d,e). It is believed that the extent of undercooling / cooling rate is higher than the critical rate for liquid phase separation during solidification of these particles, i.e. the

cooling rate of this region is higher than  $1.8 \times 10^7 \text{ Ks}^{-1}$  (ignoring the slight effect of Cu in promoting the liquid phase separation according to theoretical calculation). Indeed, the cooling rate of the thermal sprayed coating is estimated to be higher than  $10^7 \text{ Ks}^{-1}$  according to literature <sup>[20]</sup>. The calculation of cooling rate in the previous section indicates that the cooling rate of Al-12wt.%Sn is  $5.2 \times 10^7 \text{ Ks}^{-1}$ . This value is higher than the critical cooling rate calculated. Accordingly, a fine scale dispersion of liquid Sn droplets entrapped by the high velocity of growing Al grains will always tend to form in these as-sprayed coatings. It should be emphasised that regions of the Al-rich solid also contain a certain amount of Sn in solution, beyond the level predicted for equilibrium cooling. It is therefore possible that thermal spikes that subsequently pass through the sequentially deposited layered structure also act to promote local tin precipitation in the solid state thus, generating further precipitates of Sn particles within the aluminium grains in the as-sprayed coatings. The fine Sn droplets could also be pushed ahead of a solidifying Al growth front or triple point during the final stages of solidification. This would lead to a coalesced form at the interface between the aluminium grains (Figure 4.24a,d). The thermal spikes that subsequently pass through the sequentially deposited layered structure are another possible cause of Sn particle diffusion to the grain boundary interface or triple points.

For those large powders with a semi-molten core, the Sn interdendrites have melted, whilst the Al matrix have partially melted. The solidification of the molten Sn in semi-molten Al should be considered depending upon the extent of melting. If more surrounding Al matrix has been dissolve by the molten Sn, in view of the high levels of local superheat absorption available (Figure 4.18 a,d), the Sn particle size distributed in the matrix becomes very fine. A liquid phase separation mechanism could explain the microstructure formation. For the intermediate heat absorption

region (Figure 4.18 b,e), less Al matrix is dissolved by the melted Sn, and relatively coarser Sn particles are formed in this region. Liquid phase separation has also happened in this region, but the local composition of this region is higher than Al-12wt%Sn. The separated Sn droplets readily coarsen to form a large Sn droplet which is retained in the following rapid solidification process. The other reason for the large Sn distribution is that some of the melted Sn has no time to mix with Al (Figure 4.18c). Figure 4.22 and Figure 4.23 are TEM images reflecting the partially melted Sn distribution in the interdendrite region. In the limited heat absorption region, the molten Sn with little superheat has insufficient time to dissolve the surrounding Al, retaining the original powder dendritic structure (Figure 4.18c). Other relatively large scale Sn particle dispersions distributed through the coating with a chain like structure (Figure 4.21, circled B) also arise from insufficient time to dissolve Al. Such microstructures are recognisable as broken up distributions of the original Sn inter-dendritic structures in the larger gas atomised powder particles.

The reason for the small Al region free from Sn particles (Figure 4.22, circled region, Figure 4.23d, Figure 4.24 ) suggests that a certain amount of recovery and / or recrystallisation has occurred during the thermal spray process. The HVOLF thermal spray process transfers a high local kinetic energy to the powder particles. This leads to the deformation of the semi-molten powder particles when they impact on the substrate and the pre-deposited layer. This will plastically deform the solid, with e.g. the introduction of tangles of dislocation (Figure 4.24b,e). In particular, a very high concentration of vacancies are known to be associated with the Al-Sn system and these might be expected to agglomerate and form dislocation loops as a consequence of the rapid solidification process.

## 4.5 Summary

The microstructure of Al<sub>12</sub>Sn<sub>1</sub>Cu alloy is dominated by a critical cooling rate or extent of undercooling. If the cooling rate is lower than the critical cooling rate, then an equilibrium eutectic reaction will occur and this generates a microstructure comprising Al dendrites surrounded by large interdendritic Sn particles. If the cooling rate is higher than critical cooling rate, (e.g. due to rapid solidification), liquid phase separation occurs whereupon a nano-scale Sn dispersion within the Al matrix is formed. The logarithm of cooling rate versus undercooling has a linear relationship.

For the gas-atomised powder, there is a competition between two different solidification mechanisms. The large ( $> 10\ \mu\text{m}$ ) Al<sub>12</sub>Sn<sub>1</sub>Cu powder particles and the thick shell identified around some of these powder particles undergo an equilibrium reaction. The very small ( $\leq 10\ \mu\text{m}$ ) powder particles and the instances of thin shell structures suggest the action of a liquid phase separation process. The rate of cooling and hence extent of undercooling below the liquid separation gap also affects the size distribution of the resultant Sn particles, depending on whether or not local coalescence to form slightly larger Sn particles is allowed to occur. It is considered that the presence of 1wt%Cu in the alloy slightly enhances the process of liquid phase separation, promoting liquid separation to occur within larger powder particles as observed, compared with theoretical prediction. The irregular shape of the some of the very small particles also suggests that the cooling rate affects the microstructure formation.

Similarly, the microstructure of HVOLF thermal spray coatings shows several levels of complexity due to the molten and semi-molten states of the powder particles during processing. In the fully molten regions, liquid separation occurs to

form distributions of nanoscale Sn dispersions due to the high cooling rate. Parts of the larger scale Sn distributions are attributed to semi-molten regions of material, arising from limited melting during the process of spray deposition. Other regions of large scale Sn particles are also considered to arise from compositional effects, e.g. molten Sn / Al liquid with a higher Sn content makes it easier for coalescence of Sn droplets to occur during the solidification process. Recrystallised Al grains, dislocation loops and dislocation tangles were also identified within the as-sprayed coatings. High velocity impingement of molten powder to the pre-deposited layer and the subsequent stresses generated is considered responsible for these phenomena.

## References

1. S. J. Harris, D. G. McCartney, A. J. Horlock and C. Perrin., *Production of ultrafine microstructure in Al-Sn, Al-Sn-Cu and Al-Sn-Cu-Si alloys for use in tribological application*. Materials Science Forum, 2000. **331-337**: p. 519-526.
2. A. J. Horlock, *HVOF Spraying of Novel Bearing Materials*, in *School of Mechanical, Materials, Manufacturing Engineering and Management*. 1999, University of Nottingham (PhD thesis): Nottingham.
3. W. T. Kim and B. Cantor, *Solidification of tin droplets embedded in an aluminium matrix*. Journal of Materials Science, 1991. **26**: p. 2868-2878.
4. W. T. Kim, D. L. Zhang and B. Cantor, *Nucleation of solidification in liquid droplets*. Metallurgical Transactions A, 1991. **22**(October): p. 2487-2501.
5. D. A. Porter and K.E. Easterling, *Phase Transformation in Materials and Alloys*. 1983: Van Nostrand Reinhold (UK) Co. Ltd.
6. The ASM Committee, *Metallography, structures and phase diagram, 8th edition*. Metal Handbook. 1973. **8**: American Society for Metal.
7. N. G. Saunders, Thermal Technology Ltd, Guildford, Surrey, UK (Private communication).
8. C. G. Levi, *The evolution of microcrystalline structures in supercooled metal powders*. Metallurgical Transactions, 1988. **19A**: p. 699-708.
9. David R. Lide and H.P.R. Frederikse, *Handbook of Chemistry and Physics*. Vol. 78th Edition. 1997-1998: CRC press, Inc.
10. T. W. Clyne, R. A. Ricks, and P.J. Goodhew, *The production of rapid-solidified aluminium powder by ultrasonic gas atomization Part I: Heat and fluid flow*. International Journal of Rapid Solidification, 1984-85. **1**: p. 59-80.
11. S. Sampath and H. Herman, *Rapid solidification and microstructure development during plasma spray deposition*. Journal of thermal spray technology, 1996. **5**(4): p. 445-456.
12. D. L. Zhang, W.T. Kim and B. Cantor. *Melt spun Al bearing alloys*. in *Advanced aluminium and magnesium alloy*. 1990. p 409-413, Amsterdam, The Netherlands.
13. D. C. Van Aken and H. L. Fraser. *The microstructure of rapid solidification hyper-eutectic Al-Be alloys*. Acta Metall. Mater. 1985. **33** (60): p963-974.
14. J. W. Elmer, M. J. Aziz, L. E. Tanner, P. M. Smith and M. A. Wall., *Formation of bands of ultrafine berllium particles during rapid solidification of Al-Be alloys: Modelling and direct observation*. Acta Metall. Mater., 1994. **42**(4): p. 1065-1080.
15. G. Petzow and G. Effenberg, *A comprehensive compendium of evaluated constitutional data and phase diagrams*. Ternary Alloys. Vol. 3. 1990: VCH, Germany. p 23-37.



16. A. K. Srivastava, *On cooling rate, interface velocities and particle sizes in spray atomization*. Journal of Materials Science Letters, 2000. **19**: p. 1217-1219.
17. J. R. Rogers and R. H. Davis, *Modelling of collision and coalescence of droplets during microgravity processing of Zn-Bi immiscible alloys*. Metallurgical Transactions A, 1990. **21**(January): p. 59-68.
18. X. Y. Lu, C. D. Cao, and B. Wei, *Microstructure evolution of undercooled iron-copper hypoperitectic alloy*. Materials Science and Engineering A, 2001. **313**(1-2): p. 198-206.
19. D. Duflos and J.-F. Stohr, *Comparison of the quench rates attained in gas-atomised powders and melt-spun ribbons of Co- and Ni- base superalloys: influence on resulting microstructures*. Journal of Materials Science, 1982. **17**: p. 3641-3652.
20. C. Moreau, et al., *Temperature evolution of plasma-sprayed niobium particles impacting on a substrate*. Surface and Casting Technology, 1991. **46**: p. 173-187.

## Chapter 5

### Heat treatment of Al-12wt.%Sn-1wt.%Cu coatings

---

#### 5.1 Introduction

In general, bearing materials are used with microhardness in the range of 35-55 kgf/mm<sup>2</sup> in order to achieve the desired conformity and compatibility. In some special applications, microhardness values up to 60 kgf/mm<sup>2</sup> can be tolerated. The as-sprayed Al12Sn1Cu coatings exhibit high microhardness (from 65-80 kgfmm<sup>-2</sup> depending on spray conditions) due to the dispersion of the nanoscale Sn particles, dislocations, residual elastic stress and Sn / Cu in solid solution formed in the spray process. Therefore, heat treatment is used to lower the microhardness. In addition, heat treatment is used to reduce the chemical reactivity <sup>[1]</sup>. At the same time, heat treatment may cause some additional precipitation as well as undesirable reactions at the coating / substrate interface. Chapter 4 focused on the microstructure evolution of the gas atomised powder and the as-sprayed coating and the formation mechanism of those microstructures. In this chapter, the effect of heat treatment on the microstructure evolution of the coatings and their mechanical properties are investigated.

#### 5.2 XRD spectra of annealed coatings

Figure 5.1 show the XRD patterns from the HVOLF thermally sprayed Al12Sn1Cu coating in the as-sprayed condition and after heat treatment at 300°C for times of 15 minutes to 5 hours. There is no evidence for phases other than Al and Sn

in the spectra. Figure 5.2 shows XRD spectra of coatings annealed for 1 hour at different temperatures, i.e., 250, 300, 400 and 450°C. Again, there are no peaks showing the presence of additional phases. The small peaks present at  $2\theta$  angles of 28° and 47° come from the Si powder used as a reference standard.

### 5.3 The effect of heat treatment on the microhardness of the coatings

Figure 5.3 shows the microhardness variation of the as-sprayed coating measured using a 200 gf load with distance from the coating / substrate interface to the coating surface. Testing was performed at 6 points having different distances from the substrate / coating interface. The results show that the microhardness varies within the range 60 to 63 kgfmm<sup>-2</sup> throughout the coating. This means that the coating is relatively uniform in hardness throughout the thickness. This range of microhardness is a little higher than that required for a bearing application. Annealing is thus necessary to reduce the microhardness.

Figure 5.4 shows the variation in microhardness of the Al<sub>12</sub>Sn<sub>1</sub>Cu coatings with increasing annealing time at 300°C. The indent points were in the mid-plane of the coating and every coating had 15 indent points. Error bars show the calculated standard deviation values. The microhardness reduces greatly within the first hour of annealing at 300°C, but the rate of change then tends to slow down.

#### 5.3.1 Change in Sn particle size with heat treatment

##### SEM micrographs

Although high magnification SEM and TEM images allow investigation of the micron or sub-micron Sn and nanoscale Sn particles in the as-sprayed coatings, quantitative analysis of the Sn particle size evolution with annealing is an important topic. Thus, low magnification BSE images were selected to get statistical

information from the as-sprayed and annealed coatings. Figure 5.5 shows BSE images of the Al<sub>12</sub>Sn<sub>1</sub>Cu as-sprayed coating and coatings annealed at 300°C for 1 hour and 5 hours, respectively. The light regions within these images correspond to large Sn particles and the dark regions correspond to the Al-rich matrix, whilst the intermediate grey contrast regions are attributed to dispersions of nanoscale Sn within the coating, known from the results of Chapter 4. The Sn dispersions are so fine that individual Sn particles cannot be resolved in the BSE image at this magnification. It is apparent that the area fraction of grey contrast regions within these BSE images decreases as the annealing time increases. However, changes in the light contrast Sn regions due to the effect of annealing are less easy to distinguish. Accordingly, statistical analysis of these images was performed using the ImageJ software package to produce a quantitative analysis of the number of large Sn particles as a function of their projected area.

### **Quantitative analysis of large Sn particles**

Figure 5.6 illustrates the large Sn particle distribution within the as-sprayed coating and those annealed at 300°C for 1 hour and 5 hours, according to the BSE images of Figure 5.5. The analysis procedure was described in Chapter 3. The number of large Sn particles decreases with increasing particle area, and tends to zero for an area value of greater than  $1.0 \mu\text{m}^2$  (Figure 5.6a). The histogram of the number of large particles against projected area is shown for particle projected areas less than  $1.0 \mu\text{m}^2$  (Figure 5.6b). The results show that the number of Sn particles with areas between  $0.1 \sim 0.3 \mu\text{m}^2$  within the same volume decreases slightly after 1 hour of annealing at 300°C, as compared with the as-sprayed coating, but decreases significantly after 5 hours of annealing (arrowed A). For Sn particles of area between

0.3 ~ 0.45  $\mu\text{m}^2$ , there is little difference in the number of Sn particles within coatings annealed for 1 hour and 5 hours (arrowed B). For the Sn particles with area greater than ~ 0.45  $\mu\text{m}^2$ , the number of Sn particles slightly increases after 5 hours of annealing as compared with the 1 hour annealed coating (arrowed C). These results indicate that the sub-micron Sn particles tend to coarsen as the annealing time is increased.

### Associated TEM micrographs

The TEM images of Figure 5.7 are used to illustrate the development of the nanoscale Sn particles with increasing annealing time. These images, selected from a large number of micrographs, representatively show the as-sprayed coating and coatings annealed at 300°C for 1 hour and 5 hours, respectively. Images focus on illustrating the coarsening of the nanoscale Sn particles, i.e. regions of grey contrast in the BSE images of Figure 5.5. The nanoscale Sn particles in the as-sprayed coating (Figure 5.7 a) coarsen slightly after 1 hour annealing at 300°C (Figure 5.7 b), whilst these particles further coarsen after 5 hours of annealing (Figure 5.7 c). It is noted that many nanoscale Sn particles are no longer spherical with annealing, but become elongated and irregular in shape within the Al matrix due to the merging of two or more particles. The evidence reflects the different stages of these coalescing particles generated by the annealing process. However, no quantitative statistical work on has been done on these nanoscale particles in view of TEM images because the Sn particle distribution is not uniform throughout the whole coating (e.g. Figure 5.7). Therefore, there is some measure of caution here because the small number of high magnification TEM images may not reflect the real distribution of Sn particles.

### 5.3.2 Cu in the annealed coatings

#### EDX-TEM results

In addition to the coarsening of the Sn particles, the heat treatment at 300°C also induced the formation of rod-like precipitates within the 1 hour and 5 hour annealed coatings (Figure 5.7b,c, arrowed). TEM and EDX was used to analyse these fine scale particles in the Al12Sn1Cu coatings annealed at 300°C for 1 hour (Figure 5.8 and Figure 5.9) and 5 hours (Figure 5.10). The TEM image (Figure 5.8a) shows the dark round contrast and elongated particles for the coating annealed at 300°C for 1 hour. EDX analyse for the round particle (Figure 5.8b) and elongated particle (Figure 5.8c) arrowed b and c in Figure 5.8a both present strong Sn peaks in addition to Cu and Al peaks. This indicates that both particles were Sn-rich. The Cu peaks may be from the background scintillation from the supporting washer and the Al peaks will come from the matrix. Figure 5.8(d) represents the matrix region where only Al and Cu peaks show in the spectrum. Again Cu peaks are from background scintillation from the supporting washer because 1wt% of Cu in the Al12Sn1Cu alloy could not show such a strong intensity in the EDX signal. In the same sample, small grey contrast precipitates were also found within the Al matrix, with both elongated and spherical shape in the TEM images of Figure 5.9 (a,d). EDX spectra for the precipitates (Figure 5.9b,e) from the regions arrowed in Figure 5.9(a,d), respectively, show only Al and Cu peaks are present. No Sn particles were detected in this region. The small Fe peak in Figure 5.9 (b) may be an impurity from the substrate or may be tentatively attributed to background scintillation from the TEM rod. The EDX spectrum from the matrix region (Figure 5.9c) shows both Al and Cu peaks. So, part of the Cu peak may be from scintillation from the Cu washer supporting the sample. The high level of Cu signal from this small rod like features, however, suggests the

possibility of them being Al-Cu precipitates. The background scintillation of the TEM prohibits a definitive result. However, such Al-Cu features were also found in the coating annealed at 300°C for 5 hours (Figure 5.10a-c). The EDX spectrum of Figure 5.10(d) again indicates the presence of Al, and enhanced Cu at the precipitate. Such precipitates were also characterised using EELS and EFTEM, as follows.

### **EELS and EFTEM results**

The precipitates in the Al<sub>12</sub>Sn<sub>1</sub>Cu coating heat-treated at 300°C for 1 hour were analysed by energy filtered TEM (EFTEM) and electron energy loss spectroscopy (EELS) as shown in Figure 5.11. The EEL spectrum of Figure 5.11(a) indicates that there are two Cu energy peaks ( $L_3$  with energy 930eV and  $L_2$  with energy 951eV as arrowed) from the region of the precipitate. EFTEM maps for Sn, Cu and Al were acquired from this feature at energies of  $Sn_M$  (485eV),  $Cu_L$  (931eV) and  $Al_K$  (1560eV), respectively (Figure 5.11b-d). The maps delineate a precipitate of approximately 10 nm by 30 nm in size, rich in Cu and depleted in Al, whilst no Sn was found to be present. Slight distortion of the Al map has occurred due to sample drift during the long exposure time.

### **5.3.3 The orientation relationship between the Sn particles and the Al matrix for the coating annealed at 300°C for 1 hour**

An orientation relationship between some of the Sn particles and the Al matrix was found from an HRTEM investigation of the coating annealed at 300°C for 1 hour. The high-resolution images of Figure 5.12 show that the Sn (200) plane is parallel to the Al (111) plane. Although this particular Sn particle is in a strong diffraction projection [010], the surrounding aluminium matrix shows no strong crystallographic relationship with the Sn particle for other planes.

Figure 5.13 and Figure 5.14 are two Moiré images of Sn particles from a thick region of the TEM foil. The Moiré calculation results show that the aluminium (111) planes are parallel to the Sn (200) or Sn (110) planes. In this instance, the high-resolution image of Figure 5.12 suggests the most likely result to be  $(111)_{\text{Al}} // (200)_{\text{Sn}}$ .

Figure 5.15 illustrates another orientation relationship between the Al matrix and a Sn particle, i.e.  $(200)_{\text{Al}} // (200)_{\text{Sn}}$ . Figure 5.16 additionally shows an example of the aluminium (220) plane parallel to the Sn (411) or (420) plane, according to the Moiré calculation.

Figure 5.17 also shows the impression of a Sn particle within the Al matrix. Figure 5.17(a) shows a region of the Sn (200) plane parallel to the Al (200) plane, whilst in the Figure 5.17(c,d), atomic columns of aluminium are identified in the Sn particle region. It is possible that these images represent the shape of a Sn particle, the bulk of which had been lost from the TEM sample foil.

#### **5.4 The effect of heat treatment time and temperature on the coating / substrate interface**

The heat treatment not only brings about a microstructural change to the coating but also to the interface of the coating and substrate. The microstructure of the Al<sub>12</sub>Sn<sub>1</sub>Cu coating / mild steel substrate interface has therefore been investigated using BSE imaging and EDX analysis. Figure 5.18 represents the coating / substrate interface for the Al<sub>12</sub>Sn<sub>1</sub>Cu in the as-sprayed condition. The BSE image of Figure 5.18(a) shows the general irregular interface of the coating (upper part) / substrate (lower part). The interface reactant arrowed in the BSE image of Figure 5.18(b) shows that it contains iron oxide, according to the EDX spectrum and analysed data of Figure 5.18(c).



The interface of the Al<sub>12</sub>Sn<sub>1</sub>Cu coating /substrate annealed at 300°C for 1 hour does not show any significant changes (Figure 5.19). The EDX spectrum of Figure 5.19(c) similarly shows that the arrowed region in Figure 5.19(b) is composed of iron oxide.

The interface of the Al<sub>12</sub>Sn<sub>1</sub>Cu coating / substrate annealed at 300°C for 5 hours again did not show any great changes from the previous observations. Figure 5.20(a) is a BSE image. Again, the EDX spectrum of Figure 5.20(b) shows that the region arrowed in Figure 5.20(a) denoted (b) is iron oxide and iron. The region arrowed (c) in Figure 5.20(a) may be Al<sub>2</sub>O<sub>3</sub> grit from the grit blasting process used to roughen the substrate before spraying. Such features are also found at the coating interfaces of the coatings both as-sprayed and annealed at 300°C for 1 hour. At the coating / substrate interface of the sample annealed at 300°C for 5 hours, the iron oxide seems to have developed in some regions, as compared with the interface of the as-sprayed and annealed at 300°C for 1 hour samples (shown Figure 5.20d,e). The EDX spectrum and analysed data (Figure 5.20e) indicate that the iron oxide may be FeO.

The coating annealed at 450°C for 1 hour showed a significant reaction of the Al<sub>12</sub>Sn<sub>1</sub>Cu coating and the mild steel substrate (Figure 5.21 and Figure 5.22). Figure 5.21(a) is a low magnification BSE image showing the coating and substrate. In addition to the interface reaction, the coating exhibits many shrinkage cracks after annealing at 450°C for 1 hour (Figure 5.21a arrowed). The BSE images of Figure 5.21(b,d) illustrate the reaction product at the interface in more detail. The EDX spectrum and the analysed data (Figure 5.21c) of the arrowed region of image Figure 5.21(b) show that the product may be FeAl<sub>3</sub> according to the atomic ratio. The EDX spectrum of Figure 5.21(e) shows that the white region arrowed (e) in Figure 5.21(d)

is mainly pure Sn, whilst the EDX spectrum of Figure 5.21(f) of the region arrowed (f) in Figure 5.21(d) may be a mixture of Fe and FeO. Figure 5.22 is an additional feature identified at the coating /substrate interface of the sample annealed at 450°C for 1 hour. The spectrum of Figure 5.22(b) shows the black irregular block Figure 5.22(a) to be Al<sub>2</sub>O<sub>3</sub> grit, which comes from the grit blasting process. The extra Fe peaks are because of the electron probe interaction volume is larger than the grit particle. The EDX spectrum of Figure 5.22(c) shows that an arrowed region (c) in Figure 5.22(a) is mainly FeO.

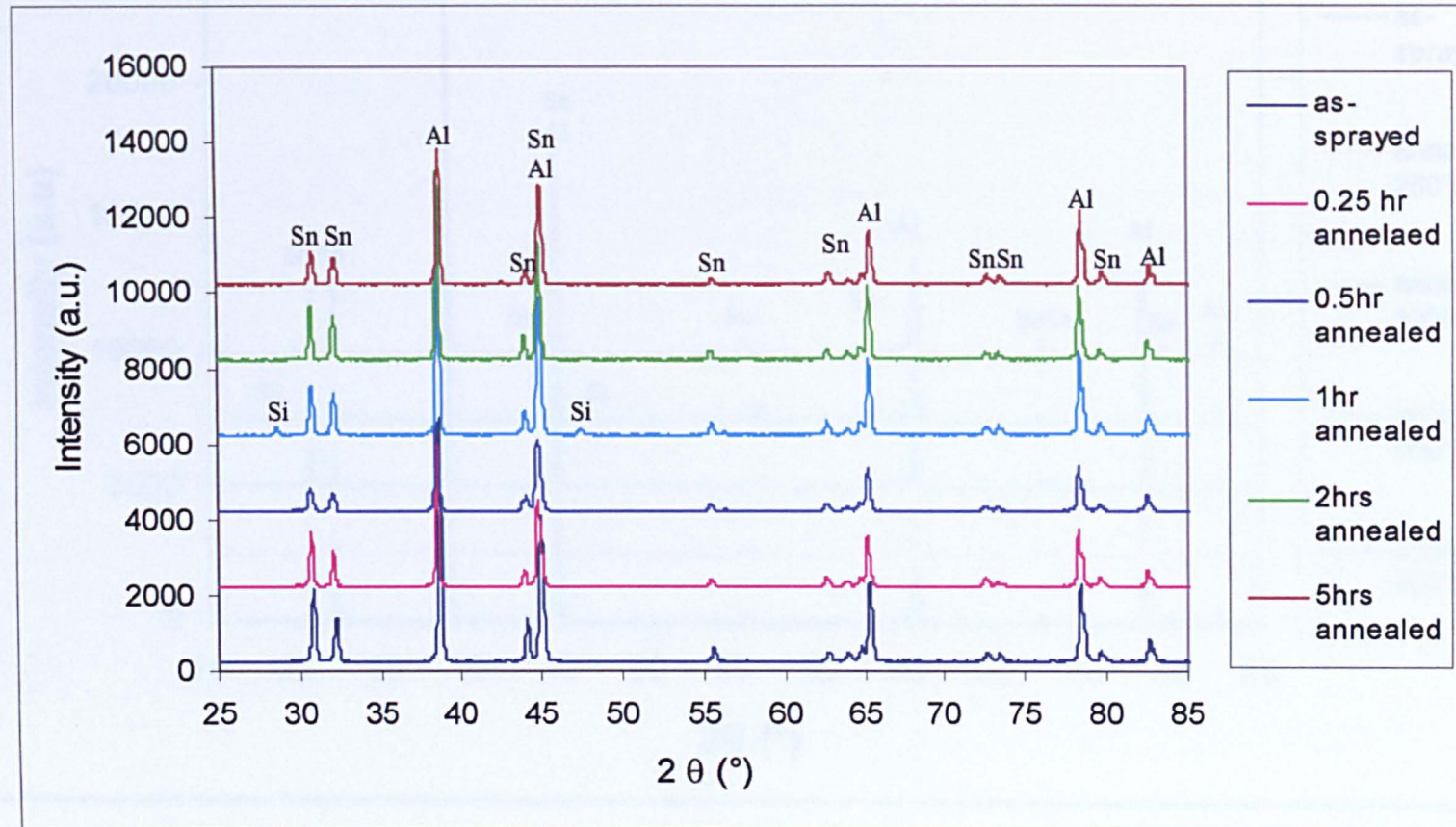


Figure 5.1 XRD spectra of the Al<sub>12</sub>Sn<sub>1</sub>Cu as-sprayed coating and following annealing for different times at 300°C

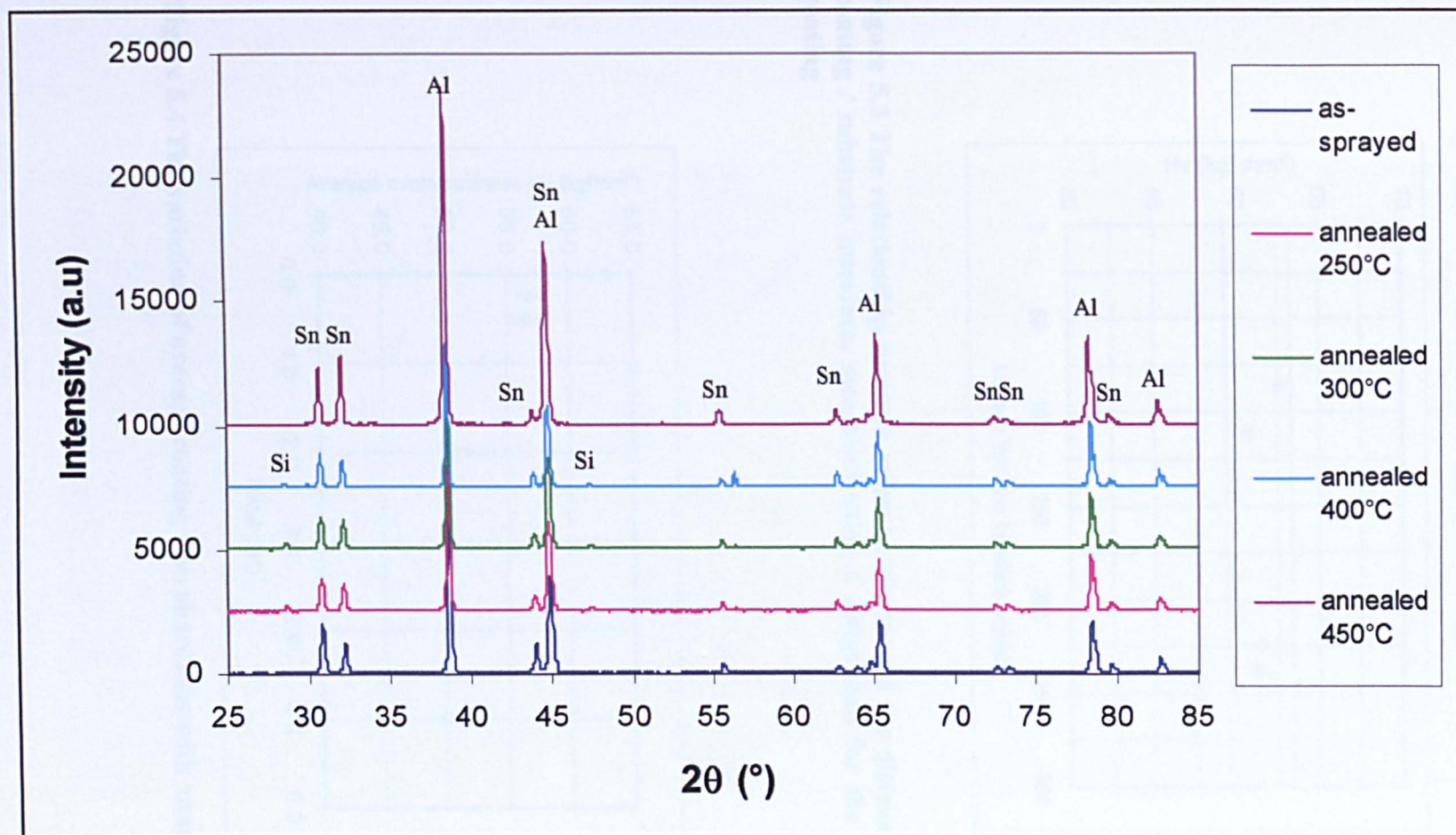
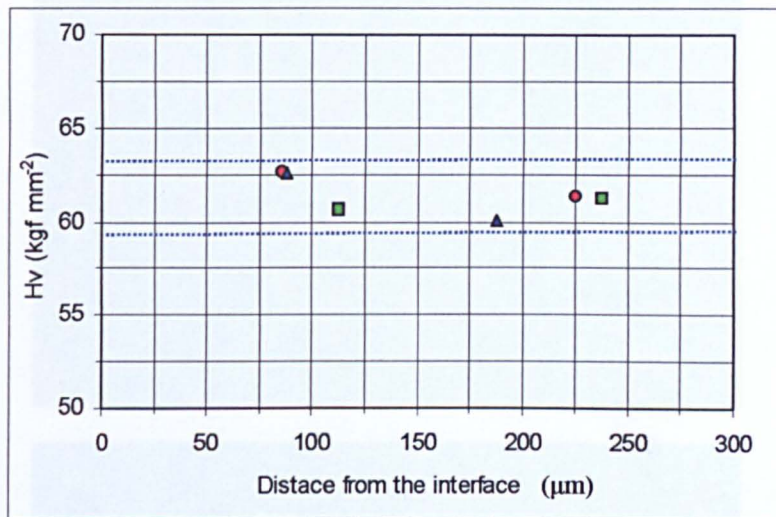
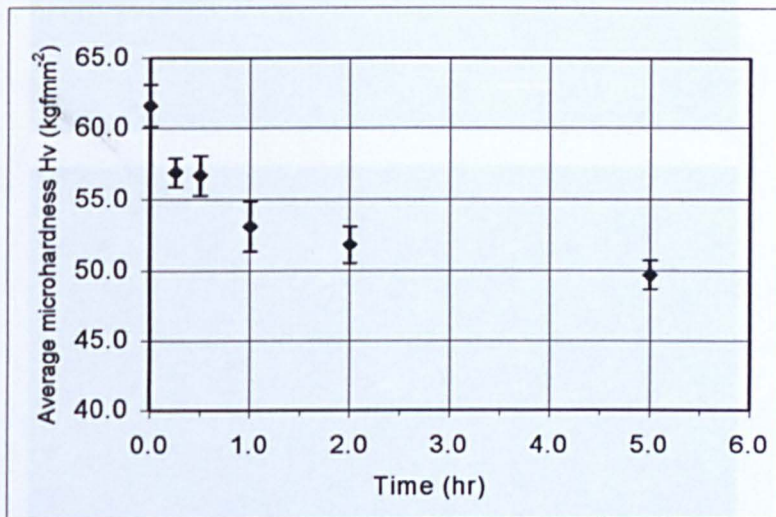


Figure 5.2 XRD spectra of the as-sprayed coating and following annealing for 1 hour at different temperatures





**Figure 5.3** The relationship between microhardness and the distance from the coating / substrate interface, measured using a 200gf load for the as-sprayed coating



**Figure 5.4** The variation of average coating microhardness with annealing time

Figure 5.5 BSE images of Al12Sn1Cu coatings: (a) As-sprayed; (b) annealed at 200°C for 1 hour; (c) annealed at 200°C for 5 hours.

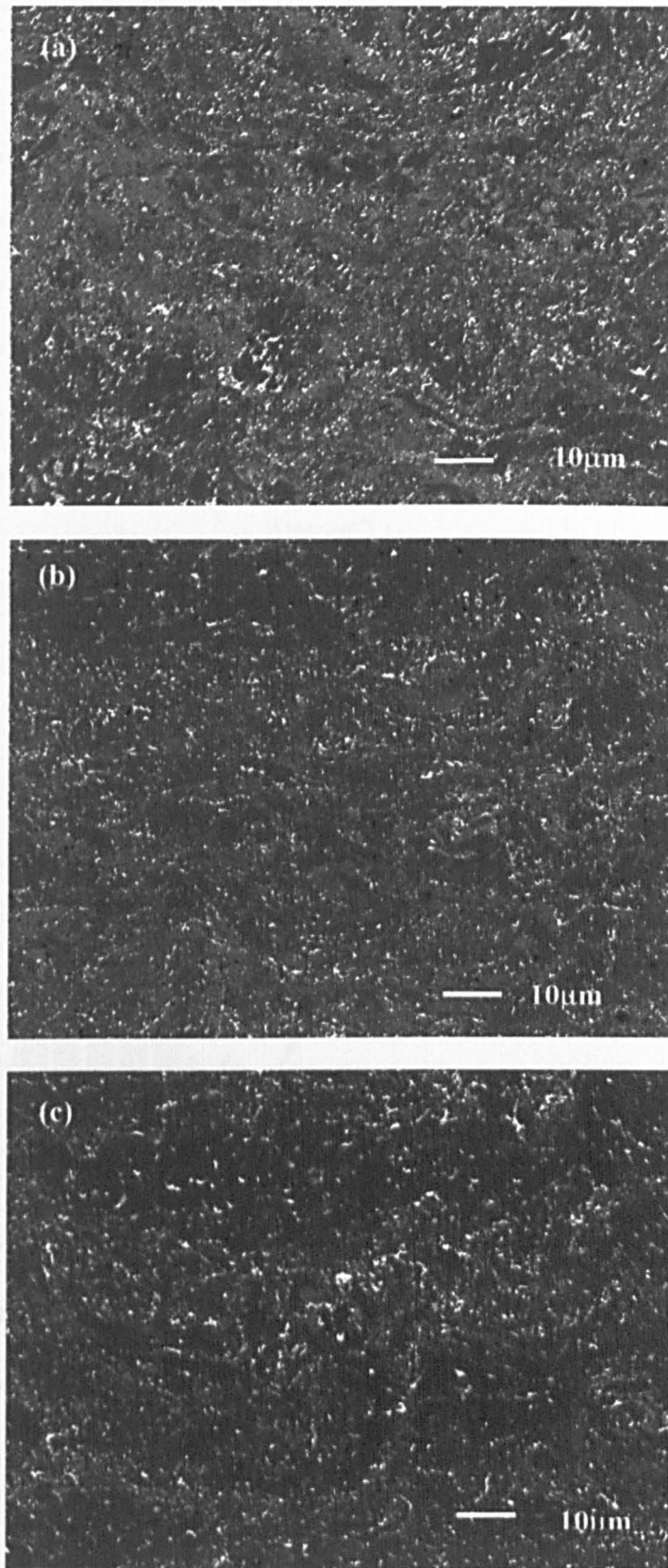


**Figure 5.5** BSE images of Al12Sn1Cu coatings: (a) As-sprayed; (b) annealed at 300°C for 1 hour; (c) annealed at 300°C for 5 hours.

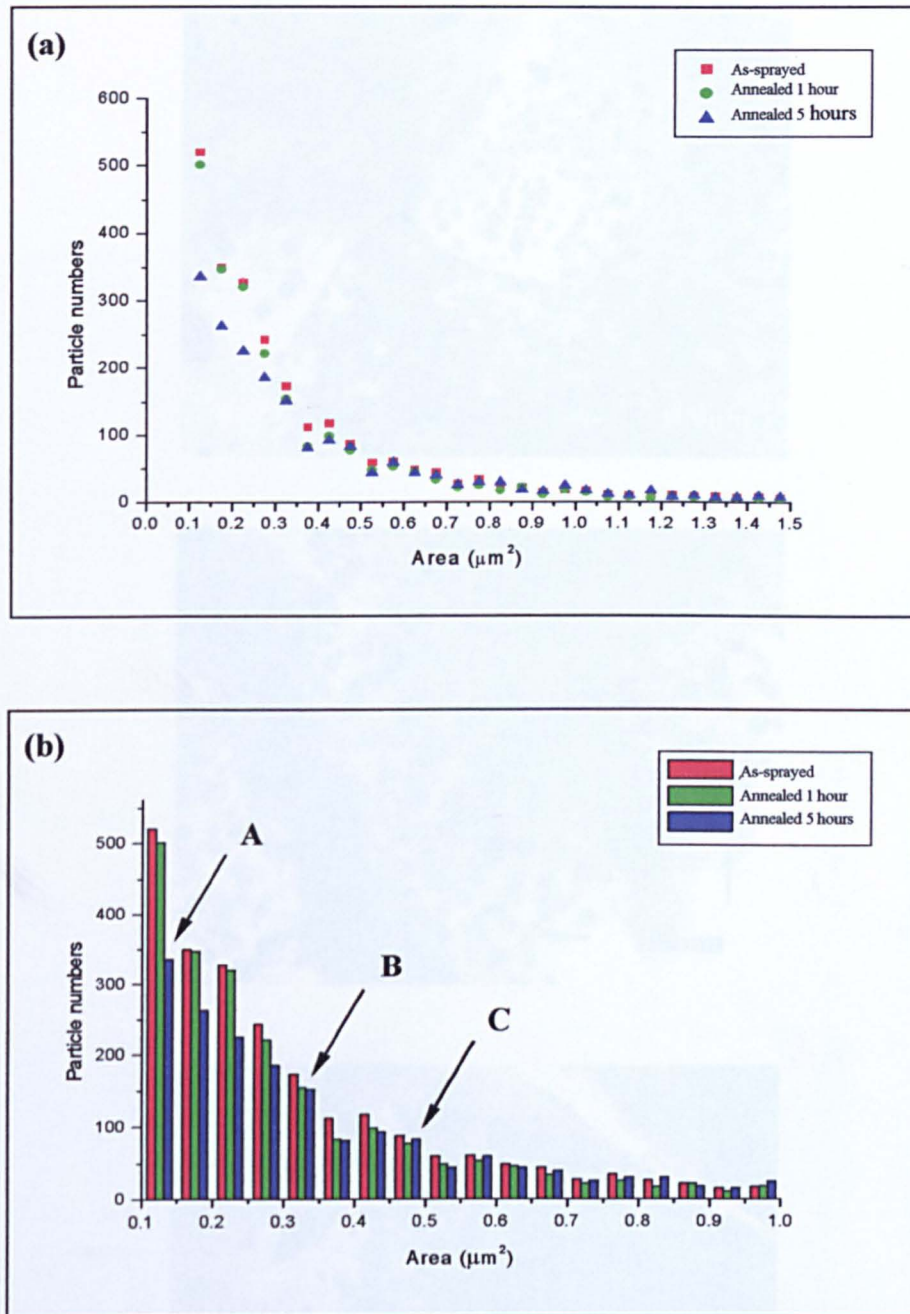


**Figure 5.6** The statistics of micron / sub-micron Sn particles. (a) Frequency histogram of Sn particle projected areas; (b) bar histogram of Sn particle projected areas (same data as (a), different format).

Figure 5.7 TEM images of Al12Sn1Cu coatings showing the fine scale Sn particle distribution: (a) As-sprayed; (b) Annealed at 300°C for 1 hour and (c) Annealed at 300°C for 5 hours.



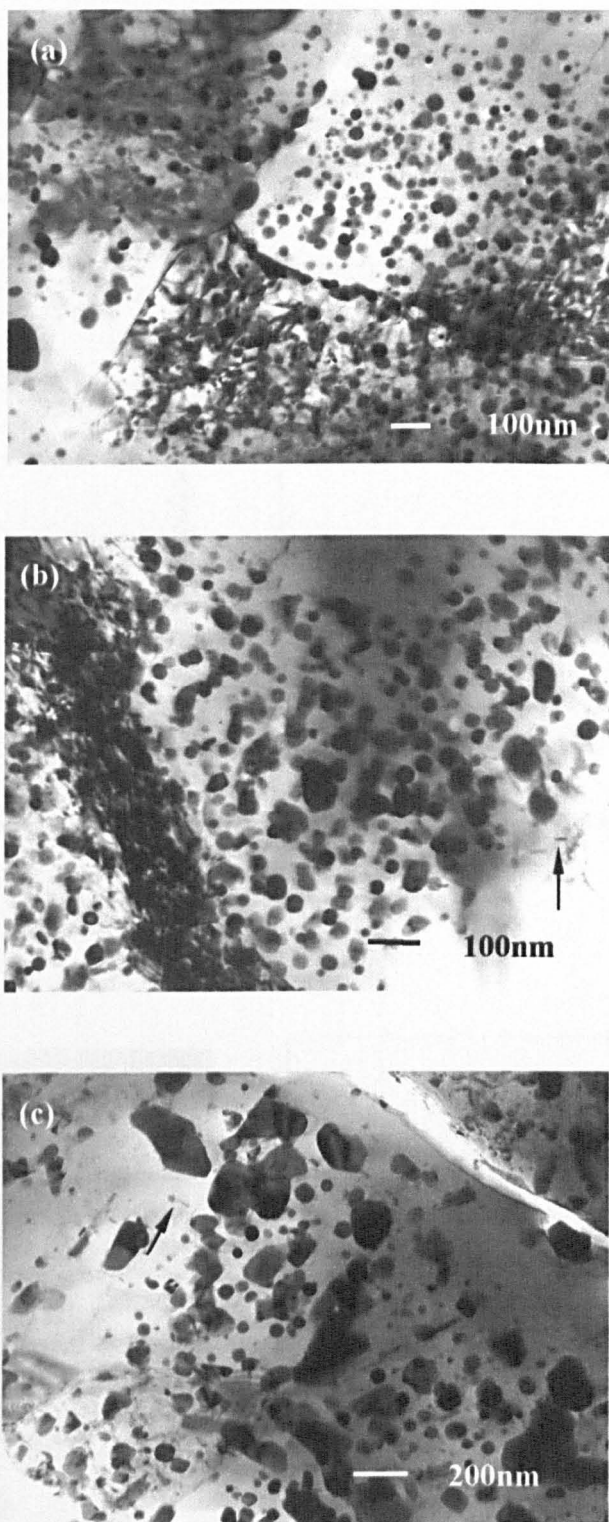


**Figure 5.7** TEM images of Al<sub>12</sub>Sn<sub>1</sub>Cu coatings showing the fine scale Sn particle distribution: (a) As-sprayed; (b) Annealed at 300°C for 1 hour and (c) Annealed at 300°C for 5 hours.



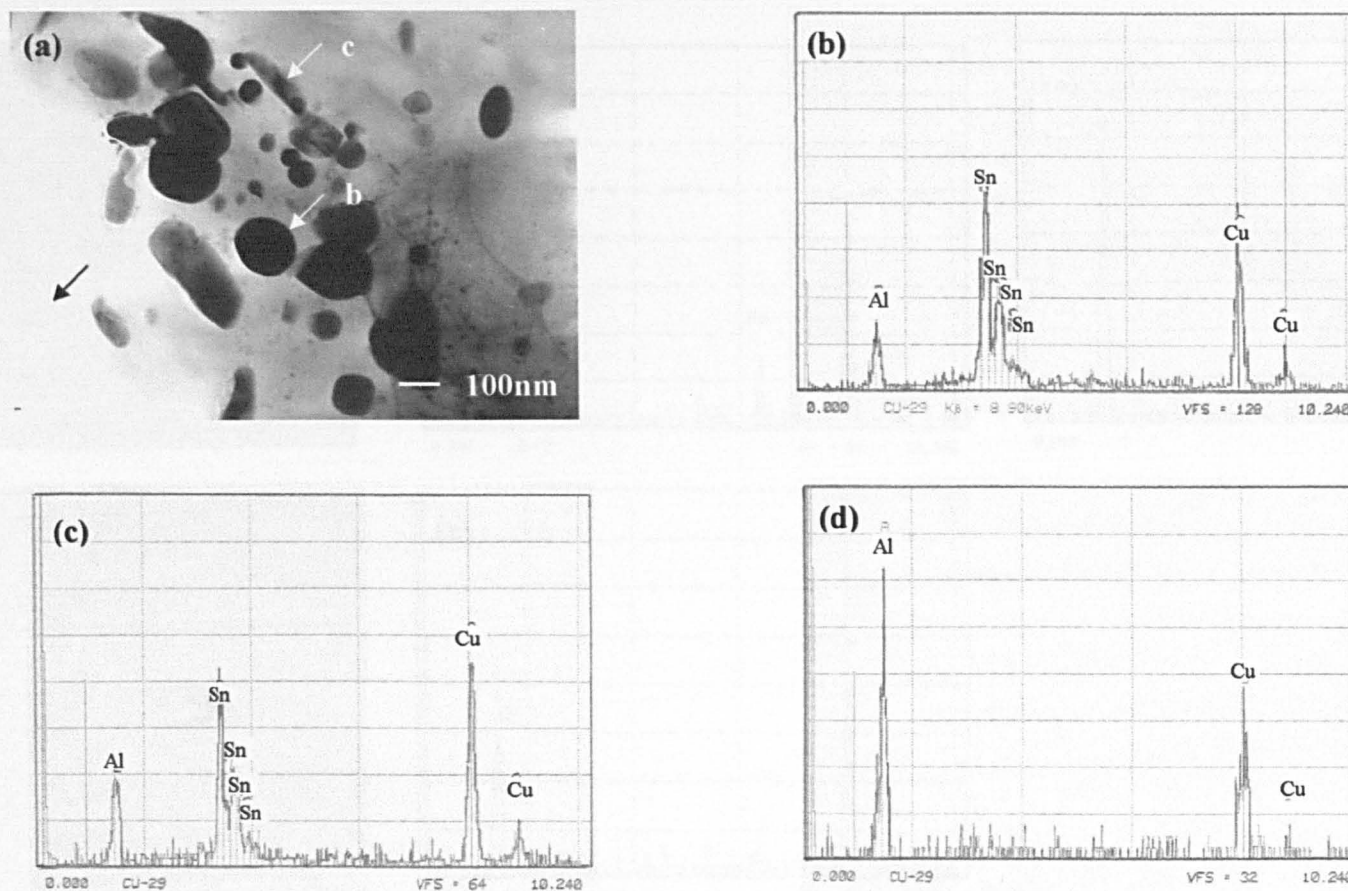


**Figure 5.8** TEM image and EDX spectra of the Al<sub>12</sub>Sn<sub>1</sub>Cu coating annealed at 300°C for 1 hour. (a) TEM image of Sn particles; (b) EDX spectrum of the arrowed round particle; (c) EDX spectrum of the arrowed elongated particle and (d) EDX spectrum of the arrowed matrix region.

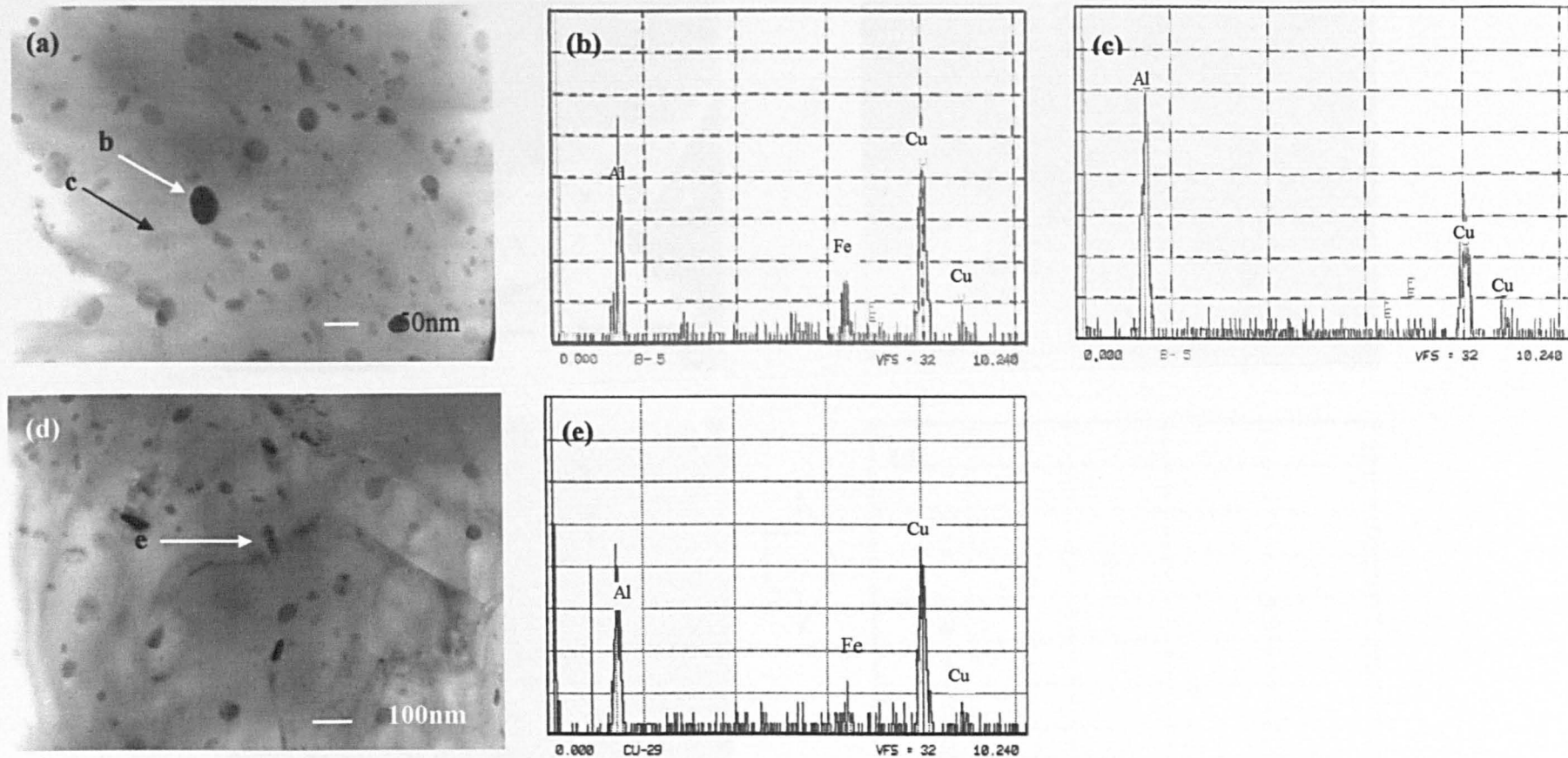


**Figure 5.9** TEM image and EDX spectra of the Al<sub>12</sub>Sn<sub>1</sub>Cu coating annealed at 300°C for 1 hour. (a,d) TEM micrographs of Cu-rich precipitates; (b,c) EDX spectra of the arrowed precipitate and matrix; (e) EDX spectrum of arrowed precipitate.

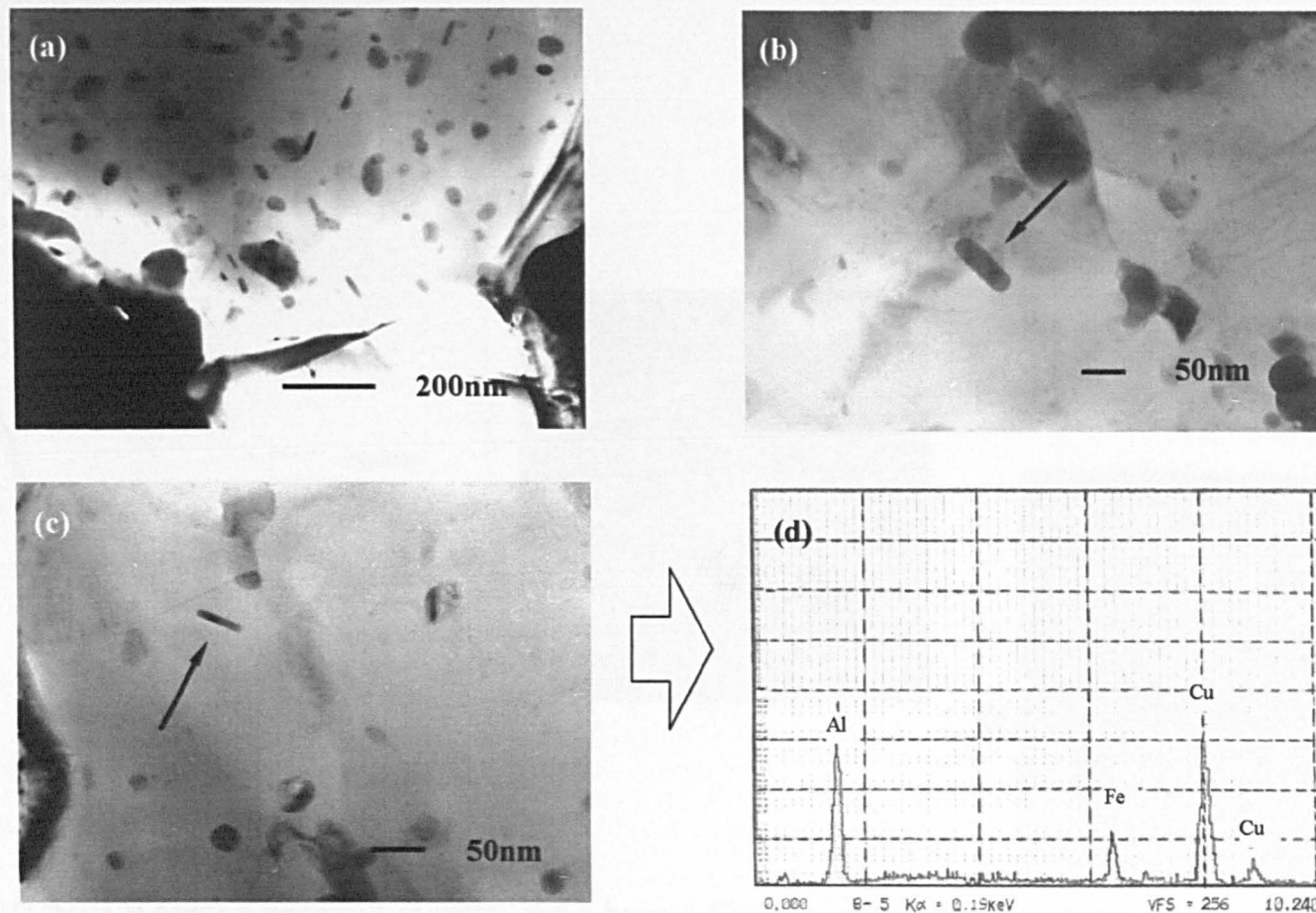


**Figure 5.10** TEM image and EDX spectrum of the Al<sub>12</sub>SnCu coating annealed at 300°C for 5 hours. (a-c) TEM images of Cu-rich precipitation; (d) EDX spectrum of region arrowed in (c).

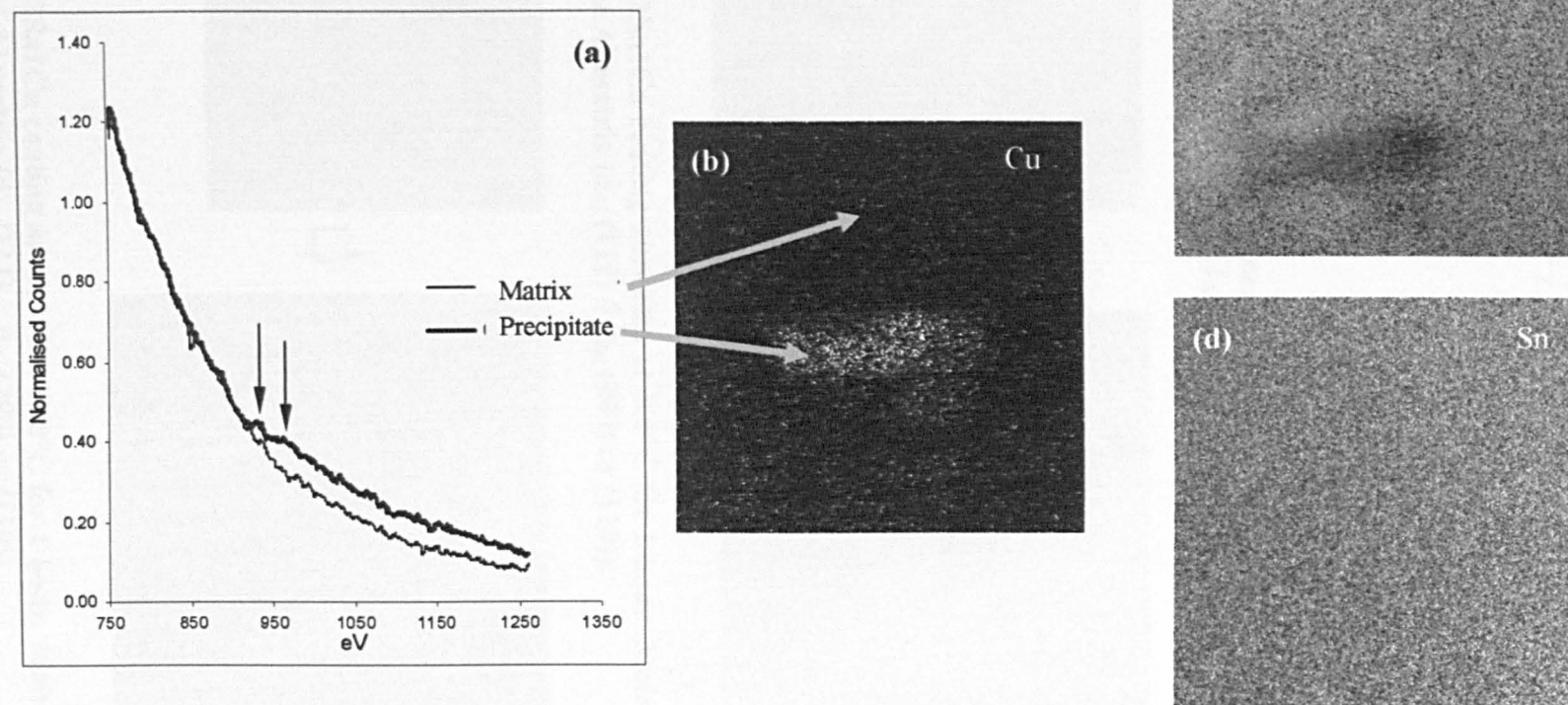


**Figure 5.11** The Al<sub>12</sub>Sn<sub>1</sub>Cu coating annealed at 300°C for 1 hour. EFTEM and EELS results from an elongated precipitate. (a) EEL spectrum of the matrix and the precipitate; (b-d) EFTEM maps of the Cu, Al and Sn distribution, respectively. (Data acquired by Dr MikeFay)



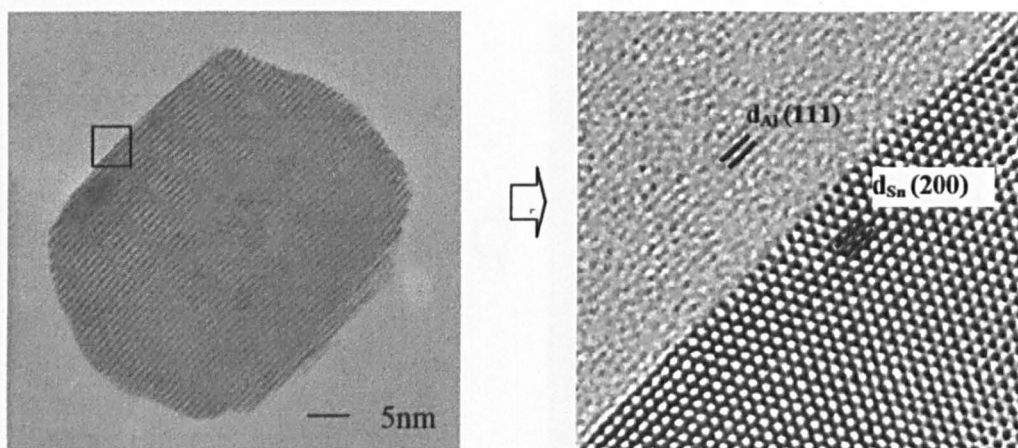


**Figure 5.12** The Al<sub>12</sub>Sn<sub>1</sub>Cu coating annealed at 300°C for 1 hour. HRTEM of a Sn particle embedded in the Al matrix ( $d_{Al}(111) // d_{Sn}(200)$ ).

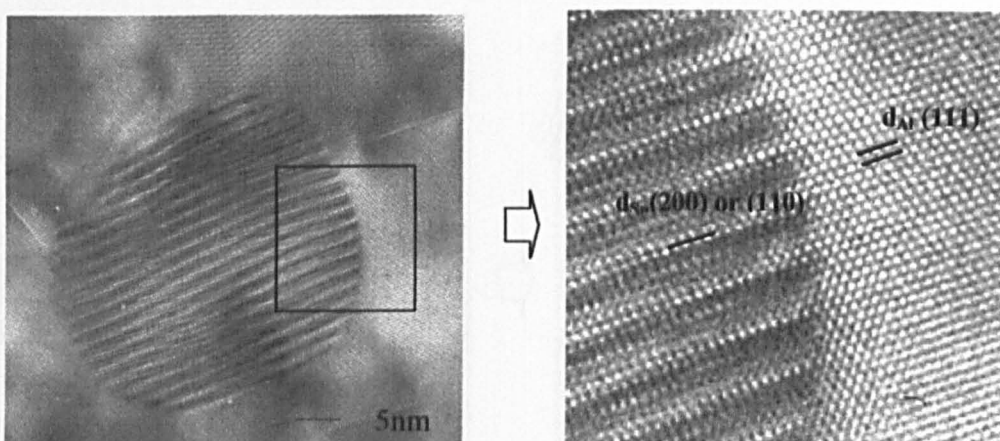


**Figure 5.13** The Al<sub>12</sub>Sn<sub>1</sub>Cu coating annealed at 300°C for 1 hour. Moiré fringes of a Sn particle in the Al matrix ( $d_{Al}(111) // d_{Sn}(200) \text{ or } (110)$ ).

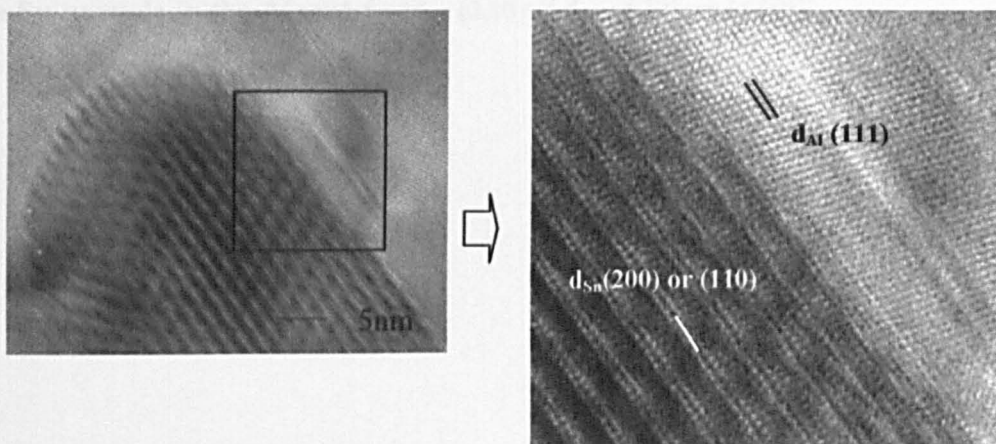


**Figure 5.14** The Al<sub>12</sub>Sn<sub>1</sub>Cu coating annealed at 300°C for 1 hour. Moiré fringes of a Sn particle in the Al matrix ( $d_{Al}(111) // d_{Sn}(200) \text{ or } (110)$ ).

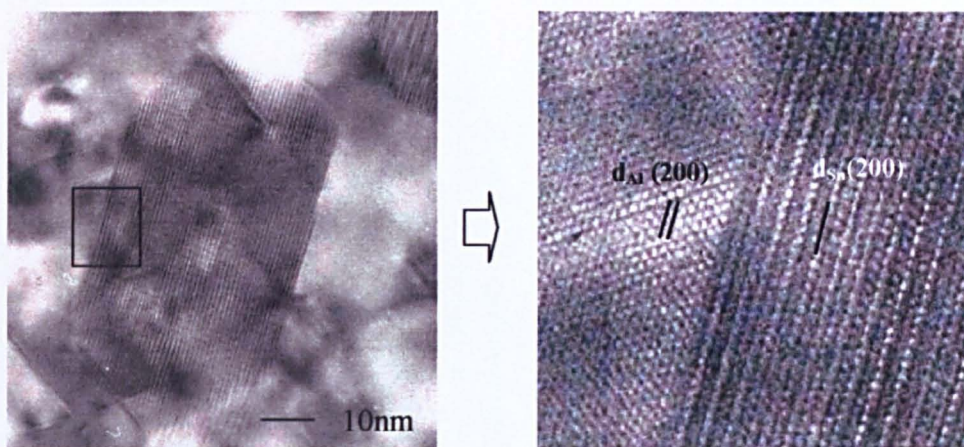


**Figure 5.15** The Al<sub>12</sub>Sn<sub>1</sub>Cu coating annealed at 300°C for 1 hour. Moiré fringes of a Sn particle in the Al matrix ( $d_{\text{Al}}(200) \parallel d_{\text{Sn}}(200)$ ).

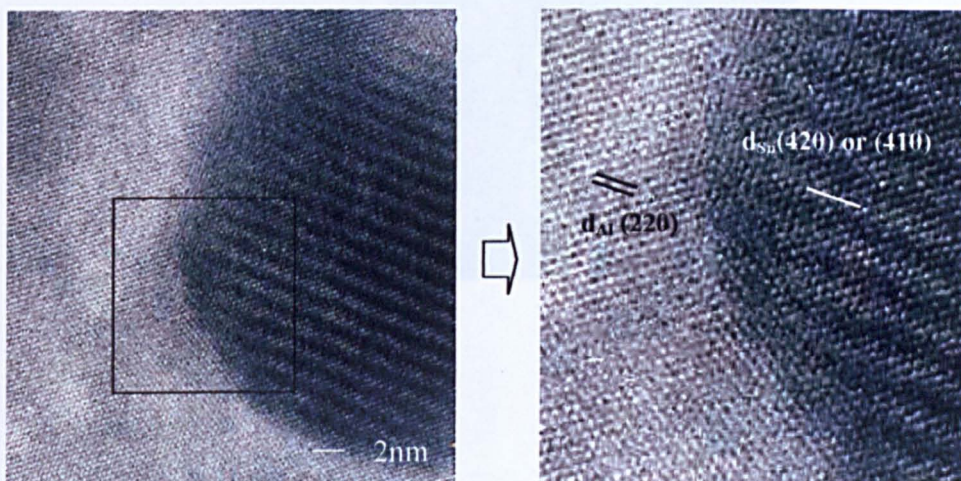


**Figure 5.16** The Al<sub>12</sub>Sn<sub>1</sub>Cu coating annealed at 300°C for 1 hour. Moiré fringes of a Sn particle in the Al matrix ( $d_{\text{Al}}(220) \parallel d_{\text{Sn}}(420) \text{ or } (410)$ ).

Figure 5.17 Al<sub>12</sub>Sn<sub>1</sub>Cu coating heat treated at 300°C for 1 hour. HRTEM image of Sn particle shape in the Al matrix. (a)  $d_{\text{Al}}(200) \parallel d_{\text{Sn}}(200)$ ; (b) an impression of a Sn particle in Al matrix; (c, d) showing only Al atom distances.

(Figures 5.15-5.17 recorded by Dr. Paul D. Brown using Jeol 400EX at the Department of Materials Science and Metallurgy, University of Cambridge. With thanks to Professor Colin Humphreys)



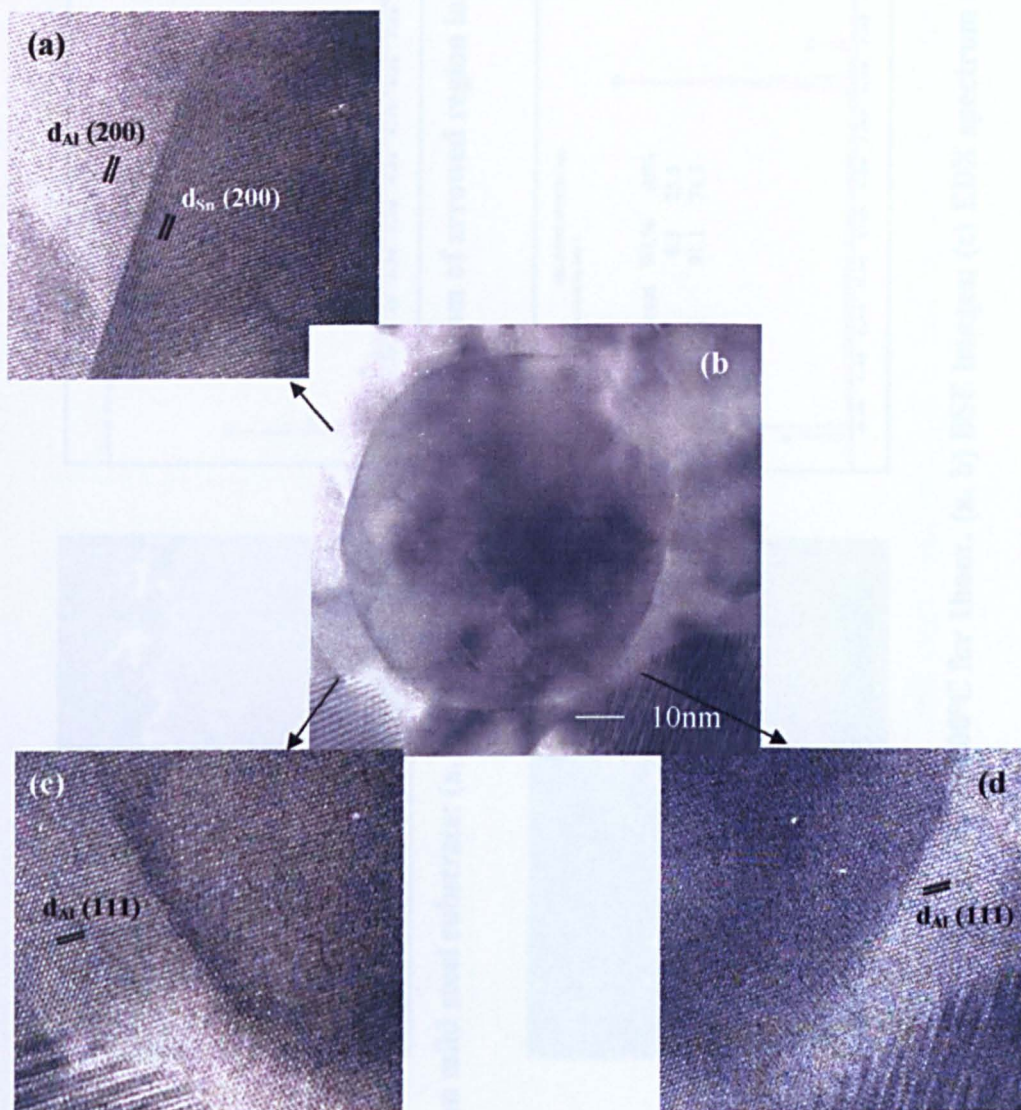


**Figure 5.17** AlSnCu coating heat treated at 300°C for 1 hour. HRTEM image of Sn particle shape in the Al matrix. (a)  $d_{Al} (200) \parallel d_{Sn} (200)$ ; (b) an impression of a Sn particle in Al matrix; (c, d) showing only Al atom distances.

(Figures 5.12-5.17 recorded by Dr. Paul D. Brown using Jeol 400EX at the Department of Materials Science and Metallurgy, University of Cambridge. With thanks to Professor Colin Humphreys)



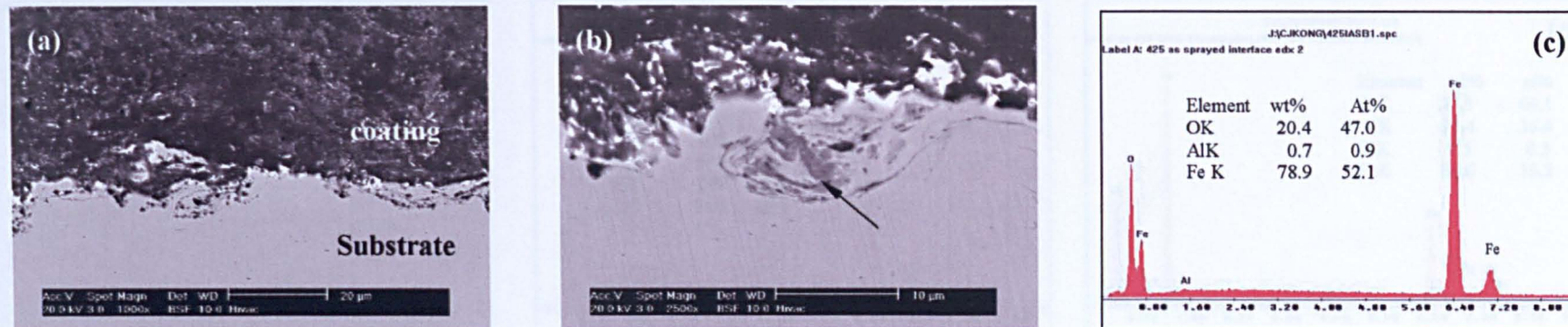


Figure 5.18 Al12Sn1Cu as sprayed coating on mild steel substrate: (a, b) BSE images; (c) EDX spectrum of arrowed region in (b).

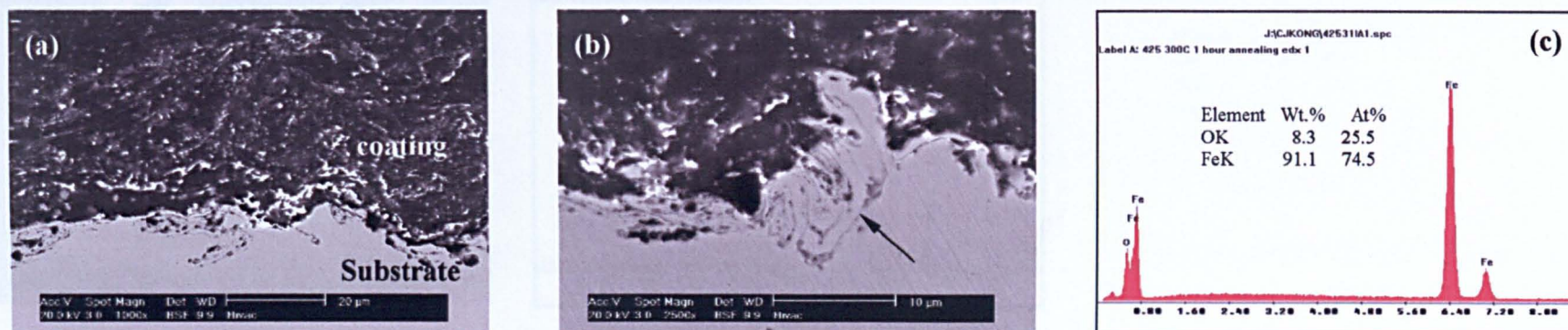


Figure 5.19 Al12Sn1Cu coating on a mild steel substrate annealed at 300°C for 1 hour. (a, b) BSE images; (c) EDX spectrum of arrowed region in (b).



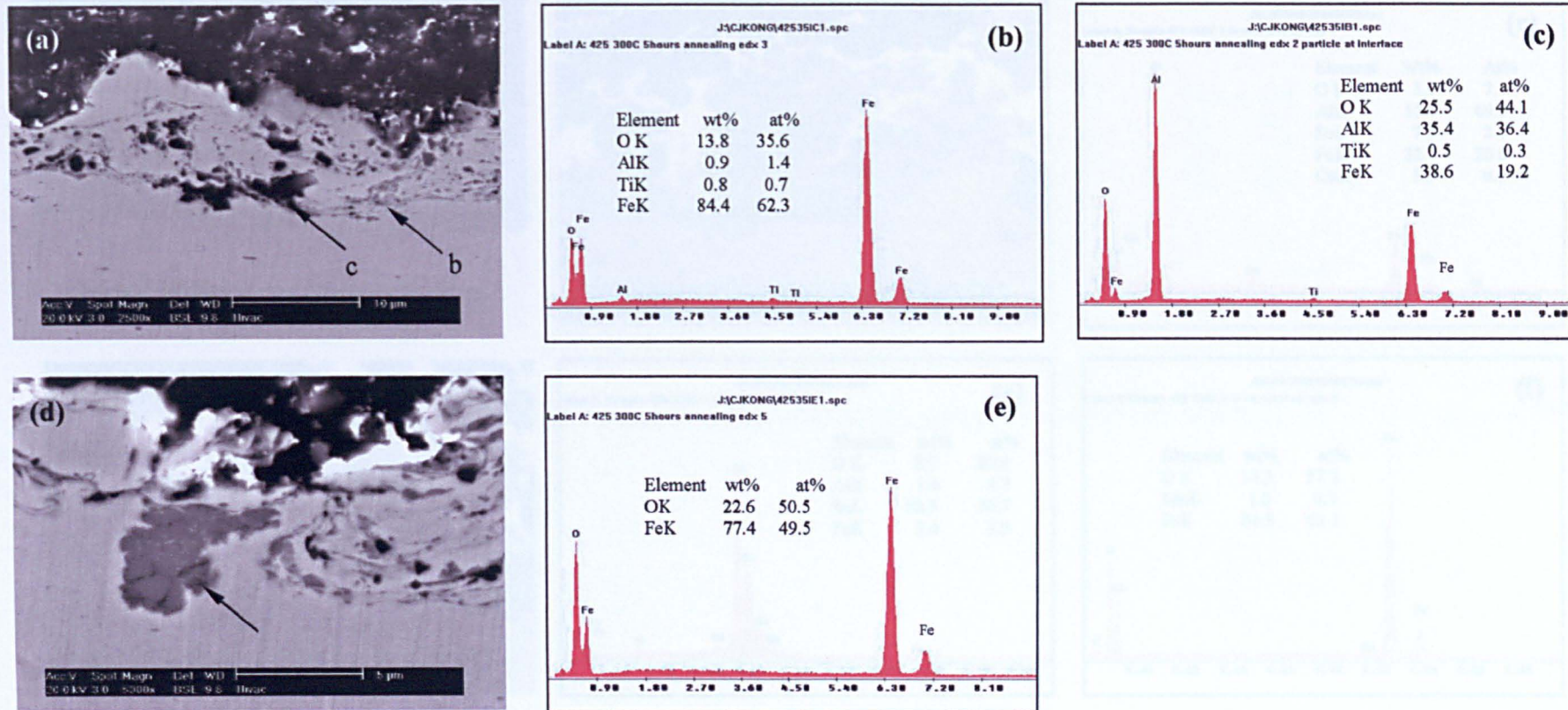


Figure 5.20 Al12Sn1Cu coating annealed at 300°C for 5 hours on a mild steel substrate: (a, e) BSE images; (b, c) EDX spectra of arrowed regions in (a); (e) EDX spectrum of arrowed region in (d).

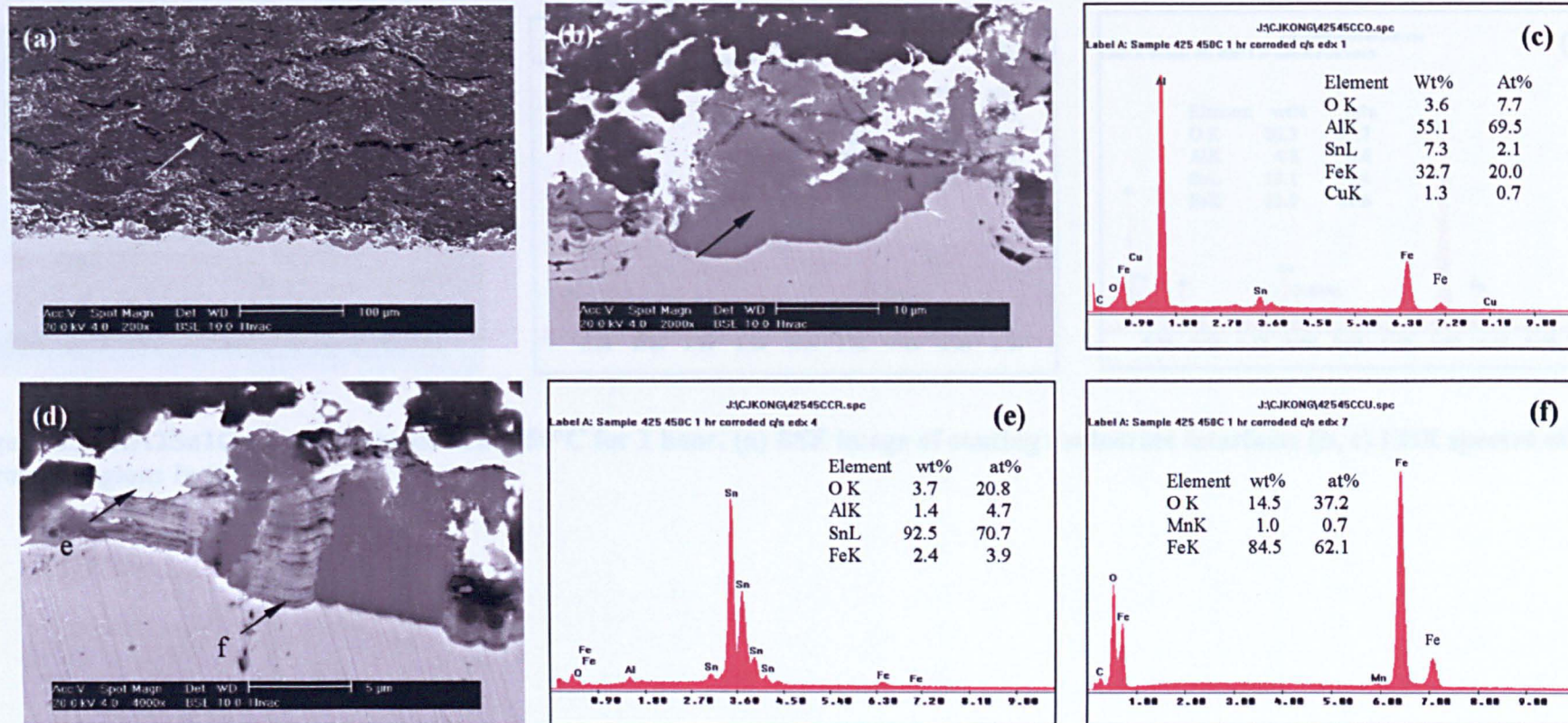
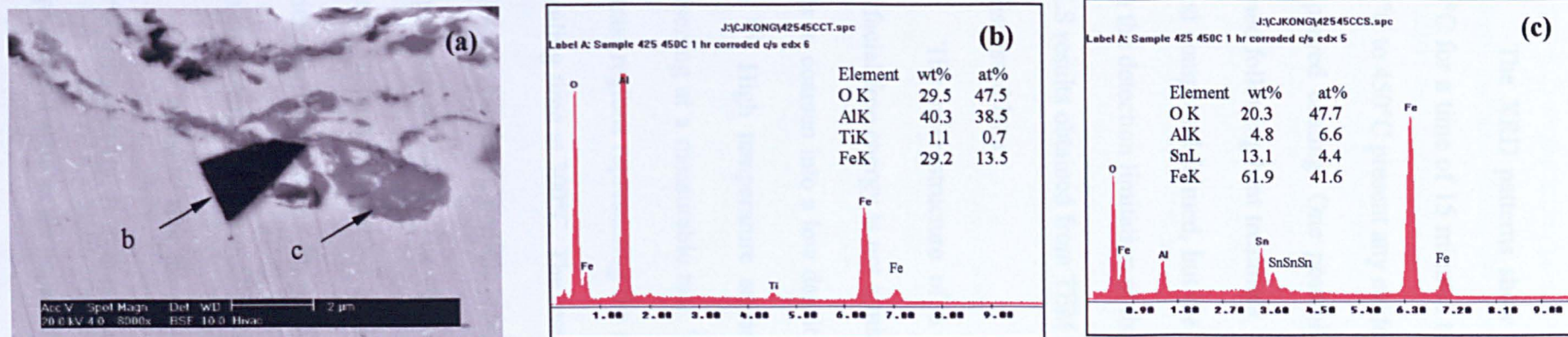


Figure 5.21 Al<sub>12</sub>Sn<sub>1</sub>Cu coating annealed at 450°C for 1 hour on a mild steel substrate. (a, b and d) BSE images showing the interface and interface reactant; (c) EDX spectrum of the arrowed region in (b); (e, f) EDX spectra of the arrowed regions in (d).





**Figure 5.22** Al12Sn1Cu coating annealed at 450°C for 1 hour. (a) BSE image of coating / substrate interface; (b, c) EDX spectra of arrowed regions in (a)

## 5.5 Discussion

The XRD patterns show that neither the Al12Sn1Cu coatings annealed at 300°C for a time of 15 minutes to 5 hours nor the coatings annealed at 1 hour from 250°C to 450°C present any evidence of Cu-based precipitates, as compared with the as-sprayed coating. One possibility is that there is no Cu containing compound formed following heat treatment. The other possibility is that there may be some Cu-based compound formed, but the volume fraction of the Cu-based precipitate is less than the detection limitation of the instrument which is ~ 2wt.%. However, EDX and EELS results obtained from TEM show evidence for an Al-Cu compound which will be discussed later.

The microstructure of a two-phase alloy is always unstable if the total interfacial free energy is not a minimum. Therefore, a high density of a small phase tends to coarsen into a low density of larger particles with a smaller total interfacial area [2]. High temperature annealing provides a kinetic opportunity for particle coarsening at a measurable rate. The BSE images of Figure 5.5 show that the grey contrast regions representing the nanoscale Sn distribution decrease with increasing annealing time at 300°C. The result is confirmed by the TEM images of Figure 5.7, i.e. the nanoscale Sn particle size increases with increasing heat treatment time at a temperature of 300°C. The statistical analysis Figure 5.6 also shows that the sub-micron Sn particles coarsen to form larger scale Sn particles. Thus, nanoscale Sn particles and sub-micron Sn particles all agglomerate to become larger Sn particles with an increase in the annealing time.

It is noted [3] that the melting point of pure Sn and Al is about 232°C and 660°C, respectively. It is thus expected that sub-micron and nanoscale Sn particles adopt a liquid state in the solid Al matrix during annealing at 300°C. More than two

spherical Sn particles merging to form a larger irregular shaped of Sn particle (Figure 5.7) in the annealed coating indicates that the liquid Sn droplets move as a coherent particle within the solid phase. A possible mechanism of liquid droplet migration and coarsening in the solid matrix has been introduced in Chapter 2. This indicates that in the presence of a local temperature gradient, movement of the liquid phase in the solid matrix may occur<sup>[4]</sup>. The Al<sub>12</sub>Sn<sub>1</sub>Cu coatings annealed at 300°C may develop many local thermal gradients within the coatings. Liquid droplets of Sn dissolve solid Al at the hot end each particle and condense Al at the trailing, cold end. This mechanism provides the basis for liquid droplet migration up a temperature gradient in the solid matrix. When two or more liquid Sn droplets approach, they will start to merge to form a larger Sn particle. The TEM images of Figure 5.7(b,c) illustrate the different periods of migration of the liquid Sn droplets, frozen following annealing, where the coarsening particles adopt irregular or elongated shapes depending on the length of annealing time. The longer the time of annealing, the coarser the Sn droplets formed. Thus, the coatings annealed at 300°C for 5 hours exhibit coarser Sn particles in size, as compared with the coatings annealed for 1 hour and those as-sprayed. In order to reduce the surface energy, Sn droplets tend to change from an elongated shape to spherical to reduce the surface area, given sufficient time at a high enough temperature, assuming the coarsening particle stays within the Al grain. If the coarsening Sn particles are located at the Al grain boundaries, their shape will be restrained by the grain boundaries.

The lack of evidence for Cu compounds existing within the Al<sub>12</sub>Sn<sub>1</sub>Cu as-sprayed coating may indicate that the Cu remains in solid solution within the Al matrix following rapid solidification, associated with the HVOLF thermal spray process. The EDX results from the Al<sub>12</sub>Sn<sub>1</sub>Cu coatings annealed at 300°C for 1

hour (Figure 5.8 and Figure 5.9) and 5 hours (Figure 5.10) do indicate the presence of Al-Cu precipitates, whilst the EEL spectra and EFTEM elemental maps from the coating annealed at 300°C for 1 hour confirm this result. According to Figure 2.18, the precipitates arising from 1wt% Cu within an Al matrix may be the  $\theta'$  phase if an Al-Cu alloy is annealed. The same result might be expected following annealing of Al12Sn1Cu.

The microhardness of the as-sprayed coating is relatively uniform throughout the coating. The main reason for the microhardness decreasing with increasing time of annealing is attributed to the coarsening of the sub-micron and nanoscale Sn particles (Figure 5.5 to Figure 5.10). The other possible reason causing the microhardness decrease is that annealing may release local strain in the form of dislocations stored in the as sprayed coatings. That is, annealing acts to decrease the resistance to dislocation movement. The precipitation of  $\theta'$  might be expected to slightly increase the microhardness of the annealed coatings by dispersion strengthening. However, the microhardness clearly decreases with increasing annealing time at 300°C. This means the volume fraction of  $\theta'$  is not high enough to significantly affect the microhardness, as compared with the effect of coarsening Sn. Loss of Sn and Cu from the Al solid solution during annealing also decreases the microhardness.

Two main orientation relationships for the Sn particles in the Al matrix were obtained for coatings annealed at 300°C for 1 hour (Figure 5.12, Figure 5.15 and Figure 5.17) with  $(111)_{\text{Al}} // (200)_{\text{Sn}}$ , and  $(200)_{\text{Al}} // (200)_{\text{Sn}}$ . These two orientation relationships were similar to those identified within melt spun AlSn alloys <sup>[5, 6]</sup> and ion implantation Sn in an Al matrix <sup>[6]</sup>, i.e. from  $\{111\}_{\text{Al}} // \{100\}_{\text{Sn}}$  with  $\langle \bar{2}11 \rangle_{\text{Al}} // \langle 011 \rangle_{\text{Sn}}$ ; and  $\{100\}_{\text{Al}} // \{100\}_{\text{Sn}}$  with  $\langle 011 \rangle_{\text{Al}} // \langle 011 \rangle_{\text{Sn}}$ . However, there was no

clear evidence of such a strong projection alignment of Sn within these HVOLF Al alloy coatings. Indeed, the Sn particle in Figure 5.12 shows a strong diffraction projection of [110], whilst the surrounding Al matrix shows no other crystallographic relationship except for alignment of the (111) plane. Further,  $d_{\text{Sn}}$  particle values calculated from the moiré fringes indicate some extent of partial alignment with the Al matrix for the strong [110] diffraction projection. An additional relationship (Figure 5.16) was also identified from moiré fringes, i.e.,  $(220)_{\text{Al}} // (420)_{\text{Sn}}$  or  $(410)_{\text{Sn}}$ . Thus, it is concluded that there is a loose orientational relationship of some of the Sn particles in the Al matrix of the annealed HVOLF samples. The alignments are less pronounced than those found for other formation processes, such as melt spinning <sup>[5]</sup> and ion implantation <sup>[6]</sup>, due to the very rapid cooling rate associated with the HVOLF process. Nevertheless, the partial alignments are associated with a reduction of the local energy and strain release with annealing, as expected.

The coating / substrate interface plays a very important role in defining the performance of the bearings. Results from Figure 5.18 to Figure 5.20 show that the Al<sub>12</sub>Sn<sub>1</sub>Cu coatings annealed at 300°C for 1 hour and 5 hours do not exhibit significant changes of the interface microstructure, with just the identification of some interface reactant, FeO. It is likely that such interface reactants are formed during the spraying process, during the impingement of high temperature melted powder particles on the steel substrate. A relatively large-scale region of FeO was only occasionally found in the coating annealed at 300°C for 5 hours (Figure 5.20d) which tentatively suggests that long time annealing at 300°C may slightly increase the amount of FeO present.

However, the Al<sub>12</sub>Sn<sub>1</sub>Cu coating heat treated at 450°C for 1 hour formed additional interfacial reaction products (Figure 5.21b,d). Interlayer cracks appeared



(Figure 5.21a arrowed) in this annealed coating with the migration of some Sn to the coating / substrate interface. It is possible that the migration of the Sn phase to the surface and the coating / substrate interface during 450°C high temperature annealing leaves voids between the splats. Two kinds of interfacial reaction products were formed, i.e. FeO (e.g. (f) in Figure 5.21d) and FeAl<sub>3</sub> (arrowed in Figure 5.21b), with the annealing temperature of 450°C for 1 hour. Furthermore, Sn was observed to agglomerate at the interface (Figure 5.21e) because a long time of annealing allows molten Sn to flow to the interface. The molten Sn might play a role to promote the formation of FeAl<sub>3</sub> by dissolving Al and Fe. This creates an opportunity chance for Al to react reacting with Fe.

The identification of angular Al<sub>2</sub>O<sub>3</sub> in the steel, at the interface (Figure 5.18 dark contrast region) and within subsequently annealed samples at 300°C (Figure 5.20(a), arrowed c) and 450°C (Figure 5.22(a), arrowed b) is attributed to residual grit from the process of grit blasting prior to coating deposition.

The above evidence shows that an annealing temperature of 300°C for the Al12Sn1Cu coatings is better than that of 450°C because of the formation of the brittle phases of FeAl<sub>3</sub> which may degrade the interface properties of the coatings, especially the interface bonding strength. The technique of the grit blasting needs to be improved to avoid remnant the Al<sub>2</sub>O<sub>3</sub> grit embedded in the mild steel substrates.

## 5.6 Summary

The microhardness of Al12Sn1Cu HVOLF sprayed coatings decreases with increasing annealing time at 300°C. Coarsening of nanoscale and sub-micron Sn particles is an important factor alone with elimination of residual stress and dislocation. Although annealing also causes the additional precipitation of Al-Cu

compounds, presumed to be  $\theta'$ , this has negligible effect in hardness due to the small volume fraction of  $\theta'$  precipitation and weak the dispersion strengthening effect.

Two main Al/Sn orientation relationships were identified in the Al12Sn1Cu coatings annealed at 300°C for 1 hour. The orientation relationships are  $(111)_{\text{Al}} // (200)_{\text{Sn}}$  and  $(200)_{\text{Al}} // (200)_{\text{Sn}}$ . An additional relationship was found from the analysis of moiré fringes, i.e.  $(220)_{\text{Al}} // (420)_{\text{Sn}}$  or  $(410)_{\text{Sn}}$ . This partial alignment of Sn particles in Al the matrix is consistent with the release of some strain during annealing.

A heat treatment temperature of 300°C is a suitable annealing condition for Al12Sn1Cu coatings used for bearing, as compared with 450°C. The latter temperature induces the formation of many interface reaction products, which will degrade the interface and hence bearing properties.

## References

1. A. J. Horlock, *HVOF Spraying of Novel Bearing Materials*, in *School of Mechanical, Materials, Manufacturing Engineering and Management*. 1999, University of Nottingham (PhD thesis): Nottingham.
2. D. A. Porter and K. E. Easterling, *Phase Transformation in Materials and Alloys*. 1983: Van Nostrand Reinhold (UK) Co. Ltd.
3. The ASM Committee, *Metallography, structures and phase diagram, 8th edition*. Metal Handbook. 1973. 8: p. 263, American Society for Metal.
4. M. McLean and M.S. Loveday, *In-situ observations of the annealing of liquid lead inclusions entrained in an aluminium matrix*. Journal of Materials Sciences, 1974. 9: p. 1104-1114.
5. W. T. Kim and B. Cantor, *Solidification of tin droplets embedded in an aluminium matrix*. Journal of Materials Science, 1991. 26: p. 2868-2878.
6. E. Johnson, C. R. H. Bahl, V. S. Touboltsev and A. Johansen. *Nanoscale Sn inclusion in Al-structure and melting-solidification properties*. in *Materials Research Symposium Proceedings*. 2000: p. 177-182, Materials Research Society.

## Chapter 6

# The relationship of corrosion resistance to the microstructure

---

### 6.1 Introduction

Corrosion of the AlSnCu bearing alloy is not generally a problem for the traditional cast and roll bonded materials. However, it was found that HVOGF as-sprayed Al12wt.%Sn coatings reacted very easily with water and the anodic polarisation curve in 1wt.% NaCl solution could not be measured <sup>[1]</sup>. The addition of 1wt.%Cu was found to increase the corrosion resistance as indicated by the ability to measure the complete anodic polarization curve <sup>[1]</sup>. Anodic polarization curves were obtained for the HVOLF as-sprayed and annealed coatings. The experimental procedure to obtain the anodic polarization curves is described in Chapter 3. The surface morphology and the cross-section of the corroded coatings were characterised using high resolution SEM and EDX analysis. The results are combined with the microstructural understanding of the Al12Sn1Cu coatings (Chapters 4 and Chapter 5) to suggest a corrosion mechanism of the coatings.

### 6.2 Polarization curves of the Al12Sn1Cu thermally sprayed coatings

Anodic polarization curves for the Al12Sn1Cu as-sprayed and annealed coatings are shown in Figure 6.1. In the as-sprayed condition, the current density in the anodic

part of the plot is seen to rise quickly after  $E_{\text{corr}}$  (-1300mV vs SCE) and the coating rapidly corroded. The  $E_{\text{corr}}$  of the coating was raised by 50mV after annealing at 300°C for 1 hour, but thereafter the current density again increased rapidly and the coating remained active. The major influence of heat treatment on the corrosion behavior arose when the annealing temperature was raised to 450°C. The coating  $E_{\text{corr}}$  was increased by 110mV and a region of passivation in the potential range -1150 and -930mV resulted. At -1100mV the current density decreased by three orders of magnitude from 10 to  $10^{-2}$  mAcm $^{-2}$ . Eventually, the passivation begins to break down and the coatings become pitted as the potential is increased above an  $E_{\text{pit}}$  value of approximately -920mV.

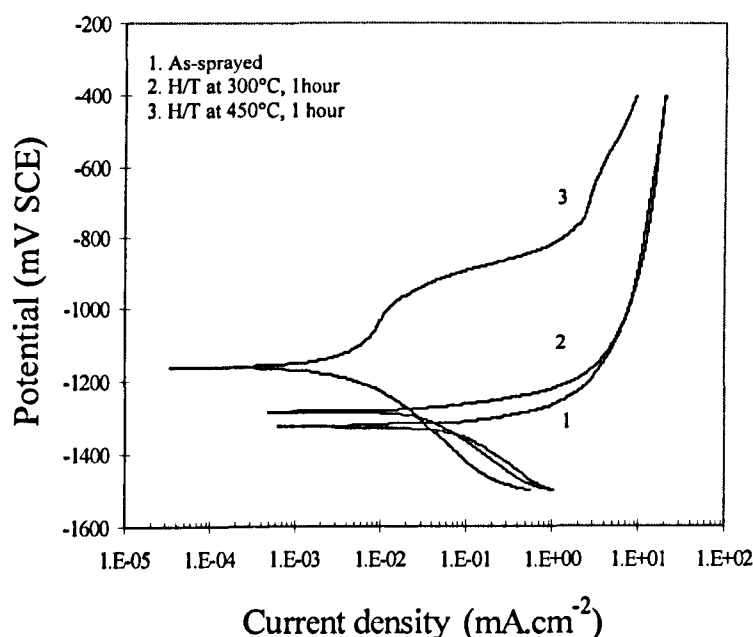


**Figure 6.1** The anodic polarization curves of Al12Sn1Cu as-sprayed and annealed coatings <sup>[2]</sup>

### 6.3 SEM analysis of the corroded as-sprayed and annealed coatings

The corroded coatings were examined using SEM to reveal the surface morphology and the cross-sectional microstructure. In order to maintain the original

surface morphology, the Wet Mode of the XL30 ESEM-FEG was used to observe the surface of the corroded samples using SE imaging, because the samples were encased in non-conducting resin for the purpose of the corrosion test. Then, the corroded coatings were removed from the non-conducting resin and cut in cross-section to re-mount in conducting resin for further observation. BSE imaging and EDX analysis were used to examine the samples.

### **6.3.1 The corroded as-sprayed coatings**

#### **Surface observation**

Figure 6.2 shows the corroded surface morphology of the Al12Sn1Cu as-sprayed coating. The field of view is limited by the aperture size in this low magnification SEM image (Figure 6.2a). Many observations at higher magnification show that most of the surface is covered by interlaced cracks (Figure 6.2b). Corroded pits (Figure 6.2c) and extended cracks (Figure 6.2d) were confined only to some regions of the sample. Some regions also displayed the traces of grinding scratches produced by sample preparation prior to the corrosion tests. The higher magnification SEM image of Figure 6.3(a) suggests that the cracks are relatively deep (arrowed). Semi-quantitative EDX data are noted within each EDX spectrum for comparison because the intensity is arbitrary. EDX analysis (Figure 6.3b) of this entire region showed the presence of strong Al, Sn and O peaks and weak Cu, Na and Cl peaks. Semi-quantitative data (Figure 6.3b) also shows a significant proportion of oxygen which indicates oxide formation in such regions. The SE image of Figure 6.3(c) illustrates a surface with visible grinding scratches. The EDX spectrum and related quantitative analysis (Figure 6.3d) show that there is lower oxygen and Sn content, and more Al associated within this region as compared with the more

strongly corroded region of Figure 6.3(a). The Na and Cl peaks are still found in the region with grinding mark.

### **Cross-section observation**

Figure 6.4 shows BSE images and EDX analysis of the cross-section of the corroded as-sprayed coating. The low magnification image of Figure 6.4(a) suggests that the corroded region extends about 50-100  $\mu\text{m}$  below the coating surface. This means the surface of the as-sprayed coatings has been attacked by solution and reaction products and cracks propagating into the coating have formed due to the action of the corroding medium. Figure 6.4(b) shows the detail of one attacked region. Cracks are evident in the coating. The corroded depth of this region is much deeper compared with other places. The SE image (Figure 6.4c) of the same region suggests the reaction product may be insulating because of some localised charging effects. EDX analysis of the arrowed region (Figure 6.4b) shows strong peaks of C, O and Al, and weak peaks of Cu and Sn. The carbon possibly comes from the grinding and polishing process that might cause conducting resin to fill the cracks and holes of the corroded coating. The high oxygen content suggests the reaction product is some kind of metal oxide. The suggestion is this product might be aluminium oxide according to the elemental ratio from the EDX data and the charging effect in the SE image of Figure 6.4(c). Figure 6.5 shows details of the middle region and the bottom region of the corrosion zone in Figure 6.4(b,d), at higher magnification. Cracks (Figure 6.5a,b) seem to have formed in the heavily corroded region where the oxygen content is very high according to the EDX analysis and the crack directions seem random. The images of Figure 6.5(c,d) show the interfacial zone between the corroded region and the original as-sprayed coating. Reaction appears to



have occurred around the Sn concentrated regions leaving many small holes. Figure 6.6(a,b) indicates that cracking (dark contrast lines) happens preferentially at the interlamellar regions of the thermal splats. A very important observation is that the unmelted regions in splats appear to be attacked less by the solution (Figure 6.6a, arrowed and 6.10b, arrowed A). This demonstrates that the melted and unmelted regions of the coating respond in different ways to the process of corrosion. Further, a reaction product is identified at the surface of the as-sprayed coating (Figure 6.6b, arrowed B). The EDX analysis (Figure 6.6c) shows the presence of a large amount of oxygen and chlorine in addition to Al and C. The C signal is probably from the electron beam interaction with the mounting resin. The Cl may be remnant of the sodium chloride.

### **6.3.2 The corroded coatings annealed at 300°C for 1 hour**

#### **Surface observation**

The corrosion test experiments were also performed on the Al<sub>12</sub>Sn<sub>1</sub>Cu thermal sprayed coatings after heat-treatment at 300°C for 1 hour. The corroded surface shows a similar roughness as compared with the as-sprayed coating in the low magnification SE image (Figure 6.7a). The higher magnification images of Figure 6.7(b,c) again show the interlocking of cracks and grinding scratches. This is similar to that observed in the corroded as-sprayed coating (Figure 6.2b). The associated EDX spectrum and analysis of Figure 6.7(d) shows high contents of O, Al and Sn. Again, Cu and Cl elements are also found in this region.

#### **Cross-section observation**

The thermal sprayed Al<sub>12</sub>Sn<sub>1</sub>Cu coatings annealed at 300°C for 1 hour adopt a similar cross-sectional morphology to the as-sprayed coatings after corrosion testing

(Figure 6.8a). The corroded layer is about 50  $\mu\text{m}$  in depth in this instance. The high magnification image of Figure 6.8(b) shows that the melted regions, i.e. the Sn particle distributed regions, have been easily corroded. The un-melted regions are less easily attacked (Figure 6.8b, arrowed). The backscattered image of Figure 6.8(c) shows dark contrast in the vicinity of a corroded region. The associated EDX analysis (Figure 6.8d) indicates a high content of oxygen in this area, in addition to Al, Sn, Cu, C and Cl. The elemental ratio in the EDX data again suggests it might be aluminium oxide. The peak of C is again attributed to contamination from the grinding and polishing process, whilst the Cl peak comes from the penetration and reaction of the sodium chloride solution. Since the C is probably from the sample grinding and polishing process, it wasn't included in the semi-quantitative calculation.

### **6.3.3 The corroded coatings annealed at 450°C for 1 hour**

#### **Surface observation**

The corroded surface morphology of the coating annealed at 450°C for 1 hour (Figure 6.9) is quite different as compared with the as-sprayed and the 300°C, 1 hour annealed coatings. Less roughness is apparent in the same low magnification image (Figure 6.9a) as compared with the other two coatings. The remnant grinding scratches are very clear in the higher magnification images (Figure 6.9b-d). Bright particles appear to delineate the boundaries of the thermally sprayed splats. Occasionally, corroded pits were found, randomly distributed across the surface (Figure 6.9c). Figure 6.10 analyses a region with bright and dark contrast. The EDX analysis of a bright particle region (Figure 6.10b, arrowed B) shows a moderate amount of oxygen in this region, in addition to Sn and Al. The content of Sn here is very high 34.8wt%, as compared with

the nominal Sn content of 12wt%. This suggests the white particles are Sn particles or tin oxide. However, the detection of Al in this region suggests that the incident electron beam penetrates the small particles on the surface causing the generation of X-ray signals from the matrix underneath. In this context, the oxide here may be aluminium oxide, because Al is more susceptible to oxidation as compared with Sn. The EDX analysis (Figure 6.10c) of the darker region (arrowed C in Figure 6.10a) shows a similar weight percent of oxygen content as the bright region (Figure 6.10b), in addition to high Al and low Sn contents. This suggests the dark region is predominantly matrix Al and aluminium oxide. The oxygen content is much lower as compared with that detected in the surface of the corroded coatings, as-sprayed and annealed at 300°C for 1 hour (Figure 6.7d). A corrosion pit is shown in Figure 6.11(a,b) at low and high magnification, respectively. The associated EDX analysis of the grey contrast region (arrowed C in Figure 6.11b) suggests that again, the predominant composition is matrix Al and aluminium oxide, i.e. there is a high content of Al, O and a low content of Sn. EDX analysis (Figure 6.11d) of the bright particles (arrowed D in Figure 6.11b) shows the main element content is again Al and Sn, O and Cu. The weight percent of Sn is slightly high as compared with the analysis shown in Figure 6.10(b). The same reason could be used to explain the presence of Al and O peaks in this analysis as for Figure 6.10(b). This again emphasizes that the bright particles are predominantly Sn. The high magnification image (Figure 6.11b) also shows that the surrounding Al has been corroded leaving Sn phase (arrowed D) on the pitting corrosion point.

### **Cross-section observation**

A cross-section of the thermal sprayed Al12Sn1Cu coating annealed at 450°C for 1 hour is shown in Figure 6.12. A large number of cracks have formed within the coating, after annealing at this temperature (Figure 6.12a, circled). The surface of the coating also shows some pitting (Figure 6.12a, arrowed) after the potential dynamic test. However, no corroded dark contrast reactant could be observed from this magnification of the surface layer. The high magnification image of Figure 6.12(b) shows bright contrast (Sn) and grey contrast (Al matrix). The associated EDX analysis (Figure 6.12c) shows the grey contrast region (Figure 6.12b, arrowed C) mainly comprises Al and Cu, whilst no Sn signal was detected. This suggests the region is the Al-rich matrix. Conversely, associated EDX analysis of the bright contrast region (Figure 6.12b, arrowed D) indicates a large amount of Sn. In addition, Al peaks also could be observed since the probe of the electron beam is larger than the feature size. Oxygen was also found in this EDX analysis, which again indicates a reactant of aluminium oxide or tin oxide in this region.

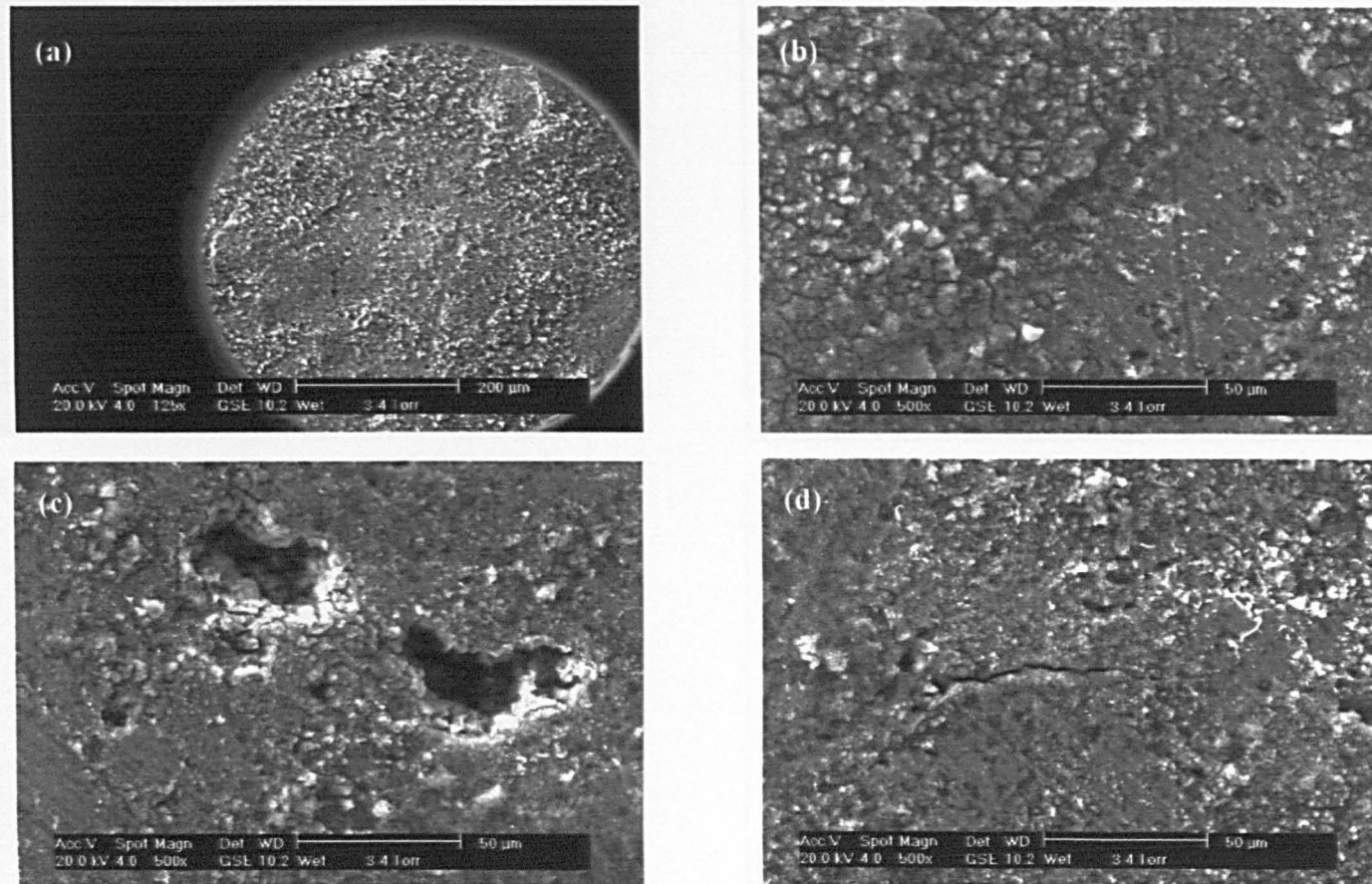


**Figure 6.2** SE image showing the corroded surface morphology of the as-sprayed Al<sub>12</sub>Sn<sub>1</sub>Cu coating. (a) Low magnification image; (b) higher magnification image; (c) pitting points and (d) surface cracks.



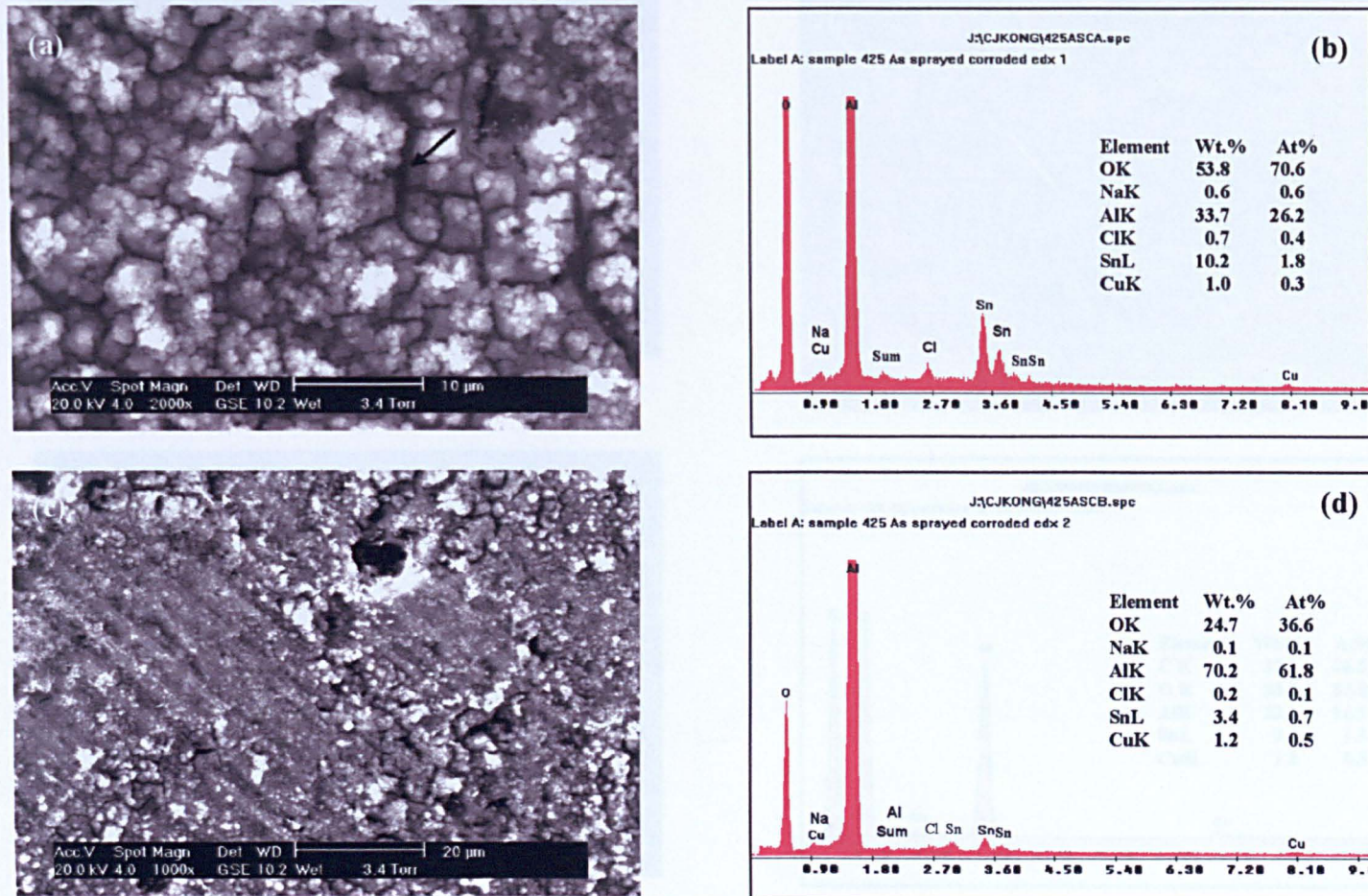
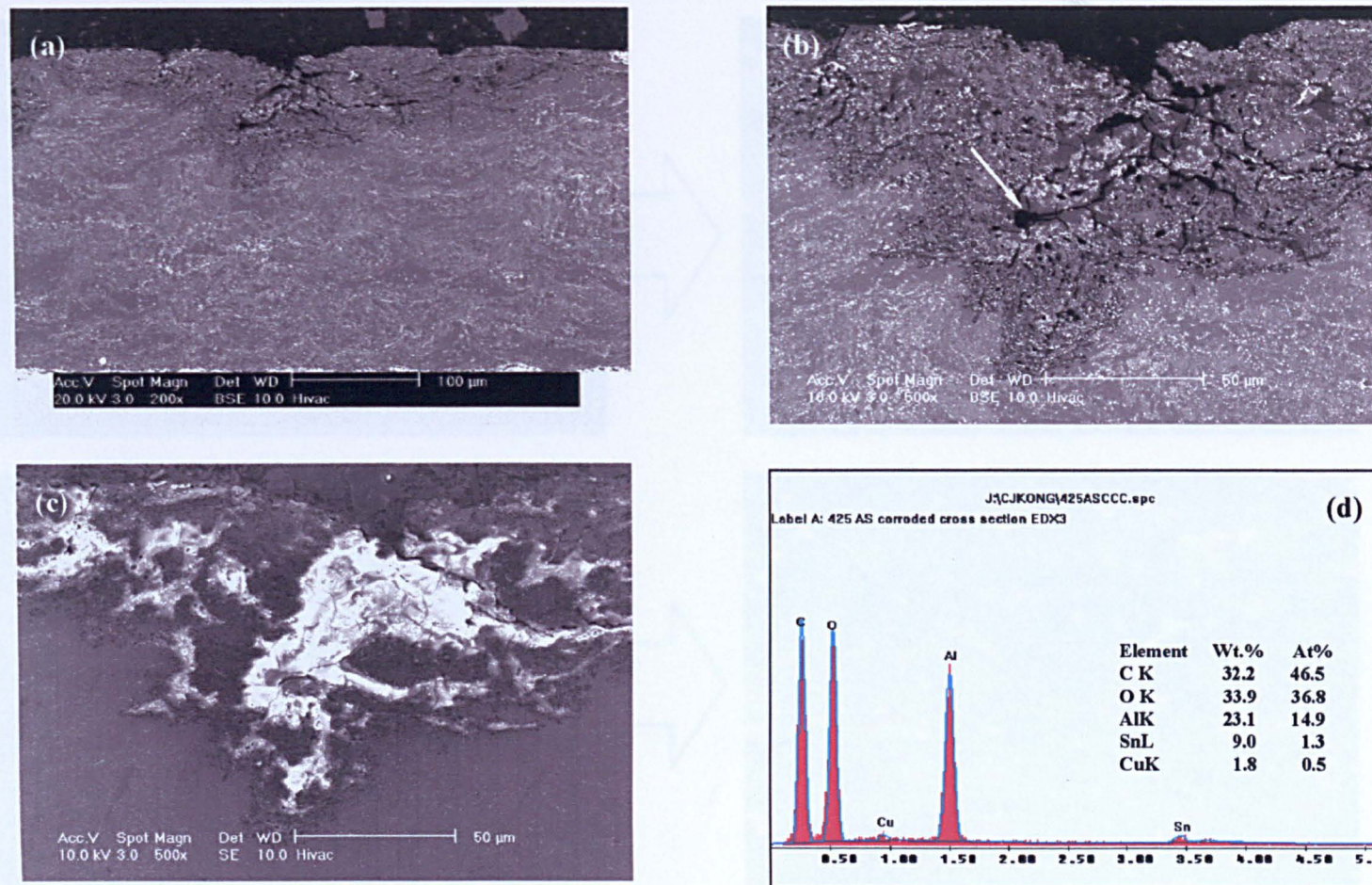


Figure 6.3 Corroded surface morphology of the as-sprayed Al<sub>12</sub>Sn<sub>1</sub>Cu coating. (a,c) SEM morphology; (c,d) EDX spectra of images (a,b), respectively.





**Figure 6.4** Cross-section of a corroded as-sprayed Al<sub>12</sub>Sn<sub>1</sub>Cu coating. (a) Low magnification BSE image; (b) higher magnification BSE image showing the corroded region; (c) SE image showing the same region of (b); (d) EDX spectrum of the region arrowed in (b).



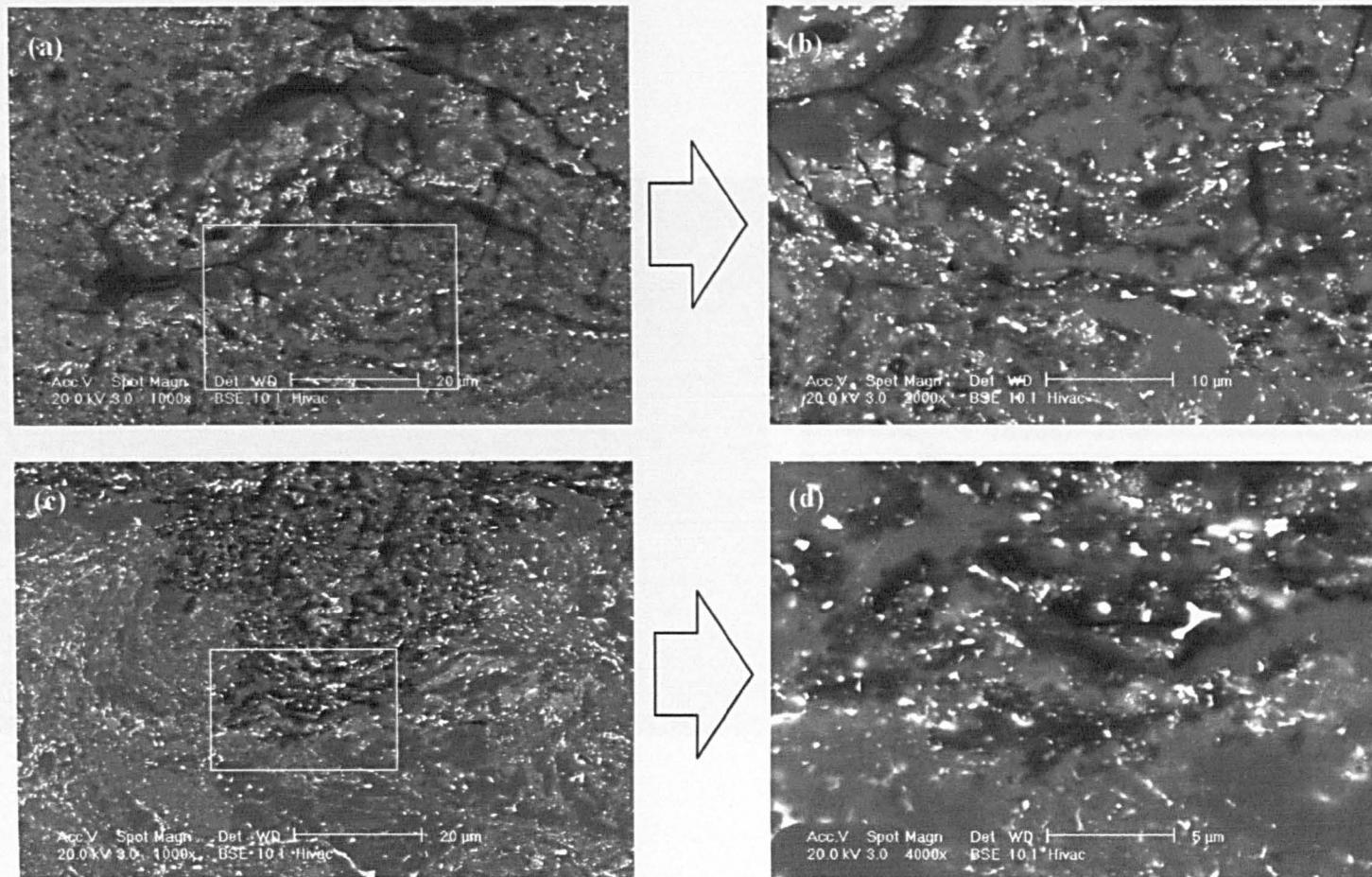


**Figure 6.5 BSE images showing details of the corroded as-sprayed Al12Sn1Cu coating. (a,c) Details of the middle region and bottom region of Figure 6.4(b), respectively; (b,d) higher magnification of the boxed regions in (a,c) respectively.**

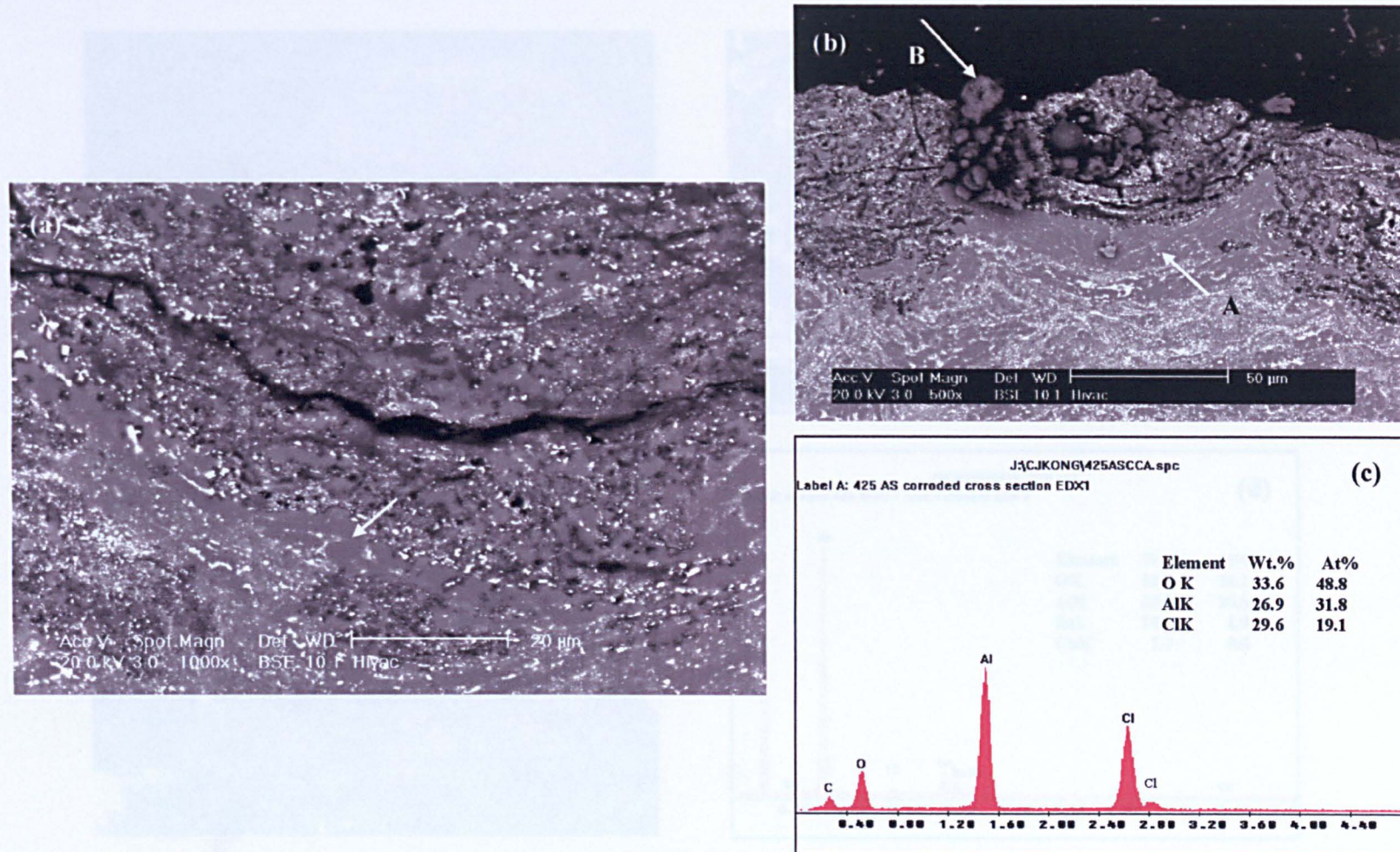


**Figure 6.6** Details of a corroded cross-section of an as-sprayed Al<sub>12</sub>Sn<sub>1</sub>Cu coating (a) BSE image showing the corrosion cracks and voids; (b) BSE image of the surface reactant; (c) EDS analysis of the arrowed region B in image (b)



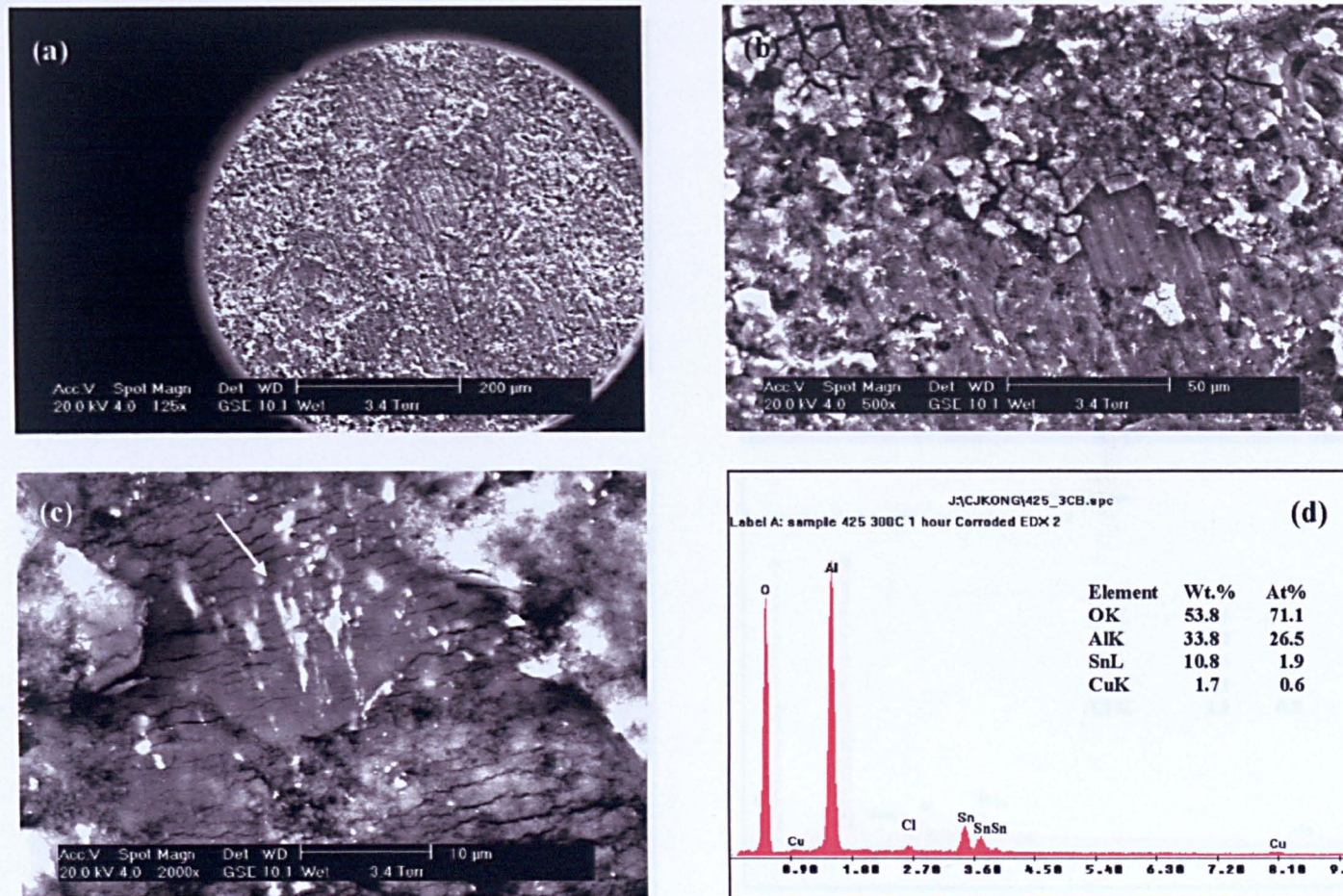


Figure 6.7 SE images and EDX spectrum showing the corroded Al<sub>12</sub>Sn<sub>1</sub>Cu coating surface annealed at 300°C for 1 hour and the composition of the coating reactant. (a) Low magnification image; (b,c) higher magnification of surface reactant; (d) EDX spectrum of the arrowed region in (c).



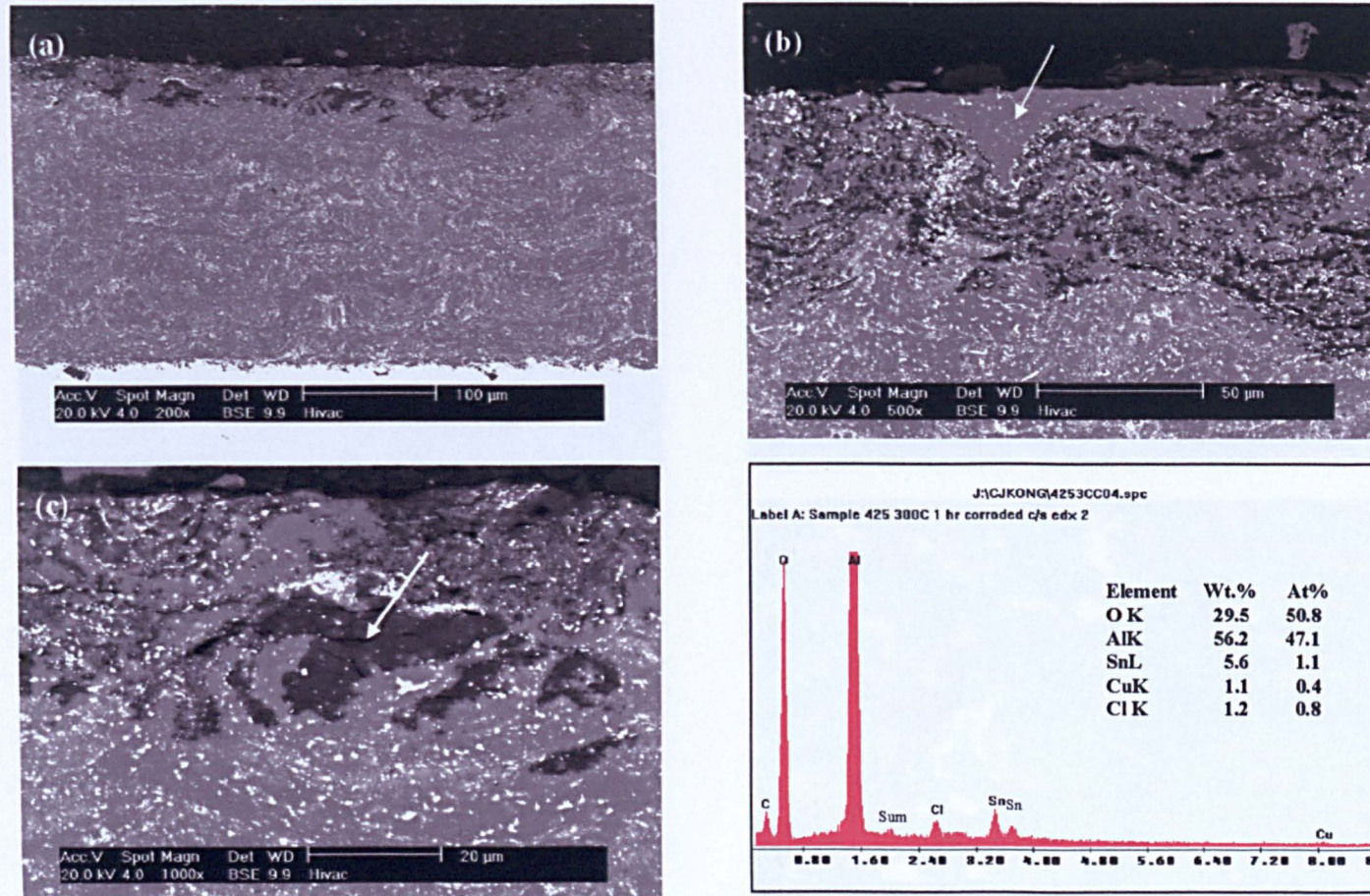
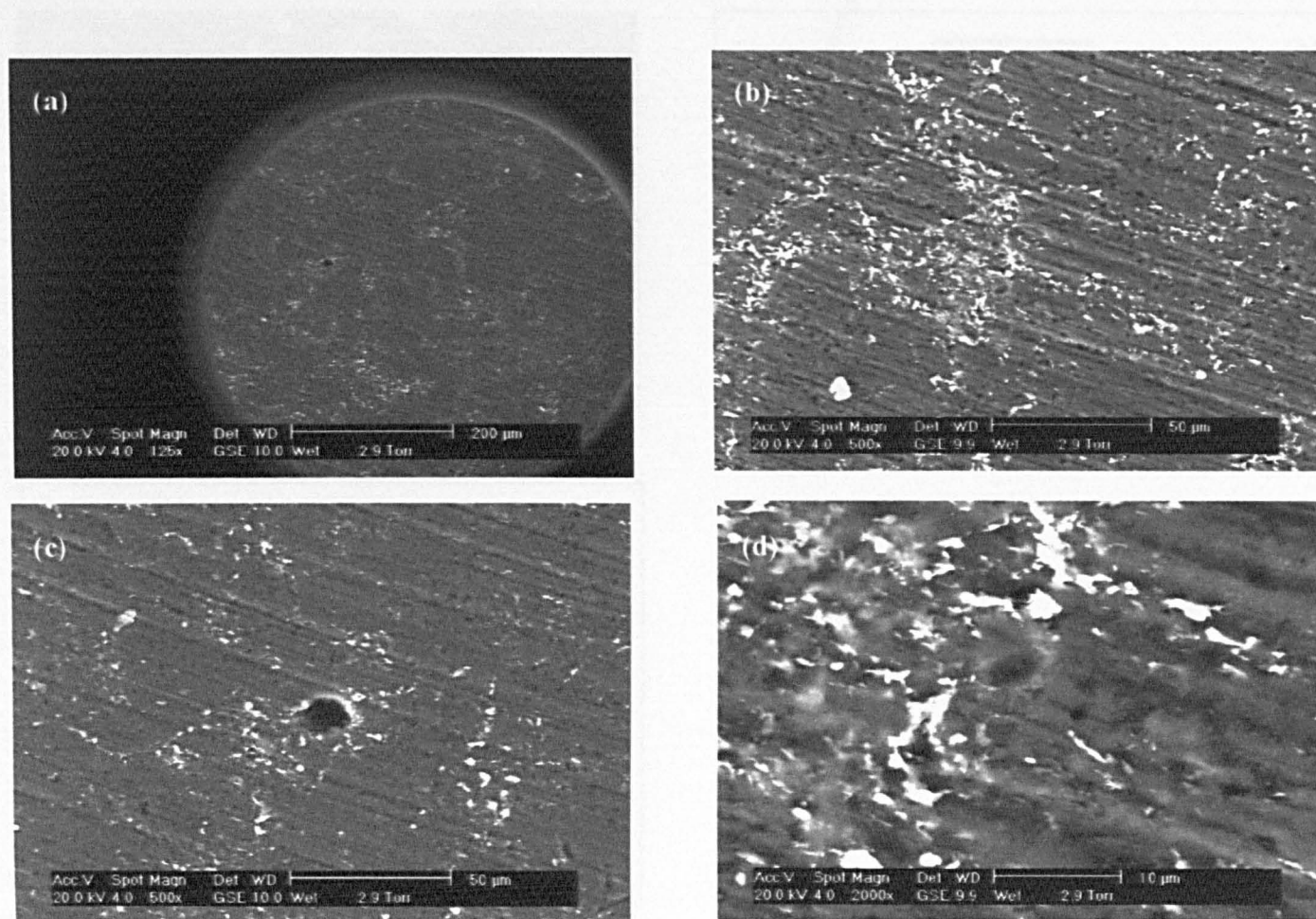


Figure 6.8 Corroded cross section of Al<sub>12</sub>Sn<sub>1</sub>Cu coating annealed at 300°C for 1 hour. (a) BSE low magnification image; (b) BSE higher magnification of the corroded region; (c) BSE image showing details of corroded region; and (d) EDX spectrum of arrowed region in (c).



**Figure 6.9** SE images showing the corroded surface morphology of an Al<sub>12</sub>Sn<sub>1</sub>Cu coating annealed at 450°C for 1 hour. (a) Low magnification image; (b, c) higher magnification images and (d) details of the surface



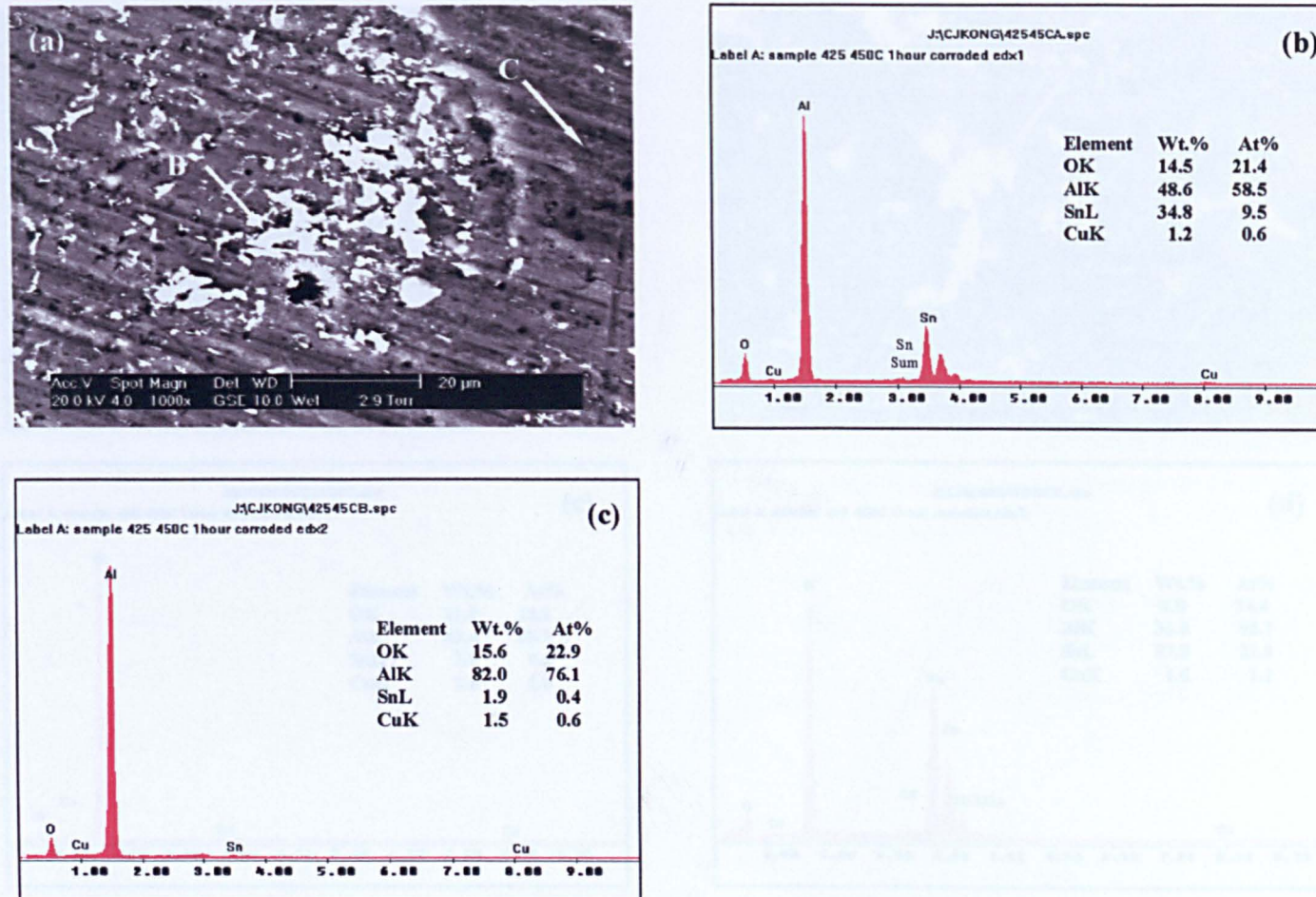


Figure 6.10 Corroded Al<sub>12</sub>Sn<sub>1</sub>Cu coating annealed at 450°C for 1 hour. (a) SEM surface morphology; (b,c) EDX spectra of the regions in (a) arrowed B and C, respectively.

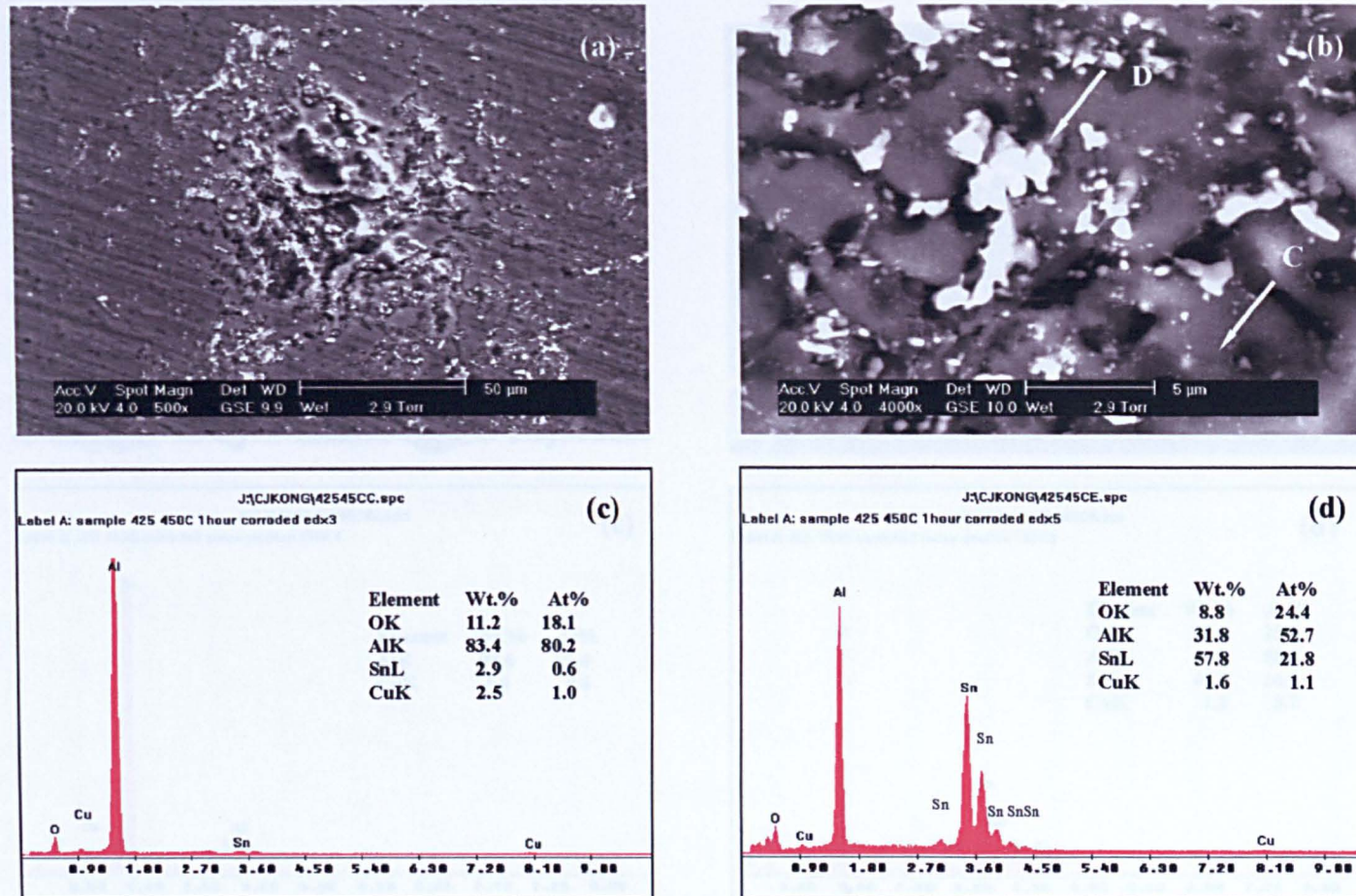


Figure 6.11 Corroded Al<sub>12</sub>Sn<sub>1</sub>Cu coating annealed at 450°C for 1 hour. (a,b) Low and high magnification SE images showing a pitting point; (c, d) EDX spectra of regions in image (b) arrowed C and D , respectively.



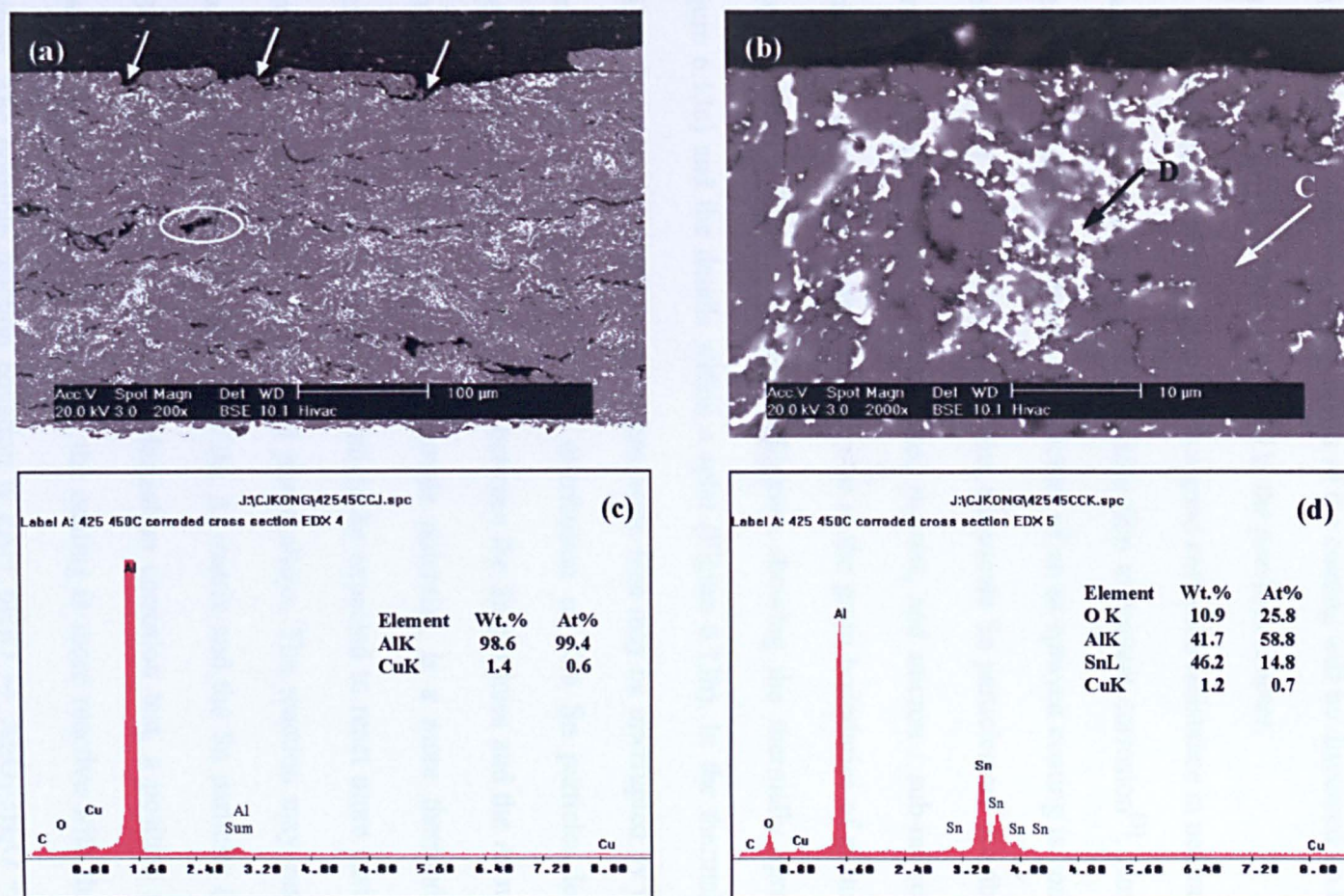
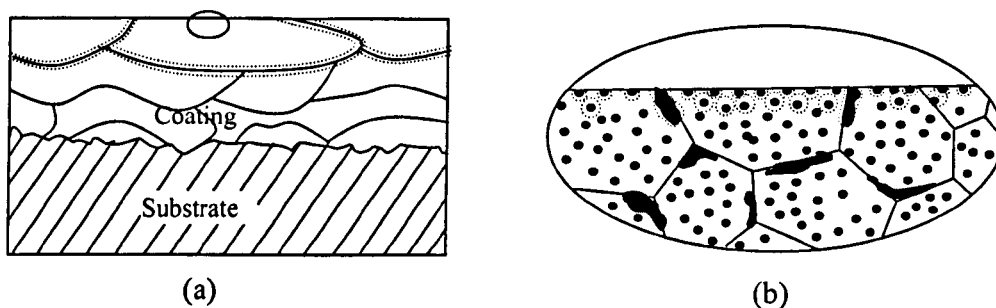


Figure 6.12 Corroded cross-section of an Al<sub>12</sub>Sn<sub>1</sub>Cu coating annealed at 450°C for 1 hour. (a, b) Low and high magnification BSE images; (c,d) EDX spectra of grey (arrowed C) and light (arrowed D) regions, respectively.

## 6.4 Discussion

In this section, the results obtained from the corrosion experiments will be compared and the corrosion mechanisms of the coating will be discussed on the basis of the microstructural evolution established in the previous chapter.

Literature shows that pure Al has a good corrosion resistance in neutral solutions, because pure Al forms an aluminium oxide film to prevent corrosion<sup>[3]</sup>. However, it is noted from Chapter 4 that the microstructure of an as-sprayed coating is constructed of layer on layer of splats. Within each splat, nanoscale Sn particles are distributed in the Al matrix, corresponding to fully melted regions, and micron / sub-micron scale Sn particles are distributed in the Al matrix or at the grain boundaries of partially melted regions. Figure 6.13 is a schematic diagram showing the thermally sprayed splats (Figure 6.13a) and the details within a splat (Figure 6.13b). In the thermally sprayed coating, the natural protective aluminium oxide film may be interrupted by these finely distributed Sn particles. Indeed, the distribution of fine Sn particles leads to the development of a large interface area between the Sn particles and the Al matrix. Pure aluminium, as indicated<sup>[3]</sup> by its electrode potential, is a more thermodynamically reactive metal than Sn. Therefore, Al might be expected to react more easily with the corrosion solution than Sn in the dual phase alloys. The reaction may easily happen between the splat and the interface of the Al matrix and the Sn particles (e.g. Figure 6.13a,b dotted line). In the anodic polarization corrosion test, a positive potential is imposed on the coating and the Al in the coating is more reactive with the corrosion solution. The possible reaction equation is  $2\text{Al} + 6\text{H}_2\text{O} \rightarrow \text{Al}_2\text{O}_3 \cdot 3\text{H}_2\text{O} + 3\text{H}_2$ . It is considered that the sodium chloride within the solution acts to enhance this reaction.



**Figure 6.13 Schematic of the corrosion of an as-sprayed coating. (a) Splat structure of an HVOLF thermal sprayed coating; (b) Detailed intra-splat microstructure (elliptical in (a))**

Figure 6.5d shows the interface region of corroded and original material, where pure Al in the Al / Sn interface has reacted with the sodium chloride water solution. This represents the beginning of the corrosion reaction of the surface, schematically shown in Figure 6.13(b). The reaction leads to the formation of  $\text{Al}_2\text{O}_3$ , as indicated by EDX analysis (Figure 6.3b,d and Figure 6.4d). The volume change by forming  $\text{Al}_2\text{O}_3$  causes cracks to form in the corroded regions. Then, cracks develop along the inter-splat interface (Figure 6.6a,b) or in perpendicular directions (Figure 6.4a-c and Figure 6.5a,b). The developing cracks form interlaced structures (Figure 6.2 and Figure 6.3a,b). Further, the cracks formed enable more sodium chloride solution to penetrate into the coating which causes corrosion to continue deeper into the coating. The corrosion is relatively uniform from the surface because the nanoscale Sn particle distribution provides many interface region that are attacked. However, preferential corrosion could also happen to cause deep pitting points (Figure 6.2c and the top region of Figure 6.4b). Small cracks also could develop to become larger cracks (Figure 6.2d and Figure 6.4b, arrowed region).

The unmelted regions show better characteristics of resistance to corrosion in the cross-sectional images (Figure 6.6a, arrowed and Figure 6.6b arrowed A) and in the surface morphology image (Figure 6.3c). This is because the Sn particle size in the unmelted regions are micro-scale or even larger which reduces the Al /Sn interfacial area to be attacked. The Cl and Na peaks detected by EDX in the surface of the coating (Figure 6.3b,d and Figure 6.6b,c) is probably due to residual NaCl based on interfacial area for corrosion.

The above explanation could explain why the Al<sub>12</sub>Sn<sub>1</sub>Cu as-sprayed coating is easily corroded in the NaCl solution, according to the anodic polarisation curves (Figure 6.1).

The corrosion resistance of the coating annealed at 300°C for 1 hour did not significantly change as compared with the as-sprayed coating. The reason for the development of the corrosion is very similar to the as-sprayed coating. As is known from Chapter 5, the number of sub-micron Sn particles did not decrease greatly according to the statistical analysis (Figure 5.6). From the SEM statistical analysis and TEM examination of these samples (Chapter 5), the nanoscale Sn particles and sub-micron Sn particles did not coarsen greatly during 1 hour of annealing at 300°C. This means the extent of initial interfacial reaction between Al and Sn did not change significantly for the coating annealed at 300°C for 1 hour as compared with the as-sprayed coating. Therefore, the corrosion resistance of this coating did not significantly change.

A similar surface roughness (Figure 6.7a-c) and cross-sectional corroded zone were found in the 300°C, 1 hour annealed coating as compared with the as-sprayed coating. Corrosion again happened at the surface layer of the coating between splats and

the Sn and Al interfaces (Figure 6.8a-c). It is again considered that aluminium oxide formed in the surface layer (Figure 6.7c,d) promoted the corrosion cracking of the layer (Figure 6.8c,d). Again, the semi-molten regions (Figure 6.8b, arrowed) showed much stronger corrosion resistance as compared with the fully melted regions. The better corrosion resistance of the semi-molten regions is attributed to the existence of fewer nanoscale and sub-microscale Sn particles in this region.

The thermal sprayed Al<sub>12</sub>Sn<sub>1</sub>Cu coating annealed at 450°C for 1 hour showed a significant increase in the corrosion resistance, with improved passivity and increased corrosion potential,  $E_{\text{corr}}$  (Figure 6.1). Greater coarsening of the Sn particles has been observed in the associated BSE images (Figure 6.12a,b). It might be considered that the inter-spalt cracks are formed by high temperature annealing (Figure 6.12a, circled region) and this might cause the mechanical properties to deteriorate. Indeed, previous work<sup>[4]</sup> has shown that nanoscale Sn particles seldom exist in the HVOGF thermal spray coatings annealed at 450°C for 1 hour. Therefore, we can assume a comparable microstructure within HVOLF thermal sprayed coatings annealed at 450°C for 1 hour prior to testing. Thus, the availability of the Al / Sn interfaces for attack by sodium chloride solution is reduced greatly due to the lower interface area. Since reaction preferentially happens at the interface of the Al and Sn particles, more pitting corrosion rather than uniform corrosion would be expected and this was found in these annealed samples (Figure 6.12a, arrowed region). The progression of corrosion solution occurs preferentially at the Al / Sn interfaces leading to the result of a greater extent of aluminum oxide formation at these interface regions (Figure 6.12d) rather than within

the Al matrix region (Figure 6.12c). It is noted that the formation of interlayer cracks as a consequence of corrosion may affect the mechanical properties of the coatings.

## 6.5 Summary

The Al<sub>12</sub>Sn<sub>1</sub>Cu as-sprayed coating does not exhibit good corrosion resistance in 1wt% NaCl solution, as assessed by potential dynamic tests. The reason is attributed to the presence of nanoscale and micron / sub-micron Sn particles leading to a larger surface area of Al / Sn interfaces to be attacked. The coating annealed at 300°C for 1 hour does not increase its corrosion resistance significantly, as compared with the as-sprayed coating because a large amount of nanoscale and sub-micron Sn particles still exist within the coating. The coating annealed at 450°C for 1 hour induced passivity in the anodic polarization curve which is attributed to the formation of coarser Sn and a reduction in the Al / Sn interfacial area available for attack. However, this annealing condition is not suitable for these coatings because interlayer cracks are formed accompanying this level of annealing which will degrade the mechanical properties of the coatings.

Possible annealing conditions to increase the corrosion resistance of Al<sub>12</sub>Sn<sub>1</sub>Cu coatings may be between 300-350°C for duration longer than 1 hour. This could allow the development of a microstructure with fewer nanoscale / sub-micron Sn particles and hence a lower Al/Sn interfacial area.



## References

1. A. J. Horlock, A. H. Dent, D. G. McCartney and S. J. Harris. *Controlling sacrificial corrosion properties of sprayed aluminium alloy coatings*. in *Proceedings of the 15th International Thermal Spray Conference, 25-29, May, 1998*. p. 38-41, Nice, France.
2. A. J. Horlock, *Unpublished Internal Report*. 2003.
3. J. R. Davis, Corrosion of aluminium and aluminium alloys. 1999. ASM International, The Materials Information Society, Materials Park, OH 44073-0002.
4. C. J. Kong, P. D. Brown, A. J. Horlock, S. J. Harris and D. G. McCartney, *Influence of high velocity spraying conditions on microstructure and properties of an Al-12wt.%Sn-1wt.Cu alloy*. Materials Science Forum, 2002. **396-402**: p. 1133-1138.

---

## Chapter 7

### Characterisation of the Al-20wt.%Sn-3wt.%Si alloy

---

#### 7.1 Introduction

An Al-20wt.%Sn-3wt.%Si (Al<sub>20</sub>Sn<sub>3</sub>Si) alloy was also investigated as a potential material for use as a bearing, for its excellent seizure, wear, fatigue and corrosion resistance <sup>[1, 2]</sup>. The selection of Si was made for a number of reasons. First, although Cu content increasing could strengthen Al matrix, the precipitation of Cu compounds such as  $\theta'$  may occur during the annealing process, or during service, which may negatively influence the performance of the coatings. Secondly, Si is found to increase the wear resistance of bearings and the Si phase is also relatively stable at the service temperature of  $\sim 180^\circ\text{C}$ . However, the effect on corrosion by substituting Si for Cu is unknown. The Sn alloy content investigated was increased from 12 weight percent to 20 weight percent to achieve the required compatibility and conformability of the bearing. The manufacturing parameters of these thermally sprayed coatings are described in Chapter 3. In this chapter, the microstructure of the gas atomised feed stock powder, the as-sprayed coating and the subsequently annealed Al<sub>20</sub>Sn<sub>3</sub>Si coatings are characterised by XRD, SEM, TEM and HREM techniques. The structure formation mechanism is also discussed in the light of the models proposed in previous Chapters.

## 7.2 Characterisation of gas atomised Al<sub>20</sub>Sn<sub>3</sub>Si powder

### 7.2.1 XRD spectrum of the Al<sub>20</sub>Sn<sub>3</sub>Si

Figure 7.1 presents the XRD spectrum from the gas atomised Al<sub>20</sub>Sn<sub>3</sub>Si powder. The spectrum reveals the existence of the fcc  $\alpha$ -Al phase and the bct Sn phase. Weak, broad Si peaks are also evident.

### 7.2.2 SEM microstructure of the Al<sub>20</sub>Sn<sub>3</sub>Si gas atomised powder

The microstructure of the gas atomised Al<sub>20</sub>Sn<sub>3</sub>Si powder shows many similarities to the gas atomised Al<sub>12</sub>Sn<sub>1</sub>Cu powder. The size distribution of the Al<sub>20</sub>Sn<sub>3</sub>Si powder particles is in the range of 22 – 45  $\mu\text{m}$ , which is significantly smaller than that of the Al<sub>12</sub>Sn<sub>1</sub>Cu powder (40 – 106  $\mu\text{m}$ ). As a result, the spraying process adopted different parameters which have been described in Chapter 3. The Malvern particle size distribution is shown in Chapter 3. The gas-atomised Al<sub>20</sub>Sn<sub>3</sub>Si powder again adopts a spherical shape, as shown in the low magnification BSE image of Figure 7.4 (a). A dendritic, Al-rich phase and an interdendritic Sn-rich phase characterised the larger scale powder particles (Figure 7.4b, c). At high magnification (Figure 7.4c), details of the cellular-dendritic structure are observed. Since the atomic numbers of the elements Al and Si only differ by one, it is difficult to distinguish them using backscattered electron imaging. EDX spot analysis spectra acquired from a region of dark contrast (arrowed d) and light contrast (arrowed e) of Figure 7.4 (c) both confirm the presence of Al, Sn and Si, with the bright contrast region showing a higher Sn and Si content. It is noted that the spot size is small, but the beam spreading which occurs in the sample is large compared with the interdendritic spacing in this sample. Oxygen and carbon were

also detected from the bright region of the sample, which may be from contamination.

The microstructures of a small powder particle and a large powder particle with a shell structure are shown in Figure 7.5. The small powder particle exhibits a sub-micron Sn particle dispersion distributed throughout the Al matrix (Figure 7.5 a). Low and high magnification BSE images show that the microstructure of the powder shell (Figure 7.5b,c and d,e) exhibits a nanoscale Sn particle dispersion within the Al matrix. The EDX analysis (Figure 7.5 f) of the boxed region in image Figure 7.5(e) again shows the presence of Al, Sn and Si. Semi-quantitative analysis, by weight percent, of the element close to the nominal composition of 20wt% Sn and 3wt% Si.

### **7.3 Characterisation of as-sprayed Al<sub>20</sub>Sn<sub>3</sub>Si coatings**

#### **7.3.1 XRD spectrum of the as-sprayed Al<sub>20</sub>Sn<sub>3</sub>Si coatings**

Figure 7.2 presents the XRD spectrum of the as-sprayed Al<sub>20</sub>Sn<sub>3</sub>Si coating. Again, the spectrum shows strong fcc  $\alpha$ -Al phase peaks and the bct Sn phase. However, the weak, broad Si peaks observed in the gas atomised powder are not readily apparent.

#### **7.3.2 SEM microstructure of the as-sprayed Al<sub>20</sub>Sn<sub>3</sub>Si coatings**

Cross sectional BSE images of the thermally sprayed Al<sub>20</sub>Sn<sub>3</sub>Si coating are shown in Figure 7.6. The thickness of the coating was about 280  $\mu\text{m}$  according to Figure 7.6(a). The high magnification of image Figure 7.6(b) shows that the as-sprayed coating was composed of melted (grey contrast) and semi-melted regions (dark contrast). Higher magnification SEM images (Figure 7.7) present the details of the boxed region of Figure 7.6(b). Figure 7.7(a,d) are images of a partially melted

region. In Figure 7.7(a), a cellular  $\alpha$ -Al with interdendritic Sn (bright contrast regions) still exists, similar to the gas atomised powder. The interdendritic Sn has formed a linear structure in Figure 7.7(d) possible indicating a strong deformation of the semi-melted powder particle during deposition. Figure 7.7(b,e) also show semi-melted regions with a greater degree of melting. In these images, the presence of more regions with fine scale Sn dispersion contrast (grey) indicates a greater degree of melting has been achieved in these regions. The dark regions represent Al that has not melted and so is of low Sn content. Figure 7.7(c,f) show fully melted regions, where large scale Sn and fine scale Sn have become redistributed within the Al matrix, again showing grey contrast in these BSE images. Figure 7.7(f) reveals Sn which has accumulated linearly along intersplat boundaries.

### 7.3.3 TEM microstructure of the as-sprayed Al<sub>20</sub>Sn<sub>3</sub>Si coatings

The TEM montage of the as-sprayed Al<sub>20</sub>Sn<sub>3</sub>Si coating (Figure 7.8) shows the fine scale details of the molten and semi-molten regions. The right side of the image shows a more highly molten region as compared with the left. Both micron / sub-micron Sn / Si and nanoscale Sn / Si particles are distributed throughout the coating. Linear Sn regions are also distributed between the splats, e.g. in the middle bottom region of Figure 7.8 (arrowed). The left side of the montage shows a partially molten region with pure Al grains surrounded by fine scale Sn / Si dispersoids. Higher magnification images (Figure 7.9) show details of the coatings. Figure 7.9(a,d) present fully molten regions with nano-scale dispersoids distributed through the Al matrix. It is evident that a fine particle denuded zone exists at the grain boundaries in Figure 7.9(a). The fine Sn / Si particle size is also not uniformly distributed within different Al grains, e.g. Figure 7.9(d). Figure 7.9(b,e) and (c,f) illustrate partially molten regions of a coating with a region of Al surrounded by fine

scale Sn / Si particles. The high magnification images of Figure 7.9(e,f) show details of the fine scale Sn / Si particle distribution in seen at lower magnification Figure 7.9(b,c), respectively. Both sub-micron and nanoscale Sn / Si particles exist in the original dendritic regions. The Sn / Si particle size in the interdendritic regions is much coarser compared with the fully molten regions of Figure 7.9(a,d). Bright field images and their associated diffraction patterns were used to clarify whether discrete Si particles existed in this coating. Figure 7.10(a) shows a fully molten region of the coating with a fine-scale dispersoid distribution. The continuous diffraction pattern rings of Figure 7.10(b) corresponding to this region confirm the existence of Al, Sn and Si phases. Figure 7.10(c) shows a semi-molten region with the Al matrix surrounded by Sn/Si particles. The associated diffraction pattern of Figure 7.10(d) from this region also shows a continuous Si ring, discontinuous ring corresponding to Al and some weak diffraction spots corresponding to particles of Sn. The diffraction ring of Si is too blurred to be distinguished in the print.

The bright field image and associated diffraction patterns of one Al grain with a fine scale dispersoid are shown in Figure 7.11(a,b). This selected area diffraction pattern shows Si, Sn and Al diffraction spots along the same systematic row indicating, for some particles, that the Sn {200} and Si {111} planes are parallel to the Al matrix {111} plane, i.e.  $(111)_{\text{Si}} // (200)_{\text{Sn}} // (111)_{\text{Al}}$ . The dark field image of Figure 7.11(c) was formed by moving the Si diffraction spot towards the optic axis (circled in Figure 7.11d). Since the objective aperture is too large and the diffraction spots of Si and Sn are closely spaced, both elements may contribute to the formation of this dark field image and it is not possible to separate out which features correspond to Sn or Si, respectively. However, it is believed that Figure 7.11(c) highlights some of the Si particles within the Al grain. The possibility for Sn



diffraction spots being included, will also lead to Sn particles also being highlighted in this dark field image.

#### 7.3.4 HRTEM microstructure of the as-sprayed Al<sub>20</sub>Sn<sub>3</sub>Si coatings

As revealed in the previous section, conventional TEM has difficulty in distinguishing the Sn and Si particles in the as-sprayed coating. Therefore, high resolution TEM (HRTEM) was used to confirm the existence of Si particles. Figure 7.12 illustrates Sn and Si particles within the Al matrix of the as-sprayed coating. Figure 7.12(a) shows a Sn particle with a fringe on the (101) plane. There is no clear orientation relationship between this plane and the Al matrix. Figure 7.12(b) exhibits several particles. At the right-top side, a large, dark contrast Sn particle has the orientation relationship  $d_{\text{Sn}}(200) // d_{\text{Al}}(111)$ . A small particle, marked particle 1, is identified as being a Sn particle, according to its diffraction plane  $d_{\text{Sn}}(101)$ . The marked particle 2 corresponds to a small Si particle with  $d_{\text{Si}}(111) // d_{\text{Al}}(111)$ . Particle 3 corresponds to a small Sn particle with  $d_{\text{Sn}}(200) // d_{\text{Al}}(111)$ , where the (200) plane of Sn is at a small angle to the Al (111) plane. Figure 7.12(c) shows another series of particles within the Al matrix. The top, dark-contrast, Sn particle is another part of the large Sn particle shown in Figure 7.12(b), so, again, has an orientation relationship of  $d_{\text{Sn}}(200) // d_{\text{Al}}(111)$ . Particle 1 is a smaller Sn particle with the same orientation relationship, i.e.  $d_{\text{Sn}}(200) // d_{\text{Al}}(111)$ . Particle 2, identified as being Si, has an orientation relationship  $d_{\text{Si}}(111) // d_{\text{Al}}(111)$ . Misfit and distortion of planes is also shown in this particle. Another small particle, marked 3, shows an interplanar spacing of 0.325nm, which is a little larger than the standard fcc Si (111) plane. Furthermore, the orientation of this (111) plane is not parallel to the Al (111) plane, which makes it difficult to identify unambiguously.

## 7.4 Characterisation of the Al<sub>20</sub>Sn<sub>3</sub>Si coatings annealed at 300°C for 1 hour

### 7.4.1 XRD spectrum of the Al<sub>20</sub>Sn<sub>3</sub>Si coatings annealed at 300°C for 1 hour

Figure 7.3 present the XRD spectrum from the Al<sub>20</sub>Sn<sub>3</sub>Si coating after annealing at 300°C for 1 hour. Peaks from the fcc  $\alpha$ -Al phase and the bct Sn phase are present in the spectrum and weak Si peaks also appear. The intensity of the Sn peaks is stronger in the annealed coating as compared with the Sn peaks in the as-sprayed coating and the gas atomised powder.

### 7.4.2 SEM microstructure of the Al<sub>20</sub>Sn<sub>3</sub>Si coatings annealed at 300°C for 1 hour

A cross-sectional BSE image of the Al<sub>20</sub>Sn<sub>3</sub>Si coating annealed at 300°C for 1 hour is shown in Figure 7.13. The coating appears to have a relatively uniform microstructure in the low magnification image Figure 7.13(a). Some precipitation is, however, evident in the form of bright contrast features at the top surface. The higher magnification image of Figure 7.13(b) shows a string-like coarsening of the Sn as compared with the as-sprayed coating. Figure 7.14 shows higher magnification BSE images illustrating the detail of different regions in this annealed coating. Figure 7.14(a,b) show annealed regions (300°C, 1 hour) of, presumably, fully melted regions in the as-sprayed condition. The Sn particles have coarsened rapidly, from these images, leaving less nanoscale Sn / Si dispersoid from these BSE image observations (Figure 7.14a). Figure 7.14(c,d) show annealed regions of presumably partially melted regions in the as-sprayed condition. No significant microstructural change is observed in this instance, as compared with similar regions in the as-sprayed coating.

Annealing at 300°C for 1 hour additionally caused the development of some linear and spherical dark contrast regions, as shown in Figure 7.15(a,c) at higher magnification. EDX analysis (Figure 7.15b,d) shows that these dark regions (arrowed Figure 7.15a,c) are associated with oxygen, in addition to the acquisition of signals from Al, Sn and Si.

Spherical, irregular shaped precipitation was present on the top of the coating after annealing at 300°C for 1 hour (Figure 7.16a,e). The EDX analysis (Figure 7.16b) shows the bright region (arrowed b) is composed of pure Sn, whilst the dark region within the bright precipitation (arrowed c) is aluminium (Figure 7.16c). The higher magnification image of Figure 7.16(d) illustrates the detailed grain structure of pure Sn in the region arrowed (b) in Figure 7.16(a).

#### **7.4.3 TEM analysis of the Al<sub>20</sub>Sn<sub>3</sub>Si coatings annealed at 300°C for 1 hour**

TEM montages of the Al<sub>20</sub>Sn<sub>3</sub>Si coating annealed at 300°C for 1 hour show the detailed evolution of the micron / sub-micron and nanoscale Sn / Si particles (Figure 7.17). Micron / sub-micron Sn particles are concentrated along the Al-rich phase boundaries (arrowed at the top of the image), whilst fine-scale Sn / Si particles of different size ranges are present within different regions of the Al-rich phase (circled). Particle free regions are also shown in the images (marked A).

Details of these features are shown in Figure 7.18. Linear Sn particles are distributed along the Al grain boundaries, as shown in Figure 7.18(a). The nanoscale Sn / Si particles cluster towards the centre of the Al grains leaving a wide, particle-denuded zone near the grain boundaries (Figure 7.18b, c). Some Al grains are surrounded by micron / sub-micron Sn (Figure 7.18b), whilst others showed no evidence of being surrounded by coarsen (Figure 7.18c). A featureless Al grain surrounded by coarsened Sn is shown in Figure 7.18(d). Moreover, another Al grain

surrounded by nanoscale Sn / Si particles is shown in Figure 7.18(e). Figure 7.18(f) shows the details of the nanoscale particles of Figure 7.18 (e).

Bright field and dark field images and their associated diffraction patterns (Figure 7.19) also allowed the unambiguous identification of Si particles in the annealed coating. The Si ring appears discontinuous in the diffraction patterns. The light particles in the dark field image of Figure 7.19(c) arise from the highlighted region of a Si diffraction spot (ringed in Figure 7.19d). Again, it is not possible to eliminate the contribution of Sn to this dark field image. Figure 7.20 is two series of images showing the coarsened Si particle after 300°C for 1 hour annealed in the Al<sub>2</sub>O<sub>3</sub>Sn<sub>3</sub>Si coatings. Figure 7.20 (a,d) are bright field images of the annealing coating. The diffraction patterns Figure 7.20 (b,e) associated with these two bright field images show the presence of Si. Dark field images of Figure 7.20 (c,f) highlight the Si particles which selected from the spots of Si (111) spot ringed in Figure 7.20 (b,e).

**7.5 The microhardness of the Al<sub>2</sub>O<sub>3</sub>Sn<sub>3</sub>Si gas atomised powder, as-sprayed coatings and coatings annealed at 300°C for 1 hour**

The corresponding values of mean microhardness of the as-sprayed and annealed Al<sub>2</sub>O<sub>3</sub>Sn<sub>3</sub>Si coatings are listed in Table 7.1. It is evident that the coating heat treatment at 300°C for 1 hour greatly decreases the microhardness.

**Table 7.1** The relationship between the treatment condition and the microhardness of the coatings

Coating condition	as-sprayed	heat treated 300°C/1hr
Hv (kgfmm <sup>-2</sup> )	95 ± 4	50 ± 2

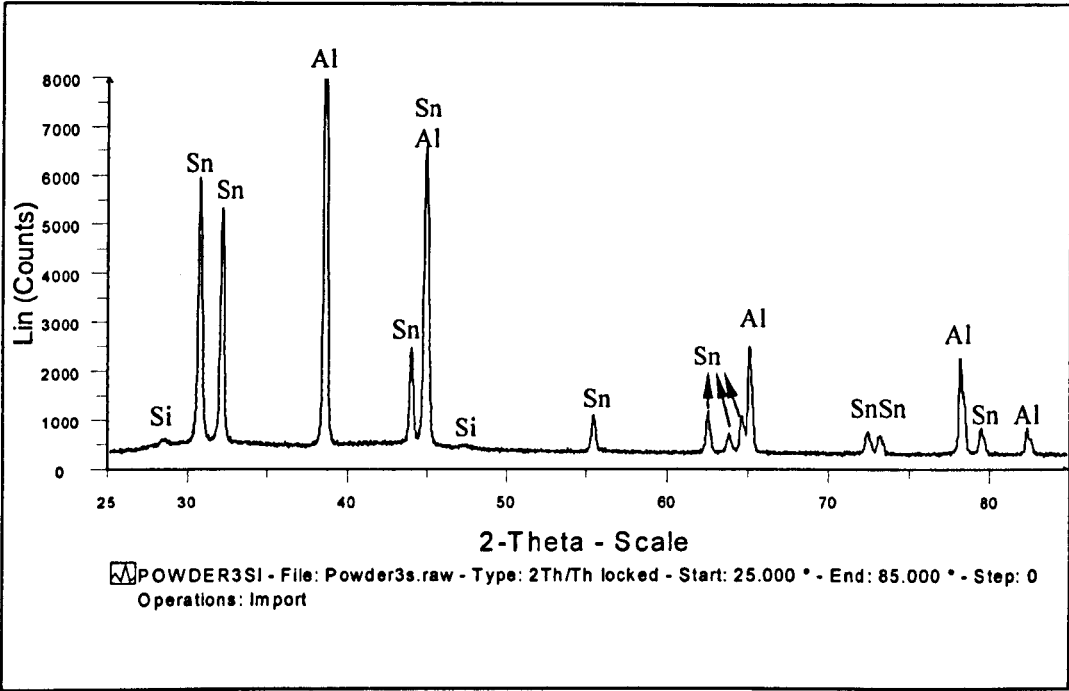


Figure 7.1 XRD pattern of the gas atomised Al<sub>20</sub>Sn<sub>3</sub>Si powder

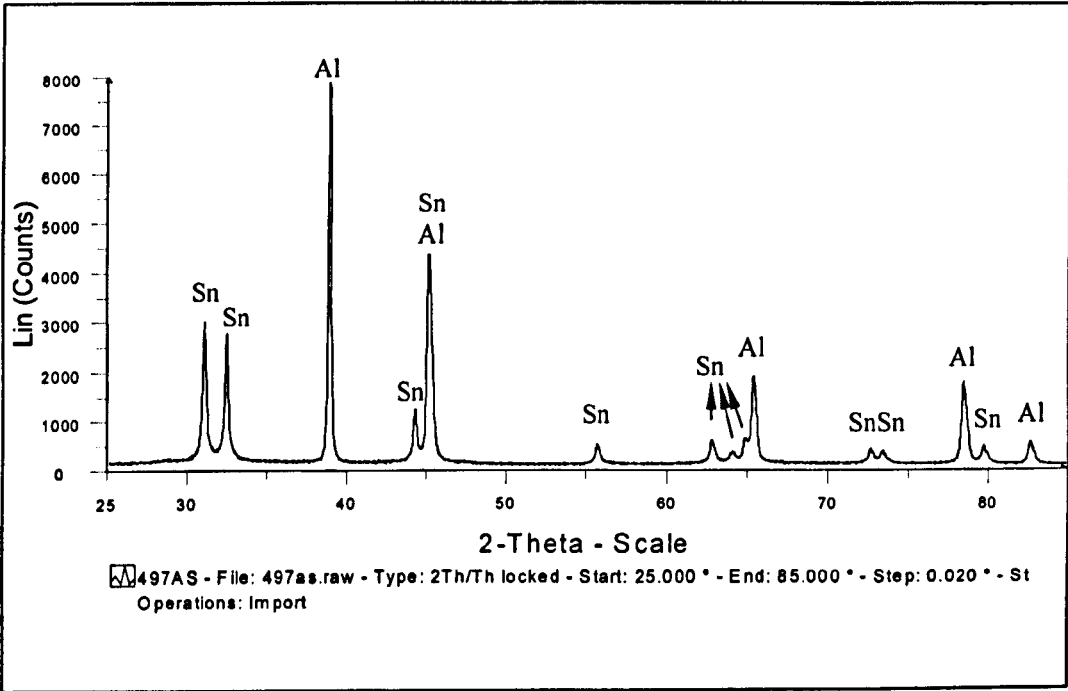
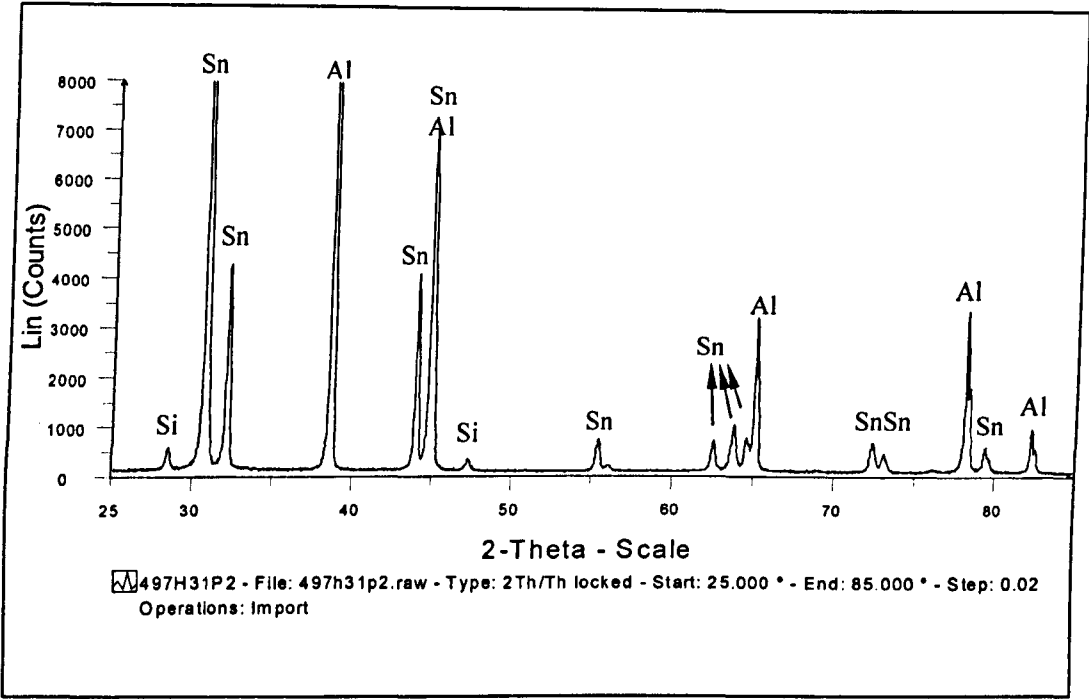


Figure 7.2 XRD pattern of the as-sprayed Al<sub>20</sub>Sn<sub>3</sub>Si coating



**Figure 7.3 XRD pattern of the sprayed Al<sub>2</sub>O<sub>3</sub>Sn<sub>3</sub>Si coating annealed at 300°C for 1 hour**



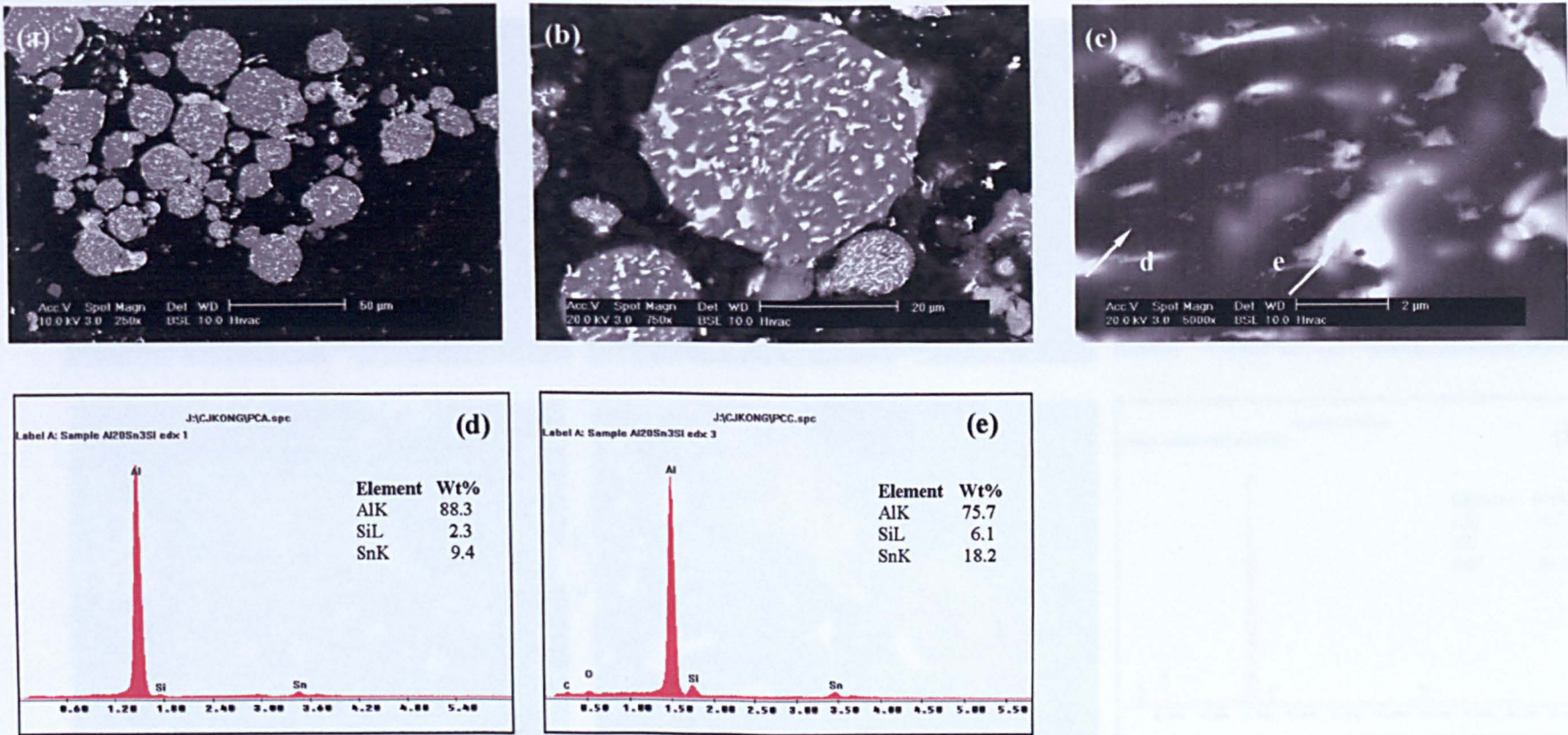


Figure 7.4 BSE images and EDX spectra of large scale Al<sub>20</sub>Sn<sub>3</sub>Si powder particles. BSE images in (a, b) low magnification; (c) high magnification; (d,e) EDX spectra of arrowed regions in the image (c)



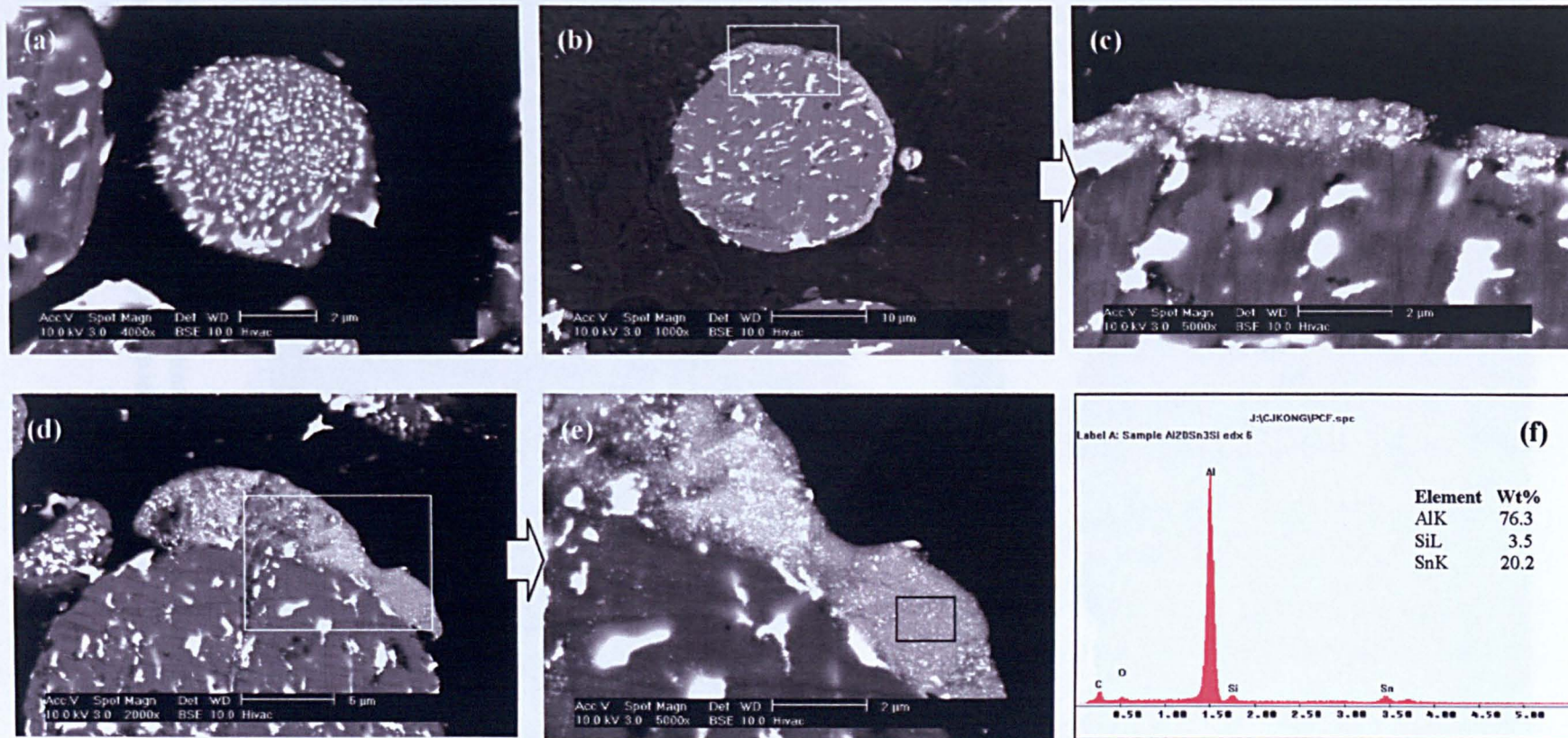
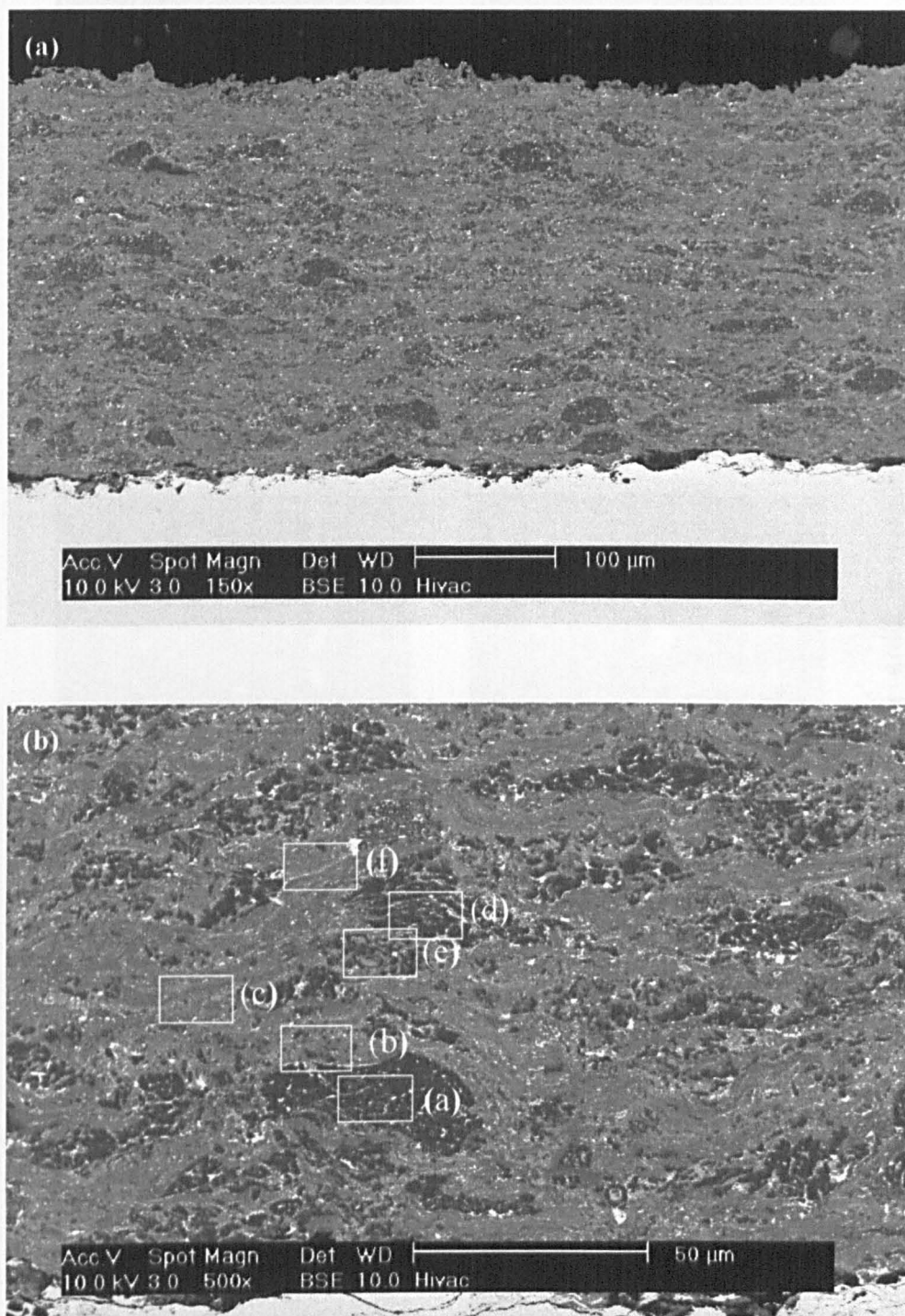
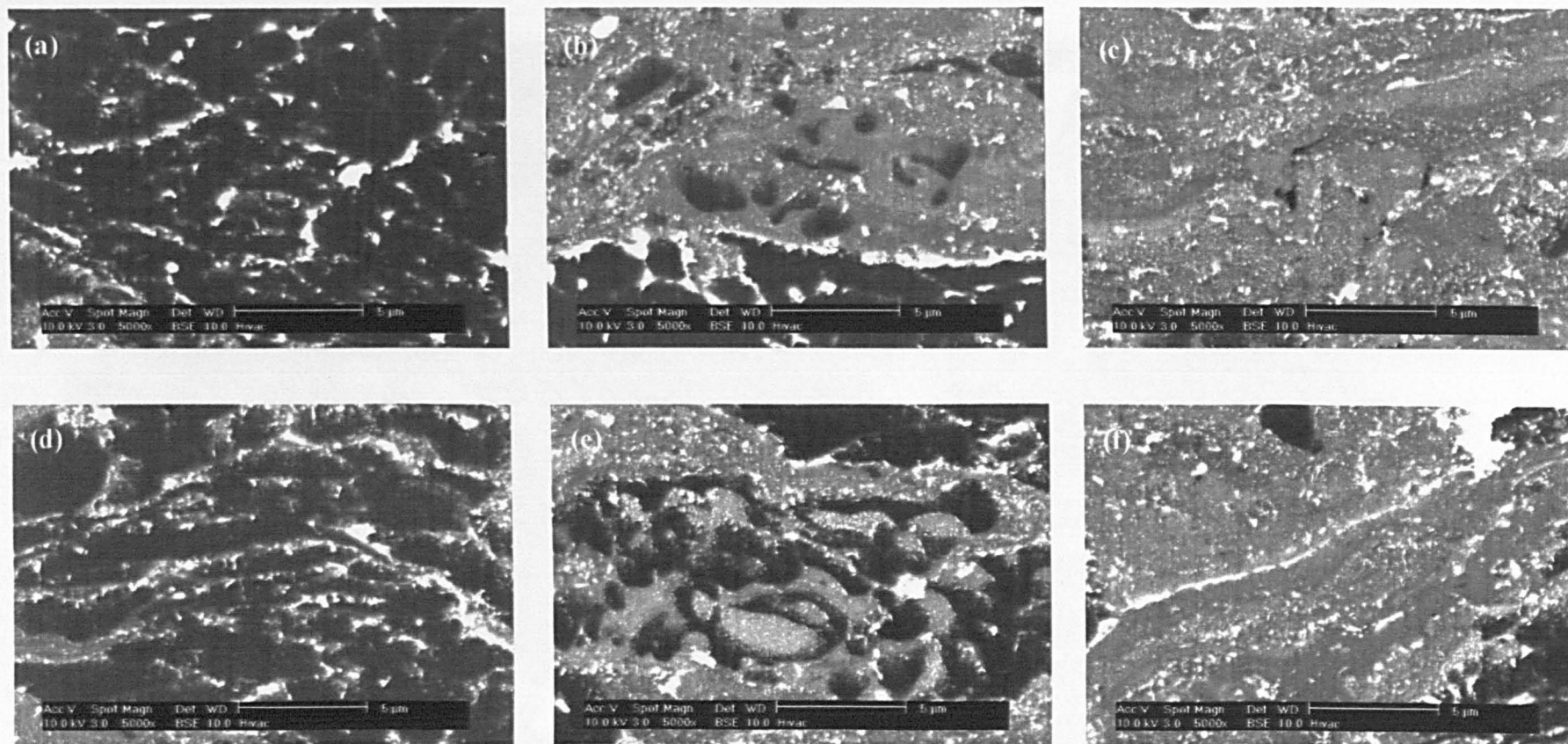


Figure 7.5 BSE images and EDX analysis of a small powder particle and the shell structures of the Al<sub>20</sub>Sn<sub>3</sub>Si powder particles. (a) Small powder particle; (b, d) large powder particles with shell; (c, e) detail of the shell structure in (b) and (d), respectively; (f) EDX spectrum of the boxed region in (e)



**Figure 7.6** BSE images of a cross section of Al<sub>20</sub>Sn<sub>3</sub>Si as-sprayed coating. (a) Low magnification; (b) high magnification. The boxes labelled (a)-(f) are shown in more detail in Figure 7.7.

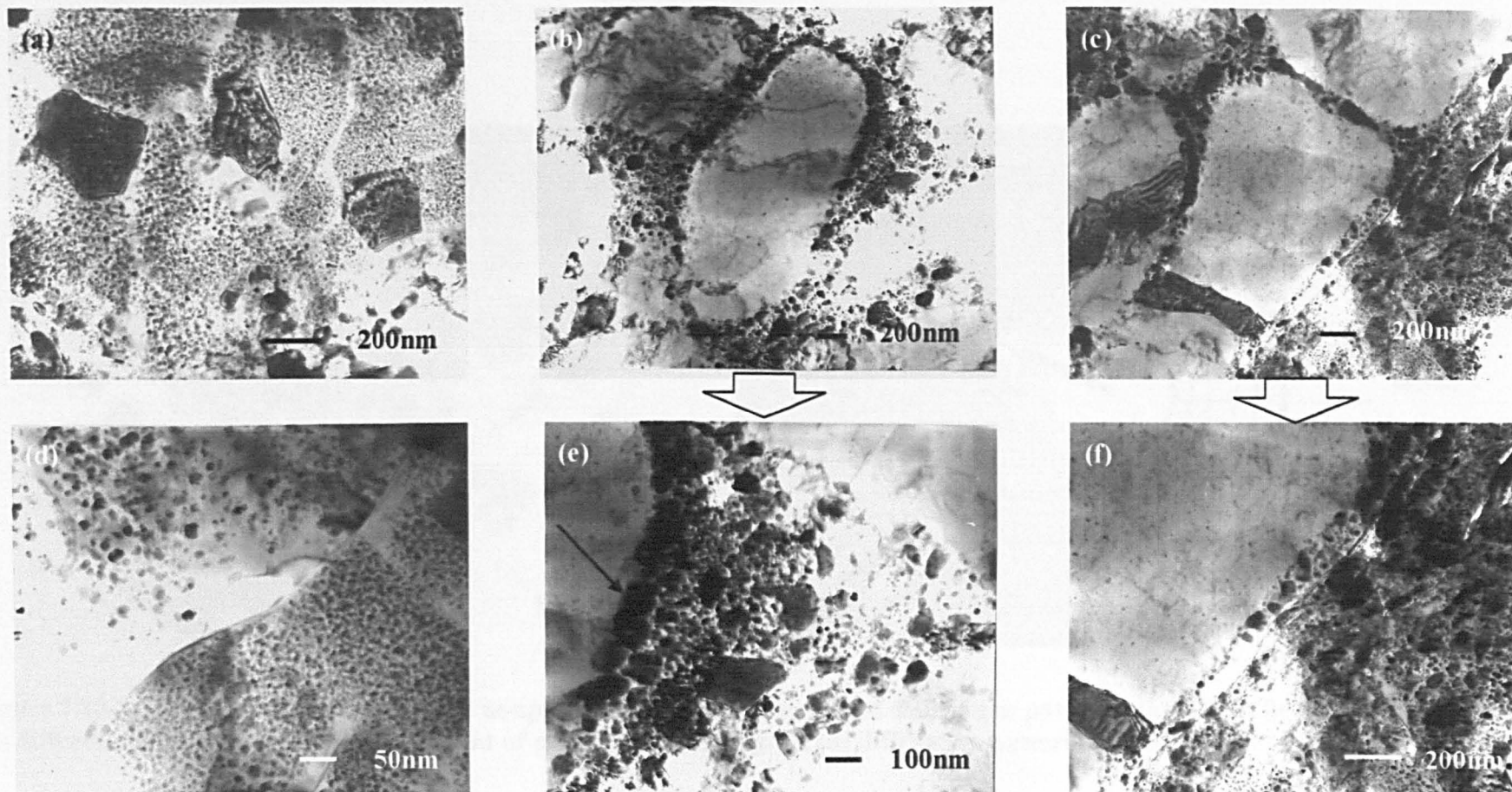




**Figure 7.7** High magnification BSE images of the Al<sub>2</sub>O<sub>3</sub>Sn<sub>3</sub>Si as-sprayed coating, corresponding to the boxes of Figure 7.6 (b). (a, d) Partially melted region; (b, e) melted but not-fully mixed regions; (c, f) melted and fully mixed regions.

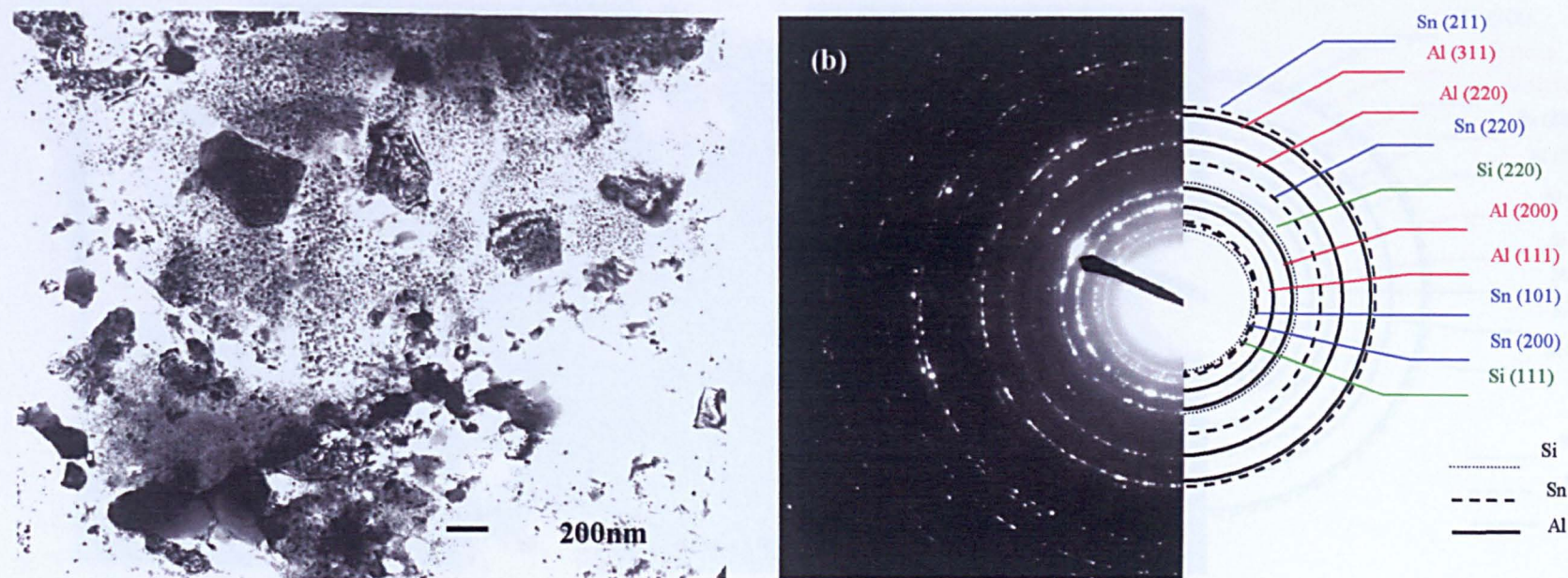


Figure 7.8 TEM montage of the as-sprayed Al<sub>2</sub>O<sub>3</sub>Sn<sub>3</sub>Si coating



**Figure 7.9** High magnification TEM images of the Al<sub>2</sub>O<sub>3</sub>Sn<sub>3</sub>Si as-sprayed coating. (a, d) Fully melted region; (b, e) partially melted region; (c, f) partially melted region.





**Figure 7.10** TEM images of the Al<sub>20</sub>Sn<sub>3</sub>Si as-sprayed coating and associated diffraction patterns. (a) Bright field of fully melted region; (b) diffraction pattern of (a); (c) Bright field of partially melted region, (d) diffraction pattern of (c).



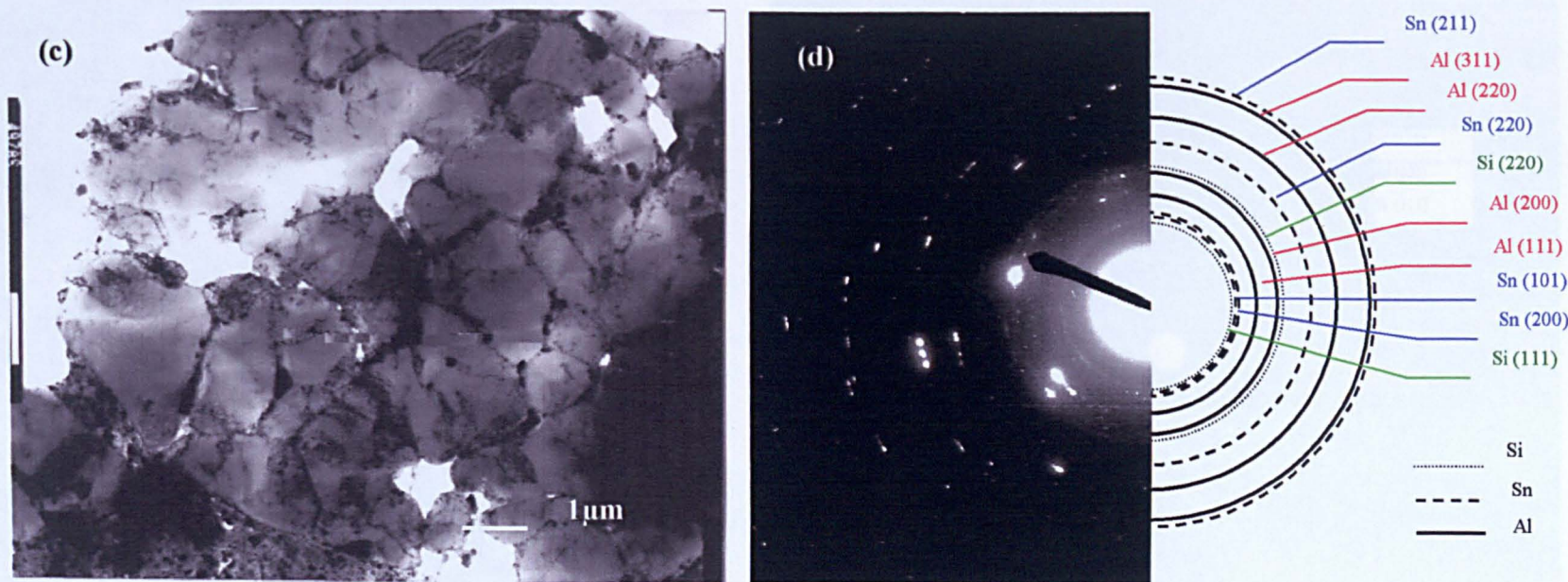


**Figure 7.10 (Continue) TEM images of the Al<sub>20</sub>Sn<sub>3</sub>Si as-sprayed coating and associated diffraction patterns. (a) Bright field of fully melted region; (b) diffraction pattern of (a); (c) Bright field of partially melted region, (d) diffraction pattern of (c).**

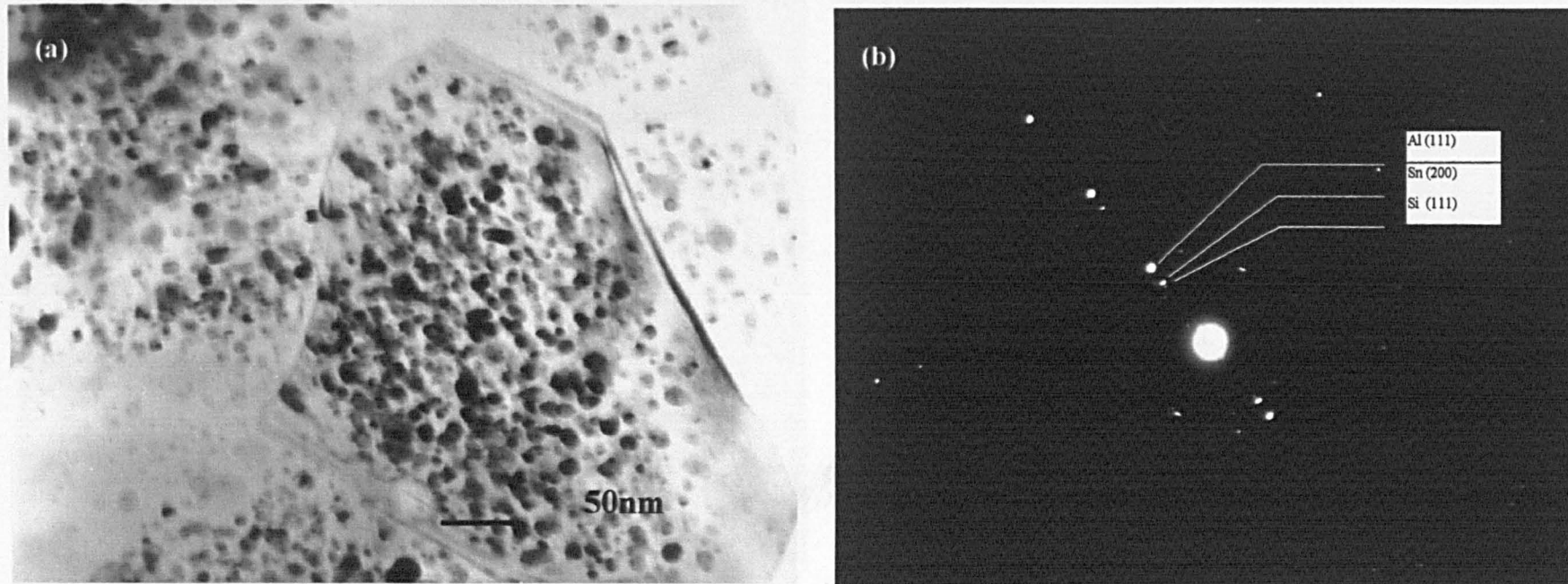


**Figure 7.11** TEM images of the Al<sub>20</sub>Sn<sub>3</sub>Si as-sprayed coating. (a) Bright field image of a fully melted region; (b) associated diffraction pattern of (a); (c) dark field image, (d) associated dark field diffraction pattern (ring denoting position of objective aperture attempting to capture the diffraction spot due to Si (111)).



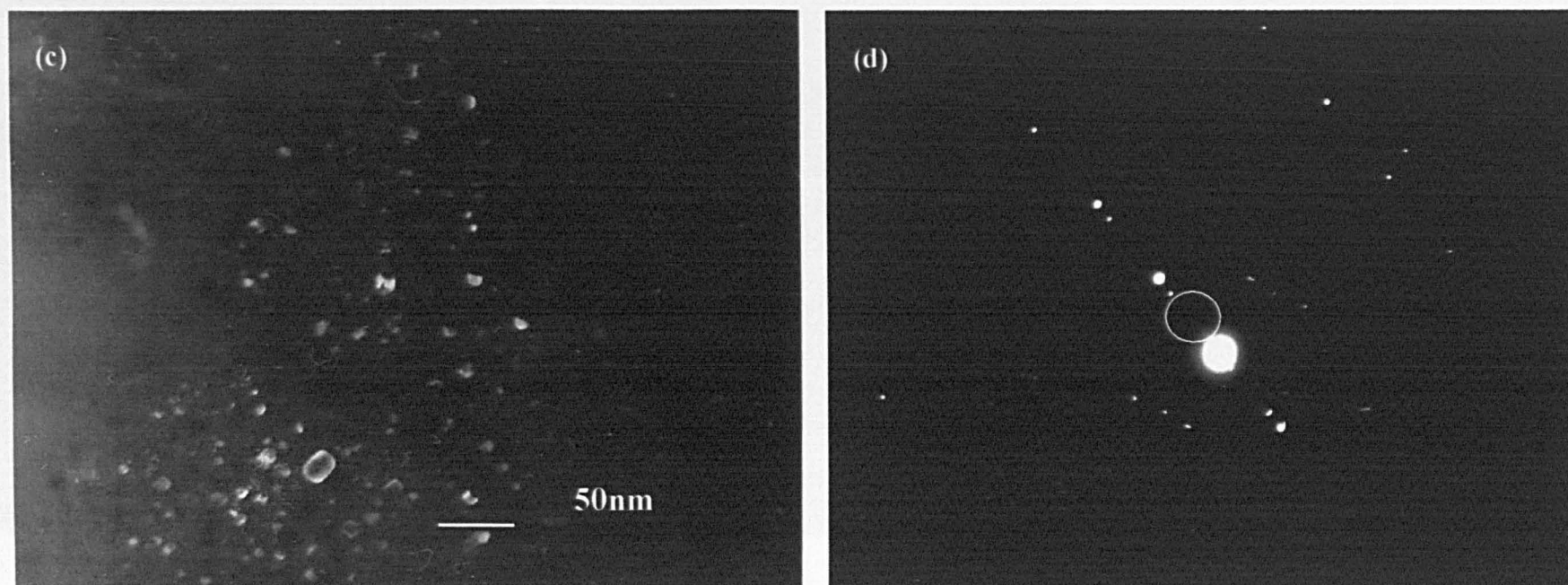


**Figure 7.11 (Continue)** TEM images of the Al<sub>20</sub>Sn<sub>3</sub>Si as-sprayed coatings. (a) Bright field image of a fully melted region; (b) associated diffraction pattern of (a); (c) dark field image, (d) associated dark field diffraction pattern (ring denoting position of objective aperture attempting to capture the diffraction spot due to Si (111)).

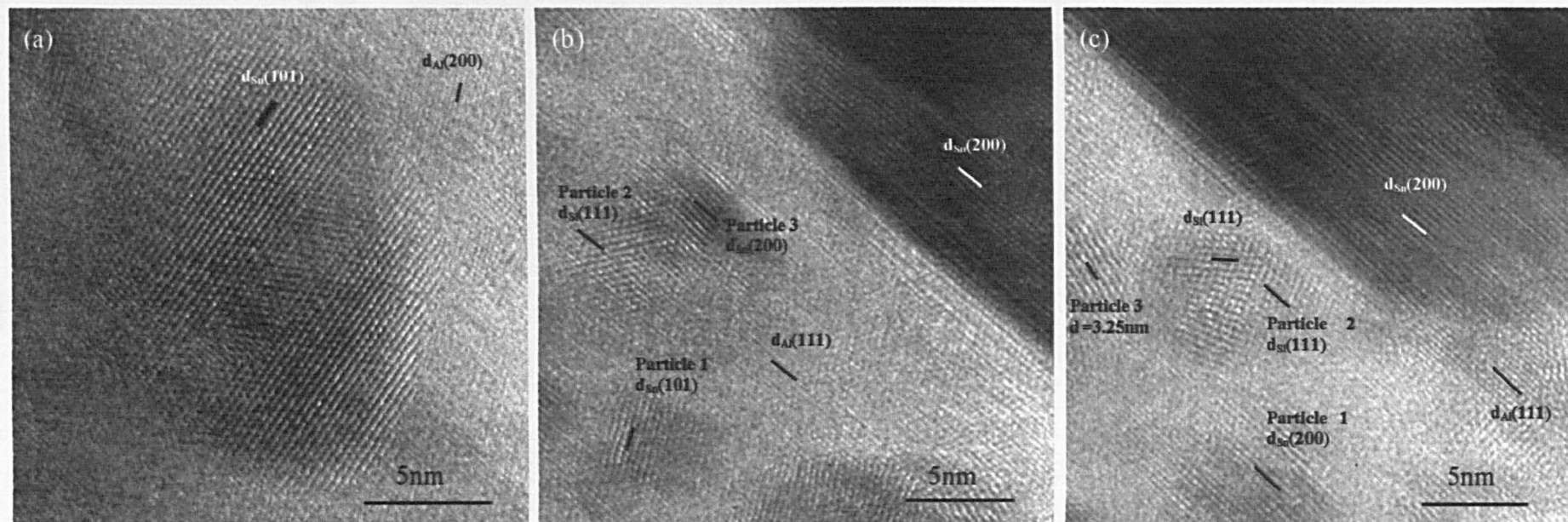


**Figure 7.12** HRTEM images showing the Sn/Si particles in the as-sprayed Al<sub>20</sub>Sn<sub>3</sub>Si coating. (a) A Sn particle (101) plane without clear orientation relationship with the matrix Al. (b) Large Sn particle with  $d_{\text{Sn}}(200) \parallel d_{\text{Al}}(111)$ ; particle 1 with Sn(101) fringe without a clear orientation relationship with the Al matrix; particle 2 with  $d_{\text{Si}}(111) \parallel d_{\text{Al}}(111)$ ; and particle 3 with  $d_{\text{Sn}}(200) \parallel d_{\text{Al}}(111)$ ; (c) Large Sn particle  $d_{\text{Sn}}(200) \parallel d_{\text{Al}}(111)$ ; particle 1 with  $d_{\text{Sn}}(200) \parallel d_{\text{Al}}(111)$ ; particle 2 with  $d_{\text{Si}}(111) \parallel d_{\text{Al}}(111)$ ; particle 3 unidentified

(Recorded by Dr. Mike Fay in Department of Electrical and Electronic Engineering, University of Sheffield)

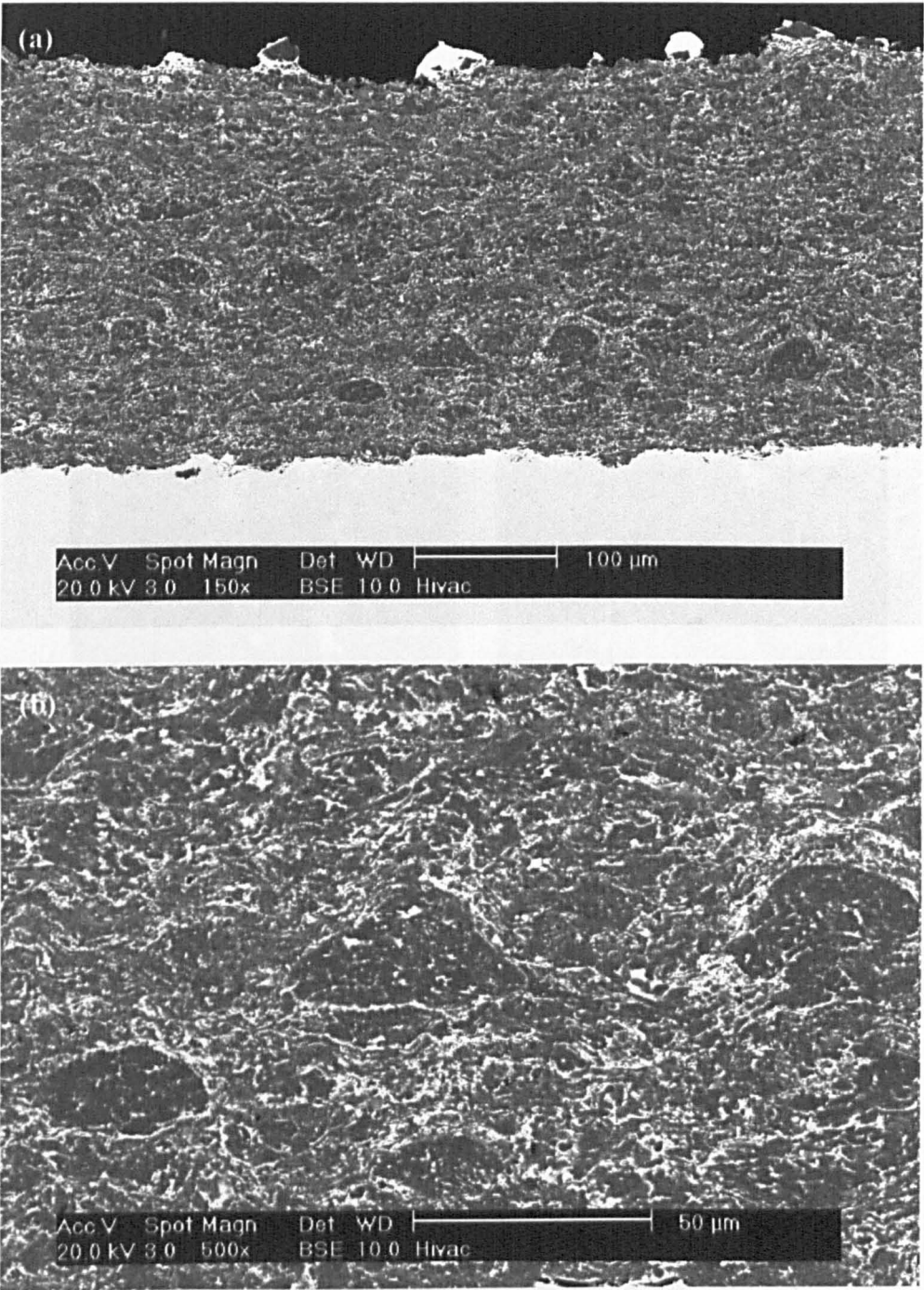


**Figure 7.13 BSE cross-sectional images of the Al<sub>2</sub>O<sub>3</sub>Sn<sub>3</sub>Si coating annealed at 300°C for 1 hour. (a) Low magnification; (b) higher magnification**



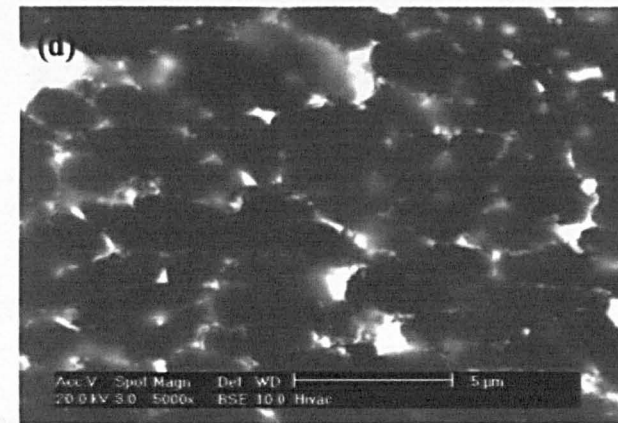
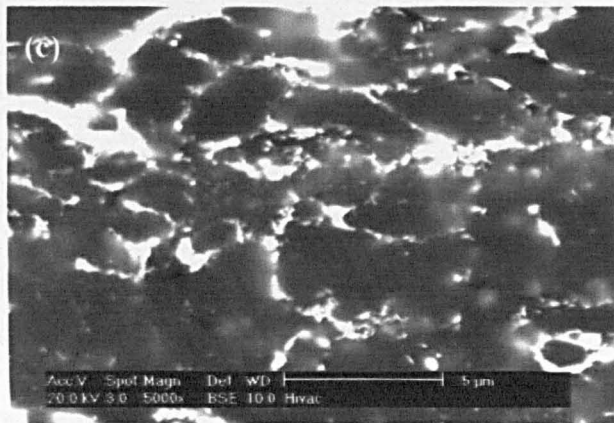
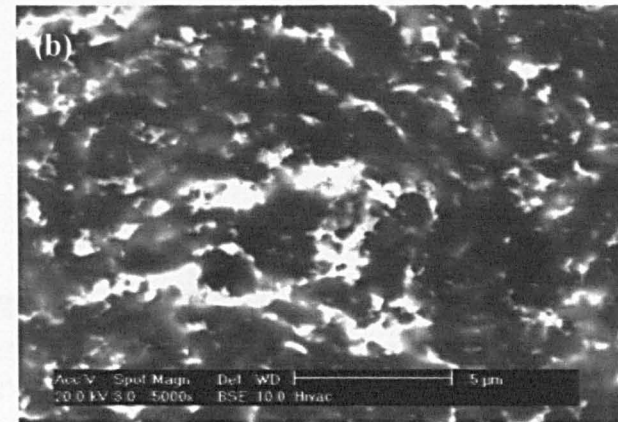
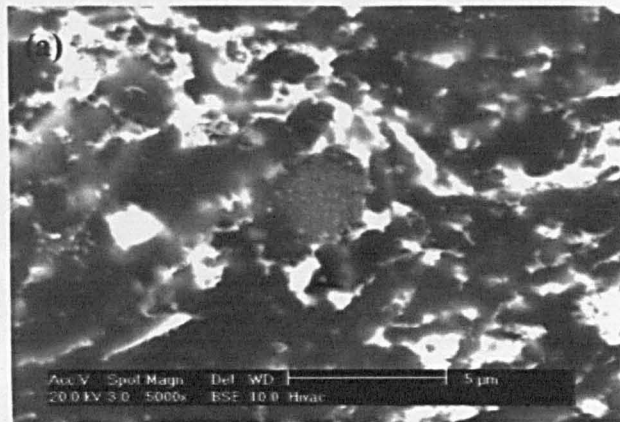


**Figure 7.14** High magnification BSE images of the Al<sub>2</sub>O<sub>3</sub>Sn<sub>3</sub>Si coating annealed at 300°C for 1 hour. (a, b) Originally melted as-sprayed region; (c, d) originally unmelted as-sprayed region.

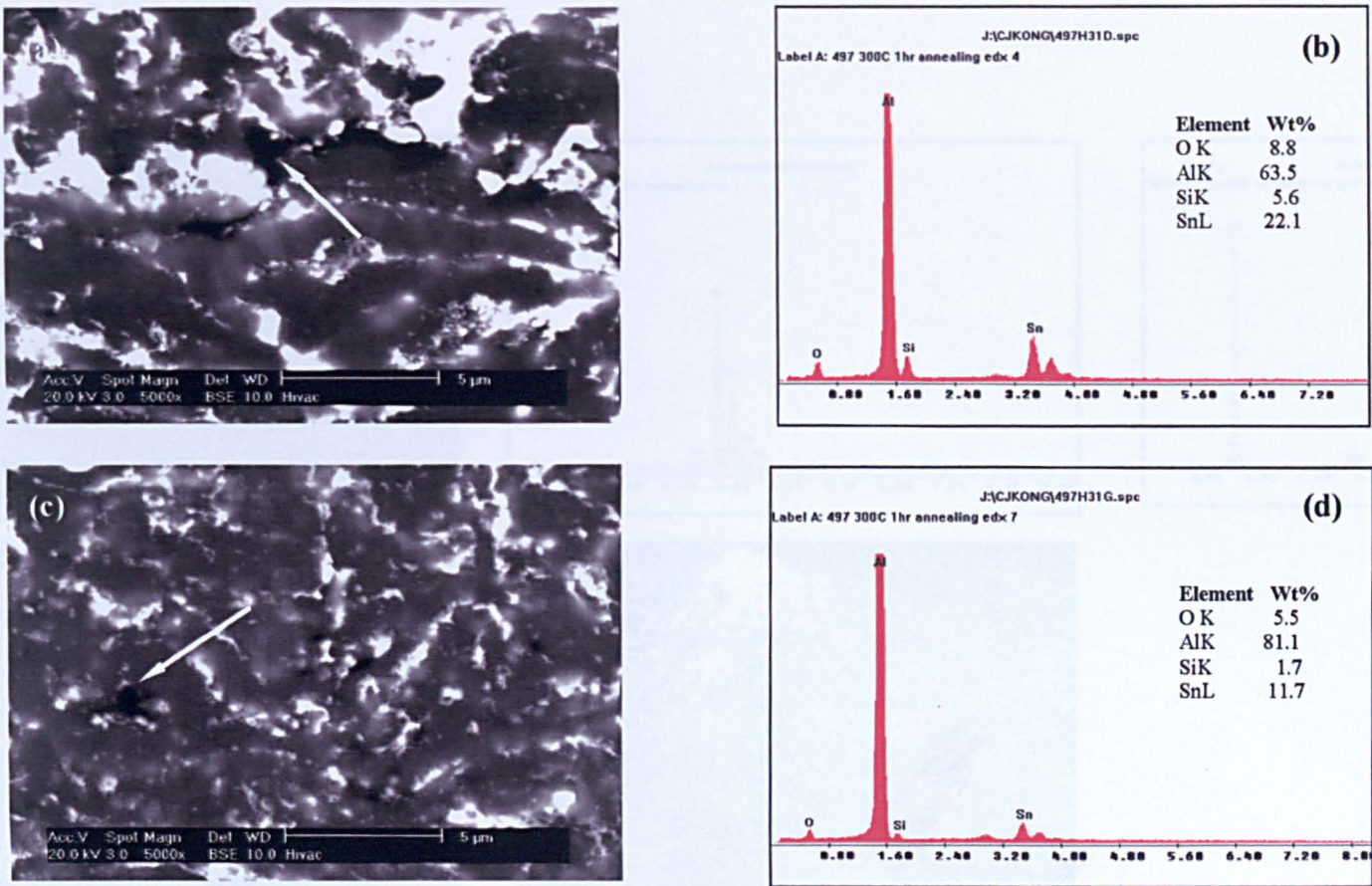
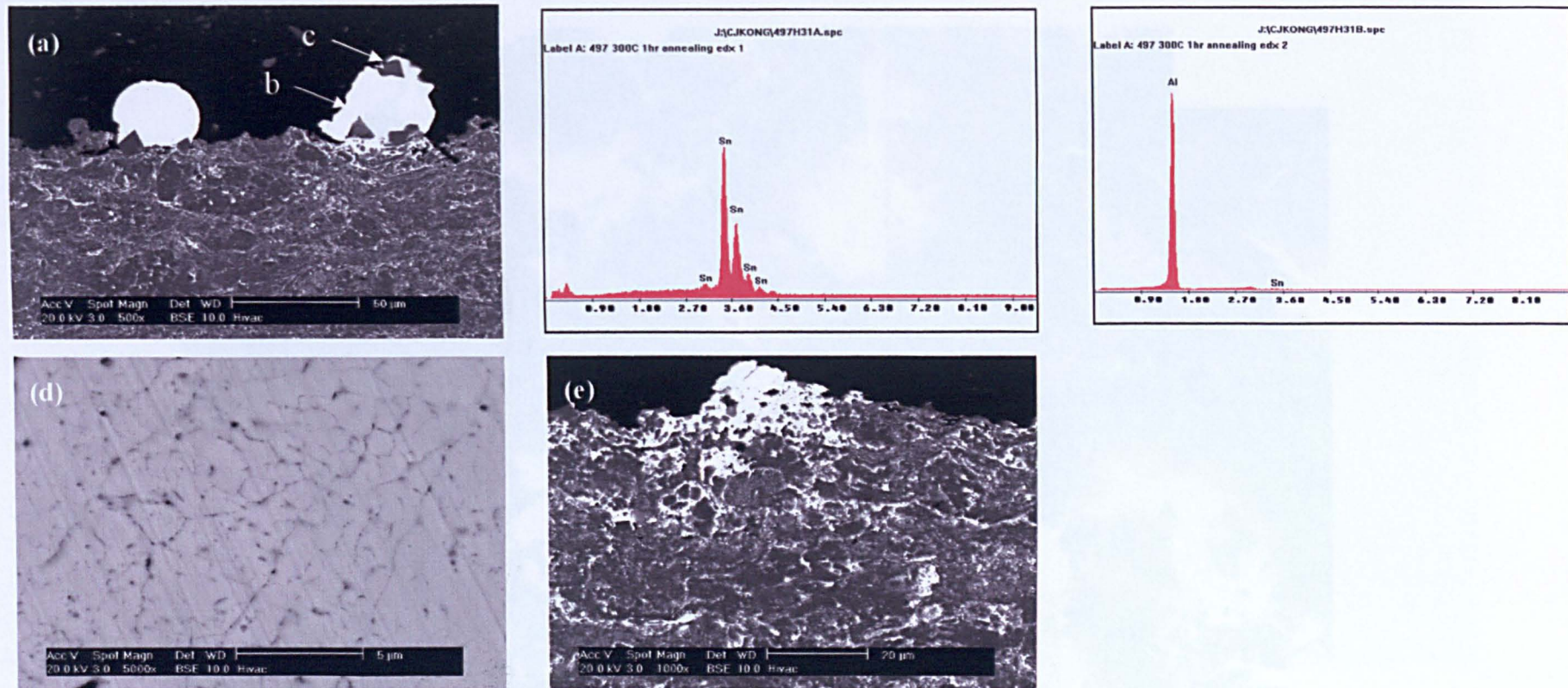


Figure 7.15 High magnification BSE images of the Al<sub>2</sub>O<sub>3</sub>Sn<sub>3</sub>Si coating annealed at 300°C for 1 hour. (a,c) Coating with crack or oxide; (b,d) EDX spectra of arrowed regions in (a,c), respectively.





**Figure 7.16** Surface precipitates on the Al<sub>20</sub>Sn<sub>3</sub>Si coating annealed at 300°C for 1 hour. (a,e) BSE images of surface precipitate; (c,d) EDX spectra of arrowed regions (b) and (c), respectively (d) high magnification BSE image of arrowed region (b) in image (a)



**Figure 7.17** TEM montage of the Al<sub>2</sub>O<sub>3</sub>Sn<sub>3</sub>Si coating annealed at 300°C for 1 hour.



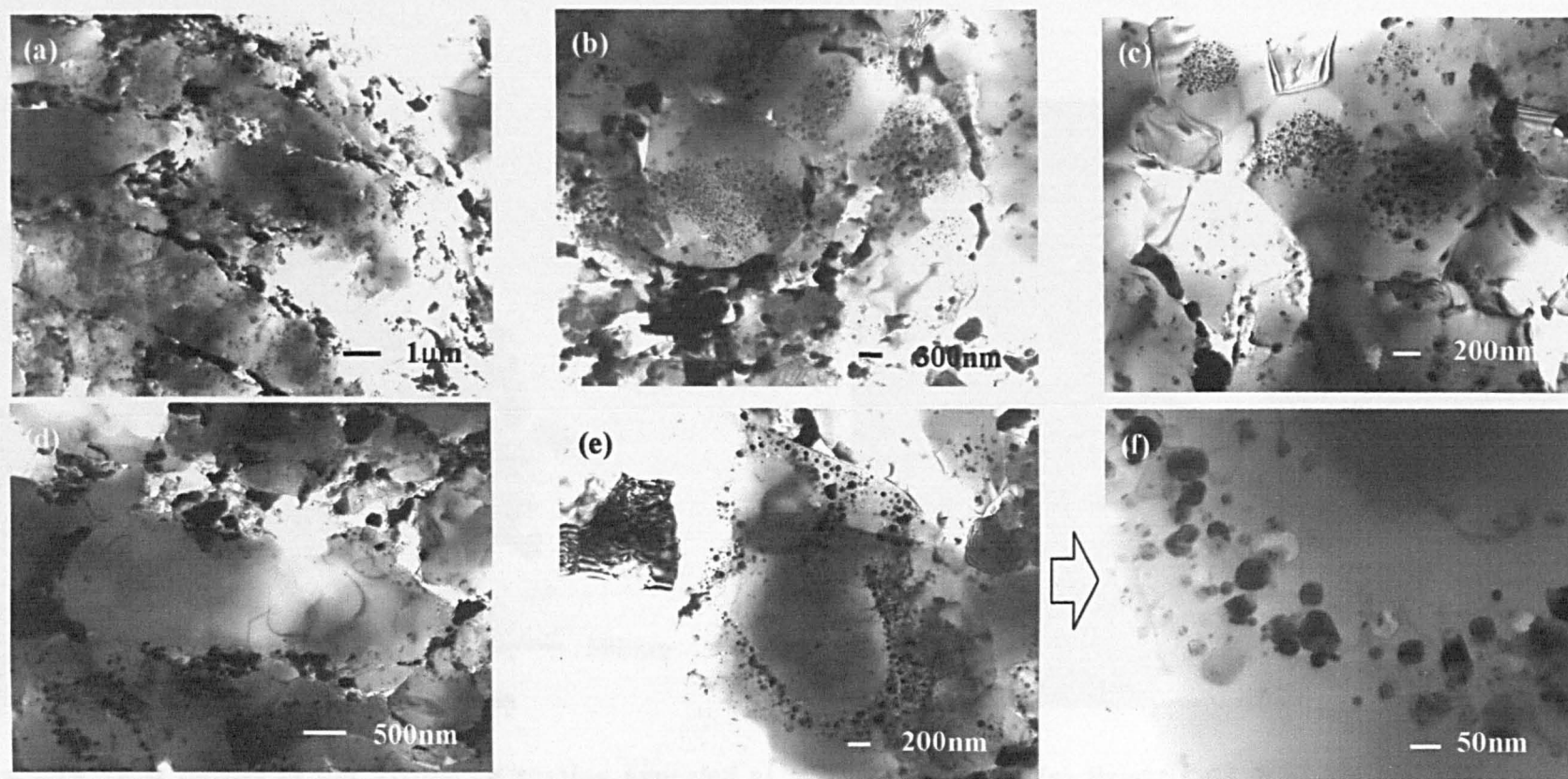


**Figure 7.18** TEM images of the Al<sub>20</sub>Sn<sub>3</sub>Si coating annealed at 300°C for 1 hour. (a) Linear Sn phase; (b, c) nanoscale Sn/Si particles; (d) Al grain decorated with coarse Sn particles; (e) Al grain decorated with fine Sn particles and (f) detail of (e).

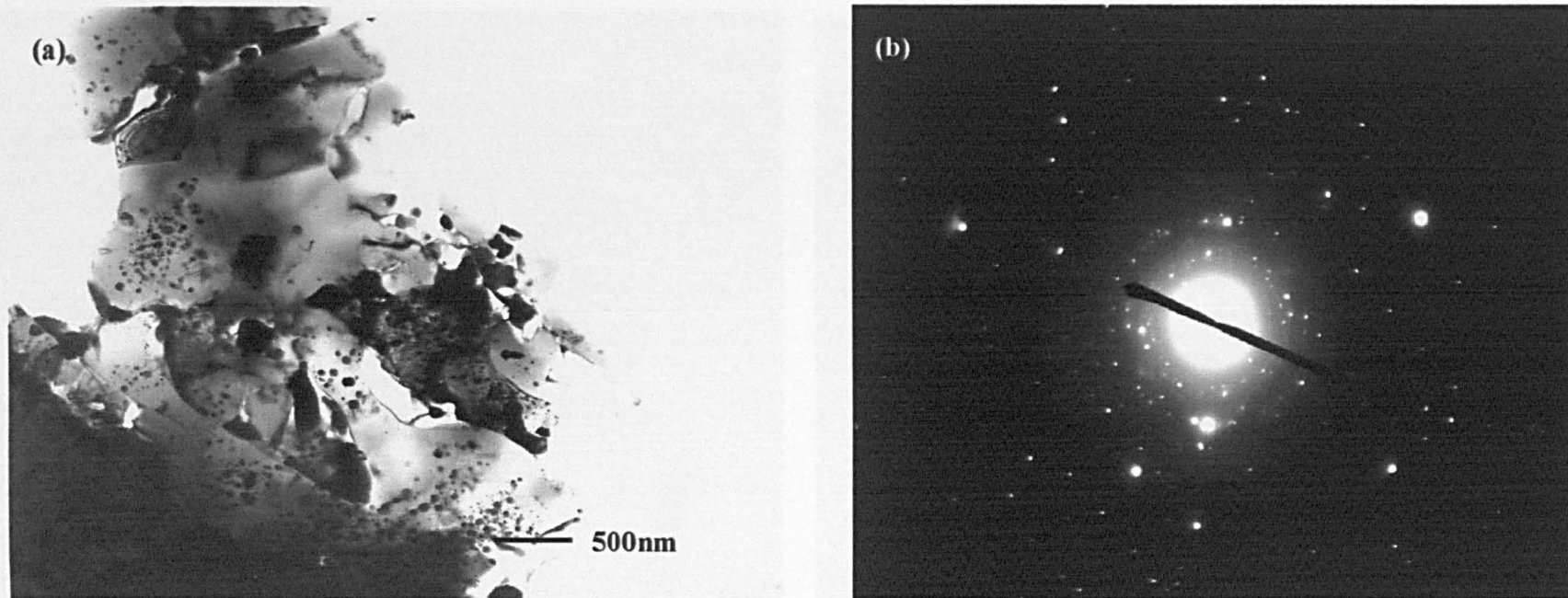


**Figure 7.19** TEM images of the Al<sub>2</sub>O<sub>3</sub>Sn<sub>3</sub>Si coating annealed at 300°C for 1 hour. (a) Bright field image; (b) associated diffraction pattern; (c) dark field image; (d) associated diffraction pattern.

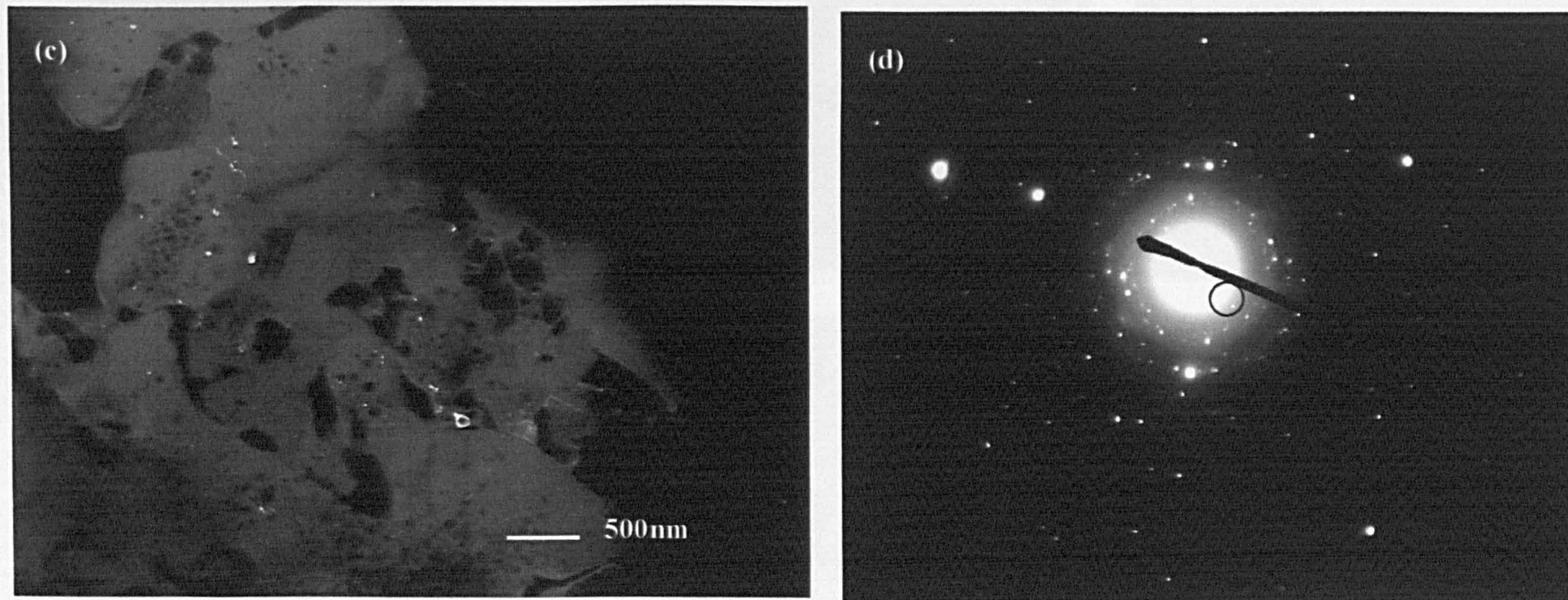


**Figure 7.19 (Continue) TEM images of the Al<sub>20</sub>Sn<sub>3</sub>Si coating annealed at 300°C for 1 hour. (a) Bright field image; (b) associated diffraction pattern; (c) dark field image; (d) associated diffraction pattern.**



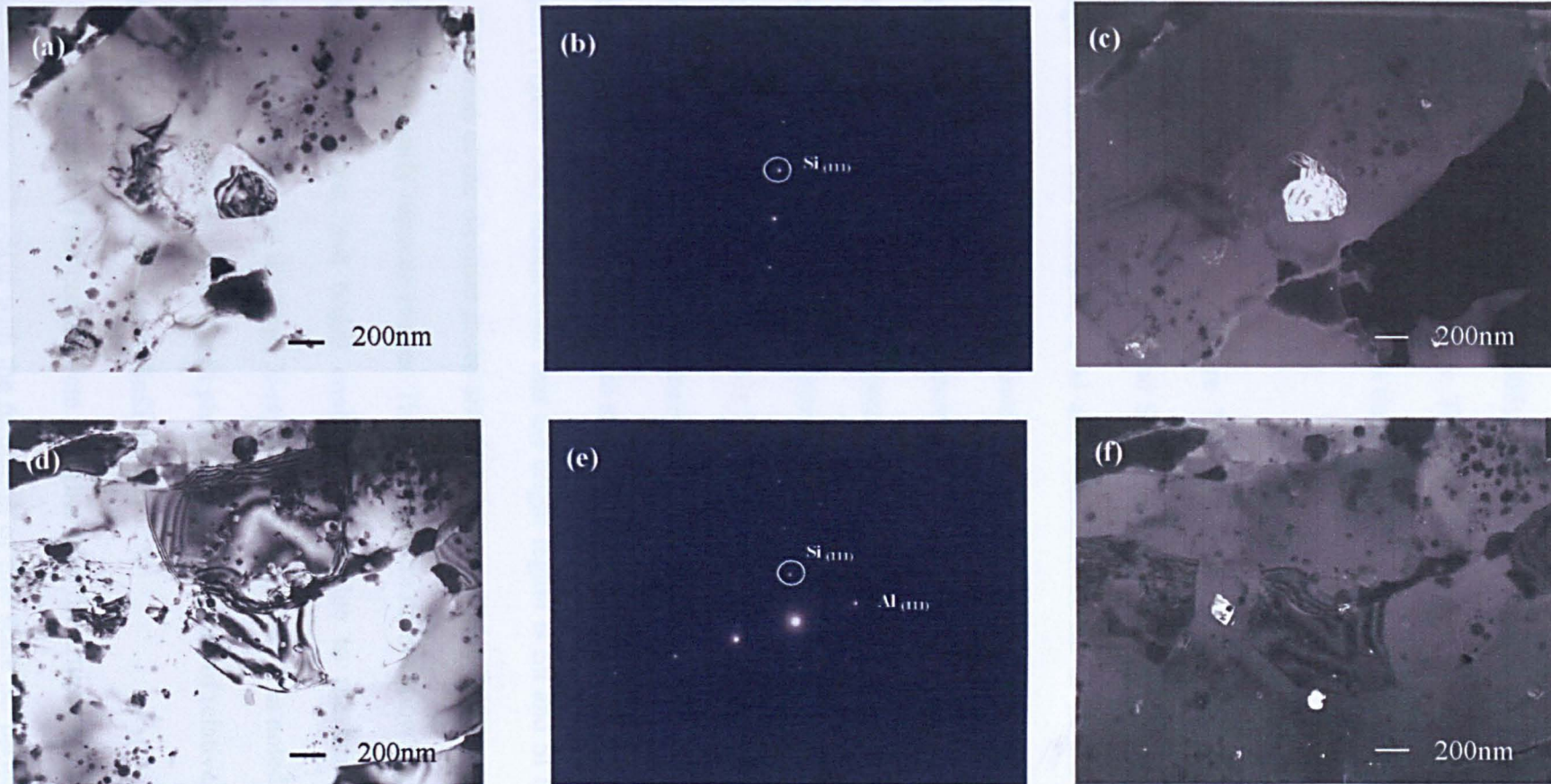


Figure 7.20 Si particle in the Al<sub>2</sub>O<sub>3</sub>Sn<sub>3</sub>Si coating annealed at 300°C for 1 hour. (a) Bright field image; (b) selected area diffraction pattern of Si particle (c) dark field image highlights the Si particle; (d) bright field image; (e) selected area diffraction pattern of (d); (f) dark field images highlight Si particles

## 7.6 Discussion

The thermally sprayed Al<sub>20</sub>Sn<sub>3</sub>Si coatings show many features, which are common with the Al<sub>12</sub>Sn<sub>1</sub>Cu alloy. Thus, the following discussion will focus on the microstructural differences between the Al<sub>12</sub>Sn<sub>1</sub>Cu and Al<sub>20</sub>Sn<sub>3</sub>Si alloys.

### 7.6.1 Gas atomised powder

The XRD spectrum (Figure 7.1) of the gas atomised Al<sub>20</sub>Sn<sub>3</sub>Si powder indicates that there exist Al, Sn and Si phases in these powder particles. The SEM images confirm that dendritic  $\alpha$ -Al and interdendritic Sn or Si are present in the large gas atomised Al<sub>20</sub>Sn<sub>3</sub>Si powder (Figure 7.4). Sub-micron and nanoscale dispersed Sn / Si particle are distributed within the small powder particles, and also in the shells which decorate the larger powder particles. Again, the critical cooling rate (discussed in Chapter 4) appears to control the formation of the final microstructure. If the cooling rate is lower than the critical cooling rate i.e. large powder, a cellular-dendritic Al structure with interdendritic Sn / Si forms. The comparative EDX analysis data from matrix region (Figure 7.4d) and bright contrast region (Figure 7.4e) demonstrate that the bright region is Sn and Si rich. However, the limitation of the electron probe size in relation to these small particles makes it difficult to identify separate phases. The EDX spectra do not show a great difference between the matrix and bright contrast regions due to the small size of the interdendritic phase and the large X-ray excitation volume. It is noted <sup>[3]</sup> that the Sn phase readily forms alongside the Si phase under conditions of relatively low cooling rate, i.e. for conventionally cast AlSnSi alloys.

Conversely, if the cooling rate is higher than the critical cooling rate, liquid phase separation will occur with the formation of fine scale Sn particles embedded



within the Al matrix. Small powder particles and the shell structures surrounding the larger powders particles (Figure 7.5) have undergone this kind of microstructure formation mechanism. Although the Si phase could not be unambiguously distinguished from the BSE images, the small Si peaks in the XRD pattern (Figure 7.1) clearly confirm the presence of the Si phase in the gas atomised powder.

### 7.6.2 As-sprayed Al<sub>20</sub>Sn<sub>3</sub>Si coatings

The cooling rate in thermal spraying is high enough for liquid phase separation in the AlSnSi alloy. Therefore, nanoscale Sn particles formed from the fully melted powder and micron / sub-micron plus nanoscale Sn particles formed in semi-melted powder (Figure 7.6 to Figure 7.9). The non-uniformities of the local cooling rate and the local composition also lead to the distribution of the fine scale Sn particle sizes in the different regions (Figure 7.8 and Figure 7.9). The Sn / Si particle sizes in the Al<sub>20</sub>Sn<sub>3</sub>Si as-sprayed coating (Figure 7.9a,d) are finer than those of the Al<sub>12</sub>Sn<sub>1</sub>Cu as-sprayed coating (Figure 4.2a,b). One possible reason is that Si, unlike Cu, does not promote the Al and Sn liquid phase separation during the rapid solidification process. Another possibility is that the Al<sub>20</sub>Sn<sub>3</sub>Si coating had undergone a higher cooling rate than during deposition than the Al<sub>12</sub>Sn<sub>1</sub>Cu alloy in this instance, due to the smaller average size of the powder particles.

XRD did not show a Si peak in the as-sprayed coating suggesting the volume fraction of Si is less than 2% and that the  $\alpha$ -Al matrix was supersaturated with Si. However, bright field diffraction patterns associated with fully melted and semi-melted regions (Figure 7.10) indicate that very fine scale Si particles exist in both regions according to the continuous Si diffraction rings (Figure 7.10b,d). In particular, the diffraction patterns of Al and Sn for the semi-melted regions (e.g. Figure 7.10d) show discrete spots, which means the Al and Sn grains, are

comparatively large and not numerous enough to satisfy every diffraction orientation. The challenge was to try to distinguish the Si from the Sn particles. A bright field image of nanoscale Sn / Si particles and the associated diffraction pattern are shown in Figure 7.11(a,b). The diffraction pattern shows the existence of an orientation relationship between some of the Sn / Si particles and the Al grain, i.e.  $d_{\text{Si}}(111) // d_{\text{Al}}(111)$  and  $d_{\text{Sn}}(200) // d_{\text{Al}}(111)$ . Since the interplanar spacing of Si(111) and Sn(200) is too close, the attempt to highlight the Si particle by dark field imaging was unsuccessful (Figure 7.11c).

However, the HRTEM images were able to distinguish Si particles from Sn particles. The HRTEM images show that some large Sn particles adopt an orientation relationship to the Al matrix with  $d_{\text{Sn}}(200) // d_{\text{Al}}(111)$ , whilst other orientations such as the (101) plane of Sn have no strong relationship to the Al matrix. The HRTEM images also confirm the existence of discrete Sn and Si particles with a size range less than 10 nm in the as-sprayed coating. Some of the small Sn particles adopt the same orientation relationship as the large Sn particles, whilst others show fringes attributed to the (101) plane without a strong orientation relationship to the Al matrix. The Si particles show the lattice parameter misfit in the HRTEM images and adopt the orientation relationship of  $d_{\text{Si}}(111) // d_{\text{Al}}(111)$ . The HRTEM results confirm the existence of nanoscale Si particles and the orientation relationship between the Sn and Si particles to the matrix is same as that indicated by the TEM diffraction pattern (Figure 7.11b). The partial orientation relationship between Sn and Al matrix and apparent distortion of a Si particle with the Al matrix may all attributed to the rapid cooling rate the alloy undergoes.

The formation of these fine scale Sn and Si particles is related to the solidification process. However, unlike the AlSnCu system, we need to consider

possible mechanisms for the formation of dispersed Si as well as dispersed Sn. The possible solidification sequence is as follows: First, it can reasonably be assumed that liquid phase separation occurs as  $L \rightarrow L_1(\text{Sn}) + L_2(\text{Al})$ , in the same fashion as the AlSnCu system. Then, at a low temperature, the Al-rich liquid solidifies with a high interface velocity. In this alloy, however, the  $L_2$  contains appreciable levels of Si. Hence, there are two possibilities. Either Si forms directly from the melt along with the Al, or Si precipitates from a supersaturated Al solid solution. In view of the fine scale of the Si particles, the latter seems the more likely mechanism.

### 7.6.3 The Al<sub>20</sub>Sn<sub>3</sub>Si coatings annealed at 300°C, 1 hour

The XRD spectrum of the annealed coating shows the presence of distinct Si peaks and this is taken as evidence for Si particle precipitation during the annealing process (Figure 7.3). The Al<sub>20</sub>Sn<sub>3</sub>Si coatings annealed at 300°C for 1 hour show a coarsening of the nanoscale and micron / sub-micron Sn particles in the BSE images of Figure 7.13 and Figure 7.14, and the TEM images of Figure 7.17 and Figure 7.18. The mechanism of liquid droplet movement within the solid matrix driven by a local temperature gradient<sup>[4]</sup> may again be used to explain the sub-micron and nanoscale Sn particle coarsening within the Al grain (Figure 7.17 circled region and Figure 7.18 b,c). Another possible mechanism<sup>[5]</sup> is that the recrystallization of the Al grains pushes the Sn particles to the grain boundaries, causing the coarsening (Figure 7.17 marked A and Figure 7.18 d-f). The latter mechanism could also be used to explain the particle denuded zone (Figure 7.18 b,c).

The presumed precipitation of the Si particles, however, would require a diffusion mechanism<sup>[6]</sup>. Bendijk<sup>[7]</sup> has reported that melt spinning Al-Si alloys greatly increases the metastable solid solubility of Si in Al due to the fast cooling rate. Liu<sup>[8]</sup> also reported that reheating of melt spun Al-Si alloys results in Si

precipitation within the Al grains for a 1wt% Si composition and the formation of Si precipitates at the Al grain boundaries for a 4wt% Si composition. Therefore, the heat treatment may promote supersaturated Si to precipitate from the Al matrix, which formed during the rapid solidification process. The discrete diffraction pattern rings of Si in the annealed coating (Figure 7.19 b,d) confirm the coarsening of Si particles because the number of Si particles cannot satisfy all the orientation relationships. The relatively larger Si particles have been identified from dark field images of Figure 7.20(c, f).

Annealing at 300°C for 1 hour also causes Sn migration to the surface in the Al<sub>20</sub>Sn<sub>3</sub>Si coating (Figure 7.16). Micron scale cracks or oxide also form in the annealed coating. This indicates that a lower annealing temperature or a shorter annealing time could be required for this coating.

In a similar fashion to the Al<sub>12</sub>Sn<sub>1</sub>Cu coatings, the microhardness of the Al<sub>20</sub>Sn<sub>3</sub>Si coatings decreases after 1 hour of annealing at 300°C. The combined effects of Sn and Si particle coarsening and Si precipitation from matrix will contribute to this. The relief of residual stress or even more the recrystallization of Al and Al grain growth also contribute to this microhardness decrease.

## 7.7 Summary

The pre-deposited gas atomised Al<sub>20</sub>Sn<sub>3</sub>Si powder adopts a cellular-dendritic structure for the larger powder particles (22-45 µm), with sub-micron / nanoscale Sn / Si particles in the smaller powders (5 µm).

In a similar fashion to the Al<sub>12</sub>Sn<sub>1</sub>Cu coating, the as-sprayed Al<sub>20</sub>Sn<sub>3</sub>Si coating comprises fully molten and partially molten regions. In the fully molten region, both Sn and Si are present in the form of nanoscale particles, with some of the Sn particles and most of the Si particles having a size of less than 10 nm. In the

partially molten regions, the particles are distributed with both micron / sub-micron and nanoscale sizes. The liquid-liquid phase separation mechanism may also be used to explain the presence of nanoscale Sn particles within these coatings. The formation mechanism of the Si particles has two possibilities. One is that the Si remains in the Al-rich liquid when liquid phase separation of Al and Sn occurs. Then, Si particles precipitate from the melt. The other possibility is that the Al matrix is supersaturated with Si and precipitated in the solid state. This could occur during the time a splat is reheated by the deposition of subsequent layers.

The orientation relationship between the Sn / Si particles and the Al matrix is confirmed by both selected area diffraction patterns and the HRTEM images. The Sn particles adopt a partial orientation relationship with the Al matrix, i.e.  $d_{\text{Sn}}(200) // d_{\text{Al}}(111)$ . The Si particles similarly exhibit an orientation relationship with the matrix, i.e.  $d_{\text{Si}}(111) // d_{\text{Al}}(111)$ .

In the coating annealed at 300°C for 1 hour, both Sn and Si particles coarsen greatly. The mechanism of liquid droplet movement within the solid matrix driven by a local temperature gradient may be used to explain the sub-micron and nanoscale Sn particle coarsening within the Al grains. Grain boundary movement caused by recrystallization of the Al could explain the Sn/Si particle coarsening in the grain boundaries and particle denuded zone. The Si particles will precipitate during the annealing process by a mechanism involving solid state diffusion, nucleation and growth.

With annealing at 300°C for 1 hour, the microhardness of the Al<sub>20</sub>Sn<sub>3</sub>Si coatings decreases greatly. This is attributed to the Sn / Si particle coarsening and the release of local residual stress from the as-sprayed process.

## References

1. G. Yuan, Z. Li, Y. Lou and X. Zhang, *Influence of silicon content on friction and wear characteristics of new Al-Sn-Si alloys*. Chinese Journal of Nonferrous Metals, 1998. 8(Sept.): p. 101-105.
2. T. Tanaka, M. Sakamoto and Y. Sato, *Multilayer aluminium-based alloy bearing having superior compatibility and superior fatigue resistance*. 1994: USA, Patent: US5362574.
3. G. C. Yuan, Z. J. Li, Y. X. Lou and X. M. Zhang, *Study on crystallization and microstructure for new series of Al-Sn-Si alloys*. Materials Science and Engineering, 2000. A280: p. 108-115.
4. M. McLean and M.S. Loveday, *In-situ observations of the annealing of liquid lead inclusions entrained in an aluminium matrix*. Journal of Materials Sciences, 1974. 9: p. 1104-1114.
5. M. F. Ashby and R.M.A. Centamore, *The dragging of small oxide particles by migrating grain boundaries in copper*. Acta Metallurgica, 1968. 16(September): p. 1081-1092.
6. D. A. Porter and K. E. Easterling, *Phase Transformation in Materials and Alloys*. 1983: Van Nostrand Reinhold (UK) Co. Ltd.
7. A. Bendijk, L. Katgerman, TH. H. Dekeijser, E. J. Mittemeijer and N. M. Vanderpers, *Characterization of Al-Si-alloy rapidly quenched from the melt*. Journal of Materials Science, 1980. 15: p. 2803-2810.
8. Lin Liu and Y. Dong, *Structural characteristic of rapidly quenched Al-Si alloys*. Journal of Materials Science and Technology, 1994. 10: p. 232-234.



---

## Chapter 8

### Conclusions

---

#### 8.1 Introduction

It has been demonstrated that high velocity oxy-liquid fuel (HVOLF) thermally sprayed Al alloy coatings have significant potential for application as automotive shell bearings. The microstructure of two principal alloy systems has been investigated, i.e. Al-12wt.%Sn-1wt.%Cu and Al-20wt.%Sn-3wt.%Si, in the form of gas atomised powder, as-sprayed and annealed coatings.

#### 8.2 The Al<sub>12</sub>Sn<sub>1</sub>Cu gas atomised powder and as-sprayed coatings

The characterisation of the Al<sub>12</sub>Sn<sub>1</sub>Cu gas atomised powder and HVOLF as-sprayed coatings indicates that the microstructure formation of this alloy is different depending on the cooling rate / undercooling of solidification. There exists a critical cooling rate for this alloy with a metastable miscibility gap. If the cooling rate is lower than the critical cooling rate,  $\alpha$ -Al primarily nucleates to form Al dendrites with interdendritic Sn, as characterised in large (>10  $\mu\text{m}$ ) gas atomised powders. If the cooling rate is higher than the critical cooling rate, liquid phase separation first occurs to form Al-rich and Sn-rich liquid regions, then the solid  $\alpha$ -Al nucleates and grows to entrap separated Sn droplets forming a dispersion of nanoscale Sn particles distributed within the Al matrix. Such microstructures were identified in small (<10  $\mu\text{m}$ ) gas atomised particles and within the thermally sprayed coatings.

The critical cooling rate of an Al12Sn alloy for liquid phase separation is calculated to be approximately  $1.8 \times 10^7 \text{ Ks}^{-1}$  which has been estimated by constructing a relationship between cooling rate and the extent of undercooling, in accordance with the literature. The calculated atomised particle size for liquid phase separation with  $\text{N}_2$  atomising gas is  $3\mu\text{m}$  for an Al12Sn alloy which is close to the experimental observations in the Al12Sn1Cu gas atomised powder ( $<10 \mu\text{m}$ ). The discrepancy between the calculated value and the experimental observation is attributed to the approximations in the calculation and the effect of the Cu addition on the phase equilibrium.

The cooling rate of the as-sprayed Al-Sn based coatings is higher than the critical cooling rate. Thus, the as-sprayed coatings exhibit a distribution of both micron / sub-micron and nanoscale Sn particles. The nanoscale Sn particles are formed by a liquid phase separation mechanism, whilst the micron / sub-micron Sn particles are remnant features from partially melted powder particles.

The amount of the Sn and Cu in the Al matrix affects the liquid phase separation reaction of the alloy. The presence of micron / sub-micron Sn particles within as-sprayed coatings is partially due to insufficient mixing of melted Sn with the surrounding Al matrix and partially due to the coarsening of Sn droplets during the rapid solidification of high Sn content Al alloys during powder particle melting.

### **8.3 Al12Sn1Cu annealed coatings**

The Al12Sn1Cu as-sprayed coatings were annealed at different temperatures for different lengths of time. Micron / sub-micron Sn particles coarsen with increasing annealing time and temperature. The mechanism of Sn liquid droplet

coarsening within the solid Al matrix is considered to be driven by local temperature gradients and possibly matrix recrystallization.

Two main orientation relationships between the Sn particles and the Al matrix were identified for the Al<sub>12</sub>Sn<sub>1</sub>Cu coating annealed at 300°C for 1 hour. The orientation relationships are (111)<sub>Al</sub> // (200)<sub>Sn</sub> and (200)<sub>Al</sub> // (200)<sub>Sn</sub>.

The microhardness of the coatings decreases greatly within the first hour of annealing, and tends to slow down with time increasing up to 5 hours at 300°C. This corresponds to a coarsening of micron / sub-micron and nanoscale Sn particles and the release of residual stress introduced by the process of thermal spraying. Annealing also induced the precipitation of the  $\theta'$  phase in the coatings, but this does not increase the microhardness due to its small volume fraction.

The as-sprayed Al<sub>12</sub>Sn<sub>1</sub>Cu coating and those annealed for 1 hour at 300°C did not show good corrosion resistance, mainly due to the existence of nanoscale and sub-micron Sn particles. Coatings annealed at 450°C for 1 hour present improved passivity in the anodic polarization tests because of coarsened Sn particles in the microstructure.

However, heat treatment temperatures of ~ 450°C are not appropriate for a bearing application because reaction products were found at the coating/substrate interface and interlayer cracks formed within the coating. A heat treatment temperature of 300°C did not induce an interface reaction. It is suggested that a much longer annealing time than 1 hour is needed to improve the corrosion resistance at this temperature.

#### **8.4 The Al<sub>20</sub>Sn<sub>3</sub>Si gas atomised powder and thermally spayed coatings**

The same general mechanisms developed to explain the microstructure of the Al<sub>12</sub>Sn<sub>1</sub>Cu alloy can be used to explain the microstructure of the Al<sub>20</sub>Sn<sub>3</sub>Si alloy.

The larger gas atomised Al<sub>20</sub>Sn<sub>3</sub>Si powder particles adopt a cellular - dendritic structure due to the cooling rate being lower than the critical cooling rate. The small powder particles present both the sub-micron and nanoscale Sn particle distributions because a higher cooling rate occurs promoting a liquid phase separation of Al and Sn.

In a similar fashion to the Al<sub>12</sub>Sn<sub>1</sub>Cu as-sprayed coating, the Al<sub>20</sub>Sn<sub>3</sub>Si as-sprayed coating comprised a mixture of fully-molten and semi-molten splats. Nanoscale Sn particles formed in the molten splats are due to the process of liquid phase separation during cooling. Micron / sub-micron Sn particles are partially due to the remnant dendritic structure inherited from partially melted splats and partially due to the high Sn content promoting Sn droplets coarsening in the partially melted splats. The main difference between Si and Cu containing alloys is that the former gave nanoscale Si particles with a size range less than 10 nm. The orientation relationships of Sn and Si particles to the Al matrix are:  $d_{\text{Sn}}(200) // d_{\text{Al}}(111)$  and  $d_{\text{Si}}(111) // d_{\text{Al}}(111)$ .

Annealing of Al<sub>20</sub>Sn<sub>3</sub>Si coatings at 300°C for 1 hour caused Sn and Si particles to coarsen. The mechanism of liquid droplet movement within the solid matrix could explain the Sn coarsening. Again, the microhardness of the coating decreased greatly as compared with the as-sprayed coating. This is attributed to the same mechanisms used for the annealed Al<sub>12</sub>Sn<sub>1</sub>Cu coating, i.e. the Sn particles coarsen with the release of local residual stress in the matrix after annealing.

## Future Work

1. The thermally sprayed AlSnCu coatings exhibit improved corrosion resistance as compared with an AlSn coating due to the additional Cu present. However, it is not appropriate to increase the Cu content to improve the strength of the coating because more Cu may cause over ageing of the coatings in service at a temperature ( $\sim 180^{\circ}\text{C}$ ). The precipitated Cu-rich compound may coarsen decreasing the strengthening effect of the matrix Al. Therefore, the elements Si, Mn and Ni could be used to increase Al matrix strength by solid solution strengthening or fine scale second phase dispersion. The microstructure evolution of the Si containing coatings has been investigated in the thesis. Further work needs to be performed on the microstructure evolution of Ni and Mn containing alloys.
2. To investigate the mechanical, chemical properties of the AlSnCuX (X = Si, Mn, Ni) coatings, such as microhardness, wear resistance, fatigue resistance and corrosion resistance following heat treatment. To investigate the relationship between the microstructural evolution and the mechanical, and chemical properties in particular the coarsening of the precipitates with temperature and time.
3. The interface reaction of the thermally sprayed AlSnCu coatings and the steel substrate has been investigated using SEM. More details of the interface reaction products of the AlSnCu and AlSnCuX (X= Si, Mn and Ni) alloys need to be investigated using for example, TEM. The interface reaction products and their relationship to annealing time and temperature need to be investigated systematically.

4. To investigate experimentally the basic scientific question of the critical undercooling needed for liquid phase separation as a function of Sn content over a range of 1-40wt%Sn in the Al-Sn system. The results should be compared with the calculated metastable immiscibility curve for this alloy.



## Publications:

1. CJ Kong, PD. Brown, AJ. Horlock, SJ. Harris, DG. McCartney, *Influence of high velocity spraying conditions on the microstructure and properties of an Al-12wt%Sn-1wt%Cu alloy*, Materials Science Forum, **396-402** (2002)1133-1138
2. CJ Kong, PD Brown, AJ Horlock, SJ Harris, DG McCartney, *TEM assessment of HVOLF thermal sprayed Al-12wt.%Sn-1wt.%Cu alloy*, The International Conference of Rapidly Quenched & Metastable Materials, 2002, edited by K. O' Reilly, P. Warren, P. Schumacher and B. Cantor, Materials Science and Engineering A, 375-377C (2004), 595-598
3. CJ Kong, PD Brown, AJ Horlock, SJ Harris, DG McCartney, *Microstructural characteristics of high velocity oxy-fuel thermally sprayed Al-12wt%Sn-1wt%Cu alloys*, Inst. Phys. Conf. Ser. No **168**, 2001, p227-230; Electron Microscopy and Analysis 2001, Dundee, Sept. 5-7.
4. Chang-Jing Kong, Grigore Moldoven, Mike Fay, D. Graham McCartney and Paul. D. Brown, *Characterisation of dispersions within annealed HVOLF thermally sprayed AlSnCu coatings*, Institute of Physics, conference series number **179** 2003, p254-248; Electron Microscopy and Analysis 2003, Oxford, Sept 3-5.

## In preparation:

1. CJ Kong, AJ. Horlock, SJ. Harris, DG. McCartney and PD. Brown, Microstructural characterisation of AlSnCu alloy gas-atomised powders and HVOLF thermal sprayed coatings
2. CJ Kong, PD. Brown, SJ. Harris and DG. McCartney, The effect of cooling rate to liquid phase separation of Al-12Sn-1Cu alloy
3. CJ Kong, PD. Brown, SJ. Harris and DG. McCartney, Effect of cooling rate and heat treatment on Si distribution in AlSnSi alloys
4. CJ Kong, PD. Brown, SJ. Harris and DG. McCartney, The affection of Sn particle to the corrosion resistance of AlSnCu spraying coatings